JPL Publication 89-26

Proceedings of the Thirteenth NASA Propagation Experimenters Meeting (NAPEX XIII)

Held at the Red Lion Inn, San Jose, California, June 29–30, 1989

Faramaz Davarian
Editor

August 15, 1989

National Aeronautics and Space Administration

Jet Propulsion Laboratory
California Institute of Technology
Pasadena, California

Proceedings of the Thirteenth NASA Propagation Experimenters Meeting (NAPEX XIII)

Held at the Red Lion Inn, San Jose, California, June 29–30, 1989

ORIGINAL PAGE
BLACK AND WHITE PHOTOGRAPH

JPL Publication 89-26

Proceedings of the Thirteenth NASA Propagation Experimenters Meeting (NAPEX XIII)

Held at the Red Lion Inn, San Jose, California, June 29–30, 1989

Faramaz Davarian
Editor

August 15, 1989

NASA
National Aeronautics and
Space Administration

Jet Propulsion Laboratory
California Institute of Technology
Pasadena, California

This publication was prepared by the Jet Propulsion Laboratory, California Institute of Technology, under a contract with the National Aeronautics and Space Administration.

PREFACE

The NASA Propagation Experimenters Meeting (NAPEX) is a forum convened to discuss the studies supported by the NASA Propagation Program. The reports delivered at this meeting by the management and the investigators of the program summarize the recent activities as well as plans for the future. Representatives from domestic and international organizations who conduct radio wave propagation studies are invited to NAPEX for discussions and exchange of information. This proceedings records the content of NAPEX XIII.

NAPEX XIII, which took place on June 30, 1989, at San Jose, California, was organized into an opening session and three technical sessions. In the opening session, NASA and JPL managers of the program addressed the audience, and these were followed by a presentation from the NASA Propagation Information Center. The first technical session, chaired by Mr. Richard Emerson of JPL, focused on mobile satellite propagation. A total of nine presentations were made at this session. The second technical session examined the propagation effects for frequencies above 10 GHz and included eight papers. Dr. David Rogers of COMSAT Laboratories was the chair for this session. The last technical session was exclusively devoted to Olympus/ACTS studies to highlight the importance of this subject and its potential for our program. The last session was chaired by myself, where four papers were delivered.

An important development in this years's meeting was the presence of a three-member review panel. The notable panel members were:

Professor Gert Brussaard of Eindhoven University of Technology
Dr. Stewart McCormick of the Department of Communications
Dr. David Rogers of COMSAT Laboratories

This panel was formed in the spirit of the NASA review panel of 1986 which very effectively reviewed the propagation program and made a set of consequential recommendations for improving the program. The panel members addressed the audience during the "closing remarks" period at the end of the meeting.

Our international participation included such countries as Canada, Italy, Japan, the Netherlands, and the United Kingdom. I would like to express my appreciation to all the participants of NAPEX XIII, beginning with Richard Horttor, who was the guest speaker at the reception/banquet on Thursday evening, June 29, 1989. I am particularly grateful to the panel members who paid close attention to the presentations and made enlightening comments that contributed to the success of the meeting. The efforts of Professors Ernest Smith and Warren Flock of the NASA Propagation Information Center in assisting me with the organization of our meeting as well as the banquet are acknowledged. I would also like to thank Mr. John Kiebler of NASA Headquarters for his uninterrupted support of the Propagation Program. Thanks are extended to the IEEE APS Conference steering committee, particularly Dr. Ray King, for hosting our meeting at the Red Lion Inn. And, lastly, I wish to extend my gratitude to Harold Yamamoto of JPL for his assistance in compiling and preparing the proceedings for publication.

NAPEX XIV is planned for May 1990 in Austin, Texas.

Faramaz Davarian
Project Manager
NASA Propagation Studies

ABSTRACT

The NASA Propagation Experimenters Meeting (NAPEX), supported by the NASA Propagation Program, is convened annually to discuss studies made on radio wave propagation by investigators from domestic and international organizations. NAPEX XIII was held on June 29 and 30, 1989, at the Red Lion Inn, San Jose, California, and consisted of representatives form England, Italy, Japan, the Netherlands, and the United States. The meeting was organized into three technical sessions: The first focused on mobile satellite propagation; the second examined the propagation effects for frequencies above 10 GHz; and the third addressed studies devoted exclusively to the Olympus/Advanced Communications Technology Satellite (ACTS) Program.

CONTENTS

NAPEX XIII ATTENDEES

Mr. Bertram Arbesser-Rastburg
ESA-ESTEC, Mailcode: XEP
P.O. Box 299
NL-2200 AG Noordwick
The Netherlands
Phone: +31-1719-84541

Mr. Michael Barts
Virginia Tech.
Dept. of Electrical Eng.
Blacksburg, VA 24061
Phone: (703) 231-6834
FAX: (703) 231-6390

Mr. Jeffrey Berner
Jet Propulsion Laboratory, 161-228
4800 Oak Grove Drive
Pasadena, CA 91109
Phone: (818) 354-3934
FAX: (818) 393-4643

Prof. Charles W. Bostian & Freida
Virginia Tech.
Dept. of Electrical Eng.
Blacksburg, VA 24061
Phone: (703) 231-6834
FAX: (703) 231-6390

Dr. Gert Brussaard
Eindhoven University of Technology
Faculty of Electrical Engineering
EH 12.33
P.O. Box 513
5600 MB Eindhoven
The Netherlands
Home Phone: 31-40-433273
Home FAX: 31-40-456888

Dr. Richard L. Campbell
Michigan Technical University
Dept. Of Electrical Engineering
Houghton, MI 49931
Phone: (906) 487-2848
FAX: (906) 487-2949

Prof. Robert K. Crane & Emma
Thayer School of Engineering
Dartmouth College
Hanover, NH 03755
Phone: (603) 646-3843
FAX: (603) 646-2384

Dr. Faramaz Davarian
Jet Propulsion Laboratory, 161-228
4800 Oak Grove Drive
Pasadena, CA 91109
Phone: (818) 354-4820
FAX: (818) 393-4643

Dr. Khaled Dessouky
Jet Propulsion Laboratory, 161-228
4800 Oak Grove Drive
Pasadena, CA 91109
Phone: (818) 354-0412
FAX: (818) 393-4643

Mr. Richard F. Emerson
Jet Propulsion Laboratory, 238-420
4800 Oak Grove Drive
Pasadena, CA 91109
Phone: (818) 354-3848
FAX: (818) 393-6825

Dr. Ermanno Fionda
Fondazione Bordoni
Viale Europa 190
00100 Roma, Italy
(Currently visiting Ed Westwater)

Prof. Warren L. Flock
ECE Dept., CB 425
University of Colorado
Boulder, CO 80309
Phone: (303) 492-7012
FAX: (303) 492-2758

Dr. Yoji Furihama
ATR Optical and Radio
Communications Research Labs.
Sanpeidani Inuidani
Seika-cho Soraka-gun
Kyoto 619-02 Japan
Phone: +81-7749-5-1511
FAX: +81-7749-5-1508

Mr. J. Gavan
Drake Drive 1536
Davis, CA 95616
Phone: (316) 757-1127

Dr. Julius Goldhirsh
Johns Hopkins University
Building 23
Applied Physics Lab.
Laurel, MD 20707
Phone: (310) 953-5042
FAX: (301) 953-1093

Dr. Nasser Golshan
Jet Propulsion Laboratory, 161-228
4800 Oak Grove Drive
Pasadena, CA 91109
Phone: (818) 354-0459
FAX: (818) 393-4643

Mr. George H. Hagn
SRI International
1611 N. Kent St.
Arlington, VA 22209
Phone: (703) 247-8470
FAX: (703) 247-8569

Mr. Yoshihiro Hase
EERL, University of Texas
10100 Burnet Road
Austin, TX 78758
Phone: (512) 471-8606
FAX: (512) 471-8609

Ms. Loretta Ho
Jet Propulsion Laboratory, 161-228
4800 Oak Grove Drive
Pasadena, CA 91109
Phone: (818) 354-1724
FAX: (818) 393-4643

Tetsushi Ikegami
Communications Research Lab.
Kashima Research Center, MPT
Kashima, Ibaraki 314
Japan
Phone: +81-462-40-2800

Dr. Louis Ippolito
Stanford Telecommunications
1761 Business Center Drive
Reston, VA 22090
Phone: (703) 759-1069
FAX: (703) 759-1112

Mr. John Kiebler
NASA Headquarters, Code EC
600 Independence Ave.
Washington, DC 20546
Phone: (202) 453-1506
FAX: (202) 755-4786

Dr. and Mrs. Ray J. King
Lawrence Livermore Natl. Labs.
L-156 Engineering Research Div.
Livermore, CA 94550
Phone: (415) 423-2369
FAX: (415) 422-3013

Mr. John McKeeman
SATCOM Group, Dept. of EE
Virginia Tech.
Blacksburg, VA 24061-0111
Phone: (703) 555-1212
FAX: (703) 231-6390

Mr. Dean Olmstead
NASA Headquarters
600 Independence Ave.
Washington, DC 20546
Phone: (202) 453-1506
FAX: (202) 755-4786

Prof. Aldo Paraboni
Politecnico di Milano
Piazza Leonardo Da Vinci, 32
20133 Milano
Italy
Phone: +39-2-239-3586
FAX: +39-2-239-9856

V.S. Murthy Renducintala
Dept. of Electrical Eng.
University of Bradford
Bradford BD7 IDP
England
Phone: 44-274-733466, Ext. 6199
FAX: 44-274-430540

Dr. David V. Rogers
COMSAT Labs.
22300 COMSAT Drive
Clarksburg, MD 20871
Phone: (301) 428-4411
FAX: (301) 428-7747

Mr. Charles Ruggier
Jet Propulsion Laboratory, 161-228
4800 Oak Grove Drive
Pasadena, CA 91109
Phone: (818) 354-1823
FAX: (818) 393-4643

Mr. Thomas Russell
Stanford Telecommunications
2421 Mission College Blvd.
Santa Clara, CA
Phone: (408) 748-1010
FAX: (408) 980-1066

Dr. Kamran Shaik
Jet Propulsion Laboratory, 161-135
4800 Oak Grove Drive
Pasadena, CA 91109
Phone: (818) 354-9176
FAX: (818) 354-6825

Prof. Ernest K. Smith
ECE Dept., CB 425
University of Colorado
Boulder, CO 80309-00425
Phone: (303) 492-7123
FAX: (303) 492-2758

Mr. Jack B. Snider
Wave Prop. Lab., ERL/NOAA
325 Broadway
Boulder, CO 80303
Phone: (303) 492-6735
FAX: (303) 497-6750

Prof. Warren Stutzman
Virginia Tech.
Dept. of Electrical Eng.
Blacksburg, VA 24061
Phone: (703) 231-6834
FAX: (703) 231-6390

Mr. Arvydas Vaisnys
Jet Propulsion Laboratory, 161-228
4800 Oak Grove Drive
Pasadena, CA 91109
Phone: (818) 354-6219
FAX: (818) 393-4643

Dr. Wolfhard J. Vogel
University of Texas, EERL
10100 Burnet Road
Austin, TX 78758
Phone: (512) 471-8608
FAX: (512) 471-8609

Dr. E. R. Westwater
Wave Prop. Lab., ERL/NOAA
325 Broadway
Boulder, CO 80303
Phone: (303) 497-6527
FAX: (303) 497-6750

NAPEX XIII SUMMARY

Faramaz Davarian
Jet Propulsion Laboratory
California Institute of Technology
Pasadena, CA 91109

Ernest K. Smith
NASA Propagation Information Center
University of Colorado
Boulder, CO 80309

The thirteenth of the recent (1980s) series of NASA Propagation Experimenters Meetings (NAPEX XIII) was held on Friday, June 30, 1989, at the Red Lion Inn in San Jose in conjunction with the 1989 IEEE Antennas and Propagation Society International Symposium and URSI National Radio Science Meeting, June 26-30. The NAPEX meeting was preceded by a reception and a banquet on Thursday evening, June 29, also at the Red Lion Inn, at which the guest speaker was Richard Horttor, whose topic was the NASA Planetary Program. There were 38 present at the reception and banquet, which included wives, and 36 at the technical meeting, the largest attendance so far. Foreign participants included Mr. Bertram Arbesser-Rastburg of ESA-ESTEC, Mr. Yoshihiro Hase and Tetsushi Ikegami of CRL, Tokyo, Dr. Ermanno Fionda of Fondazione Bordoni in Rome, Dr. V.S. Murthy Renducinatala of the University of Bradford in England, and Prof. Aldo Paraboni of Politecnico di Milano; guests at the banquet included Dr. and Mrs. Ray J. King and Dr. Yoji Furuhama of ATR Kyoto.

A new feature of this meeting was the establishment of a Review Committee similar to the panel that carried out the NASA Science Review of the Propagation Program in September 1986. The members of the Review Committee are Prof. Gert Brussaard, Dr. K. Stewart McCormick, and Dr. David V. Rogers. NASA Headquarters was represented at NAPEX XIII by John Kiebler, Headquarters manager for the Propagation Program, and Dean Olmstead, ACTS Program Manager.

In his opening talk at the technical meeting, John Kiebler reviewed the program of the Communications and Information Division and the present budget situation. He was followed by Warren Flock who described the newly formed NASA Propagation Information Center at the University of Colorado.

The first of three technical sessions was on Mobile Satellite Propagation Experiments and was chaired by Dick Emerson of JPL. There were nine papers covering, first, the JPL work and then the experimental program in Australia which Wolf Vogel and Geoff Torrence of the University of Texas had carried out with assistance from AUSSAT last fall. Tetsushi Ikegami of the Communications Research Laboratories in Tokyo reported on experiments with ETS-V and planning for ETS-VI, Prof. Warren Stutzman of VPI gave the status of LMSS modeling work and Dr. Faramaz Davarian reported on the Aeronautical Mobile-Satellite text prepared for CCIR.

Session No. 2, Propagation Experiments above 10 GHz, was chaired by Dr. Rogers of COMSAT Labs. This session contained a review by Prof. Robert K. Crane of Dartmouth on the consistency of present propagation databases in which he found the quality control in the recent ESA program to be better than the earlier NASA one. This was followed by reports on radar rain studies by Julius Goldhirsh of Johns Hopkins Applied Physics Lab., on the extensive radiometric work carried out by the Wave Propagation Laboratory of NOAA by Jack Snider, a description of an optical study at JPL by Dr. Kamran Shaik, and two talks on European studies. The first, by Mr. Bertram Arbesser-Rastburg, summarized recent OPEX (Olympus Propagation Experiments) achievements, and the second, by Prof. Paraboni, described the Italsat experiment plan.

Session No. 3, ACTS, was chaired by Dr. Faramaz Davarian. Dean Olmstead, ACTS program manager, reviewed present status and future expectations. Dr. Davarian presented the NASA Propagation Experiments plan and announced an ACTS Propagation Workshop to be held at or near JPL in November 1989. Warren Stutzman described the U.S. activity with the Olympus Satellite (a test bed for future ACTS work) and John Kiebler presented the management plan proposed by NASA Headquarters.

The Review Committee was invited to say a few words in the wrap-up. Prof. Brussaard commented favorably on the increased cooperation evident in the program. Dr. McCormick had rated the presentation in a short term to long term scale (he clearly preferred the long view) and Dr. Rogers spoke favorably of the handbooks and CCIR participation. He also indicated that the Review Committee would be going over the 14 recommendations made by the Science Review Panel in 1986 to assess progress toward meeting their terms.

NASA'S COMMUNICATIONS AND INFORMATION SYSTEMS DIVISION

PROGRAM OVERVIEW

John Kiebler
NASA Headquarters
Washington, DC 20546

Communications Program Objectives

- Maintain U.S. Leadership in Space Communications

- Enable New and Innovative Services
  - NASA Scientific Needs
  - U.S. Industry
  - Public Sector

- Conserve the ARC/Spectrum Resource Through Technology Innovations

- Support U.S. and NASA Interests in Domestic and International Regulatory Forums

Information Systems Program Objectives

- Provide Timely and Responsive Information Systems for OSSA Scientific Research
  - Data Assimilation, Archiving, and Distribution
  - Scientific Computing
  - Networking

- Integrate OSSA Data and Information Systems Requirements
  - Achieve Economies and Efficiencies through Consolidation and Commonality
  - Influence Office of Space Station and Office of Space Operations Design and Development

- Provide Framework to Insert Advances in Information Systems Technology

Communications Program Components

- Radio Science and Support Studies
  - Orbit and Spectrum Utilization
  - Propagation
  - Advanced Studies

- Communications Systems
  - Search and Rescue
  - Mobile Satellite
  - Personal Communications

- Optical Communications
  - High-Power, Single-Frequency Laser Development
  - Advanced Composites for Lightweight Optical Antenna Systems
  - Engineering Model Optical Communications Subsystem Development (Gimbals, Array Trackers)
  - Optical Power Summing System Development

- Communications Subsystem Development
  - MMIC Phased Array Antennas
  - Modulation and Coding
  - On-board Digital Processing

- Flight Program
  - ACTS and ACTS Experiments Program

COMMUNICATIONS PROGRAM

FY 1988 AND FY 1989 NON-ACTS APPROVED FUNDING

FY 1989 - $17.6M

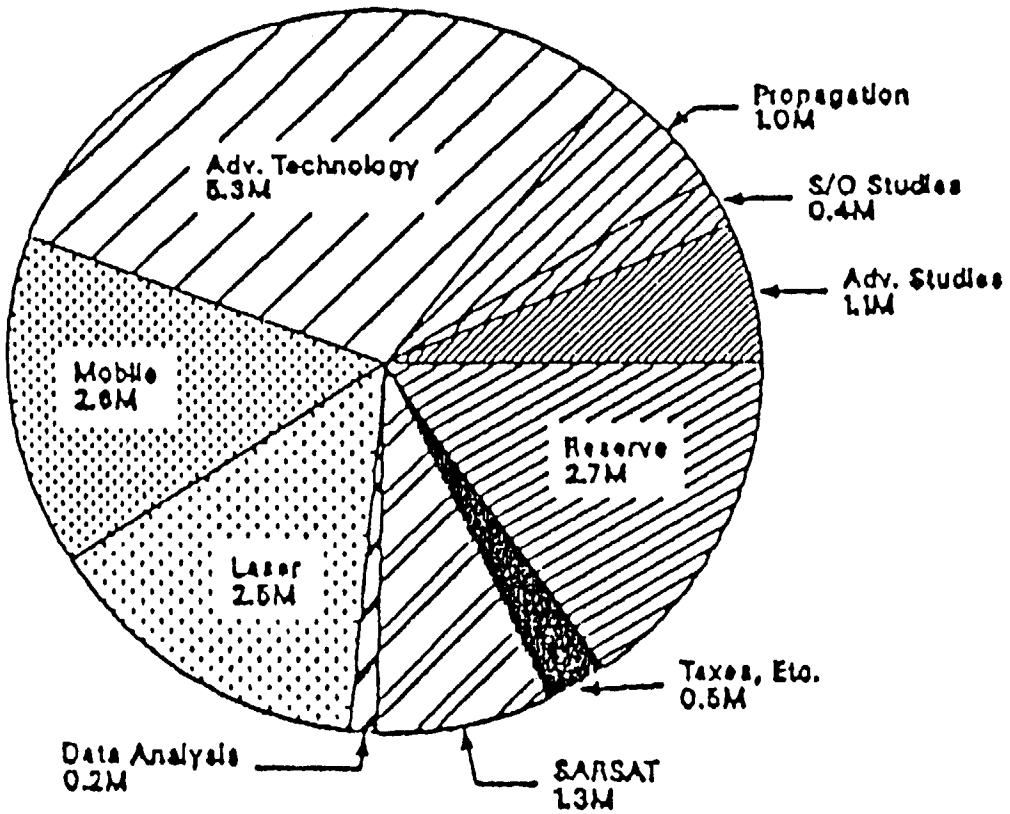

SATELLITE COMMUNICATIONS APPLICATIONS RESEARCH PROGRAM (SCAR) NRA

"The Satellite Communications Applications Research Program supports the advancement of satellite based communications technology systems which show promise for future use by the U. S. space communications industry"

GOALS

- Support innovative applied research in satellite communications, from both the private and public sectors.

- Support satellite communications research on "cutting edge" enabling technologies which could be instrumental in defining future plans and implementing new programs and services of the U. S. commercial space communications industruy.

- Support research requiring access to NASA unique facilities, both ground and space, for experimentation with new space communications devices, technologies, techniques, and applicqtions.

SATELLITE COMMUNICATIONS APPLICATIONS RESEARCH PROGRAM (SCAR) NRA

STATUS

119 Requests for Draft NRA Received

113 From Private Sector

14 From Universities

2 From Foreign Sources

Requests for the draft NRA and the following response are indicative of the level of interest.

"I would like to applaud the NASA initiative toward fostering advancement of American satellite communications technology. As in the consumer electronics industry and other areas, we have seen a constant erosion of U.S. development initiative and a loss of development and manufacturing expertise to the Japanese."

Paul Hashfield, Head
Communications Technology Research
David Sarnoff Research Center

SCAR NRA Calendar

NRA Released	July 14, 1989
Letters of Intent Due	August 11, 1989
Preproposal Conference	August 25, 1989
Proposals Due	October 13, 1989
Awards	November 30, 1989

NASA PROPAGATION INFORMATION CENTER

Ernest K. Smith and Warren L. Flock
University of Colorado at Boulder
Department of Electrical and Computer Engineering
Boulder, CO 80309

Abstract

The NASA Propagation Information Center became formally operational in July 1988. It is located in the Department of Electrical and Computer Engineering of the University of Colorado at Boulder. The Center is several things: a communications medium for the Propagation program with the outside world, a mechanism for internal communication within the program, and an aid to management. The staff consists of Professors (adjunct and emeritus) Ernest K. Smith and Warren L. Flock, and Research Assistant Lisa Leonard.

Introduction

The NASA Science Review Panel of 1986 in its report made several points. Among them were these:

- The effectiveness of the program would be enhanced by cooperative projects with other organizations.
- There should be a mechanism for monitoring propagation research of other governmental and industrial organizations.
- NASA should take a leading role in the harmonizing and pooling of propagation data from relevant organizations by defining data acquisition/processing standards.
- The acclaimed Propagation Handbooks should be updated periodically, preferably in coordination with the 4-year CCIR cycle.
- The CCIR support activities should be maintained within the propagation program.
- NAPEX meetings are a good thing and should be continued.

These points provided some of the incentive for the creation of the NASA Propagation Information Center. It is fairly modest in scope financially, The two co-directors account for one quarter of a man year between them and our secretary cum research assistant is half time during the school year, and somewhat less during the summer.

Reality has turned out somewhat differently from expectation. Cooperative programs have moved forward apace with activities

involving, or under discussion with, ESA, AUSSAT, and CRL (Japan) but the Information Center per se has had no hand in these activities. Uncovering future plans of government and industrial organizations, unless they have been published, is easier said than done. However, attendance at conferences is a good way to keep up with research that is already underway. The opportunity to contribute to the harmonizing and pooling of propagation data will logically take place at the ACTS Workshop planned for 4 to 8 months from now. However the Information Center can take pride in its contributions to the later three areas, as well as a few additional ones..

Activity

Since the initiation of the grant in July 1988 the NASA Propagation Information Center has:

a) Produced four quarterly NASA Earth-Space Propagation Newsletters with an increasing demand with each edition [W. L. Flock].

b) Carried out a review, proposed modification, and prepared the mailing list for the Ippolito handbook (Reference 2) [EKS].

c) Travelled to San Jose in October, 1988 to make initial preparations for NAPEX XIII and coordinated arrangements thereafter, working with JPL and NASA [EKS].

d) Assisted JPL in the preparation of a significant aeronautical mobile satellite text for CCIR SG-5, and participated in the U.S. preparatory work in Study Group 6 [EKS].

e) Organized and implemented a subject/author retrieval system for propagation references [WLF/LL].

f) Provided support to CCIR USSG-5/6, URSI Commission F, and the IEEE Wave Propagation Standards Committee for their meetings in Boulder.

g) Organized and coordinated a monthly Communications Policy Luncheon in Boulder.

h) One of us (E. K. Smith) taught a course with David Hogg at the University of Colorado during the Spring Term on Earth Space Propagation using the Flock Handbook (2), in part as a way to identify errors and omissions; and he will teach a second course on Fundamentals of Propagation at CU in the fall with Kenneth Davies.

i) One of us (E. K. Smith) organized and coordinated the reception and program (URSI session G1) in Boulder in January, 1989 in memory of Henry G. Booker, John A. Ratcliffe and Newbern Smith.

Some activity was curtailed due to medical problems of Professor Flock (endocarditis in December and January followed by open-heart surgery in April). Our one scheduled foreign trip during the first year would have taken Prof. Flock to ICAP'89, the Sixth International Conference on Antennas and Propagation, held at the University of Warwick, England, April 4-7, 1989. Fortunately several members of the NASA Propagation Program were in attendance so that a report on the conference could be prepared for the latest Newsletter.

Future Plans

Projected foreign travel during the second half of 1989 will take E. K. Smith to the second International Symposium on Antennas and Propagation (ISAP'89), Aug. 22-25, 1989 in Tokyo where he will give a paper and chair the Radio Meteorology session. He will also give an invited lecture to the International Satellite Communications Society headquartered in Tokyo and a talk on radio noise at the URSI Commission E Symposium on Environmental and Space Electromagnetics, Tokyo, September 4-6, 1989. He then hopes to continue on to Mainland China at personal expense where he has two invitations, one to visit Xidian University in Xi'an and the other, from the Radio Broadcast Bureau, to lecture. However, no word has come from the PRC since the June 4 Tienanmen Square massacre.

The NASA Propagation Information Center plans to continue the efforts started in the first year. In addition, more attention will be paid to the following during the upcoming year:
1) Obtaining feedback from users of the propagation program's products;
2) Assisting in the implementation of the Science Review Panel Recommendation #4 (NASA should take a leading role in the harmonizing and pooling of propagation data from relevant organizations by defining data acquisition/processing standards).
3) Upgrading our computer competence. A visiting scientist from Xidian University in the People's Republic of China had been expected to participate in this, but this plan may have to be revised.
4) Entering the latest version of the Flock Handbook (1) into Macintosh Microsoft Word or Works and adding in the corrections

which have come to our attention. The latest Ippolito Handbook (2) is already available on tape.

5) Initiating the referencing of pertinent papers on Earth-space propagation from other centers into our data base.

References

1) Flock, W. L., **Propagation Effects on Satellite Systems at Frequencies Below 10 GHz - A Handbook for Satellite Systems Design - *Second Edition.*** NASA Reference Publication 1108(02), December 1987.

2) Ippolito, L. J., **Propagation Effects Handbook for Satellite System Design - A Summary of Propagation Impairments on 10 to 100 GHz Satellite Links with Techniques for System Design - *Fourth Edition.*** NASA Reference Publication 1082(04), February, 1989.

Session 1

MOBILE SATELLITE PROPAGATION EXPERIMENTS

Chairman:

Richard F. Emerson
Jet Propulsion Laboratory

OPENING COMMENTS

Richard F. Emerson
Jet Propulsion Laboratory
California Institute of Technology
Pasadena, California 91109

The propagation studies and Mobile Satellite Experiment Programs at JPL have enjoyed a synergistic relationship over the last several years. My first contact with the propagation activities was at a workshop, held at JPL, where Wolf Vogel presented the studies on balloon-borne transmitters. That workshop brought together system designers, propagation experts, and subsystem engineers.

Data collected and analyzed by Wolf Vogel and Julius Goldhirsh have been used to develop technology to overcome or, at least, mitigate the effects of the propagation environment on communication system performance. Wolf has also provided help in designing the field measurement equipment which we use for MSAT-X.

Feedback by system designers has led to propagation experiments which have provided greater insight into not only the impact of propagation on system performance but on the nature of the propagation impairments themselves, particularly at UHF and L-Band.

NAPEX has been instrumental in continuing and broadening the dialogue between the experimenters and design engineers. The need for continuing dialogue will be even more important as systems such as PASS, operating at Ka-Band, evolve.

This morning we have a selection of papers which report on the continuing work in propagation field studies and modeling. We also have one paper which shows the importance of closing the loop from field experiments to laboratory tests of equipment. Modifications to the JPL channel simulator now allow the use of field collected data to simulate the propagation environment in the laboratory.

The LMSS and AMSS activities live in the overall governmental and international governmental world. We will conclude this session with a report on AMSS and the CCIR.

FIELD MEASUREMENTS IN MSAT-X

Khaled Dessouky and Loretta Ho
Jet Propulsion Laboratory
California Institute of Technology
Pasadena, CA 91109

Abstract

Results from the two most recent MSAT-X field experiments, the Tower-3 Experiment and the JPL/FAA/INMARSAT MARECS-B2 Satellite Experiment, are presented. Results that distinguish the unique propagation environment of the tower set-up are given and explained. The configuration and flight variables of the aeronautical experiment which used an FAA aircraft and an INMARSAT satellite are described. Results that highlight the disturbances on the aeronautical satellite channel are presented. The roles of satellite-induced signal variations and of multipath are identified and their impact on the link is discussed.

1. Introduction

Field experiments have played a major role in validating the technologies developed under MSAT-X and in evaluating the end-to-end system performance. This article summarizes results obtained in the two most recent field experiments with emphasis on propagation-related results.

The first experiment addressed is the Tower-3 (T3) Experiment conducted near Boulder, Colorado, in July and August of 1988. It was the first end-to-end mobile field experiment in MSAT-X [1]. A 1000-ft tower operated by NOAA was used as a platform to simulate a satellite transponder. As such, T3 offered only a simulated land-mobile environment, nevertheless, it served as an invaluable end-to-end system checkout.

The second, and more recent experiment, is the Joint JPL/FAA/ INMARSAT MARECS-B2 Satellite Experiment. This was a complete aeronautical mobile experiment and demonstration. The MSAT-X mobile terminal was flown on board a Boeing 727 and was successfully demonstrated during flight. Due to damage sustained by the aircraft in a windstorm immediately prior to the scheduled start of the experiment in January 1989, only a ground check-out part was conducted in January. The flight segment was postponed and successfully completed in March 1989.

In what follows, the Tower-3 experiment set-up is described first. Typical results from its unique propagation environment are then summarized. This is followed by a brief description of the FAA experiment configuration and some of its results.

2. Tower-3 Experiment and Results

2.1. The Tower Set-Up

The physical layout for the experiment is shown in Figure 1. The fixed station was set up inside the trailer located as identified in the figure. The fixed station antenna was a dual

helibowl with approximately 12 dB of gain and a 28^{o} 3-dB beamwidth in elevation. (A refined version of this antenna was used in the Marecs B2 Satellite Experiment.) The dual helibowl was placed on the roof of the trailer. To simulate a satellite, an L-band translator [1] was placed atop the tower and a patch antenna was placed facing downwards on a boom extending horizontally from the top of the tower. The patch antenna by itself, i.e., in the absence of the tower in its radiation field, is omni-directional with -7 dB of gain.

Mobile tests were performed with the mobile laboratory van travelling along the North-South (N-S) and East-West (E-W) roads (Figure 1). The quantitative link performance tests were performed at and between the calibrated points A through E, and F through H, as shown the figure. Limiting the testing to these regions was required to reduce the problem of excessive signal variation due to the change in range-- a problem that does not exist in a satellite link.

2.2. Tower Propagation Environment

Preliminary pilot strength measurement runs along the N-S and E-W roads revealed large signal fluctuations (up to 5 dB peak-to-peak). It was determined that this could be significantly reduced by minimizing reflections off the tower structure. Consequently, absorbing material was placed on the antenna mounting platform between the patch antenna and the tower. This indeed resulted in a reduction of the observed fluctuations, but also resulted in a sharp signal drop-off north of point E and immediately west of point F. The complete elimination of tower antenna pattern ripples (which cause these spatial signal fluctuations) is known to be a very difficult problem. Hence, no attempt was made to eliminate these ripples.

The pilot signal was received at the van through JPL's mechanically steered medium gain antenna. The received pilot power is shown in Figure 2 for the N-S road. Three signal variation phenomena can be seen. The fastest variation is due to multipath, which is minimal for the tower environment as will be discussed shortly. The relatively wide ripples of about 1.5 dB peak-to-peak magnitude signal variations are due to the tower antenna pattern. The deep, sharp fades correspond to the telephone poles on the west edge of the N-S road. It is worth noting that the poles do not show up on the signal strength plots taken with the van traveling along the east side of the road away from the poles. This is because the poles are no longer in the line-of-sight between the vehicle antenna and the top of the tower.

Detailed data analysis was performed on the data gathered during the experiment [2]. One of the experiment objectives was to characterize the multipath channel present at the tower site. Least squares fitting techniques were applied to a host of multipath data gathered on the N-S and E-W roads using the JPL mechanically steered, medium gain antenna. This revealed that a Rician probability density function with a k factor (ratio of direct to scattered signal powers) of 20 to 21 dB fits well the multipath environment experienced at the tower site. This is shown in Figure 3. It was found that the fit could be further enhanced if a running average is used to smooth the ripples due to the tower antenna [2]. Also of interest is the effect of the bin size on the fit obtained. This is illustrated in Figure 4. The high values of k obtained clearly indicates that the barren, flat tower site creates very little multipath. The channel behaves much like an additive white gaussian noise channel.

3. The Joint JPL/FAA/INMARSAT MARECS-B2 Satellite Experiment

The basic objective of the experiment was to demonstrate the voice and data link

performance in a typical aeronautical environment. Of particular importance was the demonstration to the FAA of the quality and robustness of the MSAT-X speech codecs. To support the objectives of the experiment, data to fully characterize the link and the disturbances on the channel was gathered.

3.1 Experiment Configuration

Figure 5 depicts the experiment set-up. The configurations of the ground segment (1/89) and the flight segment (3/89) are quite similar. The primary difference is that the Aircraft Terminal (ACT) was placed on the roof of the FAA hangar during the ground segment (and was referred to as the Ground Aircraft Terminal [GACT] [3,4]). With one exception, the ACT components are identical to those in the GACT. The exception is the aircraft antenna assembly used in the aircraft to mount the antenna to the inside of a passenger window [5]. For logistical simplicity during flight tests a separate antenna and assembly were used for each side of the fuselage. The ACT or GACT served as one end of the MSAT-X link. Another MSAT-X mobile terminal was located at INMARSAT's Coast Earth Station (CEST) in Southbury, CT. The mobile terminal was interfaced at IF to COMSAT's hardware chain [3,4]. One and two-way data and voice links were established through the MARECS-B2 satellite [4,6] located at 26^{o} west longitude.

3.2 Flight Paths

Selection of the flight paths for the flight segment proved to be one of the more intriguing aspects of the experiment. Factors relating to angle to satellite, doppler, path length, air traffic and weather conditions had to be taken into account [5]. Originally, three flights were planned, one each for the evenings of March 29, 30 and 31. Unseasonable weather patterns with severe thunderstorms interfered however. The first flight took the straight-line path shown in Figure 6 between Salisbury, MD, and Boston, MA. The middle flight scheduled for 3/30 had to be cancelled due to very severe weather and lightning at the FAA center which made fueling the plane hazardous. To avoid dangerous weather and increase the experiment duration as much as possible on the last (or second) flight, the southerly path from Atlantic City, NJ, to Charleston, SC, was taken on 3/31. Both flights were flown entirely at a cruising altitude between eight and nine thousand feet. This was to enable an airspeed in the 200 to 250 knot range. Unfortunately, that altitude placed the plane in the middle of the thunderstorms, thereby creating a very rough experiment environment replete with periods of intense turbulence.

3.3 Results

During the ground segment of the experiment both pilot and data channel signal power were recorded at the GACT and the CES. The most salient observation made for this additive white Gaussian noise (AWGN) channel (both ends are stationary) is signal power fluctuation due to variations in satellite loading. This is evident in the data collected from the digital readings of the power meter connected to the IF of the MSAT-X receiver. As seen from a typical plot shown in Figure 7, the variation in the signal power of the forward link is within +/- 0.8 dB. Smaller variation was generally observed at the CES on the return link. This is attributed to the fact that the automatic gain control on the return transponder (the high gain channel used) is normally off.

During flight, turbulence and minor course corrections added to the fluctuations in the received signal at the aircraft. From Figure 8 it is seen that the data channel signal power varies within +/- 1.5 dB. A plot of the received pilot during the same test period is given in Figure 9. It shows the general correlation and agreement between the signals received on the pilot and data channels (which are separated by 20 kHz in this experiment).

Multipath is known to have a minor effect in the aeronautical satellite link. A Rician density with k (ratio of direct to scattered powers) of 15 dB is well accepted. This small amount of multipath is embedded in the short term signal fluctuations exhibited in Figure 9. System performance is measured in terms of bit error rate versus signal to noise ratio. Preliminary analysis [5] has shown that despite flight dynamics only a small degradation of about 0.5 dB is present relative to the AWGN channel observed in the ground segment. This confirms that multipath fading does not play a significant role in the satellite aeronautical satellite link at hand.

4. Upcoming Field Measurements

The first true land mobile satellite experiment using the MSAT-X equipment will take place in July 1989 in Australia. The MSAT-X mobile laboratory will be driven between Sydney and Brisbane and in the vicinity of both cities. A wealth of propagation and system performance data will be gathered and subsequently analyzed. Future articles will report on both the propagation and system performance measurements to be made, and will aim to elucidate the effects of the propagation environment on observed system performance.

REFERENCES

1. K. Dessouky, et al., "Summary of Results from the Tower-3 Experiment," MSAT-X Quarterly No. 20, JPL Document 410-13-20, July 1989.

2. L. Ho and K. Dessouky, "Tower-3 Data Analysis," JPL Internal Report No. D-6242, February 1989.

3. T. Jedrey, et al., "The Marecs B2 Satellite Experiment: Ground Segment-- Preliminary results," MSAT-X Quarterly No. 20, JPL Document 410-13-20, July 1989.

4. T. Jedrey, et al., "The MSAT-X Marecs B2 Satellite Experiment: Ground Segment," MSAT-X Report (Draft dated March 1989).

5. K. Dessouky, "The MARECS-B2 Satellite Experiment: Flight Segment Overview," MSAT-X Quarterly No. 21, JPL Document 410-13-21, October 1989.

6. da Silva Curiel, A., "The First Generation INMARSAT System," Proceedings of the Third International Conference on Satellite Systems for Mobile Communications and Navigation, IEE Publication 222, London, U.K., June 1983.

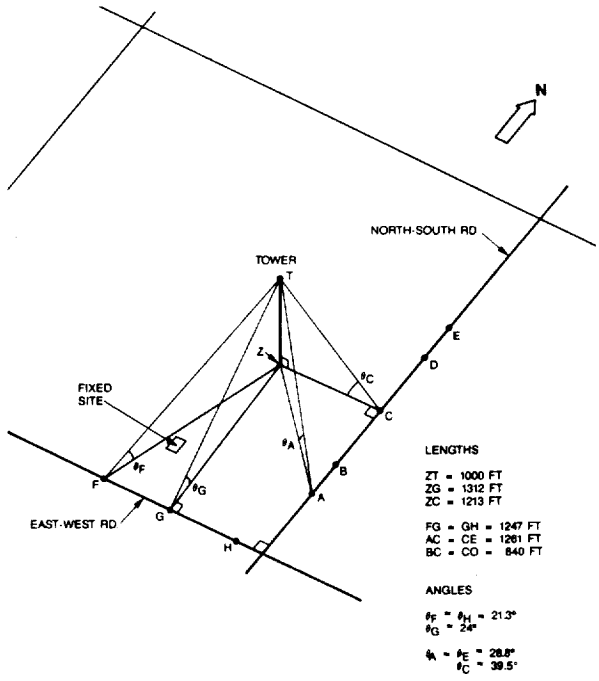

Figure 1. Layout of the Tower-3 Experiment

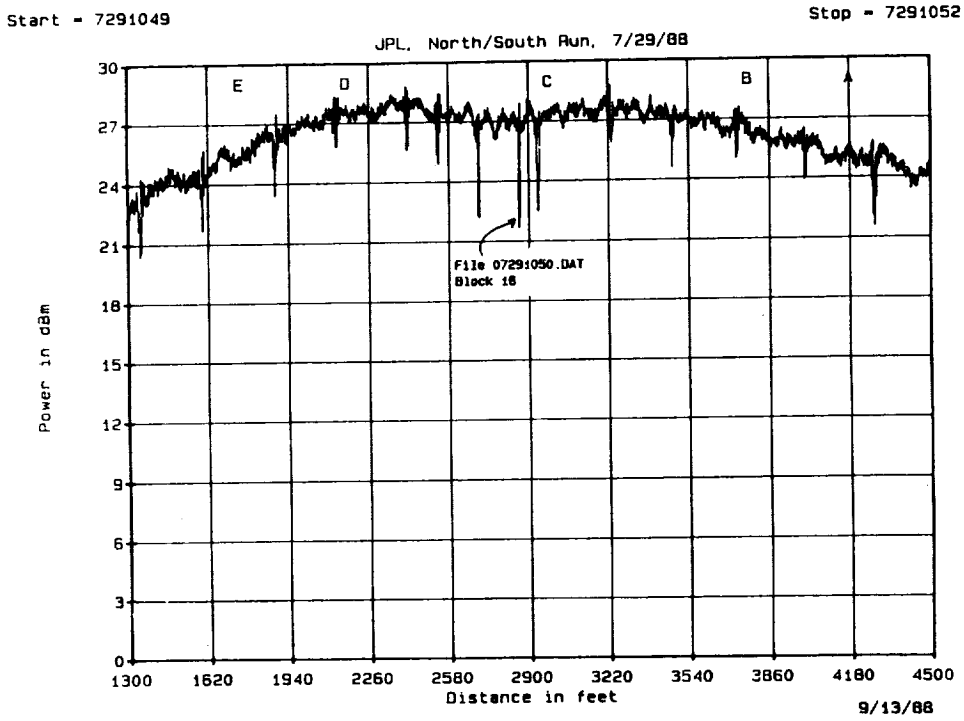

Figure 2. Pilot Signal Power Received at Van on North-South Road

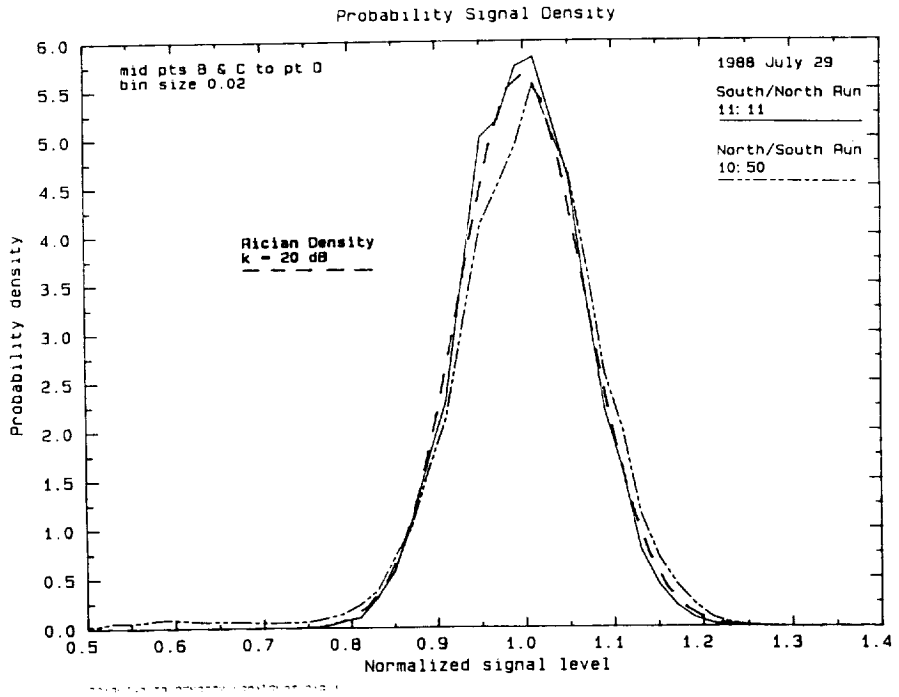

Figure 3. Rician Densities to Fit Received Pilot

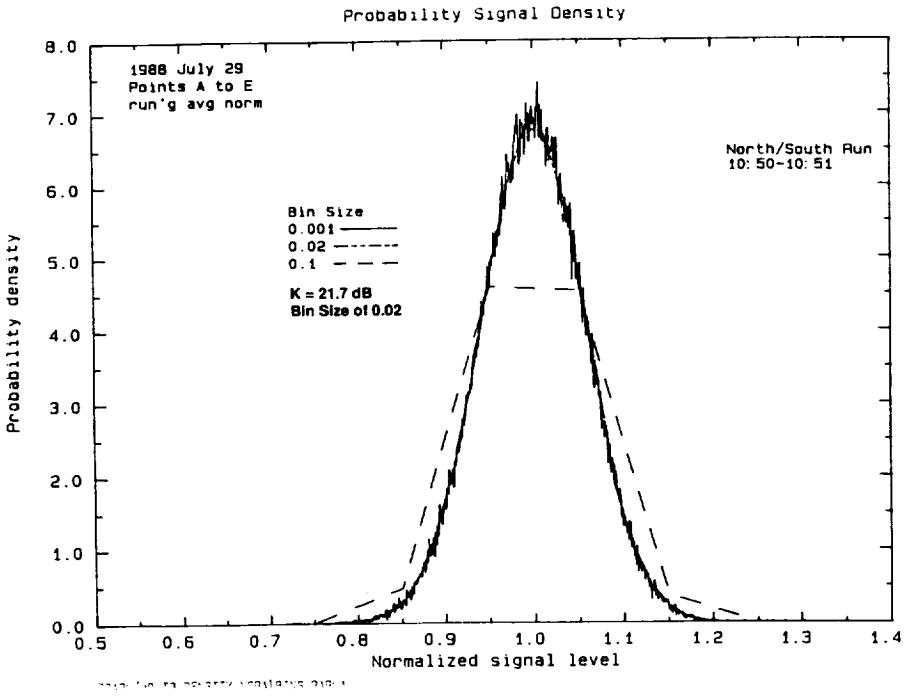

Figure 4. Effects of Bin Size Choice and Running Average Smoothing on Data Fitting

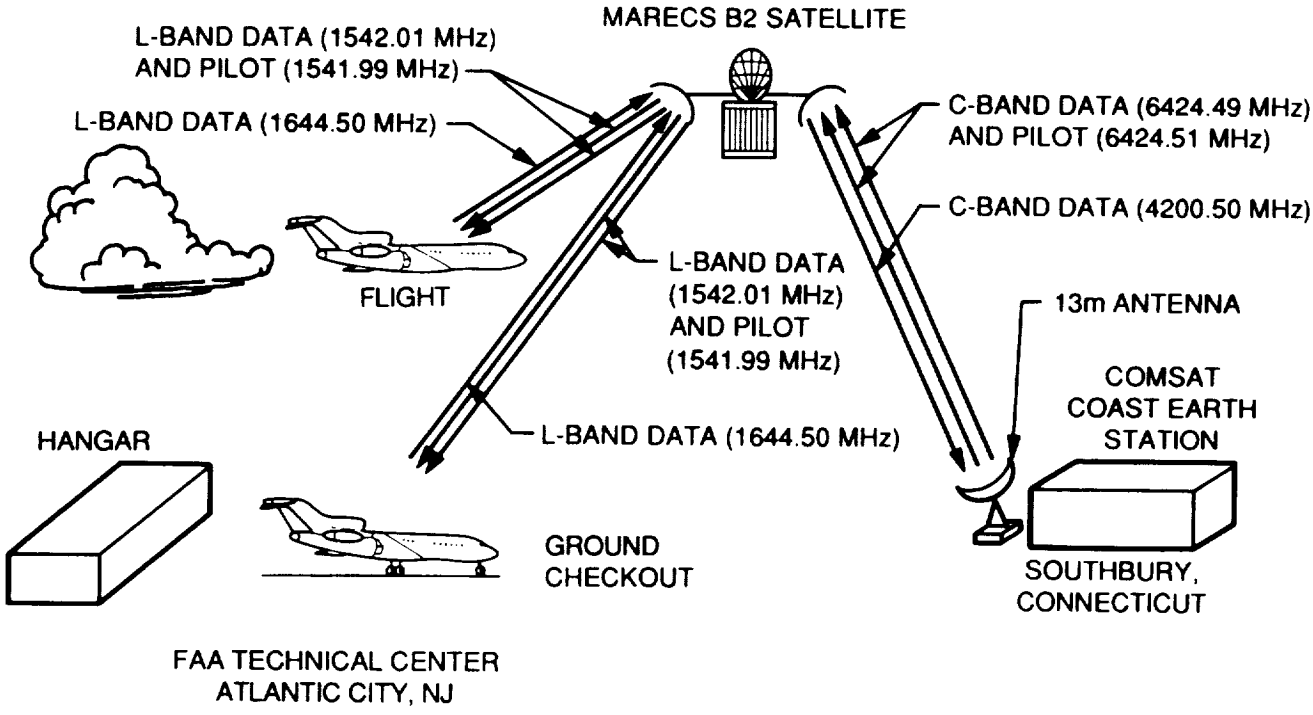

Figure 5. Configuration of JPL/FAA/INMARSAT Satellite Experiment

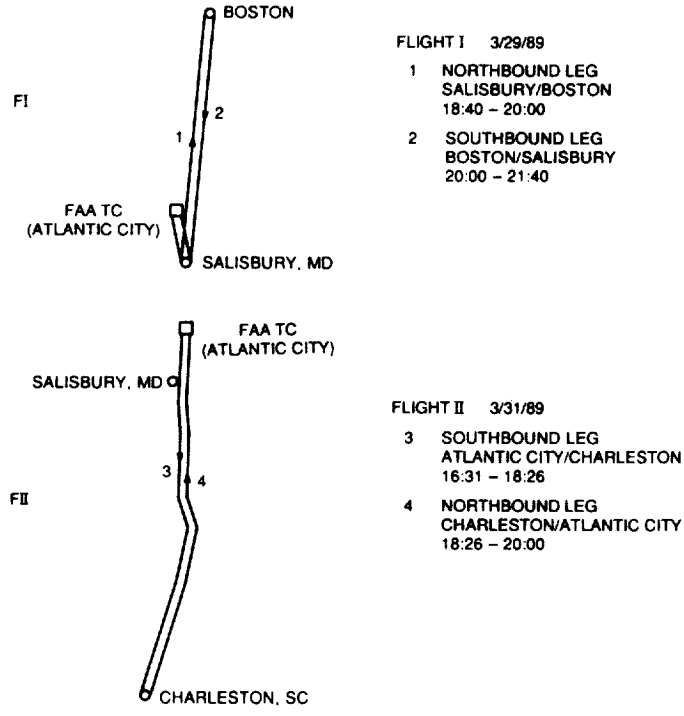

Figure 6. Flight Paths Selected In Experiment

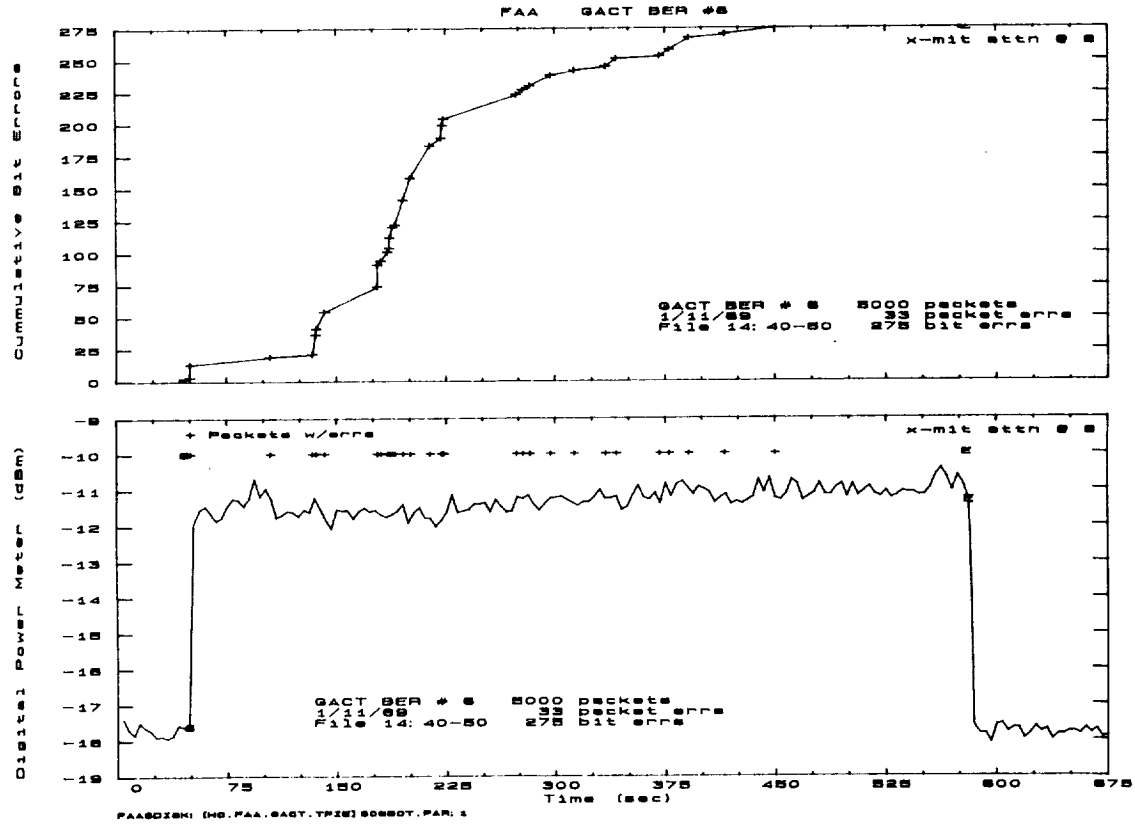

Figure 7. Data Channel Signal Level Variations in Ground Segment of Experiment

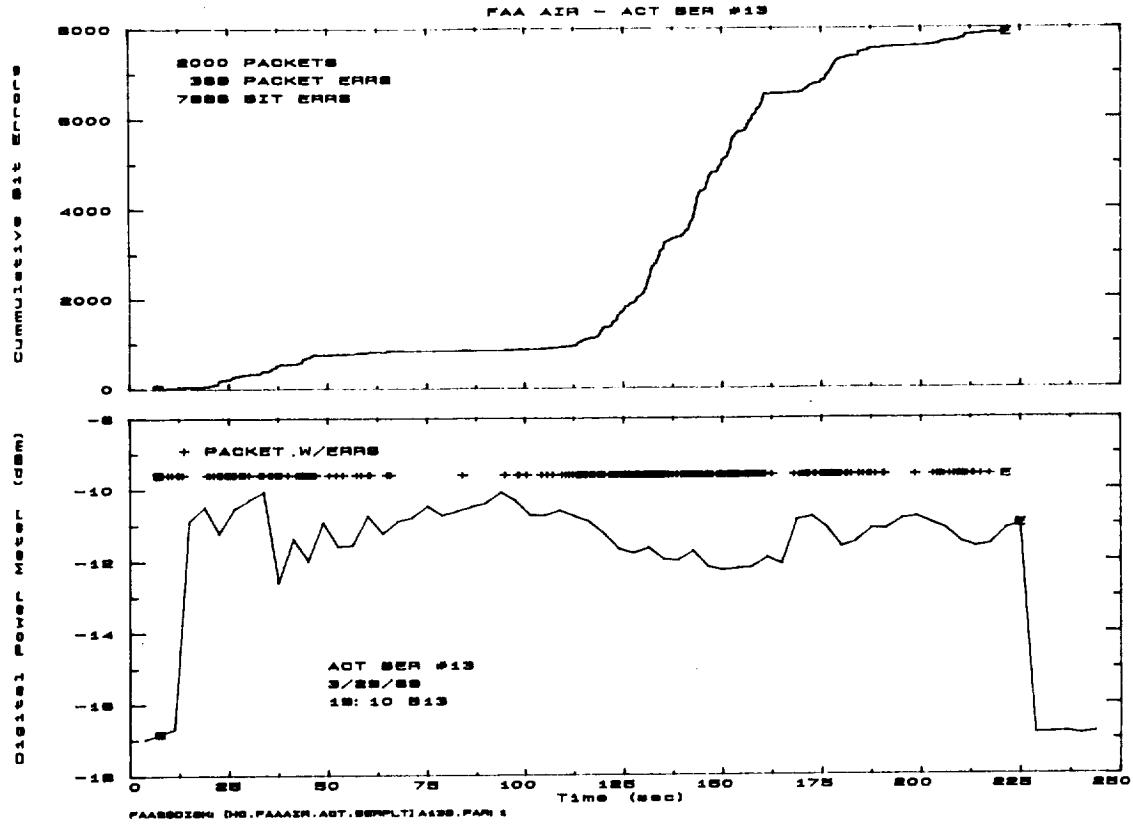

Figure 8. Data Channel Signal Level Variations in Flight Segment of Experiment

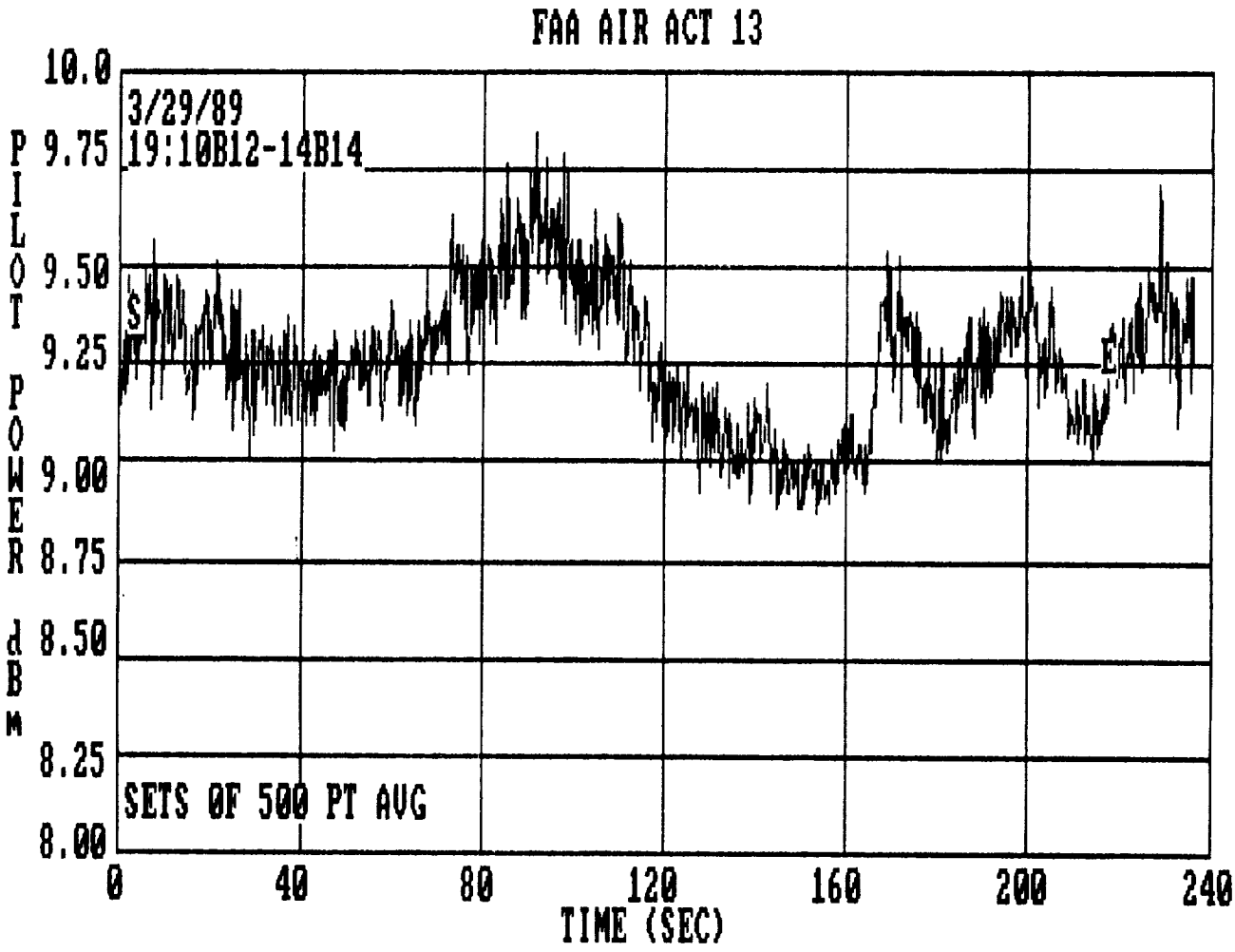

Figure 9. Pilot Signal Fluctuations During Flight Segment

CHANNEL SIMULATOR UPGRADE TO USE FIELD PROPAGATION DATA

Jeff B. Berner

Jet Propulsion Laboratory
4800 Oak Grove Drive
Pasadena, CA 91109

Abstract--The JPL Channel Simulator lab has been modified to allow full duplex links and to allow the use of field propagation data for link fading. This capability will be used to test equipment for the joint AUSSAT/NASA mobile satellite experiment in July, 1989.

1. Introduction

The JPL Channel Simulator was built by the Mobile Satellite Experiment (MSAT-X) program to facilitate the end-to-end testing of components of a mobile satellite link. The simulator was designed to simulate a one-way link with interfering sources, gaussian noise, and fading. Recently, modifications were made to allow a full-duplex link to operate with field propagation data. This paper will describe the channel simulator, discuss the changes made and the rational for them, and describe the capabilities of the simulator.

2. The Channel Simulator

The channel simulator has been described before (Davarian, 1987); we will only discuss the features that have been upgraded. Figure 1 provides a simplified block diagram of the channel simulator. The simulator has four transmitters whose output levels are independently set and then summed together. This allows a desired channel, a co-channel interferer, and two adjacent channel interferers. Each channel can independently undergo fading. Gaussian noise can be added to the combined channels. The desired channel is then selected by the receiver.

The Rician fading is accomplished by splitting the signal equally into two paths, the Line-Of-Sight (LOS) path and the Rayleigh faded path. The Rayleigh fading is accomplished by complex modulating the inphase (I) and quadrature (Q) components of the input signal by a complex simulated Rayleigh signal. The faded signal is then attenuated and combined with the LOS signal to create the Rician faded signal. The Rician K factor, defined as the ratio of the LOS power to the Rayleigh power, is set by step attenuators.

To use the channel simulator, the MSAT-X terminal processor and TCM/8DPSK modem are used. The terminal processor provides PN data at 4800 bps to the modem, which modulates the data. The modem provides an I channel and a Q channel to the transmitter. The receiver provides a 28.8 KHz IF signal to the modem for demodulation. The detected bits are then sent to the terminal processor for error detection. Operating in this one-way mode allowed the characterization of the modem under fading conditions.

3. The Upgrades

In July, 1989, the MSAT-X Propagation Measurement Van (PMV) will be conducting experiments with AUSSAT in Australia using the Japanese ETS-V satellite. A joint experiment with the National Communications Systems (NCS) was proposed. This experiment involves using secure telephones (STU III's) over the MSAT link. To accomplish this requires an adapter designed and built by Electrospace, Inc. (ESI) and a JPL built MSAT-to-ESI interface board. Due to the fact that the ESI equipment was not designed to work with the MSAT system, it was necessary to test the complete system before traveling to Australia. Also, to ensure that the Australian propagation environment would allow the establishment of secure communication, it was required that the system be tested under conditions present in Australia. To accomplish this required two changes to the channel simulator.

First, to test the full system required the ability to do full duplex communications. A second receiver was constructed to allow the return link to be detected. The desired channel transmitter was used for the forward link and the co-channel transmitter, offset from the forward link by 100 KHz, was used for the return link.

Second, to test under Australian conditions required Australian propagation data and the ability to use it. The propagation data was supplied by Dr. Wolfhard Vogel, of the University of Texas (Vogel, 1989). This data was in the form of fade amplitudes from the nominal value; this data was sampled at 500 samples/second. The Rayleigh fader was modified to use this data.

To use the field data fading, the LOS signal is turned off. Instead of complex modulating the signal with the Rayleigh data, the signal is modulated with I and Q data generated from the field propagation data (Figure 2). An IBM PC/AT with a Data Translation DT2828 dual channel Digital-to-Analog board was used to generate the data. The DT2828 provides a -10 to 10 volt capability; the nominal output value was set at 7 volts. All fades were done from the nominal value, with the I and Q channels being faded by the same value.

4. The Testing

Figure 3 provides a block diagram of the test configuration for the NCS testing. After verifying the channel simulator full duplex link, both with and without field data fading, the full secure link was tested. Due to time constraints and initial problems with the various interfaces to the MSAT equipment, only one propagation data file was used, number 394. Figure 4 provides a plot of the amplitude fades versus time for this file. The goal of the test was to achieve a secure link and maintain it with the field data fading and an E_b/N_0, due to gaussian noise, of 11 dB. This goal was achieved.

5. Conclusion

The channel simulator is now capable of supporting a full duplex link, using any propagation data to recreate the conditions a system will encounter. This allows us to go into the field with the confidence that the NCS test will succeed in Australia. Also, any improvements in MSAT equipment that are made after the AUSSAT experiment can be tested under actual field conditions. This

capability of the JPL Channel Simulator will allow measurements made by propagation experimenters to be directly used in designing and testing equipment for the MSAT system.

6. Acknowledgements

The author would like to thank Joe Sumida and Jeff Packard, of JPL, for their help in modifying the channel simulator. The NCS testing could not have been completed without Dr. Wolfhard Vogel providing his propagation data. Also, the contributions of the following individuals for their assistance in the NCS testing are acknowledged: Craig Cheetham, Richard Emerson, Thomas Jedrey, Norman Lay, Leon Truong, and Arvydas Vaisnys of JPL; Scott Phillips of Electrospace, Inc.; and Fred Lawler of Telos Aerospace.

References

Davarian, F., "Channel Simulation to Facilitate Mobile-Satellite Communications Research," IEEE Transactions on Communications, Vol. COM-35, No. 1, pp. 47-56. January 1987.

Vogel, Wolfhard J., Personal Communication, April 18, 1989.

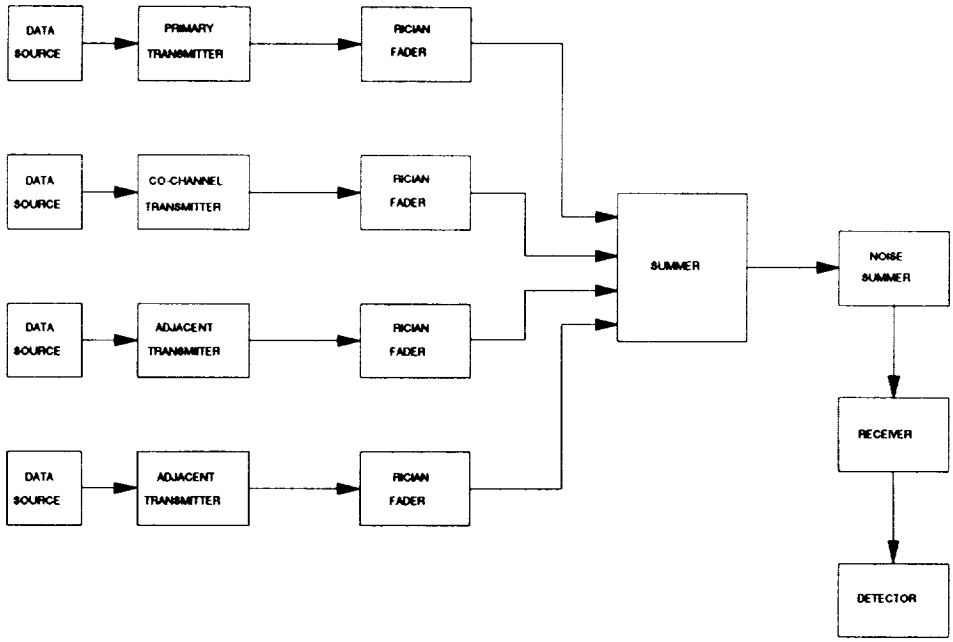

Figure 1
Channel Simulator Block Diagram

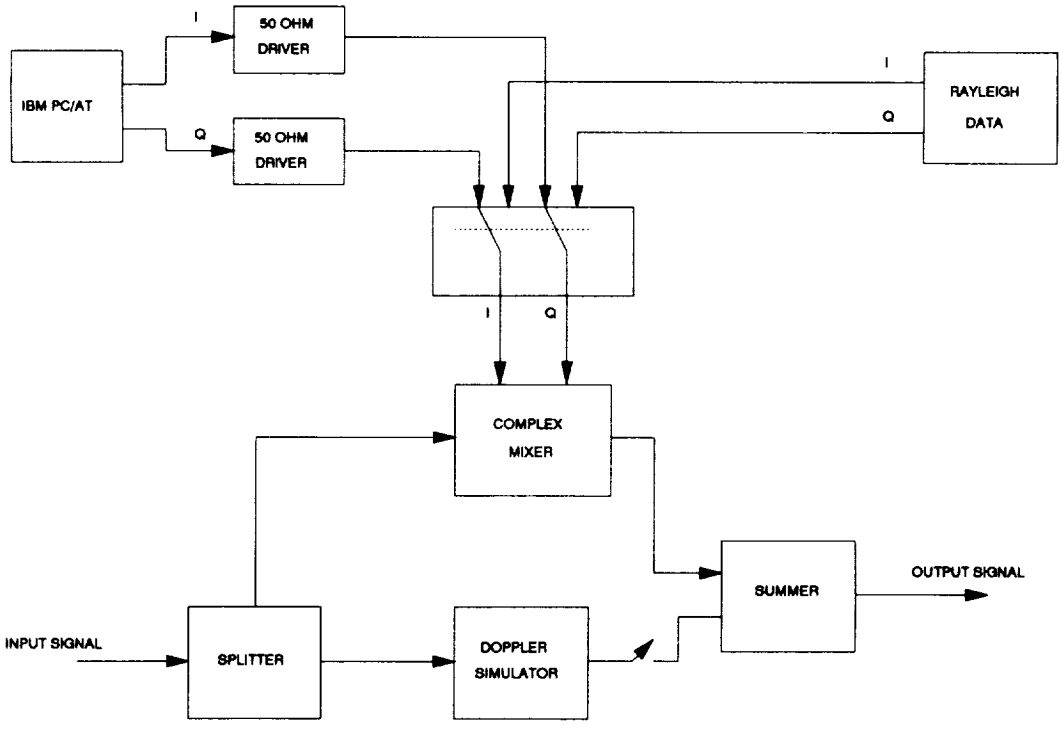

Figure 2
Fader Using Field Propagation Data

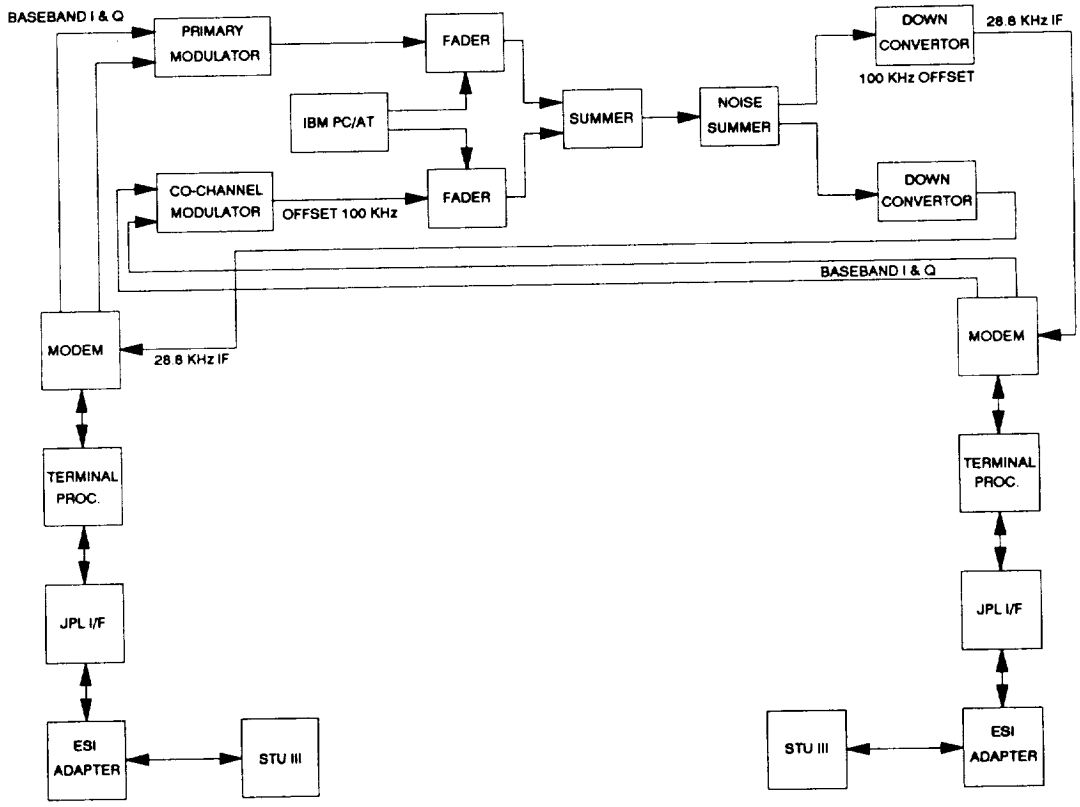

Figure 3
NCS Testing Configuration

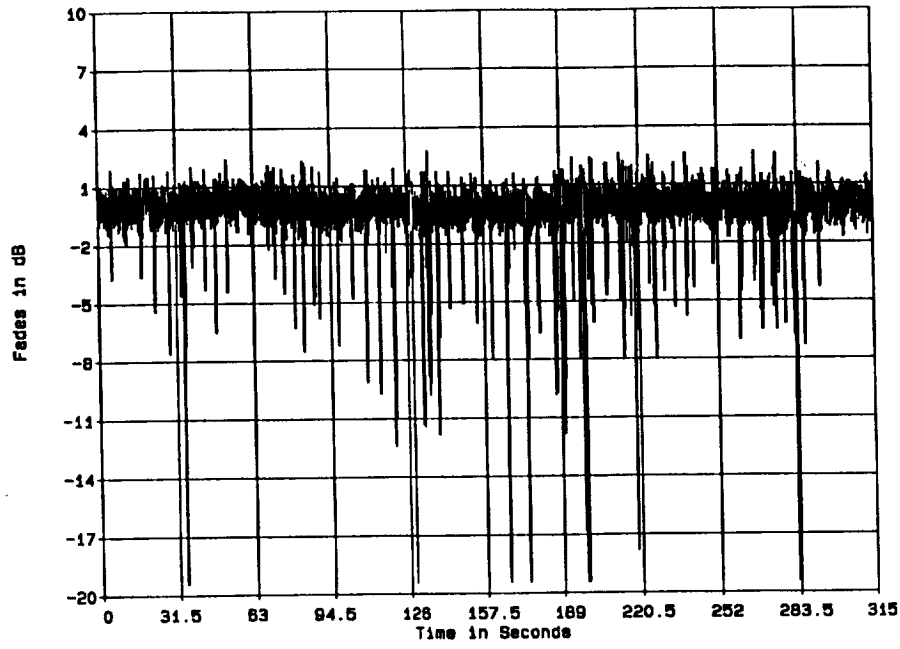

Figure 4
Amplitude Fading Versus Time

THE AUSTRALIAN EXPERIMENT WITH ETS-V

Wolfhard J. Vogel, Julius Goldhirsh, Yoshihiro Hase+

EERL	APL	CRL
Univ. of Texas	Johns Hopkins Univ.	Ministry of P&T
Austin, TX	Laurel, MD	Kashima, Japan

Abstract--Land-mobile-satellite propagation measurements were implemented at L Band (1.5 GHz) in South-Eastern Australia during an 11 day period in October 1988. Transmissions (CW) from both the Japanese ETS-V and INMARSAT Pacific geostationary satellites were accessed. Previous measurements in this series were performed at both L Band (1.5 GHz) and UHF (870 MHz) in Central Maryland, North-Central Colorado, and the southern United States. The objectives of the Australian campaign were to expand the data base acquired in the U.S. to another continent, to validate a U.S. derived empirical model for estimating the fade distribution, to establish the effects of directive antennas, to assess the isolation between co- and cross-polarized transmissions, to derive estimates of fade as well as non-fade durations, and to evaluate diversity reception. All these objectives have been met.

1. Background

Designing future mobile satellite systems, communication engineers require information on fade statistics associated with multi-path propagation in different types of terrain and shadowed line of sight transmissions due to roadside obstacles.

The objectives of earlier measurement campaigns [1 - 7] were to assess the statistics of fades under variable conditions: roadside obstacles, mountainous and flat terrain, elevation angles, side of roads and directions driven, seasonal effects, and unshadowed versus shadowed line of sight conditions.

The Australian campaign offered the opportunity to determine fade statistics for another continent having different types of foliage and terrain. It also enabled a broadening of a limited fade data base involving satellite platforms [5, 8, 9]. Transmissions from ETS-V were predominantly accessed, although signals emanating from the INMARSAT POR were also received. Major differences with previous data sets are: (a) high and low gain antennas were used, (b) transmissions from different satellites allowed probing fade variability with elevation angle, and (c) cross-polarization signals were measured during selected runs.

+ Mr. Hase was supported by a grant from the Science and Technology Agency of Japan during his 1988-1989 stay at The University of Texas as a visiting researcher.

In this effort we present fade statistics based on data selected from the campaign total of 1436 km road sampled, corresponding to 460 km of roads and encompassing 36 runs; a run representing a particular stretch of road with consistent parameters over which measurements were obtained and cataloged. Results pertaining to the following are exhibited: (1) fade distributions for different road types and differing densities of roadside obstacles (trees and utility poles), (2) overall average fade distribution and comparison with a previously derived empirical model, (3) fade distributions for different antenna patterns (high gain versus low gain), (4) fade distributions for different satellite transmitter platforms, (5) cross-polarization fade statistics, (6) fade and non-fade duration statistics, and (7) diversity gain improvement. Statistics associated with urban driving are not discussed, as terrestrial cellular systems are expected to be available at such locations.

2. Experimental Aspects

2.1 Transmitter and Antenna Systems

Left-hand circularly polarized (LHCP) CW transmissions radiated from the Japanese ETS-V satellite (EIRP = 55.9 dBm) were received at a frequency of 1545.15 MHz. Elevation angles ranged from 51° in Sydney to 56° in Coolangatta and the azimuth to the satellite was 2° counter-clockwise, relative to north. Although most of the selected measurements are for this satellite (28 runs, 446 km), measurements from INMARSAT POR (EIRP = 50 dBm, 10 runs, 68 km, RHCP, 1541.5 MHz, elev. 40°) are also included.

The low gain antennas were crossed drooping dipoles. The high gain antennas were manually pointed helixes (14 dB gain), thus restricting data acquisition to straight road sections.

2.2 Receiver and Data Acquisition System

Measurements were made with the Texas van receiver/data acquisition system. The receiver had three outputs with two noise bandwidths. Recorded were the in- and quadrature-phase detector voltages (bandwidth = 500 Hz), as well as the output from a power detector (200 Hz). The bandwidth was chosen because it did not exclude too many doppler-shifted multipath components when driving at highway speeds, yet retained a useful SNR for shadowing measurements.

Data were sampled at a 1 kHz rate and stored on magnetic disk in sequential records of 1024 samples. In addition to recording the L Band signals, the vehicle speed and time were also recorded.

The unfaded signal level was determined from the data itself. It was taken to be the mean level of the signal observed while driving in a location which produced minimal multi-path and

no shadowing. All the data reported are relative to that level. Only signal levels with at least 7 dB signal to noise are used.

2.3 Road Features

A map of the region indicating the rural roads outside the Sydney area traveled during the campaign is given in Figure 1. Measurements were made along these roads in non-contiguous blocks of about 30 to 70 km. Two major vegetation zones [10] were traversed in the experiment; forests (closed and open forms) along the coastal roads and woodlands (woodland and low-open woodland) further inland. Forests ranged from dry sclerophyll (most runs) to tropical rainforest (Run 385). The dominating tree genus in the forests was Eucalyptus. Other than tree types, more similarities than differences existed between apparent roadside conditions (tree heights, densities, setbacks) in Australia and the Eastern United States.

3. Fade Distribution Results

Fade levels are defined by 10*Log of the ratio of the measured power to the unfaded reference power. The distributions are presented with the ordinate depicting the percentage of the distance over which the attenuation exceeded the abscissa (fade) level. The distributions show fade levels from 0 to 20 dB over the probability range 1 to 100%. Low gain mode fades are calculated up to 15 dB and the high gain mode levels to 25 dB.

3.1 Worst Case Fade Levels

Consider the family of 15 fade distributions depicted in Figure 2. The runs are characterized as follows: (a) they were made in rural or suburban areas, (b) they all show fades due to trees and utility poles of 10 dB or more at the 1% probability, and (c) they represent measurements made with ETS-V in the low gain mode.

A physical interpretation relating the individual curves to specific roadside parameters is difficult; each road has varying densities of trees and utility poles along the sides with different setbacks, and also a variable local azimuth to the satellite due to bends in the roads. The worst case distribution in the set shown (Run 377) has an average 1:30 o'clock azimuth direction, but the road is winding along a small river and has large local direction changes. The many trees along this narrow road have only minimal setback and their branches frequently extend over the pavement. The smallest level fade distribution (Run 322) has an azimuth of 10:30, also in between the maximum and minimum shadowing geometry. The trees along this wide multi-lane road are not very close to its edge. We note that fades exceed values from 10 to 15 dB and 1 to 8 dB at the 1 and 10% probability, respectively.

3.2 Comparison with Empirical Roadside Shadowing (ERS) Model

In Figure 3 we have combined the distributions for the 15 individual runs of Figure 2 into a single distribution comprising 403 km of roads. Also plotted is the fade distribution as predicted by a model empirically derived from data obtained in the United States over 640 km [5], valid in the probability interval from 1% to 20%. The maximum difference between the two distributions is less than 2 dB at the 14% probability level. The ERS model has the following form:

$$F = -M * \mathrm{Ln}(P) + B \qquad (\text{for } 20\% > P > 1\%) \quad (1)$$

$$\text{where the slope} \qquad M = 3.44 + 0.0975*\theta - 0.002*\theta^2 \quad (2)$$

$$\text{and the offset} \qquad B = -0.443*\theta + 34.76, \quad (3)$$

and F is the fade depth exceeded in dB for P percentage of distance traveled. The angle θ is in degrees and corresponds to the elevation to the satellite. The model represents the average fade statistics for various road types with predominantly tree and some utility pole roadside obstacles. It includes different sides of the roads driven as well as different directions of travel. The model distribution in Figure 3 for $\theta = 51°$ is given by

$$F = -3.21 * \mathrm{Ln}(P) + 12.2 \, . \quad (4)$$

3.3 Distributions from Low and High Gain Receiving Antennas

Figure 4 illustrates a very heavy shadowing case. We note that the high gain antenna experiences consistently more fading than the low gain system, up to approximately 3 dB at 0.4% of the distance traveled. The attenuations for both antennas are due to a combination of tree absorption of the direct energy and scattering of energy out of and into the antenna beam. When the beam is narrower, less power is received via scattering. Conversely, the low gain, azimuthally omni-directional antenna receives more scattered multi-path contributions. Nevertheless, the higher gain antenna has 10 dB more gain and the net power received by it is still higher (7 dB more at 4% probability). For runs in which the line of sight was shadowed only occasionally, less than 1 dB fade differences existed.

3.4 Comparison of ETS-V and INMARSAT Measurements

Figure 5 is based on data taken over a 55 km tree lined road in the hills to the west of Sydney. This road was generally west-to-east, but made many turns in order to follow the contours of the landscape. Added into this figure have been the estimates of the median cumulative distribution functions predicted from the ERS model. For both satellites there is a tendency to overestimate fades below about 5 dB, but the error is less than

1 dB. The elevation angle dependence is well represented by the model.

4. Co- and Cross-Polarization Measurements

Figure 6 shows distribution functions for a pair of runs made sequentially along a rolling, suburban road lined with trees and utility poles, using high gain co- and cross-polarized antennas. The isolation between the two polarizations in the absence of nearby scatterers was better than 18 dB. Plotted are for Run 406 (copolarization) the percentage of the distance the fade exceeded the value on the abscissa and for Run 408 (cross-polarization) the percentage of the distance the fade was less than the abscissa. The horizontal distance between the curves gives an estimate of isolation between the two channels.

Since the data sets were not collected simultaneously, they cannot be used to determine the instantaneous polarization isolation. However, assuming that the occurrence of depolarization was highly correlated with shadowing, one can make reasonably accurate isolation estimates in the central range of percentages (about 10 to 60%). At the 10% level the fade values of 8 and 14 dB indicate an isolation of only 6 dB. The isolation is roughly inversely proportional to the fade threshold. Because of the random polarization of signals scattered by roadside obstacles, systems with any reasonable fade margin will not allow frequency re-use techniques.

5. Fade and Non-Fade Duration Statistics

From the viewpoint of designing an optimum system which transmits coded messages over designated bandwidths, it is important to know the length of time the land-mobile satellite channel is available and unavailable without interruptions. We have analyzed fade and non-fade duration distributions in order to determine the statistical characteristics of unavailability and availability, respectively.

5.1 Fade Duration

To reduce analyzing time and avoid effects of level crossings due to thermal noise, the original data were compressed by averaging over consecutive groups of eight samples. The resulting time series were quantized into two levels for each threshold examined, 2 to 8 dB at 1 dB increments. Durations have been expressed in units of distance traveled rather than in units of time, thus making them independent of the vehicle speed.

Cumulative distributions of fade durations are shown in Figure 7 for Run 383. Results were derived typical of suburban, rural, and heavy shadowing environments. Each of the many distributions could be represented by a log-normal, except at short durations of less than a wavelength (0.2 m). Contributions there are thought to be mainly due to level fluctuations caused

by the edges of obstacles. At 5 dB, all median values of duration are around 0.3 m except for the case of the high gain antenna, which has an average duration of about twice that value (0.63 m). All values of the slope are about 1.2 to 1.5 m, including the case of the high gain antenna. This means that they do not depend on either roadside or antenna parameters. Differences among the distribution curves for the various fade thresholds are small. For example, typical fade distance intervals at 1% are: 3..6 m, 4..8 m, 2..9 m, 7..10 m. Summarizing, fade durations measured in the low gain mode are shorter than those measured with a more directive antenna, but their slopes are similar.

5.2 Non-Fade Duration Analysis

Non-fade duration is defined as the continuous distance over which the fade levels are smaller than prescribed fade thresholds. A non-fade duration analysis of the data set above has been implemented using similar methods as those described for the fade duration analysis.

Typical results are shown in Figure 8. Unlike Figure 7, the ordinates in these graphs are scaled logarithmically. The cumulative distribution curves may be approximated by straight lines implying the exponential form,

$$P(d_n > x) = b\, x^{-c} \qquad (5)$$

where $P(d_n > x)$ is the percentage probability of the non-fade distance d_n exceeding the abscissa value x and where b and c are constants. The value of c, which is the slope in the graph, has a tendency to be larger for the heavier shadowing conditions. As this tendency is consistent for sufficient sample-size data, the value of c might be used as a quantitative measure of shadowing. Any difference due to threshold levels is small. Non-fade durations measured in the high gain mode are somewhat longer than those measured with the low gain antenna.

6. Phase Fluctuation Analysis

During the data analysis, phase data was extracted from the quadrature detected signals. Lower frequency components of the phase, mainly due to oscillator drift or doppler shift changes, were rejected by digital filtering. Distributions of the phase fluctuations under the condition that the received signal level is above a given fade threshold were determined. It was found that the deeper the fade threshold the larger the phase variance. Most distributions of phase fluctuations have such small variances that they will not affect a demodulator at all. Phase fluctuations with the high gain antenna are much smaller than those with the low gain antenna. This means that the influence of phase fluctuations to the demodulator can be ignored, except in the case of very heavy shadowing condition with the low gain

antenna. It is clear that the LMSS channel characteristics can be estimated by levels only, without any regard to phase.

7. Antenna Diversity Improvement

Above, it was shown that the average fade duration was of the order of 1 m, inspiring the test whether one could achieve significantly better performance of the MSS link if two antennas, separated in the direction of driving, were used instead of just one. The joint probability of the fade exceeding the threshold at two antennas was calculated for antenna separations of 1, 2, 5, and 10 m. Instead of using data collected with a second antenna, however, the original data was delayed by the time the vehicle needed to travel the separation distance. An example of the resulting family of fade distribution functions is shown in Figure 9. The diversity improvement factor DIF is defined by the ratio of the single antenna probability of failure P_0 to the joint probability of failure P_j and is a function of the fade margin. The overall result can be expressed by the relation

$$DIF = 1 + [0.2 * Ln(d) + .23] * F \qquad (6)$$

where d (1..10 m) is the antenna separation in meters and F (3..15 dB) the fade margin in dB. For a separation of 2 m and a fade margin of 5 dB, for instance, a DIF of 2.8 results, meaning that a diversity system would fail in only less than half as many locations as a single antenna system. With longer separation (10 m) and a higher fade margin (10 dB) the DIF of 7.9 would indicate an even more dramatic improvement. For the analysis presented here, switching effects were not considered. An examination of the fade duration statistics with antenna diversity also showed that the number of fade events does not necessarily decrease, but that their average duration is reduced.

8. Summary and Conclusions

The Australian campaign has provided an enhanced MSS data base of propagation information associated with shadowing, multipath, antenna directivity, and cross polarization due to roadside obstacles for various road types. The results described here complement those acquired via satellite measurements in the U.S., Canada, and Europe and provide information as to the characteristics of fade statistics in a different continent.

We conclude the following from the results:

(a) The fade statistics due to roadside trees and utility poles along rural or suburban roads in Australia are typical of those in the U.S. with similar densities of roadside obstacles.

(b) The overall average fade distribution was found to agree with the fade distribution predicted by the ERS model within 2 dB and less over the probability range of 1% to 20%.

(c) The employment of directive antennas for the severe shadowing condition resulted in more fading than with a less directive system. Although there is a fade increase for the more directive system, this is more than offset by the significant gain improvement for the system. Another advantage of the high gain antenna is the fact that the non-fade duration is longer.

(d) Comparison of fade distributions along the same section of roads employing the ETS-V and INMARSAT POR satellite transmitter platforms demonstrated the ERS model scales well with elevation angle.

(e) Frequency reuse does not appear to be a viable option for MSS communications, since depolarization due to obstacles in the vicinity of the line of sight reduces the isolation to unacceptable levels.

(f) Fade duration cumulative distributions may be approximated with log-normal fits. The fade duration expressed in m of travel has been shown to be relatively invariant to the threshold fade level. Typically, fade durations at 1% probability range from 2 to 8 m. For runs exhibiting more shadowing, fade durations are about 7 to 10 m at 1% probability. This is approximately consistent with fade duration statistics acquired in the U.S. for similar fade conditions [4].

(g) Non-fade duration cumulative distributions may be described with good accuracy by power curve fits where the exponent of the non-fade duration distance is representative of the extent of roadside shadowing. When it is approximately 0.75 or larger, heavy shadowing is prevalent. Lighter shadowing cases result in c in the range of 0.5 to 0.6.

(h) Phase fluctuations are generally so small that the channel characteristics can be estimated from the levels only.

(i) Employing two antennas on the vehicle to obtain diversity improvement, the fraction of the roads along which MSS is faded into inoperability can theoretically be reduced by a factor from 2 to 8. It may be difficult to achieve this improvement in a real system, however, when the effects of switching cannot be neglected.

9. Acknowledgements

The authors are grateful to AUSSAT for sharing in the costs of this experiment and to AUSSAT's Mobilesat group for invaluable logistical and technical support during the campaign. Many thanks are also extended to the Japanese Government for providing the satellite transmissions of ETS-V. We also acknowledge INMARSAT for enabling measurements with INMARSAT POR. This work was supported by the Jet Propulsion Laboratory for the University of Texas under Contract JPL956520 and by NASA Headquarters, Contract #N00039-89-C-5301 for APL.

References

[1] Vogel, W. J. and J. Goldhirsh, "Tree Attenuation at 869 MHz Derived from Remotely Piloted Aircraft Measurements," IEEE Trans. on Antennas and Propagation, AP-34, No. 12, pp. 1460-1464, December 1986.

[2] Goldhirsh, J. and W. J. Vogel, "Roadside Tree Attenuation Measurements at UHF for Land-Mobile Satellite Systems," IEEE Trans. on Antennas and Propagation, APS-35, pp. 589-596, May, 1987.

[3] Vogel, W. J. and J. Goldhirsh, "Fade Measurements at L Band and UHF in Mountainous Terrain for Land Mobile Satellite Systems," IEEE Trans. on Antennas and Propagation, APS-36, January, 1988.

[4] Goldhirsh, J. and W. J. Vogel, "Mobile Satellite System Fade Statistics for Shadowing and Multipath from Roadside Trees at UHF and L Band," Accepted for publication in IEEE Transactions on Antennas and Propagation, April 1989.

[5] Vogel, W. J. and J. Goldhirsh, "Mobile Satellite System Propagation Measurements at L Band Using MARECS-B2,". To be published at future date in IEEE Transactions on Antennas and Propagation (Accepted for publication 4/89).

[6] Goldhirsh, J. and W. J. Vogel, "Propagation Degradation for Mobile Satellite Systems," Johns Hopkins University, Applied Physics Laboratory Technical Digest, April-June 1988, Volume 9, Number 2, pp. 73-81.

[7] Vogel, W. J. and Ui-Seok Hong, "Measurement and Modeling of Land Mobile Satellite Propagation at UHF and L Band," IEEE Trans. on Antennas and Propagation, Vol. AP-36, pp. 707-719, May 1988.

[8] Butterworth, J. S., "Propagation Measurements for Land-Mobile Satellite Systems at 1542 MHz," Communications Research Centre, Ottawa, Canada, Tech. Note No. 723, August 1984.

[9] Jongejans, A., A. Dissanayake, N. Hart, H. Haugli, C. Loisy, and R. Rogard, "PROSAT - Phase 1 Report, European Space Agency Technical Report ESA STR-216, May 1986 (European Space Agency 8-10 Rue Mario-Nikis, 75738 Paris Cedex 15, France)

[10] Dept. of Arts, Heritage and Environment, Think Trees Grow Trees, Australian Government Publishing Service, Canberra, 1985

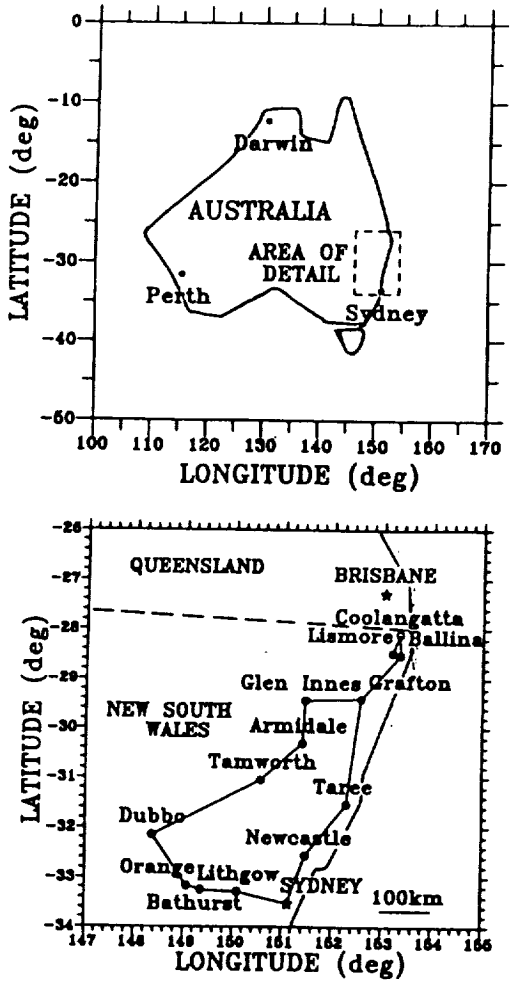

Fig. 1 The roads of South-East Australia along which measurements were taken during campaign.

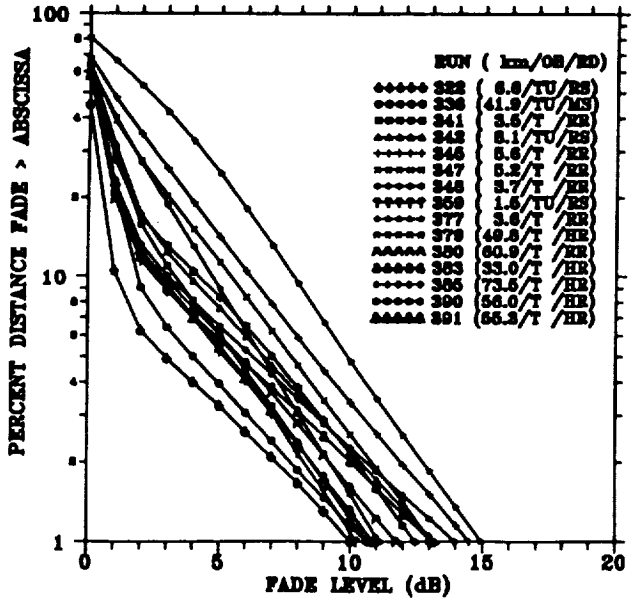

Fig. 2 Fade distributions for all tree and utility pole runs.

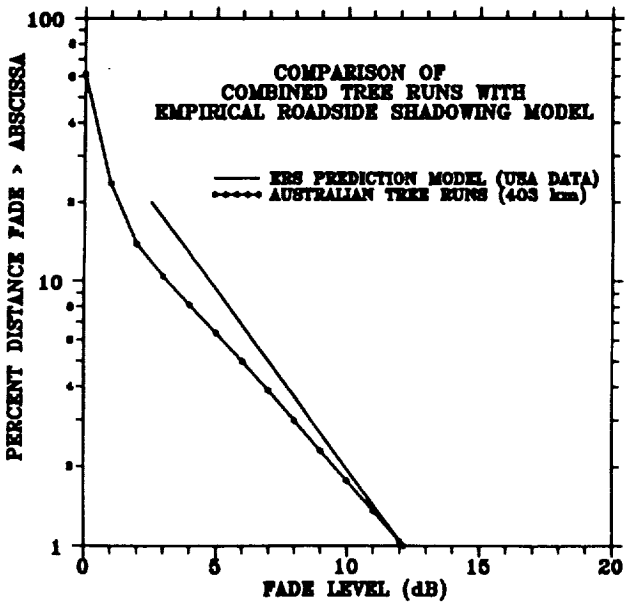

Fig. 3 Combined tree runs compared to USA derived ERS model.

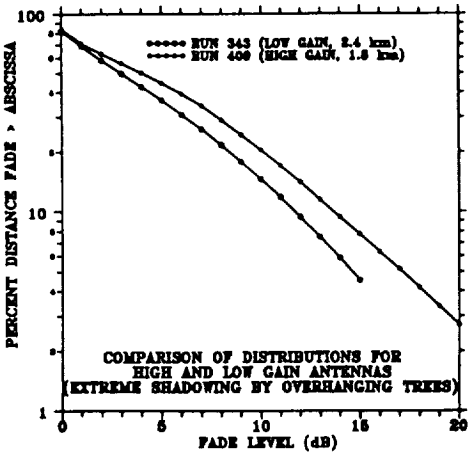

Fig. 4 Comparison of high and low gain antenna measurements under extreme shadowing.

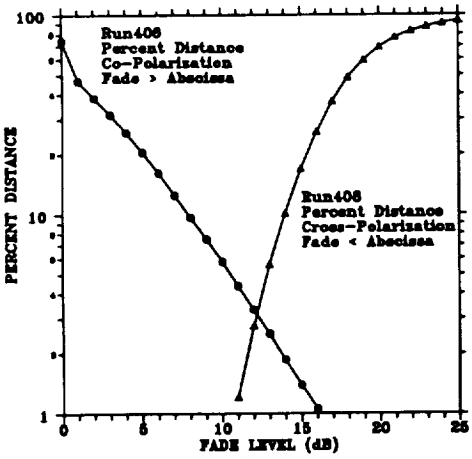

Fig. 6 Estimated cross polar isolation of high gain antenna.

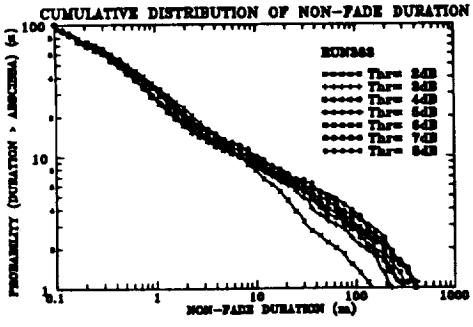

Fig. 8 Cumulative distribution of measured non-fade durations.

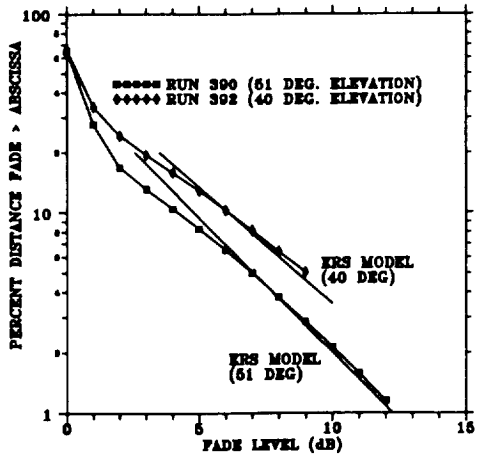

Fig. 5 Elevation angle scaling of ERS model and data from ETS-V and INMARSAT POR.

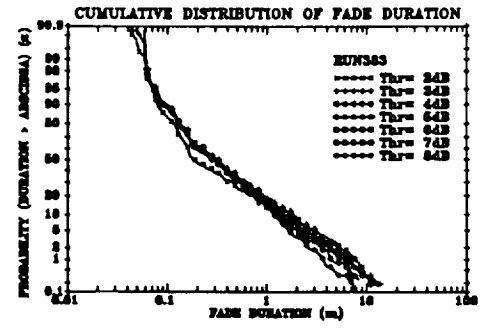

Fig. 7 Cumulative distribution measured fade durations.

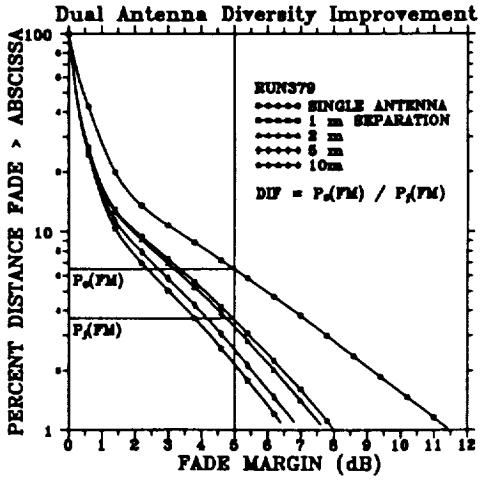

Fig. 9 Diversity improvement as a function of antenna separation.

N90-17950

LMSS DRIVE SIMULATOR FOR MULTIPATH PROPAGATION

Praveen Vishakantaiah, Wolfhard J. Vogel

Electrical Engineering Research Laboratory
The University of Texas at Austin
10100 Burnet Rd., Austin, TX 78758

Abstract--A three-dimensional drive simulator for the prediction of LMSS multipath propagation has been developed. It is based on simple physical and geometrical rules and can be used to evaluate effects of scatterer numbers and positions, receiving antenna pattern, and satellite frequency and position. It is shown that scatterers close to the receiver have the most effect and that directive antennas suppress multipath interference.

1. Introduction

Land mobile satellite service (LMSS) is a new communications system which exploits the strengths of satellites: continental coverage and mobility. It will enable telephone and data service to vehicles traveling throughout the US, especially in rural areas, away from mayor traffic arteries, where terrestrial cellular service may never be established. The design of this system is currently under way and the selection of optimal system parameters, such as antenna pattern, modulation, and coding, requires the knowledge of propagation impairments.

At L band, the intended frequency of LMSS, the two major propagation effects are: (1) fading caused by obstructions in the line-of-sight path between the vehicle and the satellite, and (2) fading caused by the interference of the direct wave with reflections from scatterers all around the vehicle. Several approaches have been followed to quantify propagation effects. Initially, hard- [Davarian, 1987] and software [Divsalar, 1985] simulators were developed based on statistical assumptions of shadowed multipath propagation derived from terrestrial mobile propagation (Ricean and/or Rayleigh multipath, log-normal shadowing). Subsequently, many field measurements of propagation effects were made [see References in Vogel, Goldhirsh, and Hase, 1989], and their results were used to develop empirical [Vogel, Goldhirsh, and Hase, 1989] and semi-empirical [Barts et al, 1987] propagation models. Recently, measurement results have also been used for refining simulators [Berner, 1989].

Although most existing simulators can estimate system performance such as bit error rate as a function of a particular coding and modulation scheme, they are incapable of predicting effects of the distance to and density of the scatterers, the channel bandwidth, or the vehicle antenna pattern. An exception to this is a simulation by Amoroso and Jones [1988], in which a random distribution of 1000 scatterers was assumed to exist in the plane of the vehicle's path. However, the drawbacks of this

study were its two-dimensional approach, which eliminated realistic elevation angle and antenna effects, and the avoidance of any scatterers in proximity to the vehicle, which in field measurements have been shown to dominate the signal variations in the absence of shadowing. The simulator described here remedies these deficiencies. It is an extension of a single scatterer multipath drive simulator [Vogel and Hong, 1988], which was based on simple physical and geometric considerations. The new version allows a vehicle to be driven through a region with many randomly distributed, point-source multipath scatterers. The output of the drive simulator are time series of signal amplitude and phase as well as Doppler spectra, all for user-specified conditions. These outputs, in turn, can be used to calculate system performance parameters. The simulator does not consider shadowing, and this limits its application to low fade margin systems, where multipath fading effects determine system performance most of the time. This is because shadowing tends to completely disrupt transmissions.

2. Model Derivation

The derivations are based on the single scatterer geometry shown in Figure 1, consisting of a satellite transmitting with wavelength w from given azimuth and elevation directions (θ_t,ϕ_t) relative to a vehicle moving with speed v along the x-axis, an arbitrary vehicle antenna pattern (directivity $D(\theta,\phi)$) , and a point-source scatterer s with a given scattering cross section σ and an arbitrary location. The resultant electrical field strength at the receiver is proportional to [Vogel and Hong, 1988]:

$$E_r(t) \propto 1 + \frac{\sqrt{\sigma}\cdot D(\theta_s,\phi_s)}{2\sqrt{\pi}R(t)D(\theta_t,\phi_t)} * \exp[-j\frac{2\pi}{w}[p-a(t)+R(t)]] \quad (1)$$

where p-a(t) is the distance between the plane wave through the origin and the scatterer and R(t) is the distance between the scatterer and the vehicle antenna. The variable part of the sum is the contribution of the single scatterer. In order to obtain the total field at the receiver due to many scatterers, the vector sum of the constant incident field and all the scattered fields e is formed and the relative total power and phase are calculated from:

$$Power_{tot} = [(1 + \Sigma e_{real})^2 + (\Sigma e_{imag})^2]^{1/2} \quad (2)$$

$$Phase_{tot} = \arctan[\frac{\Sigma e_{imag}}{1 + \Sigma e_{real}}] \quad (3)$$

where the summation includes the real or imaginary parts of each scatterer's response e to the incident wave.

The power spectral density of the received wave is calculated by accumulating values of instantaneous power and Doppler frequency at 1000 samples per second, where the instantaneous frequency is the time derivative of the phase of the combined scattered waves, excluding the direct wave:

$$f_d = \frac{\delta(\text{Phase}_{scat})}{\delta t} = \frac{\delta}{\delta t} \arctan\left[\frac{\Sigma e_{imag}}{\Sigma e_{real}}\right] \quad (4)$$

All calculations were performed for time durations of 1 second, corresponding to a driving distance of about 25 m at a speed of 55 mph.

3. Model Validation

The operation of the model was validated by comparing the predicted power and phase assuming a single scatterer to the results from measurements, both with similar parameters. One example of this is shown in Figure 2, which depicts the situation in which the satellite illuminates the vehicle from 7 o'clock with an elevation angle of 35° at a frequency of 1547 MHz. The speed is 54 mph, and a scatterer (σ = 32 m²) is located 3 m to the right and 4 m above the vehicle antenna. The measured and calculated power time series are quite similar. Furthermore, parameters such as the position of the satellite or the scatterer were varied systematically, and the results changed consistently with expectations and measurements, where available.

Another test consisted of comparing the simulated power spectral density to the theoretically expected one [Clarke, 1968]. Figure 3 demonstrates that the simulation model produces the correct Doppler spectrum, centered on the received carrier frequency. The shape shows the typical signature of mobile propagation, a sharply bandlimited spectrum with maximum power at the edges. The frequency deviation of the scattered wave (±120 Hz) agrees with the value expected from the geometry.

4. Results

4.1 Comparison with 2D simulation

The two-dimensional simulation by Amoroso and Jones considered 1000 scatterers randomly distributed in an annular region with an outer radius of 2000 m and an inner radius of 400 m, corresponding to an average scatterer density of 12,000 m²/scatterer. Their simulated fading record of unmodulated carrier power for an omni-directional antenna, reproduced in Figure 4, shows peak-to-peak variations of over 20 dB. The corresponding output of the 3D simulator, for a drooping dipole antenna and with the height of the scatterers randomly distributed between 0 and 10 m, is shown in Figure 5. The range of the received power is less than 1.5 dB and this is in

agreement with measurements made in locations where no scatterers are in the vicinity of the vehicle.

4.2 Dependence of signal variations on clearance

Similar cases to the one above, except for an outer radius of 500 m and the much higher average scatterer density of 625 m^2/scatterer, were run with inner clearance radii from 30 to 400 m. The result, depicted in Figure 6, demonstrates that multipath phenomena for LMSS are significant only if the scatterers are located closely to the vehicle. The standard deviation of the logarithmic amplitude decreases monotonically with increasing inner clearance, from 0.22 dB to 0.07 dB.

4.3 Antenna pattern effects

In order to demonstrate the efficiency of high-gain antennas in reducing multipath interference, several calculations were performed with an antenna having 80° half power beamwidth in both azimuth and elevation planes. Tests with a single scatterer located either in the direction to the satellite or opposite to it resulted for the drooping dipole antenna in fades >10 dB (both cases) and for the high-gain antenna in fades >10 dB and <1 dB, respectively. The suppression of the multipath interference by the antenna patterns remains in effect as long as the antenna is pointed at the satellite.

In an environment with many scatterers, the reduction of the fluctuations is not as extreme, but still significant. For the case of 500 scatterers within a 10 to 300 m annulus, the peak-to-peak fluctuations were reduced by a factor of 4.5, from 7.2 dB to 1.6 dB.

5. Conclusion

A three-dimensional drive simulator has been used to calculate signal level time series for LMSS. The simulator allows the realistic inclusion of many scatterers in random positions as well as arbitrary antenna patterns. The major conclusions reached from this work are:

(1) Two-dimensional simulations overestimate multipath, because the elevation angle selectivity of the receiving antenna has to be neglected. Therefore they cannot be used to predict either amplitude, phase, or bandwidth effects realistically. (2) The three-dimensional simulator demonstrates that only scatterers in the immediate vicinity of the receiver matter. As a consequence, the delay spread spectrum is narrow and has no detrimental impact on contemplated systems with channel bandwidths of 5 kHz. (3) Time-series produced with this simulator will give more realistic inputs to systems which analyze bit error performance than those based on statistical assumptions only.

References

Amoroso, F. and W. W. Jones, " Modeling direct sequence pseudonoise (DSPN) signaling with directional antennas in the dense scatterer mobile environment", Proceedings of the 38th IEEE Vehicular Technology Conference, Philadelphia, PA, June 1988

Barts, R. M., W. L. Stutzman, W. T. Smith, R. S. Schmier, and C. W. Bostian, "Land mobile satellite propagation modeling", Proceedings of 1987 IEEE Antennas and Propagation Society International Symposium, Blacksburg, VA, June 1987

Berner, J. B., "Channel Simulator Upgrade to Use Field Propagation Data", contained in these proceedings

Clarke, R. H., "A statistical theory of mobile-radio reception", BSTJ, Vol. 47, No. 6, pp.957-1000, July-August 1968

Davarian, F., "Channel Simulation to Facilitate Mobile-Satellite Communications Research", IEEE Transactions on Communications, Vol. 35, No. 1, pp. 47-56, January 1987

Divsalar, D., "JPL's Mobile Communication Channel Software Simulator", Proceedings of the Propagation Workshop in Support of MSAT-X, January 30-31, 1985, JPL Internal Document D-2208, January 1985

Vogel, W. J. and U. S. Hong, "Measurement and Modeling of Land Mobile Satellite Propagation at UHF and L-Band", IEEE Transactions on Antennas and Propagation, Vol. 36, No. 5, pp. 707 719, May 1988

Vogel, W. J., J. Goldhirsh, and Y. Hase, "The Australian Experiment with ETS-V", contained in these proceedings

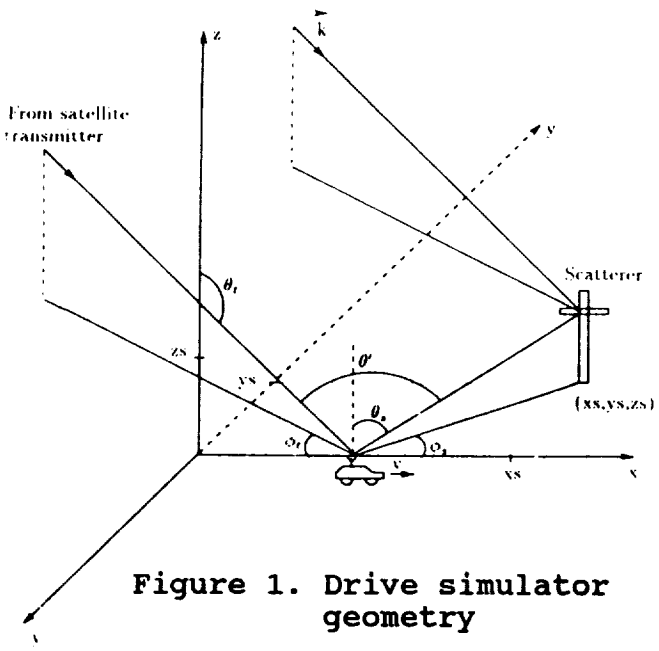

Figure 1. Drive simulator geometry

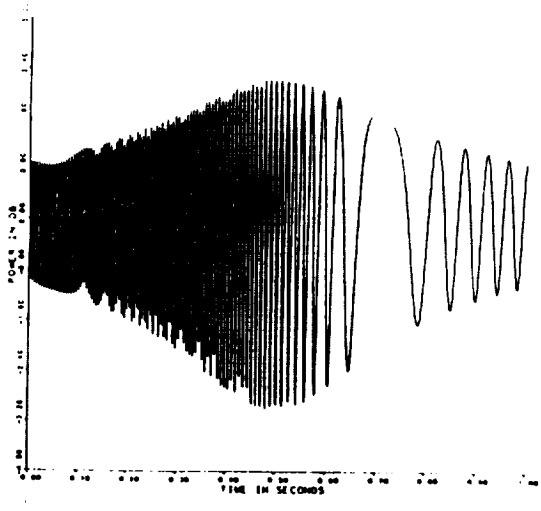

Figure 2. A single scatterer simulation output

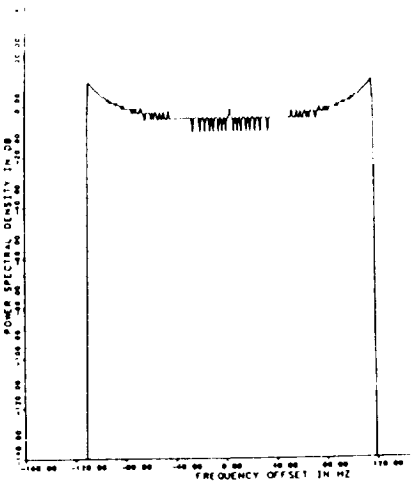

Figure 3. Doppler spectrum for one scatterer

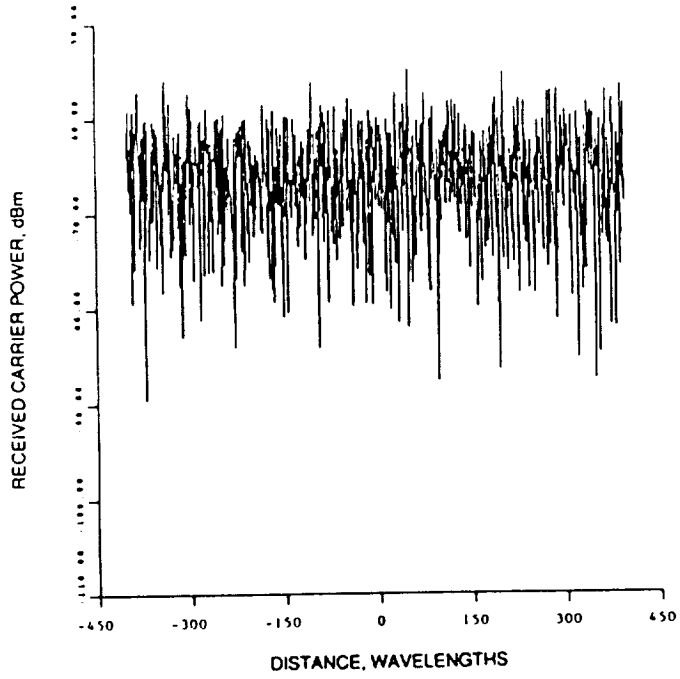

Figure 4. Amoroso's simulated fading record

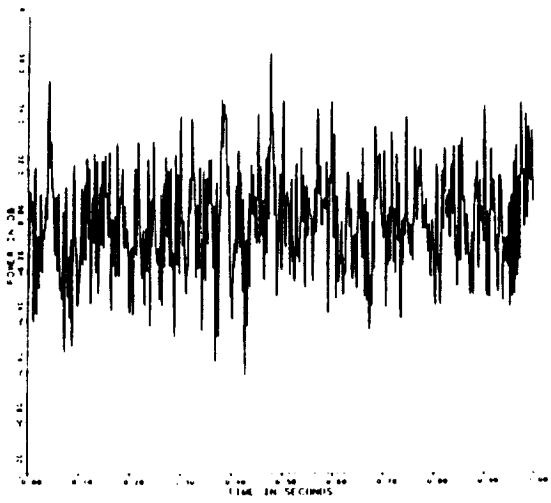

Figure 5. 3D simulation of 1000 scatterers

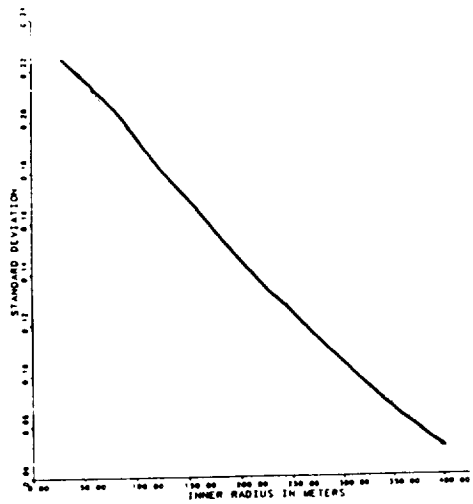

Figure 6. Power STDV as a function of inner clearance radius

JAPANESE PROPAGATION EXPERIMENTS WITH ETS-V

Tetsushi Ikegami
Kashima Space Research Center
Communications Research Laboratory
Ministry of Posts and Telecommunications
Kashima, Ibaraki 314 Japan

Abstract--Propagation experiments for maritime, aeronautical and land mobile satellite communications have been carried out using Engineering Test Satellite-five (ETS-V). The propagation experiments are one of major missions of Experimental Mobile Satellite System (EMSS) which is aimed for establishing basic technology for future general mobile satellite communication systems. This paper presents a brief introduction for the experimental results on propagation problems of ETS-V/EMSS.

1. Introduction

Ministry of Posts and Telecommunications (MPT) of Japan has promoted experiments on mobile satellite communications using an Engineering Test Satellite-five (ETS-V). The experimental system is called Experimental Mobile Satellite System (EMSS) (Hase et al, 1986). The EMSS consists of the ETS-V, a feeder link earth station at Kashima and several kinds of mobile earth stations including a small ship, an aircraft, land mobiles and a hand carried terminal. The ETS-V is maintained in a geostationary orbit over the Pacific Ocean (150deg. E).

Communications Research Laboratory (CRL) is leading the EMSS experiments, and both Nippon Telegraph and Telephone Co. (NTT) (Mishima et al, 1988) and Kokusai Denshin Denwa Co. (KDD) (Yasuda et al, 1989) are participating in the experiments to establish basic technology of future mobile satellite communication systems. This paper describes a brief introduction of the experimental results on propagation problems.

2. Maritime satellite channel

2.1 Outline of experiments

On board experiments have been carried out using a fish training ship of Hokkaido University (1700 tons). The cruising courses for the experiments are shown in Fig.1. A ship earth station for small ship consists of an improved short backfire antenna (40 cm in diameter and 15dBi in gain) with a mechanical stabilizer and of communication terminals with several kinds of MODEMs and CODECs. The antenna system has a fading reduction circuit for compensating the fading effect due to sea surface reflection, because this effect can not be neglected in low elevation areas to the satellite (Ohmori et al, 1983). Fig.2 is a block diagram of the fading reduction circuit. The circuit cancels out the co-polarized and cross-polarized signal components caused by the sea reflection by adjusting an attenuator and a phase shifter to make both components same in amplitude and out of phase each other.

2.2 Sea reflection fading

Fig.3(a)(b) show the received signal levels at elevation angle of

5.9deg. without/with a fading reduction circuit, Fig.3(c) shows the received signal level of the cross-polarized component and Fig.3(d) shows wave height measured by an onboard microwave height detector, respectively. Apparently the amount of fading is reduced by the fading reduction circuit. This fact is confirmed by considering cumulative distribution as in Fig.4 in which the received signal levels are found to fit to the Rician distribution and a fading depth of 10.9dB is reduced to 1.4dB. The observed fading depths at various elevation angles are plotted in Fig.5. It should be noted that the larger the wave height is coming up to 0.5m in standard deviation and the lower the elevation angle is going down, the fading is becoming deeper (Ikegami et al, 1989).

2.3 Blocking effect of above deck structures

The antenna system is installed on the upper deck near a radar mast in order to evaluate the blocking effect to the transmitting and receiving signal to/from the satellite. Fig.6 shows an overlook of the antenna and the mast, on which some radar antennas are installed as indicated by a dotted circle. When a beam of the antenna is shadowed by the mast, the received signals are suffered from blocking effect. Even if the beam is partly shadowed, by the scattering effects due to the mast, the received signal consists not only of a co-polarized component but of a cross-polarized component. Fig.7 shows the co- and cross-polarized components of received signals under the slight shadowing condition. The cumulative distributions of the co- and cross-components are shown in Fig.8. The co- and cross-components are found to fit to the Rician and Gaussian distribution, respectively.

3. Aeronautical mobile satellite channel

3.1 Outline of experiments

In-flight experiments were carried out using a Japan Air Line (JAL) Boeing-747 cargo plane between Tokyo and Anchorage. Three additional flights from Tokyo to Singapore, from Anchorage to Los Angles and from Bangkok to Tokyo were conducted to collect data under various kinds of antenna pointing conditions.

The onboard antenna subsystem is composed of two 16-element phased array antennas, which is installed on the top of fuselage and its gain varies from 12 to 15 dBi within scanning angles of 30 to 150 degrees in azimuth. The coverage of the antenna is shown in Fig.9. Communication terminals with several kinds of MODEMs and CODECs are installed in the upper deck of a cabin.

3.2 Experimental results

As shown in Fig.10(a), the fading effects by the sea reflection was so small as to be neglected and a stable communication channel is kept even in low elevation of 5deg. near Anchorage. The reason is that the antenna is installed on the top of the aircraft body, so the reflected signals by the sea surface were blocked by main wings and a fuselage. However, in a certain condition, slow fluctuations of about 3dB were observed as shown in Fig.10(b). Fig.11(a) illustrates the cumulative distribution of the received signal revel. This effect is considered to be the scattering from a main wing and its edge, because the beam direction corresponds to the direction of a right side main wing (Hase

et al, 1989). These experimental results are summarized in Fig.12 .

An interesting point to note is that even in the case where the elevation angles to the satellite were bellow 0 degree, the signals from the satellite could be received as shown in Fig.10(c) and Fig.11(b). This is because that at altitude of 30000ft., the satellite can be seen with the elevation angles of -3 degrees.

4. Land mobile satellite channel

The effect of fading and shadowing due to terrains, trees and such structures as buildings or traffic signs must be considered in land mobile satellite communications. In order to evaluate these effects, measurements were carried out on freeways (Tokyo-Kyoto, Tokyo-Yuzawa) and on roads in urban Tokyo. In these experiments, the elevation angles to the satellite are 46 to 48 degrees. The cumulative distributions of the received signal level with an omnidirectional antenna are shown in Fig.13. On the freeways, the fading depths for a line-of-sight path are only a few decibels, and a large amount of fade due to shadowing effects appeared only 1-2% of the time. This result indicates that the land mobile satellite communication is feasible on freeways. However, from an example of urban experiments, about 30% of places are affected by the shadowing effects. This result suggests that there would be some difficulties in offering stable communication channels in the urban areas.

Propagation experiments on a superexpress train "Shinkansen" are now in progress, and the early result indicates that the effect of electrical noise from pantographs of the train is a significant factor in satellite channels for railways.

5. Conclusion

The results of ETS-V propagation experiments are briefly reported. The most of experiments have now been in progress and a large amount of data are now analyzed. Especially experiments on land mobile satellite channels have just started. The results of the experiments on aeronautical satellite channels are expected to contribute to the early introduction of commercial aeronautical satellite services.

References

Hase, Y., Ohmori, S. and Kosaka, K., "Experimental Mobile Satellite System(EMSS) using ETS-V,"IEEE Denshi Tokyo, No.25,1986.

Mishima, H., Satoh, K. and Hagiwara, E., "Multi-Beam Mobile Satellite Communication Systems," ICC'88, 34.3, Philadelphia,1988.

Yasuda, Y., Ohashi, M., Sugaya, F., Yasunaga, M. and Karasawa, Y., "Field Experiment on Digital Maritime and Aeronautical Satellite Communication Systems using ETS-V," ICC'89, 7.2, Boston, 1989.

Ohmori, S. and Miura, S., "A Fading Reduction Method for Maritime Satellite Communications," IEEE Trans. AP., vol.AP-31, No.1, pp.184-187, Jan. 1983.

Ikegami, T., Maruyama, S., Kawasaki, K. and Ohmori, S., "Experimental Study of Fading Reduction Method for Maritime Mobile Satellite Communications," IEEE APS, San Jose, 1989.

Hase, Y., Taira, S. Wakana, H. and Ohmori, S., "ETS-V/EMSS Experiments on Aeronautical Communications," ICC'89, 7.1, Boston, 1989.

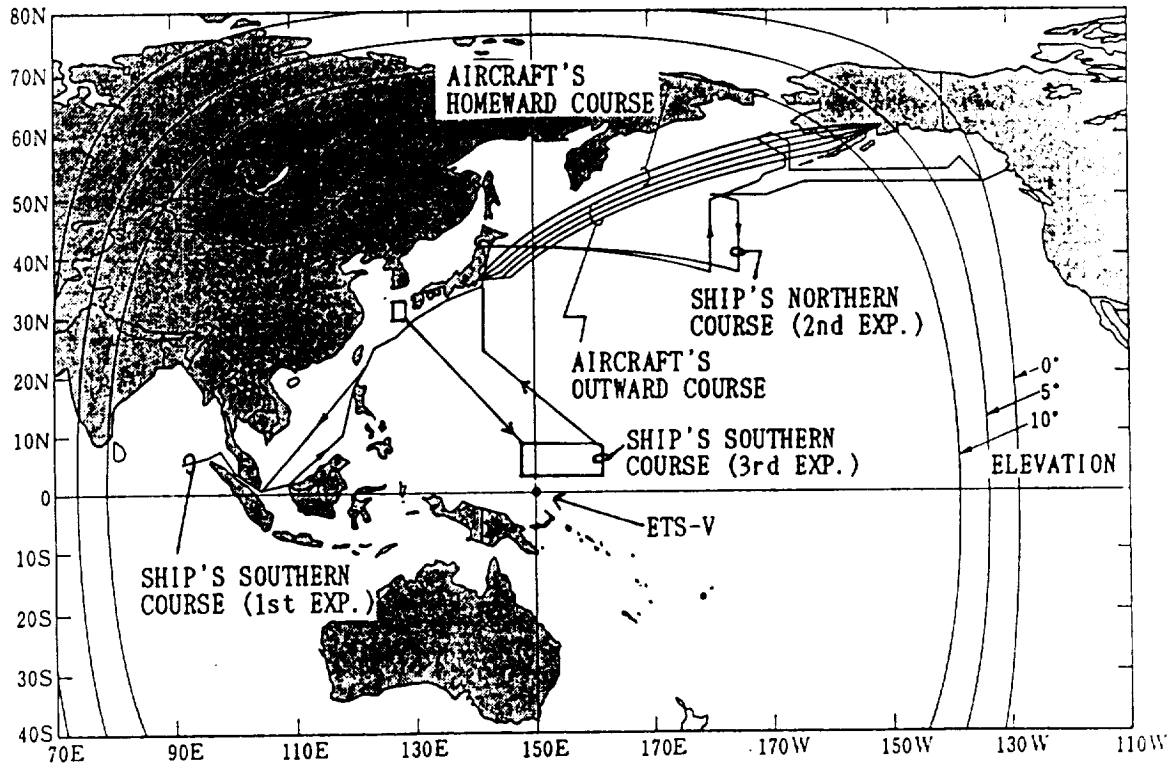

Fig.1 Cruising course of the ship and aircraft

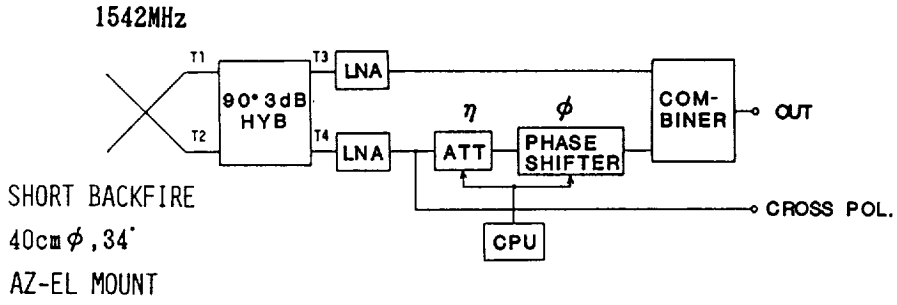

Fig.2 Block diagram of fading reduction circuit

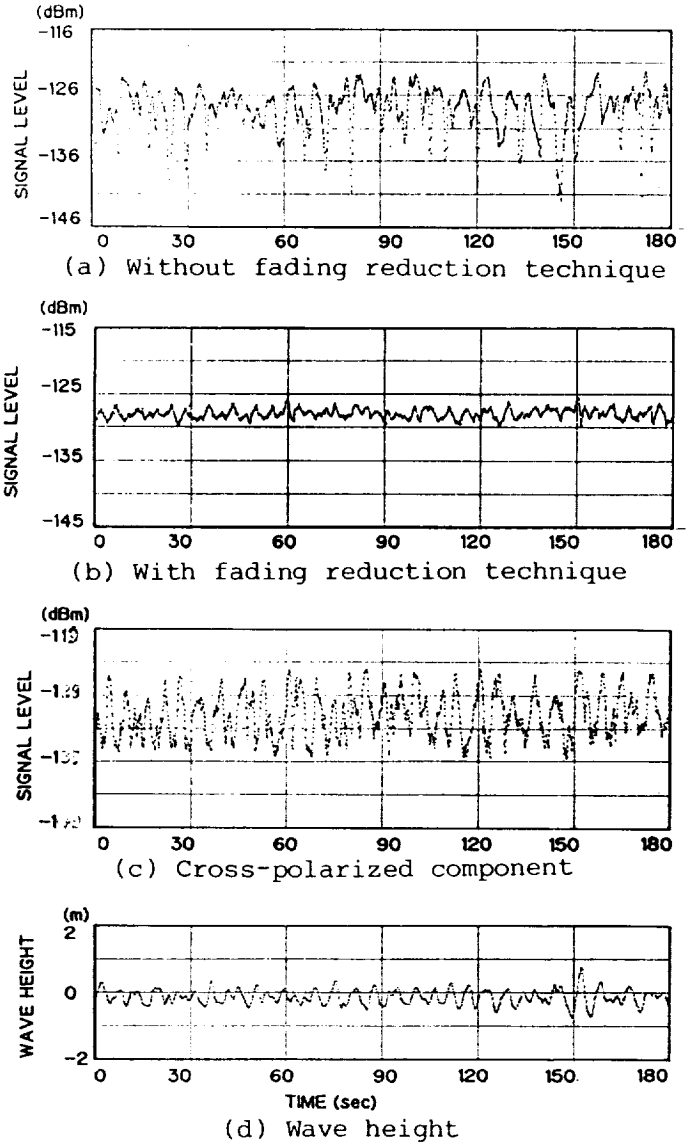

Fig.3 An example of maritime experiments

El=5.9deg.

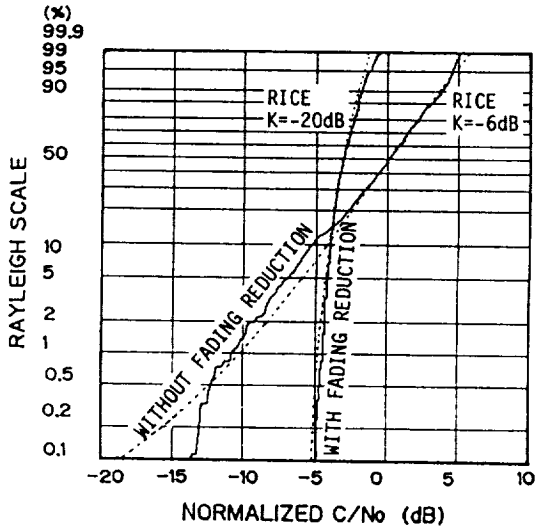

Fig.4 Cumulative distributions of received signal with and without fading reduction technique

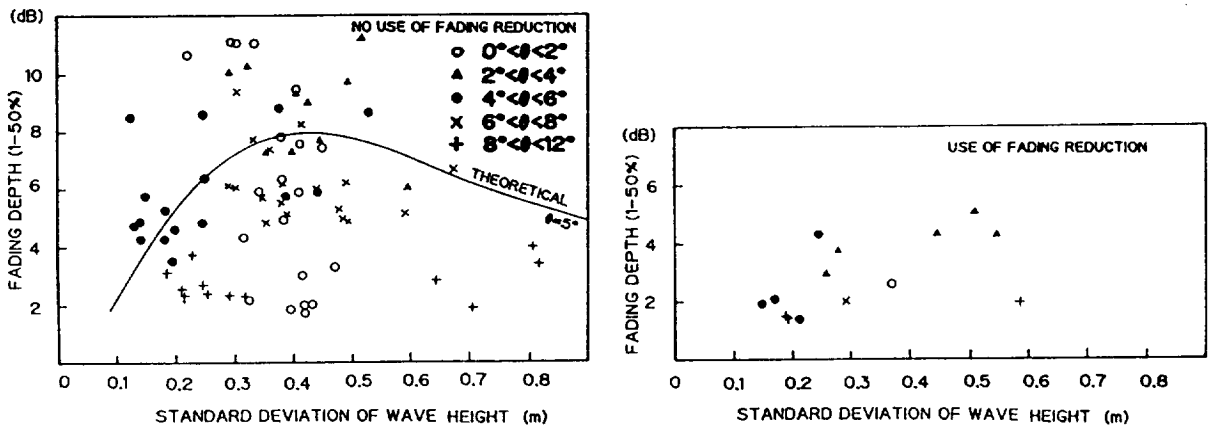

(a) No use of fading reduction technique (b) Use of fading reduction technique

Fig.5 Relation between wave height and fading depth :elevation angle

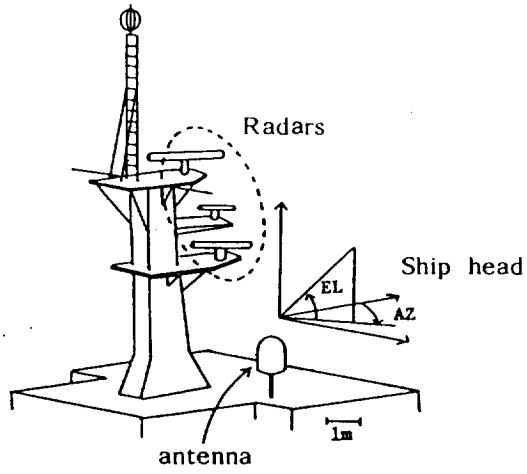

Fig.6 Overlook of the antenna and above deck structures

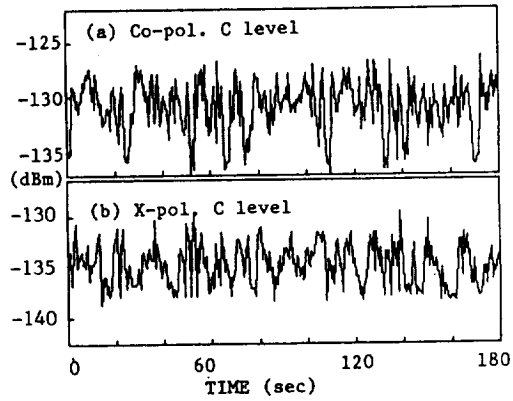

Fig.7 Co- and cross-polarized received signals under blocking conditions

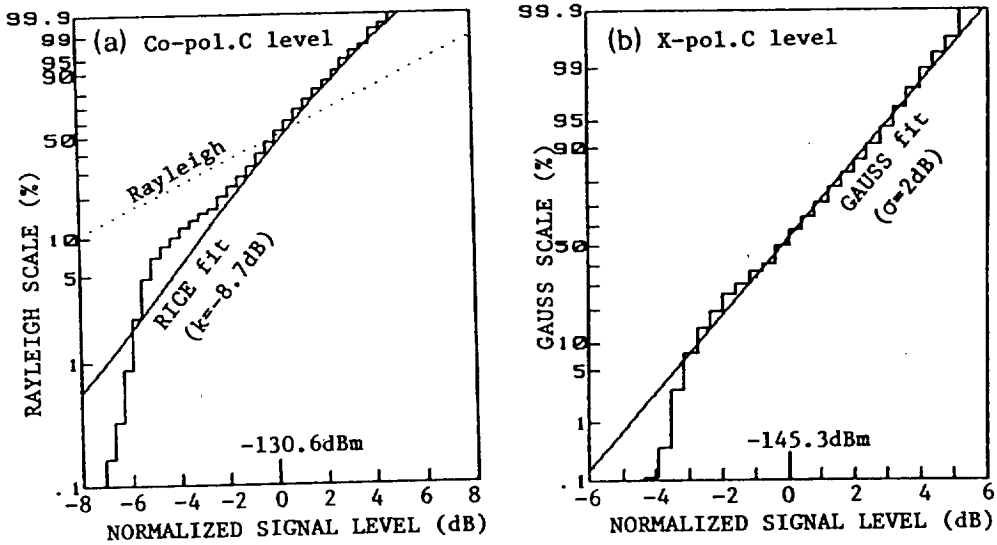

Fig.8 Cumulative distributions of co- and cross-polarized signals

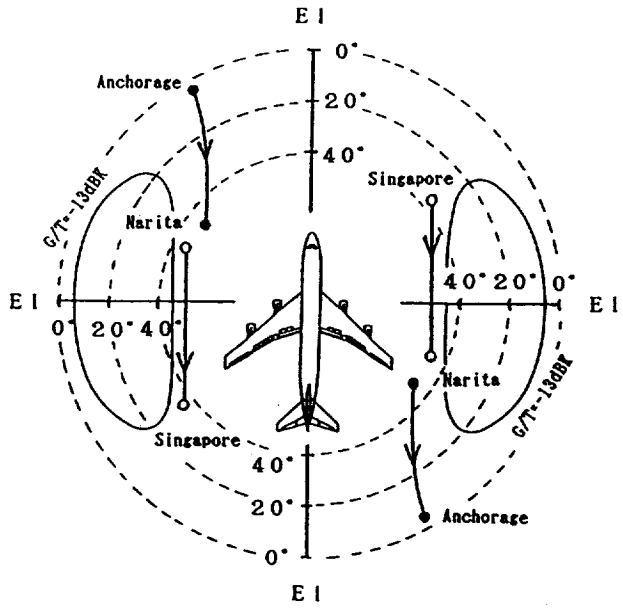

Fig.9 Coverage of airborne antenna

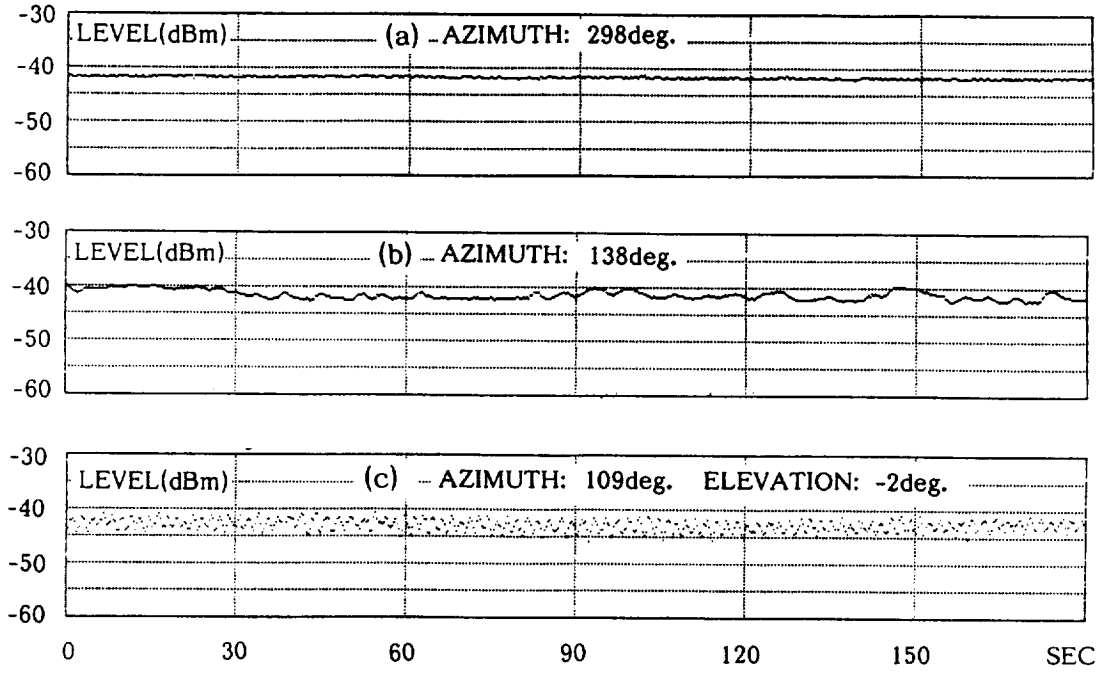

Fig.10 Received signal levels measured on the aircraft

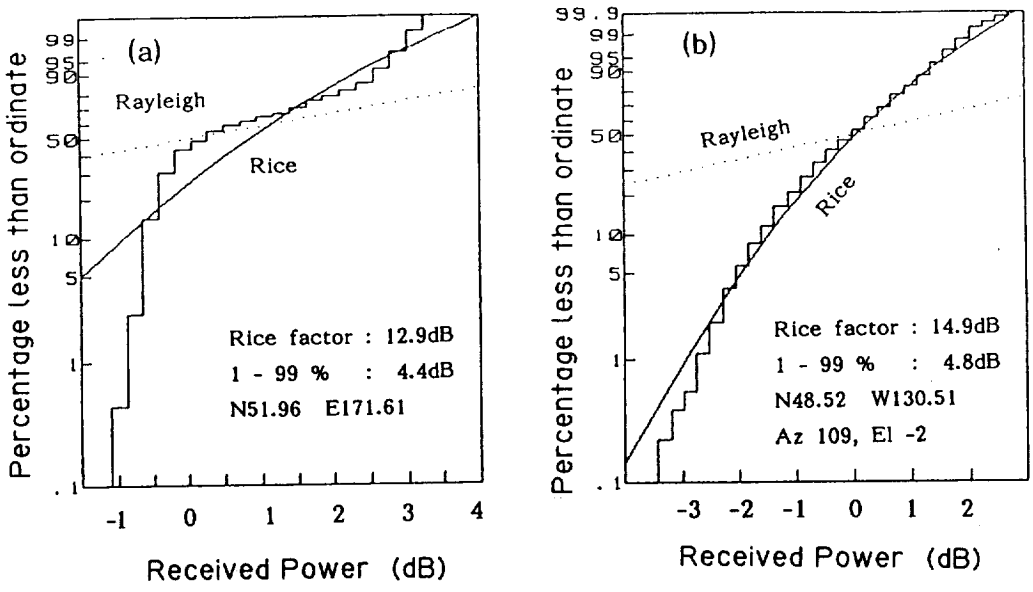

Fig.11 Cumulative distributions of received signals measured on the aircraft

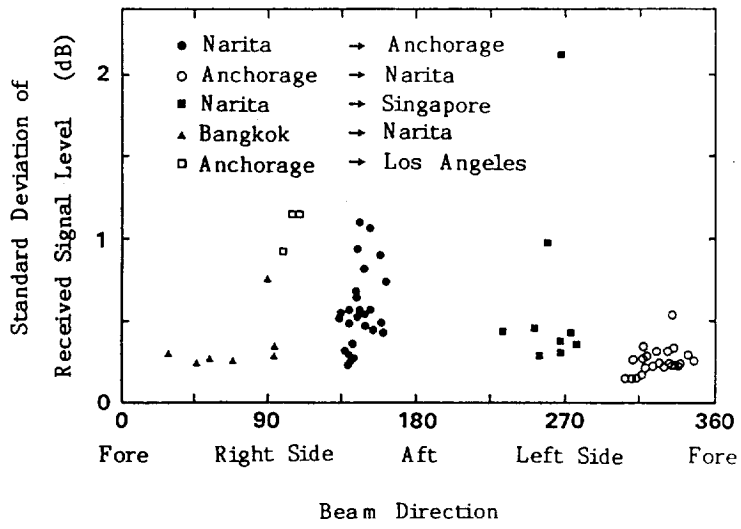

Fig.12 Standard deviation of received signals measured on the aircraft

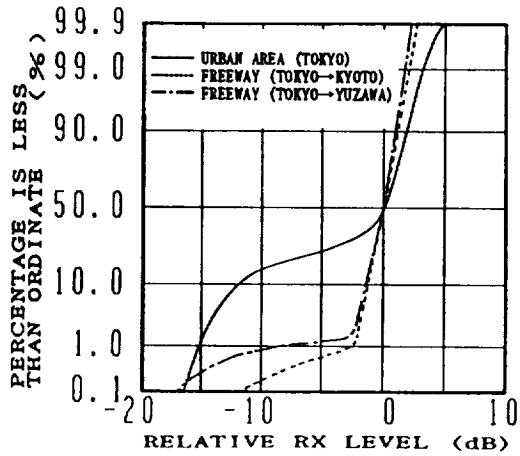

Fig.13 Cumulative distributions of received signals measured on freeways and loads

Plan of Advanced Satellite Communication Experiments using ETS-VI

Tetsushi Ikegami
Kashima Space Research Center
Communications Research Laboratory
Ministry of Posts and Telecommunications
Kashima, Ibaraki, 314 Japan

Abstract--In 1992, an Engineering Test Satellite VI is scheduled to be launched by an H-II rocket. The missions of ETS-VI are to establish basic technologies of inter-satellite communications using S-band, millimeter waves and optical beams and of fixed and mobile satellite communications using multibeam antenna on board the satellite. This paper introduces a plan of the experiments.

1.Introduction

An Engineering Test Satellite VI (ETS-VI) is a 2-ton class, three axis stabilized satellite as shown in Figure 1, which is scheduled to be launched in 1992 by an H-II rocket. One of main missions of the ETS-VI is to develop basic technologies for advanced satellite communication systems in the future. This paper presents brief introduction for a plan of propagation and communication experiments using the ETS-VI.

2.Experimental system

The major characteristics of the ETS-VI and experimental communication payloads are summarized in Table 1. The ETS-VI has basic missions to establish advanced technologies such as inter-satellite communications, mobile satellite communications and fixed satellite communications (Shiomi et al, 1988) (Nakagawa et al, 1988)(Kitahara et al, 1989). Communications Research Laboratory (CRL) has three missions, and these are summarized as follows.

(1)S-band inter-satellite communications

CRL develops S-band (2.3/2.1GHz) inter-satellite communication payload (SIC) with a multibeam phased array antenna in cooperation with National Space Development Agency of Japan (NASDA). The specification of the SIC is summarized in Table 2. The SIC is compatible with the S-band Multiple Access (SMA) system of NASA's TDRSS. CRL and NASDA plan to conduct fundamental tracking and data relay experiments between ETS-VI and low orbit satellites. The SIC can also be used for the data relay of TDRSS SMA's user satellites. Figure 2 shows a concept of an S-band inter-satellite communication system.

(2)Millimeter wave satellite communications

CRL develops a millimeter wave (43/38GHz) transponder on the basis of research through the ETS-II (1977) and Japanese ECS (1979) satellite programs. The frequencies 43/38GHz are selected considering the atmospheric attenuation allowable in personal satellite communications and the achievable technology level of millimeter devices. The major specifications of the millimeter wave transponder are summarized in Table 3. The objectives of millimeter wave mission are to develop high

data rate inter-satellite communication technology and to study the feasibility of personal satellite communication system. Figure 3 shows a concept of this mission.

(3)Optical inter-satellite communications

CRL develops an optical communication system with a telescope of 75 mm in diameter, which has a beam pointing/tracking mechanism with a gimbal mirror. The onboard optical communication payload (Laser Communication Equipment, LCE) has fundamental optical communication functions with a laser diode transmitter of wave length 0.83 micron, a beam point-ahead mechanism, a receiver of wave length 0.51 micron, modulator/demodulator subsystems, and so on. These feature are summarized in Table 4, and a concept of this mission is shown in Fig. 4.

3.Frequency bands available for propagation experiments

The following frequency bands, which are used for corresponding missions, can be used for the propagation experiments.

2.3/2.1GHz	S-band inter-satellite communications
2.6/2.5GHz	Mobile satellite communications
30/20 GHz	Feeder links for the ETS-VI
32/23 GHz	Ka-band inter-satellite communications
43/38 GHz	Millimeter wave satellite communications
590/360THz	Optical inter-satellite communications

4.Conclusion

Experiments on advanced satellite communications will start in 1992 using an ETS-VI satellite. Propagation experiments are scheduled to carry out with several frequency bands such as 2GHz, 20GHz, 40GHz and 590THz.

References

Shiomi, T. et al, "Plan of Advanced Satellite Communications Experiment Using ETS-VI," International Symposium on Space Technology and Science (ISTS), Sapporo, May 1988.

Nakagawa, K. et al, "Fixed and Mobile Multibeam Communications Experiment Payload for ETS-VI," ISTS, Sapporo, May 1988.

Kitahara, H. et al, "An Overview of Japan's Engineering Test Satellite VI (ETS-VI) Project," ICC'89, 52.3, Boston, June 1989.

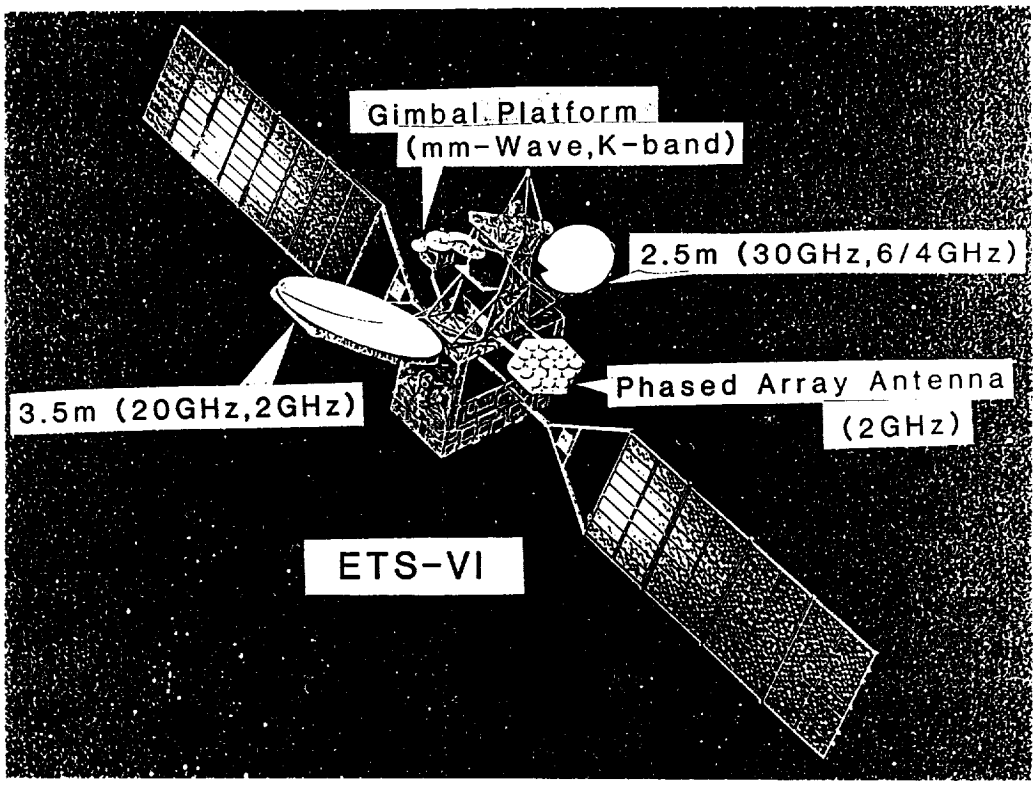

Fig. 1 ETS-VI

Table 1 Features of ETS-VI

Bus System	
Shape	Rectangular body with deployable solar paddles
Weight	Approx. 2 tons (beginning of life) Payload capacity 660 kg
Attitude Control	3-axis-stabilization
Life	10 years for satellite bus
Electric Power	4100 W (end of life at summer solstice)
Launch Vehicle	H-II rocket
Launch Date	Summer 1992
Payloads for Communications Experiment	
Fixed and Mobile Satellite Communications	
S-band Inter-satellite Communications	
K-band Inter-satellite Communications	
Millimeter-wave Satellite Communications	
Optical Satellite Communications	

Table 2 System performance of SIC

Frequency (GHz)	Forward 2.1034-2.1094 Return 2.2845-2.2905	
Data Rate	Less than 1.5 Mbps	
Modulation	PCM-PSK/SSMA	
Bandwidth	6 MHz	
Antenna	Multibeam Phased Array	
Field of View	20 degrees (covering satellites below 1000 km altitude)	
Return Link	Number of Beams	2
	Minimum Gain	27.4 dB (FOV)
	Polarization	LHC
Forward Link	Number of Beam	1
	Minimum Gain	27.1 dB (FOV)
	EIRP	35.5 dBW
	Polarization	LHC

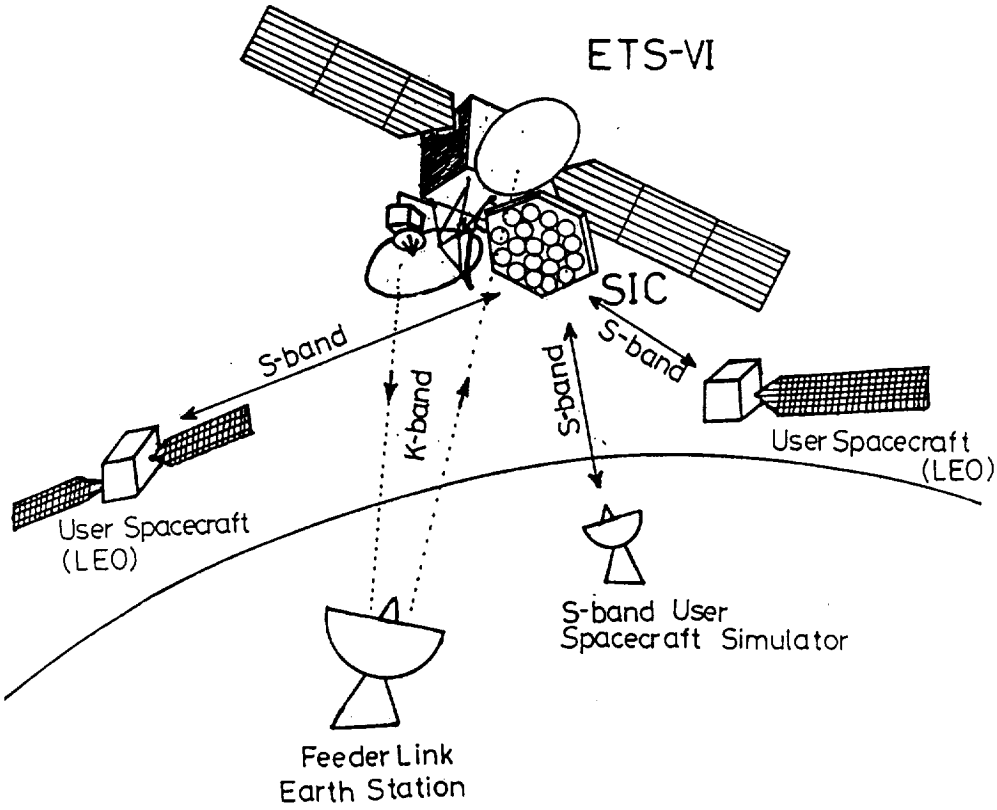

Fig. 2 S-band inter-satellite communications

Table 3 Specifications of ETS-VI millimeter-wave transponder

Frequency		
Receive	43.0	GHz
Transmit	38.0	GHz
IF	1.98	GHz
Receiver NF (LNA front-end)	6.0	dB
Transmit Power (SSPA)	0.5	W
Local Oscillator		
Stability	3×10^{-7}	(-10 to +40 deg C)
Phase Noise	-75	dBc/Hz

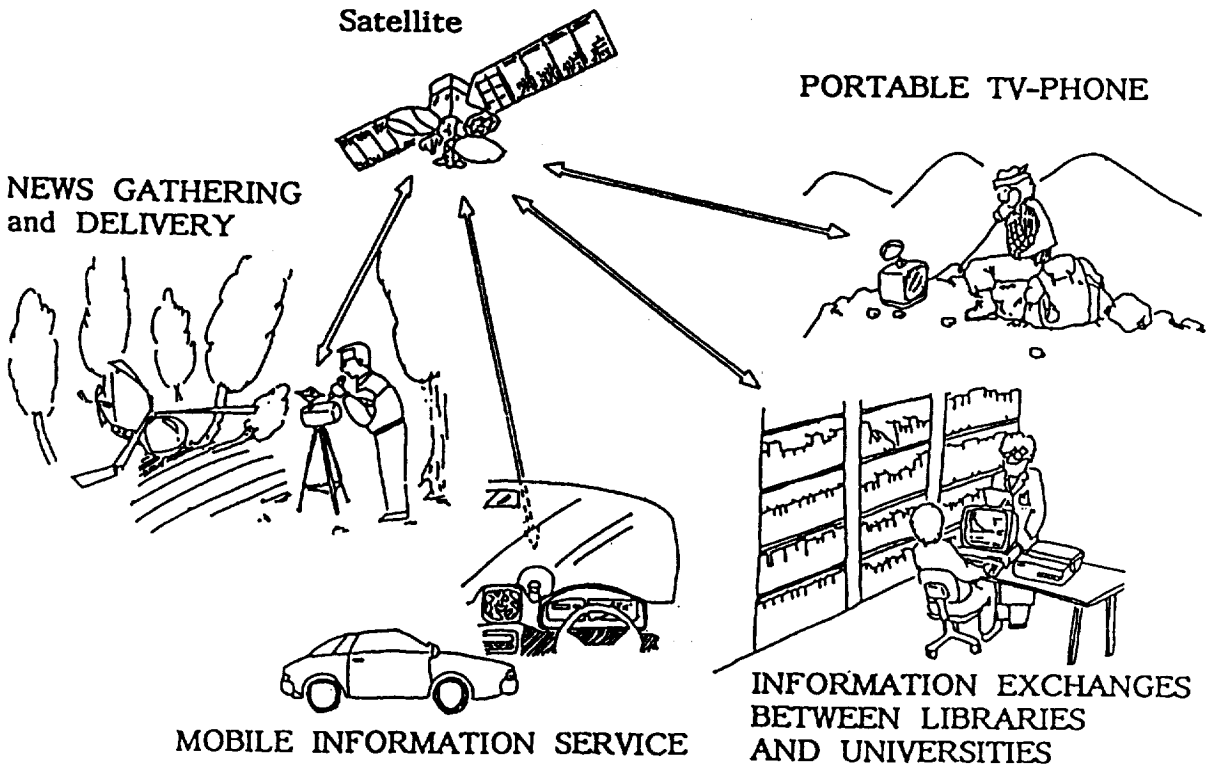

Fig. 3 Millimeter-wave personal communications via ETS-VI

Table 4 Main Features of LCE

Antenna	75 mm diameter telescope FOV 0.46 deg
Tracking and Pointing	
Coarse	Two-axis gimbal mirror and CCD sensor Beam steering angle 3.0 deg
Fine	Fine-pointing mechanism with mirrors and 4QD (FOV: 400 microrad) Pointing accuracy 2 microrad
Point-ahead Mechanism	mirrors on laminate-actuators
Receiver	Wave length 0.51 micron Bit rate 1 Mbps Detection Direct detection by APD (FOV:200 microrad)
Transmitter	Redundant laser diodes(AlGaAs) Wave length 0.83 micron Transmit power 10 mW Bit rate 1 to 10 Mbps
Modulation	Intensity Modulation with Manchester code

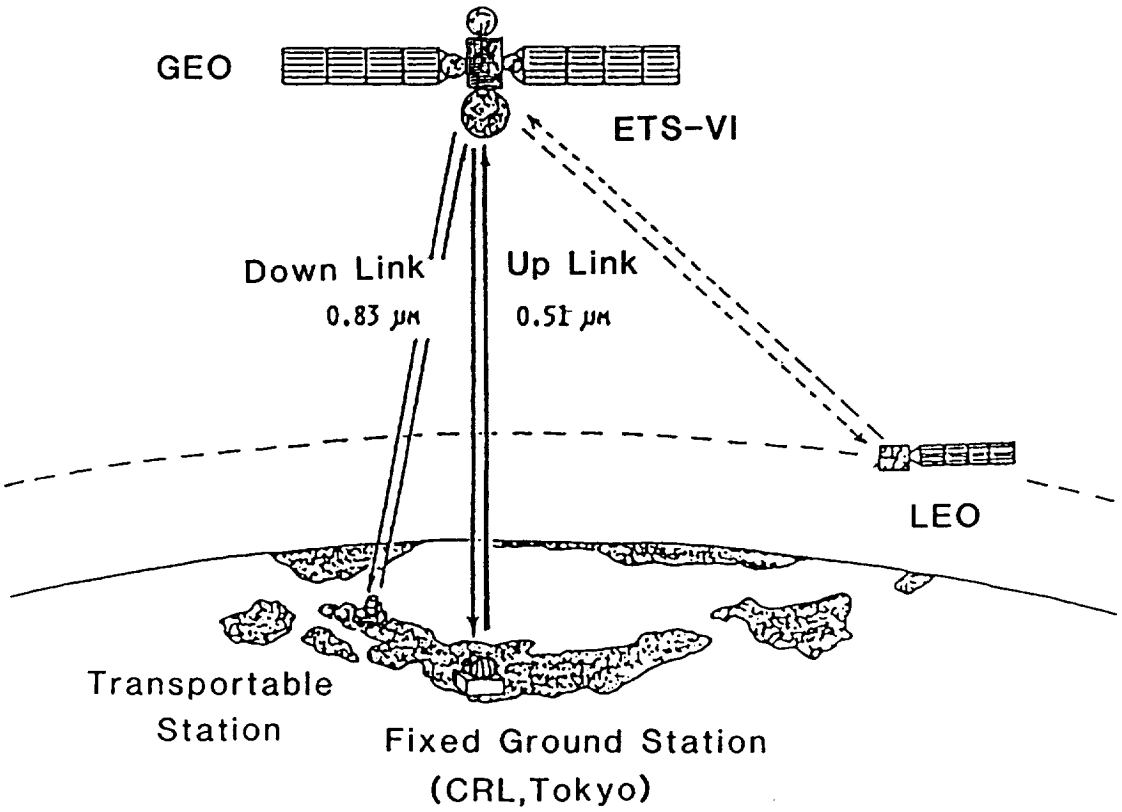

Fig. 4 Experimental system of optical satellite communications

LMSS Modeling Status Report

Warren L. Stutzman and R. Michael Barts

Satellite Communications Group
Bradley Department of Electrical Engineering
Virginia Tech
Blacksburg, VA

Abstract--The need to develop accurate models for secondary statistics of fading land mobile satellite signals has motivated a study of fading signal autocorrelations and multipath spectrum. Results of autocorrelations and power spectral densities from measured data are presented and comparisons to multipath spectrum models are made.

1. Background

Previously we have reported on the development of a software propagation simulator used to simulate fading of Land Mobile Satellite System (LMSS) signals for arbitrary propagation conditions (Stutzman, et al., 1988; Barts and Stutzman, 1988). The simulator generates signals using two data bases of signal components derived from experimental data.

The measures of performance used to evaluate the simulator are its ability to reproduce the primary fading statistics, cumulative fade distribution, and secondary (or conditional) fade statistics, average fade duration and level crossing rates, of experimental data. Previously reported results (Barts and Stutzman, 1988) have shown that the simulator reproduces primary fade statistics for a wide variety of experimentally measured propagation conditions. However, the simulator results for secondary statistics are not satisfactory.

The simulator is constructed to produce accurate primary statistics, but has no inherent model for secondary statistics. The secondary statistical behavior of the simulator is determined by the secondary statistical behavior of the data bases used to construct the simulated signal. Thus, it is important that we correctly process the experimental data when generating the simulator data bases to extract both the correct primary and secondary statistical behavior. However, the processing techniques in use only assure us of extracting primary statistics correctly.

The need for secondary statistics modeling capability led us to a review of the data processing used to generate

the simulator data bases and a study of models for secondary statistics. We began these studies by looking at the dynamic fading signal behavior as represented by the signal autocorrelation. These were used as a stepping stone for examining the spectra of fading signals and comparing them with various multipath models. With these models we are attempting to develop models for the secondary statistics, for which no satisfactory models currently exist. Our approach is based on the modeling of Jakes (1974) wherein if we can establish an appropriate model for the multipath spectrum, we can derive analytical expressions for the secondary statistics.

2. Autocorrelation Studies

The autocorrelation of a signal is a measure of how fast the signal changes with time. We can also consider it a rough measure of the duration of a scatterer's influence upon a fading signal. The broader the autocorrelation function, the slower the signal fades and the longer the period of time an individual scatterer dominates the received signal.

The autocorrelation function is defined as

$$R_{zz}(\tau) = < z(t-\tau)z^*(t) > \qquad (1)$$

where $z(t) = x(t) + j\, y(t)$ is a complex signal. A form of (1) more suitable for evaluation is

$$R_{zz}(\tau) = R_{xx}(\tau) + R_{yy}(\tau) - j[\, R_{xy}(\tau) - R_{yx}(\tau)\,] \qquad (2)$$

where $R_{xx}(\tau)$ and $R_{yy}(\tau)$ are the autocorrelations of the real and imaginary components of the complex signal, respectively. $R_{xy}(\tau)$ and $R_{yx}(\tau)$ are cross correlation between the real and imaginary signal components. We have found that for the experimental data we have that these cross correlations are usually approximately equal resulting in a real autocorrelation function, but this is not always the case, as discussed below.

The autocorrelation as defined in (1) is the expected value of $z(t-\tau)z^*(t)$. When we calculate the autocorrelation of a 1.024-second record of data, we are calculating the autocorrelation of but a single realization of a stochastic process. If we consider consecutive 1.024-second records of experimental data to be multiple realizations of the same process, we can average the resulting autocorrelations to find the expected value function. This is the technique we have used to analyze experimental data. This is also useful for calculating power spectral densities, as discussed below.

Figure 1 is an example of an autocorrelation of balloon data

collected by Vogel (1985). Notice that the real part of the autocorrelation is smooth and slowly varying. This is indicative of signal data that is relatively smooth and does not have rapid fading. Figure 2 shows the signal data from which the autocorrelation function of Figure 1 was derived. Notice that, indeed, the signal data are relatively smooth and free of rapid fading. This is due in part to the slow vehicle speed (8 mph) during data collection, but the data also suggests a scarcity of scatterers or shadowing. Notice that the imaginary component of the autocorrelation in Figure 1, while small, is not negligible. This indicates a correlation between the real and imaginary signal components that is unexplained.

Figure 3 is an example autocorrelation for helicopter data collected by Vogel and Goldhirsh (1988). Figure 4 is the corresponding signal data. Notice that the helicopter autocorrelation function falls off more rapidly and is not smoothly varying. This is indicative of rapid fading and Figure 4 confirms this. The imaginary part of the autocorrelation function for the helicopter data is very small and can be considered negligible.

These examples were taken from single 1.024-second records of data, but the are indicative of the results using averaging. Data from Vogel and Goldhirsh's measurements with the MARECS-B2 satellite (Vogel and Goldhirsh, 1988) have also been analyzed (not included here for the sake of brevity) and are very similar to the helicopter data, which is expected since the two measurements were taken in the same geographical area.

These results give us some insight into processing the experimental data to create the databases used in the propagation simulator. To create the "lognormal" data base, the lognormal component of the signal is estimated by using a running average window. The size of the window was chosen empirically. When dealing with data that are markedly different, such as balloon and helicopter data, empirically choosing the window size is not an optimum technique. By examining the autocorrelation of the signal, we can make an informed judgement about the window size.

3. Power Spectrum Studies of Fading Signals

The fading signal power spectrum is related to the autocorrelation of the signal by a Fourier transform. Using the autocorrelation of the signal to obtain the power spectral density (psd) of a signal has several advantages over using a direct FFT of the signal data. When dealing with a signal in the presence of noise, the autocorrelation

calculation acts as a noise filter, since Gaussian noise is decorrelated. This is particularly helpful when dealing with fading signals which are noisy. The resulting signal psd is not as corrupted as those from a direct FFT. Secondly, it is computationally easier to average the psds of multiple data records by averaging the record autocorrelations. By averaging the psds of multiple records, the important structures of the multipath spectrum become more clearly defined. Using this technique we calculated the multipath spectra for the experimental data from the balloon, helicopter, and satellite measurements. These spectra are used to develop and verify models for the multipath spectrum. They are also being used to design the filters for the data processing used in the propagation simulator.

Figure 5 is a spectrum average from 10 seconds of balloon data. The carrier is obvious at the edge of the graph and the multipath spectrum cuts off rather sharply at approximately 80 Hz. This was somewhat surprizing, since the vehicle speed during these measurements was approximately 8 mph. This spectrum taken alone suggests then that the velocity of the balloon was approximately 60 mph. The spike at the edge of the multipath spectrum is an important feature because it is predicted by the Jakes multipath model, which is discussed below.

Figure 6 is a spectrum average from 10 seconds of MARECS data. In this spectrum the multipath does not have a well defined cutoff. Notice also that the carrier-to-multipath ratio is much smaller than in the helicopter data. This is indicative of a larger number of scatterers in the propagation environment.

3.1 Multipath Spectrum Models

The purpose of the spectrum studies discussed above was to provide a basis for choosing a model of the multipath spectrum that could be used in developing a model for secondary statistics. The simplest and most commonly used multipath spectrum model employs an assumption of scattered waves uniformly spatially distributed around the vehicle. This is the Jakes model (Jakes, 1974). The theoretical spectrum for this model is shown in Figure 7. It has a width of $2f_m$ where f_m is the maximum doppler frequency. Notice the asymptotic behavior of the spectrum at the edges. The behavior of the balloon spectrum shown in Figure 5 corresponds closely to this model.

The MARECS spectrum of Figure 6 looks very different from the Jakes multipath model. This could be due to assumptions upon which the Jakes multipath model is based.

The model assumes that the scatterers are in the far field of the vehicle, and that the scattered fields are plane waves. This would not be true for roadside tree scatterers. Secondly, the Jakes model assumes a uniform spatial distribution for the scattered signal. This produces the asymptotes at the edges of the multipath spectrum, which are products of the scattered signals directly in front of and behind the vehicle. But, in reality, points directly in front of and behind the vehicle are relatively clear of scatterers. The assumption that the scattering from in front of and behind the vehicle is the same as the scattering from the sides is referred to as the "brick wall" fallacy.

Recent work by Campbell has produced a multipath spectrum model that agrees more closely with the result shown in Figure 6. Campbell has simulated a large number of random scatterers along the side of the road in the near field of the vehicle. Figure 8 is an example of the multipath spectrum predicted by Campbell's simulation. While this model still has a well defined cutoff, it is closer to the helicopter and MARECS spectra we observed than the Jakes model.

4. Conclusions

Our recent efforts in modeling and simulation of fading LMSS signals have concentrated on understanding the spectrum of the fading signals. In our effort we are have examined the autocorrelation of the signal as well as the signal power spectral density. In order to improve the signal processing used in the propagation simulator, we need to look at both the signal autocorrelation and power spectral density. These will allow us to make informed decisions on how to design filters used to extract the signal components.

Our study of multipath spectra is a step toward finding appropriate analytical models for the secondary fading statistics. The spectra from experimental data shown here have been compared to two different multipath spectrum models. The results indicate that the Jakes multipath model may be appropriate for slow, shallow fading, such as observed in the balloon measurements. Where there is rapid, deep fading and scatterers are in close proximity of the vehicle, the multipath spectrum produced by Campbell's simulation may be appropriate, as indicated by the helicopter and MARECS measurements.

References

Barts, R. M. and W. L. Stutzman, "Propagation modeling for land mobile satellite systems," Proceedings of the

Mobile Satellite Conference, JPL Publication 88-9, pp. 95-100, May 3-5, 1988.

Goldhirsh, J. and W. J. Vogel, "Propagation effects by roadside trees measured at UHF and L-Band for mobile satellite systems," Proceedings of the Mobile Satellite Conference, JPL Publication 88-9, pp. 87-94, May 3-5, 1988.

Jakes, W. C., editor, Microwave Mobile Communications, John Wiley and Sons, New York, pp. 20-36, 1974.

Stutzman, W. L., et. al., "LMSS propagation modeling at Virginia Tech," Proceedings of NAPEX XII, JPL Publication 88-22, pp. 27-35, June 9-10, 1988.

Vogel, W. J., Land Mobile Satellite Transmission Measurements at 869 MHz, MSAT-X Report No. 106, April 12, 1985.

Vogel, W. J. and J. Goldhirsh, Mobile Satellite Propagation Measurements in Central Maryland Employing MARECS-A, JHU/APL Report S1R88U-049, October 1988.

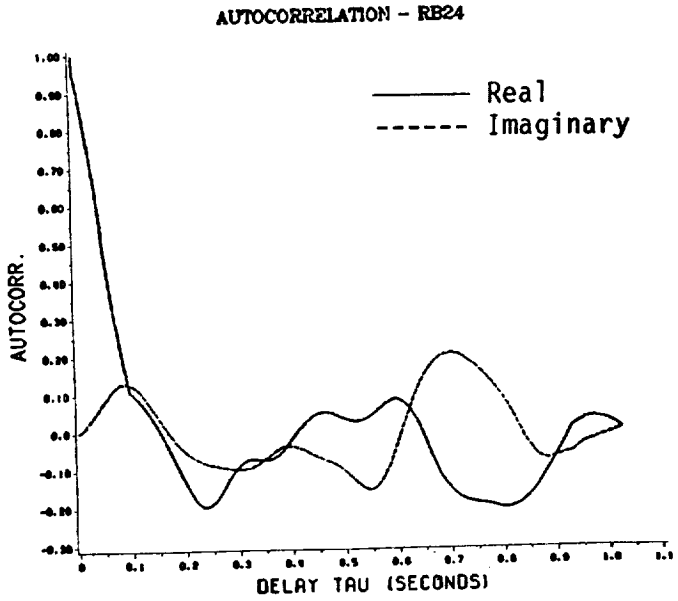

Figure 1. Autocorrelation of data from Vogel's balloon measurements.

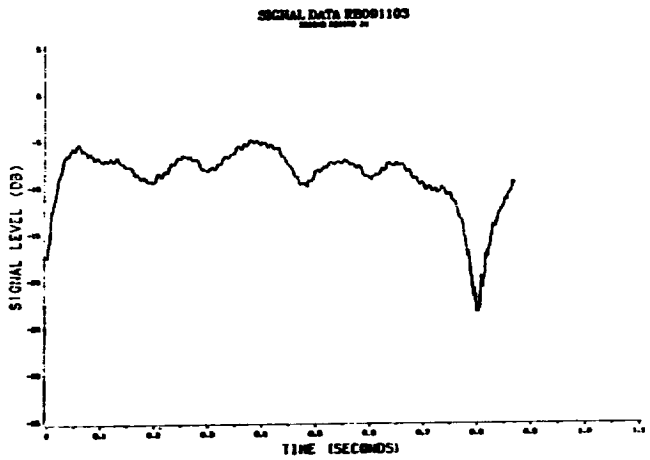

Figure 2. Signal data from Vogel's balloon measurements.

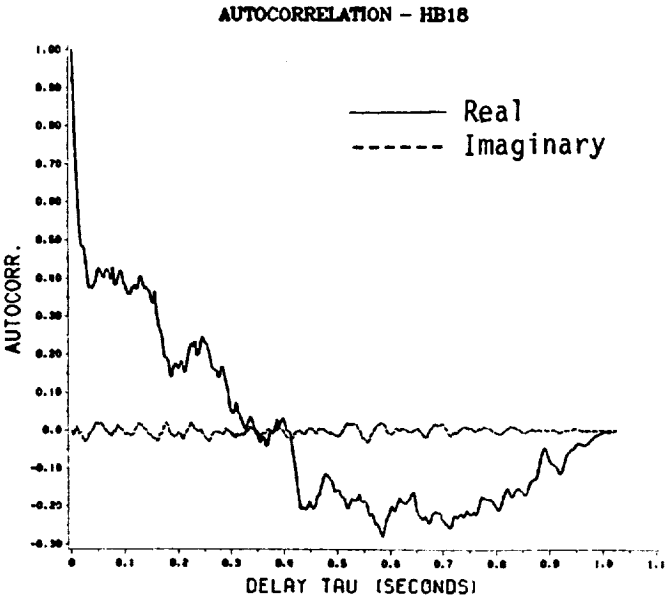

Figure 3. Autocorrelation of data from Vogel and Goldhirsh's helicopter measurements.

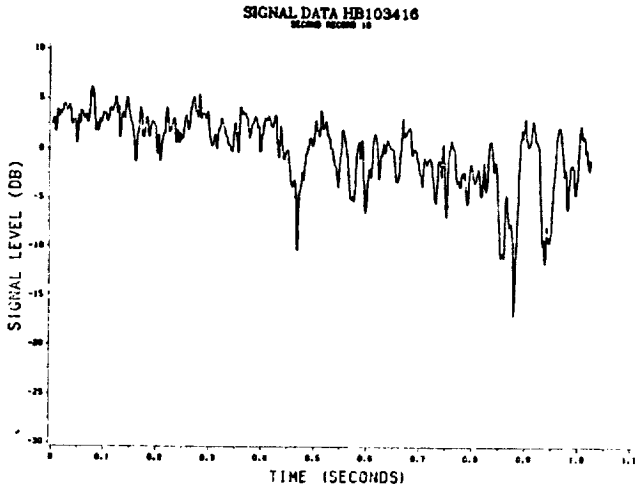

Figure 4. Signal data from Vogel and Goldhirsh's helicopter measurements.

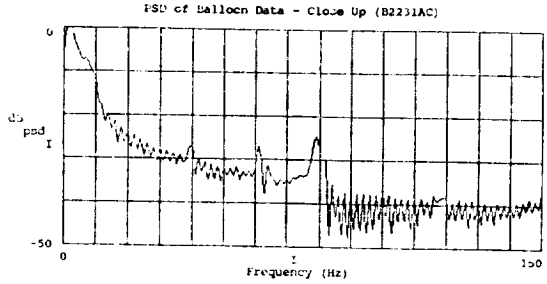

Figure 5. Signal spectrum from balloon data.

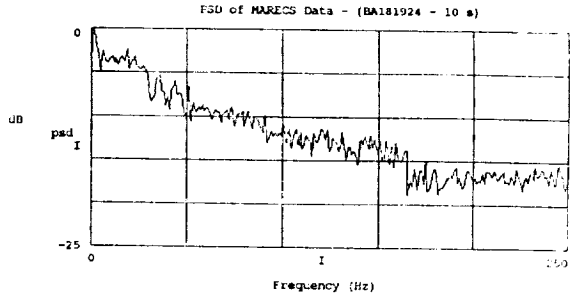

Figure 6. Signal spectrum from MARECS data.

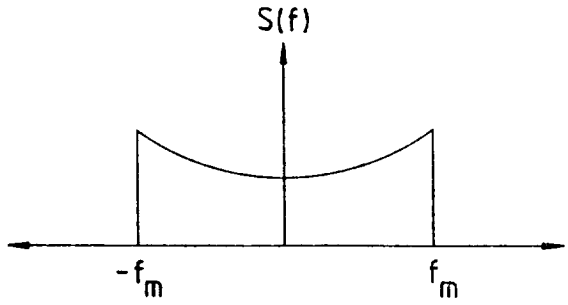

Figure 7. Multipath spectrum from Jakes' multipath model.

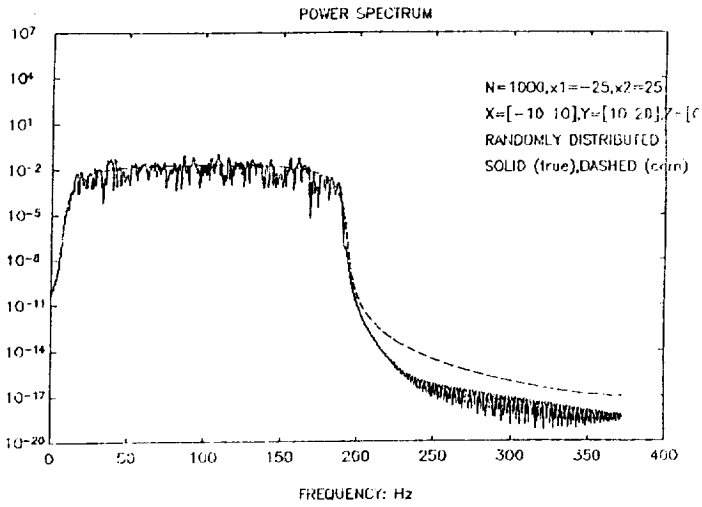

Figure 8. Multipath spectrum from Campbell's simulation.

A CCIR AERONAUTICAL MOBILE SATELLITE REPORT

Faramaz Davarian and Dennis Bishop
Jet Propulsion Laboratory
California Institute of Technology
Pasadena, CA 91109

David Rogers
Comsat Laboratories
Clarksburg, MD 20871

Ernest Smith
University of Colorado
Boulder, CO 80309-00425

The following report was prepared for and submitted to the International Radio Consultative Committee (CCIR) Study Group 5. It is intended that this report will complement the existing reports on maritime (No. 884-1) and land (No. 1009) mobile satellites.

Documents
CCIR Study Groups
Period 1986-1990

Doc. USSG 5/13
16 June 1989
Original: English

Received:

Subject: Study Programme 7C/5
Draft New Report

United States of America

DRAFT NEW REPORT

PROPAGATION DATA FOR AERONAUTICAL MOBILE-SATELLITE SYSTEMS FOR FREQUENCIES ABOVE 100 MHz

1. Introduction

Propagation effects in the aeronautical mobile-satellite service differ from those in the fixed-satellite service and other mobile-satellite services because:

- small antennas are used on aircraft, and the aircraft body may affect the performance of the antenna;
- high aircraft speeds cause large Doppler spreads;
- aircraft terminals must accommodate a large dynamic range in transmission and reception;
- due to their high speeds, banking maneuvers, and 3-dimensional operation, aircraft routinely require exceptionally high integrity of communications, making even short-term propagation effects very important.

This report discusses data and models specifically required to characterize the path impairments, which include:

- tropospheric effects, including gaseous attenuation, cloud and rain attenuation, fog attenuation, refraction and scintillation;
- surface reflection (multipath) effects;
- ionospheric effects such as scintillation;
- environmental effects (aircraft motion, sea state, land surface type).

Aeronautical mobile-satellite systems may operate on a worldwide basis, including propagation paths at low elevation angles. Several measurements of multipath parameters over land and sea have been conducted. In some cases, laboratory simulations are used to compare measured data and verify model parameters. The received signal is considered in terms of its possible components: a direct wave subject to atmospheric effects, and a reflected wave, which generally contains mostly a diffuse component.

In this Report, data are presented in terms of path elevation angle instead of grazing angle. For paths to geostationary satellites at elevation angles above 4°, and aircraft heights below 10 km, the maximum difference between elevation angle and grazing angle is 1°.

There is current interest in using frequencies near 1.5 GHz for aeronautical mobile-satellite sytems. As most experiments have been conducted in this band, data in this report are mainly applicable to these frequencies. As aeronautical systems mature, it is anticipated that other frequencies may be used.

2. Tropospheric effects

For the aeronautical services, the height of the mobile antenna is an important parameter. Estimates of tropospheric attenuation for several antenna heights are provided in Table I.

Predictions of the 30-GHz rain attenuation exceeded for 0.1 percent of the time are shown versus aircraft height for several CCIR rain zones (§ 4.2.1 of Report 563) in Figure 1 for a path elevation angle of 10°. The model assumes surface-based terminals, and may be less accurate for airborne terminals.

The received signal may be affected both by bulk refraction and by scintillations induced by atmospheric turbulence, as discussed in Report 718. These effects may be moderated for aircraft at high altitudes. Experimental data are discussed in Report 564.

3. Ionospheric effects

Ionospheric effects on slant paths are discussed in Study Group 6 texts (see Report 263). These phenomena are important for many paths at frequencies below about 10 GHz, and are strongest within ± 15° of the geomagnetic equator, and secondarily within the auroral zones and polar caps. Ionospheric effects peak near the solar sunspot maximum.

Impairments caused by the ionosphere will not diminish for the typical altitudes used by aircraft. A summary description of ionospheric effects of particular interest to mobile-satellite systems is available in § 3 of Report 884. For most communication signals, the most severe impairment will probably be ionospheric scintillation. Table I of Report 884 provides estimates of maximum expected ionospheric effects at frequencies up to 10 GHz for paths at a 30° elevation angle.

Measurements of ionospheric scintillation were conducted in one aeronautical mobile-satellite experiment [Sutton et al., 1973a]. A signal was transmitted between the ATS-5 satellite and a KC-135 aircraft parked at the Pago Pago airport (geomagnetic latitude of 17° South). During a period of severe scintillation, the peak-to-trough signal variations exceeded 4 to 6 dB, and the 1-percent fade depth approached 3.2 dB.

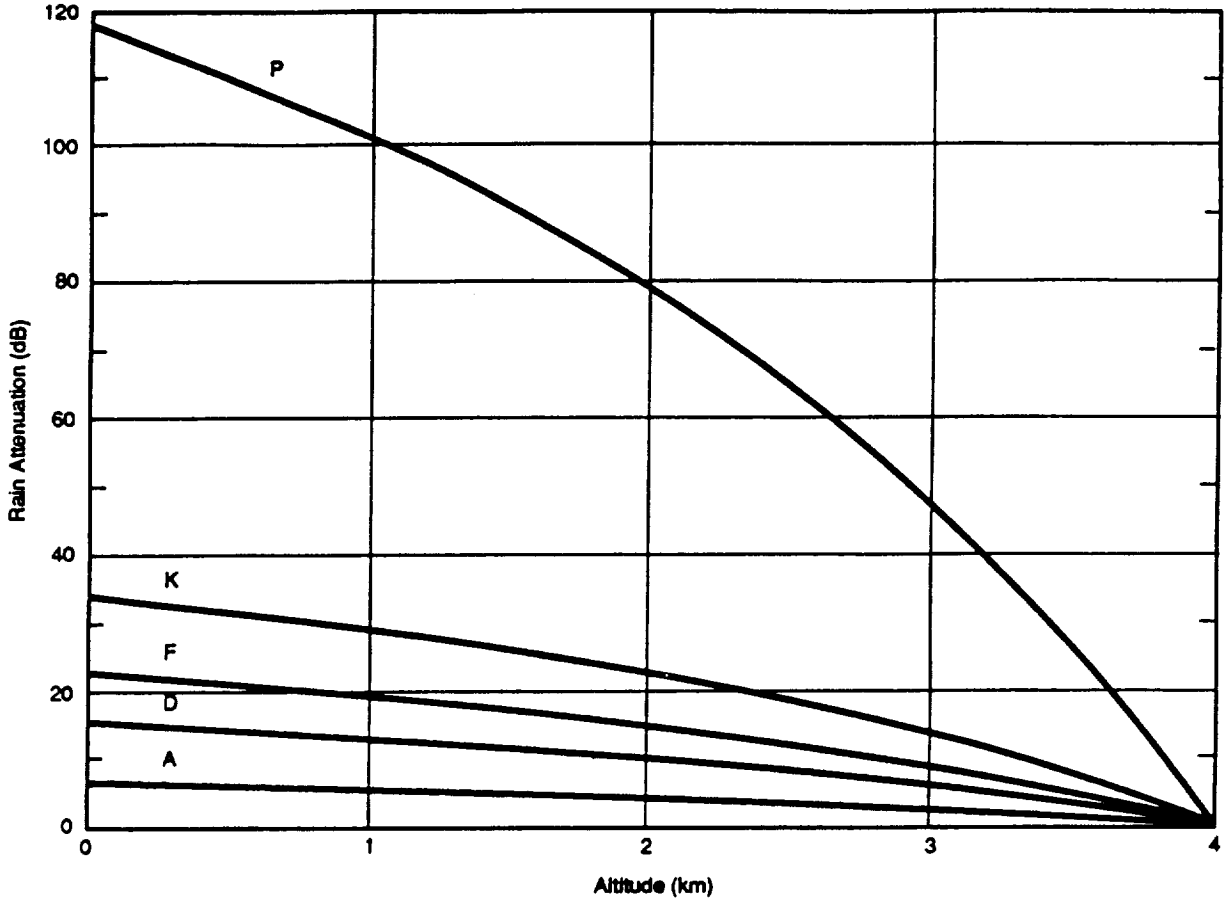

Figure 1 - Predicted 30-GHz rain attenuation at 10° elevation angle for 0.1 percent of the time vs height above sea level for several rain climate zones; latitude less than 36°

4. Fading due to surface reflection and scattering

4.1 General

Multipath fading due to surface reflections for aeronautical mobile-satellite systems differs from fading for other mobile-satellite systems because the speeds and altitudes of aircraft are much greater than those of other mobile platforms. Characteristics of fading for aeronautical systems can be analyzed with procedures similar to those for maritime systems described in Report 884, taking careful account of earth sphericity, which becomes significant with increasing antenna height above the reflecting surface [Yasunaga et al., 1986].

Table I - Estimated tropospheric attenuation for an elevation angle of 10°, one-way traversal, taking aircraft altitude into account

Effect	Magnitudes (dB) for specified frequencies (GHz)					
Altitude (km)	1.5	7.5	15	20	30	40
Oxygen attenuation[1]						
0	0.19	0.23	0.29	0.36	0.64	1.52
1	0.16	0.19	0.24	0.30	0.54	1.29
2	0.14	0.16	0.21	0.26	0.46	1.09
3	0.12	0.14	0.17	0.22	0.39	0.92
4	0.10	0.12	0.15	0.18	0.33	0.78
5	0.08	0.10	0.12	0.16	0.28	0.66
6	0.07	0.08	0.11	0.13	0.23	0.56
Water vapor attenuation[1] ($7.5\ g/m^3$)						
0	0.0016	0.043	0.26	1.35	0.98	1.17
1	0.0010	0.028	0.16	0.92	0.63	0.75
2	0.0006	0.018	0.11	0.62	0.40	0.47
3	0.0004	0.011	0.07	0.42	0.26	0.30
Cloud attenuation[2] ($1\ g/m^3$) (1 - 3 km ht)						
0	0.020	0.49	1.96	3.48	7.84	13.9
1	0.020	0.49	1.96	3.48	7.84	13.9
2	0.010	0.25	0.98	1.74	3.92	7.0
3	0.0	0.0	0.0	0.0	0.0	0.0
Fog attenuation[2] ($0.5\ g/m^3$) (0 - 150 m ht)						
0	0.0006	0.015	0.059	0.10	0.23	0.42
1	0.0	0.0	0.0	0.0	0.0	0.0
Rain attenuation[3] (0.1%, Zone K)						
0	0.013	2.17	11.1	18.2	34.2	47.8
1	0.011	1.86	9.5	15.5	29.2	40.9
2	0.008	1.43	7.3	11.9	22.5	31.4
3	0.005	0.80	4.1	6.7	12.5	17.5
4	0.0	0.0	0.0	0.0	0.0	0.0

[1] Derived from the method of § 2.1.1 of Report 564-3.
[2] Derived from models of Slobin [1982].
[3] Derived from the method of § 2.2.1 of Report 564-3 for rain climate zone K (§ 4.2.1 of Report 563-3).

4.2 Fading due to sea-surface reflections

4.2.1 Dependence on antenna height and antenna gain

Figure 2 shows the calculated relationship between antenna height and 1.54-GHz multipath fading depth under rough sea conditions for an antenna gain G_θ of 10 dBi and elevation angles θ_i of 5° and 10° (Report 884, § 4), assuming the main lobe of the antenna is expressed as

$$G(\theta) = -4 \times 10^{-4} \, (10^{G_m/10} - 1) \, \theta^2 \qquad \text{(dB)} \qquad (1)$$

where:

G_m : value of the maximum antenna gain (dB); and

θ : angle measured from boresight (deg).

The fading depth is defined as the difference (in dB) between the signal level of the direct incident wave and the threshold level exceeded by the resultant (direct plus multipath) signal for a specified time percentage; in Figure 2 the time percentage is 99 percent. Although the fading depth decreases with increasing antenna height, the fading depth for an antenna at a height of 10 km is only 1 to 2 dB less than that for a maritime system (antenna height of the order of 10 m).

Bit-error-rate data were obtained in a flight experiment conducted over the North Atlantic using a 1.54-GHz circularly-polarized signal from a MARECS-A satellite [Zaks and Anderson, 1986]. A conformal microstrip antenna with a 0-dBiC beamwidth of 130° was mounted on each side of the upper fuselage. The aircraft flew at a nominal height of 10.8 km and a nominal ground speed of 740 km/h. Carrier-to-multipath ratios estimated from the BER data appeared to vary from 8.5 to 13 dB over an elevation angle range of 4° to 17°.

4~~5~~.2.2 Frequency spectrum of fading

The frequency power spectrum of sea-reflected waves depends particularly on aircraft flight speed, path elevation angle to the satellite, and the ascending (or descending) angle of the aircraft. For level flight, the frequency spectrum tends to take a symmetrical shape with a flat portion centred about the direct wave component. The -10 dB spectral bandwidth measured from the centre frequency (i.e., the frequency of the direct wave component) is about 25 Hz and 50 Hz at path elevation angles of 5° and 10°, respectively. For ascending or descending aircraft, the spectrum becomes asymmetric with the peak displaced from the centre. For example, with both elevation angle and ascending angle of 5°, the peak is about 25 Hz from the centre of the spectrum.

4~~5~~.2.3. Delay time and coherent bandwidth

(direct and reflected)

~~The~~ correlation of fading between two radio waves with different frequencies decreases with increasing frequency separation. The dependence of the correlation on antenna gain is small for gains less than 15 dBi. Figure ~~12~~ 3 shows the relationship between antenna height and coherent bandwidth, which is defined as the frequency separation for which the correlation coefficient between two radio waves equals 0.3~~6~~7 (=1/e). The coherent bandwidth decreases as the antenna height increases, becoming about 10 to 20 kHz (delay time of 6 to 12 μsec) for an antenna at a height of 10 km. This means that the multipath fading for aeronautical systems may have so-called frequency-selective characteristics.

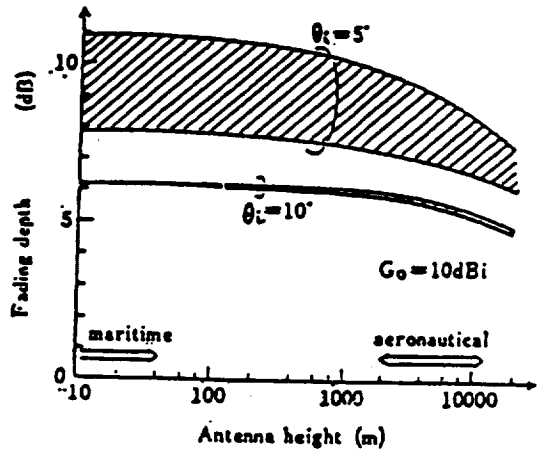

FIGURE ~~11~~ 2

Fade depth vs. antenna height for antenna gain of 10 dBi and circular polarization at 1.54 GHz under rough sea condition

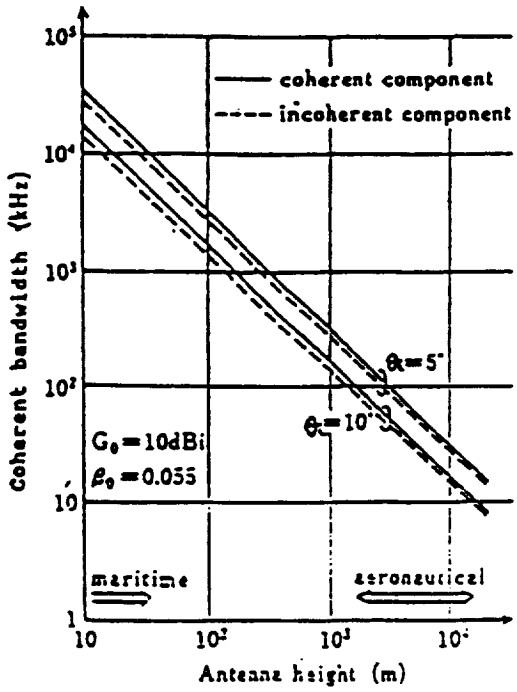

FIGURE ~~12~~ 3

Coherent bandwidth vs. antenna height for antenna gain of 10 dBi

4.3 Measurements of sea-reflection multipath effects

Extensive aeronautical multipath tests were conducted in the 1.5 to 1.6 GHz band with a KC-135 jet airplane and the NASA ATS-5 geostationary satellite [Sutton et al., 1973b]. The aircraft ground speed was 650 km/h and the orientation was generally broadside to the satellite path azimuth. The direct satellite signal was received with a 15 dBi quad-helix antenna located at the base of the vertical stabilizer; the indirect, sea-reflected signal was received with a 13 dBi crossed-dipole array.

Data were recorded during 30 over-ocean flights at elevation angles of 9° to 31° from the airplane to the satellite. Photographs of the ocean were taken (at heights of about 300 and 900 m) to determine sea surface conditions.

Measured mean multipath power normalized to the direct power (as corrected for RF channel gain differences) versus elevation angle for linear vertical and horizontal polarizations is shown in Figure 4. Each data point is derived from 6 minutes of data. Theoretical predictions are also shown (solid lines) in the figure, calculated as the product of the plane-earth reflection coefficient and the divergence factor [Staras, 1968] (see Report 1008, § 3.3).

The spectrum bandwidth (defined by the points where the spectrum amplitude is 1/e of the peak) for the sea-reflected waves is plotted versus elevation angle in Figure 5. These data were obtained by transmitting an unmodulated carrier toward the aircraft and taking the Fourier transform of the sea-reflected signal.

Another study of multipath propagation at 1.6 GHz was performed with a KC-135 aircraft and the NASA ATS-6 satellite [Schroeder et al., 1976]. The signal characteristics were measured with a two-element wave-guide array in the aircraft nose radome, with 1-dB beamwidths of 20° in azimuth and 50° in elevation. Data were collected over the ocean and over land at a nominal aircraft height of 9.1 km and nominal ground speed of 740 km/h.

Table II summarizes the oceanic multipath parameters observed in the ATS-6 measurements, augmented with results from the model [Yasunaga et al., 1986]. The delay spreads in the table are the widths of the delay-power spectral density of the diffusely-scattered signal arriving at the receiver. Coherence bandwidth is the 3-dB bandwidth of the frequency autocorrelation function (Fourier transform of the delay spectrum). Doppler spread is determined from the width of the Doppler power spectral density. The decorrelation time is the 3-dB width of the time autocorrelation function (inverse Fourier transform of the Doppler spectrum).

The mean-square scatter coefficient, Γ, in Table II is defined as

$$\Gamma = G \langle |I|^2 \rangle / \langle |D|^2 \rangle \qquad (2)$$

where:

G : adjustment to account for gain differences between the direct and indirect channels;

$\langle |I|^2 \rangle$: mean-square power in the multipath component as measured at the receiver;

$\langle |D|^2 \rangle$: mean-square power in the direct component as measured at the receiver.

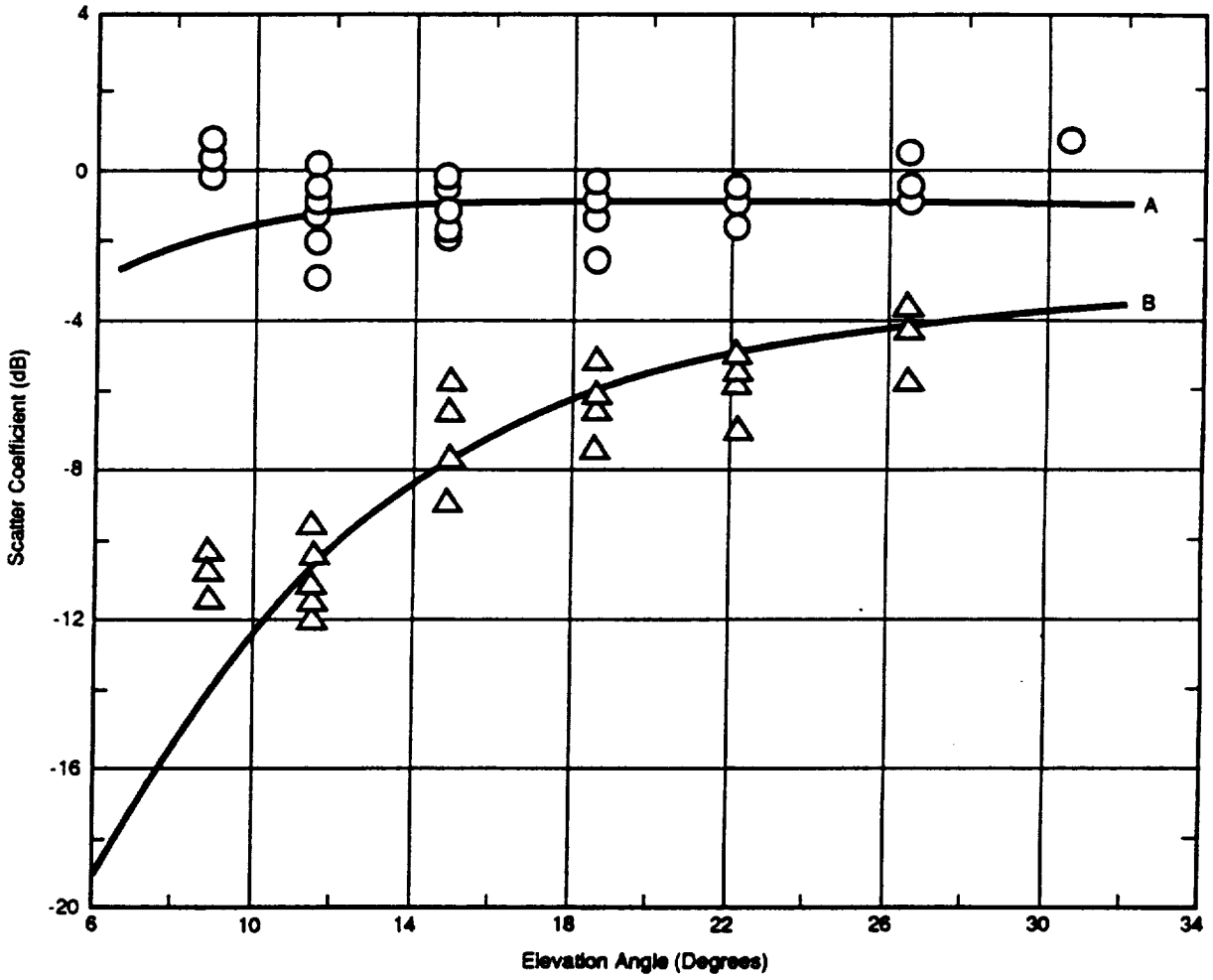

Figure 4 - Ocean mean scatter coefficient vs elevation angle for horizontal and vertical polarizations at 1.6 GHz; solid lines are product of plane-earth reflection coefficient and the divergence factor

O - Horizontal polarization measurements
Δ - Vertical polarization measurements
A - Horizontal polarization predictions
B - Vertical polarization predictions

Coefficients for horizontal and vertical antenna polarizations were measured in the ATS-6 experiments. Values for r.m.s. sea surface slopes of 3° and 12° are plotted versus elevation angle in Figure 6, along with predictions derived from a physical optics model [Staras, 1968]. Sea slope was found to have a minor effect for elevation angles above about 10°. The agreement between measured coefficients and those predicted for a smooth flat earth as modified by the spherical-earth divergence factor (Report 1008, eq. 12) increased as sea slope decreased. (The relation between r.m.s. sea surface slope and wave height is complex, but conversion can be performed [Karasawa and Shiokawa, 1984].)

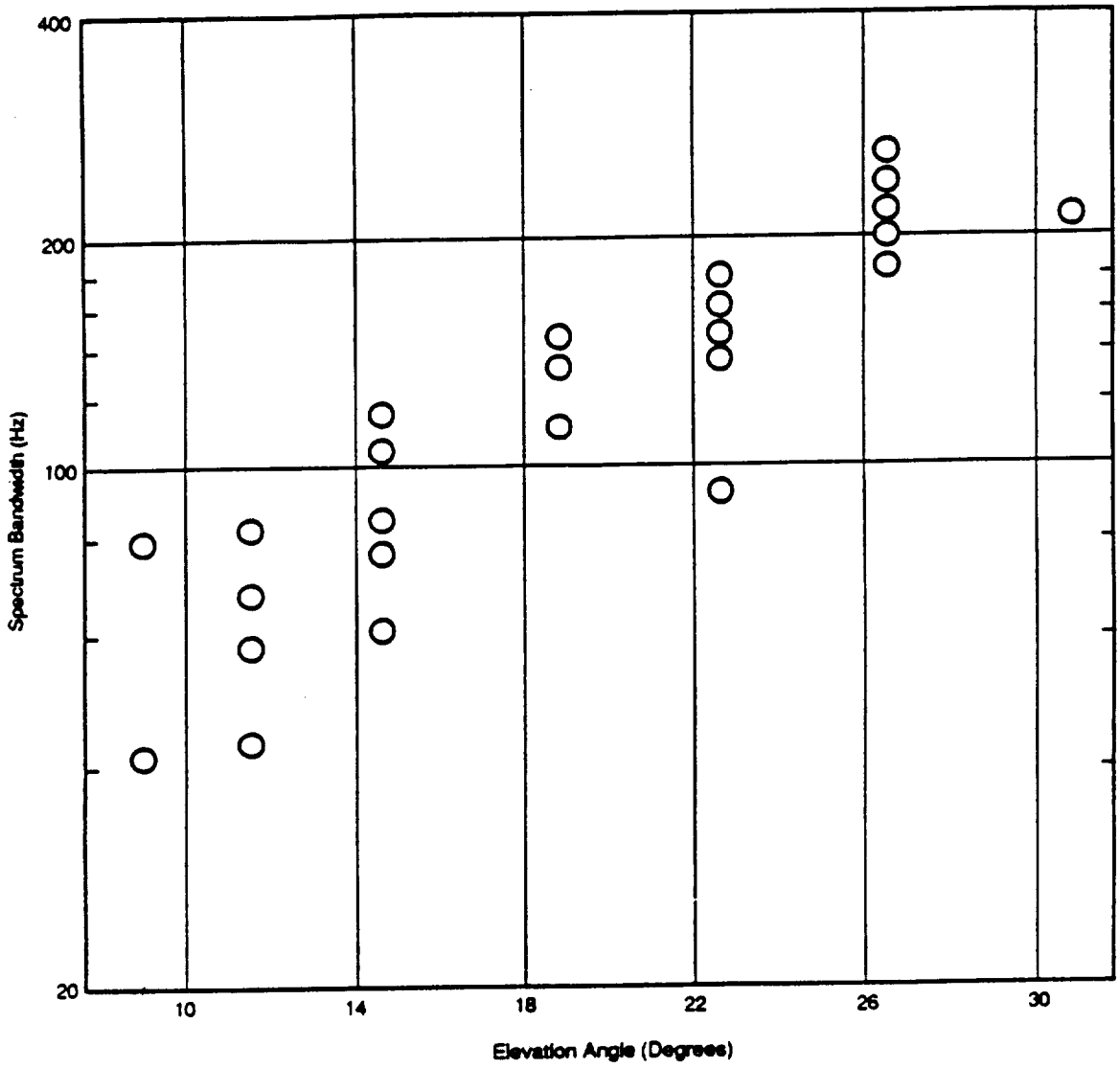

Figure 5 - Spectrum bandwidth (two-sided) of reflected waves vs elevation angle at 1.6 GHz

Table II - Multipath parameters from ocean measurements

Parameter	Measured Range	Typical value at specified elevation angle		
		8 deg	15 deg	30 deg
Mean square scatter coeff. (horizontal polarization)	-5.5 to -0.5 dB	-2.5 dB	-1 dB	-1 dB
Mean square scatter coeff. (vertical polarization)	-15 to -2.5 dB	-14 dB	-9 dB	-3.5 dB
Delay spread[2]				
3-dB value	.25 - 1.8 μs	0.6 μs	0.8 μs	0.8 μs
10-dB value	2.2 - 5.6 μs	2.8 μs	3.2 μs	3.2 μs
Coherence bandwidth[1] (3-dB value)	70 to 380 kHz	160 kHz	200 kHz	200 kHz
Doppler spread[2]:				
In-plane geometry				
3-dB value	4 - 190 Hz	5 Hz	70 Hz	140 Hz
10-dB value	13 - 350 Hz	44 Hz	180 Hz	350 Hz
		40 Hz*		
Cross-plane geometry				
3-dB value	79 - 240 Hz	63 Hz	110 Hz	190 Hz
10-dB value	180 - 560 Hz	144 Hz	280 Hz	470 Hz
		88 Hz*		
Decorrelation time[1] (3-dB value)	1.3 - 10 msec	7.5 msec	3.2 msec	2.2 msec

*Data from multipath model (Report 884, § 4) for aircraft height of 10 km and aircraft speed of 1000 km/h.
[1]One-sided.
[2]Two-Sided.

For most aeronautical systems, circular polarization will be of greater interest than linear. For the simplified case of reflection from a smooth earth (which should be a good assumption for elevation angles above 10°), circular copolar and cross-polar scatter coefficients (Γ_c and Γ_x, respectively) can be expressed in terms of the horizontal and vertical coefficients (Γ_h and Γ_v, respectively) by

$$\Gamma_c = (\Gamma_h + \Gamma_v)/2 \quad ; \quad \Gamma_x = (\Gamma_h - \Gamma_v)/2 \qquad (3)$$

for either incident right-hand circular (RHC) or left-hand circular (LHC) polarization. The horizontal and vertical coefficients are complex-valued, in general. Therefore, phase information is required to apply eq. 3 to the curves in Figure 6.

Multipath data were collected in a series of aeronautical mobile-satellite measurements conducted over the Atlantic Ocean and parts of Europe [Hagenauer et al., 1987]. Figure 7 shows the measured mean and standard deviations of 1.6-GHz fade durations as a function of elevation angle for these flights. A crossed-dipole antenna with a gain of 3.5 dBi was used to collect these data. The aircraft flew at a nominal altitude of 10 km and with a nominal ground speed of 700 km/h.

4.4 Measurements of land-reflection multipath effects

Table III supplies multipath parameters measured during the ATS-6 flights over land [Schroeder et al., 1976]; parameter definitions are the same as for Table II. Land multipath signals were found to be highly nonstationary. No consistent dependence on elevation angle was established, perhaps because the ground terrain was highly variable (data were collected over wet and dry soil, marshes, dry and wet snow, ice, lakes, etc.). Figures 8a and 8b provide the mean-square scatter coefficients measured in the over-land tests, along with theoretical values (solid lines) from the physical optics model [Staras, 1968].

5. Irreducible error rate

Multipath fading in mobile channels gives rise to an irreducible error rate floor at which increases in the direct signal power do not reduce the corresponding error rate. Simulations of an aeronautical mobile-satellite link have been performed with a differentially-encoded minimum-shift-keyed signal [Davarian, 1988]. The composite (direct plus diffusely-reflected) signal was modeled with Rician statistics, and the reflected signal was suitably delayed with respect to the direct signal. The composite signal was differentially detected and a bit-error-rate test conducted.

The results indicated that the irreducible error rate is higher for an aeronautical mobile-satellite channel than for a land mobile-satellite channel. Increased delay of the multipath component caused the irreducible error rate to increase. Other studies [Hagenauer, 1987; Korn, 1989] support these results and show that an increase in multipath power or delay will increase the irreducible error rate.

Table III - Multipath parameters from land measurements

Parameter	Measured Range	Typical Value
Mean Square Scatter Coeff. (horizontal pol.)	-18 to 2 dB	-9 dB
Mean Square Scatter Coeff. (vertical pol.)	-21 to -3 dB	-13 dB
Delay spread[2] (3-dB)	0.1 to 1.2 μs	0.3 μs
Delay spread[2] (10-dB)	0.2 to 3 μs	1.2 μs
Coherence bandwidth[1] (3-dB)	150 kHz to 3 MHz	600 kHz
Doppler spread[2] (3-dB)	20 to 140 Hz	60 Hz
Doppler spread[2] (10-dB)	40 to 500 Hz	200 Hz
Decorrelation time[1] (3-dB)	1 to 10 msec	4 msec

[1]One-sided.
[2]Two-sided.

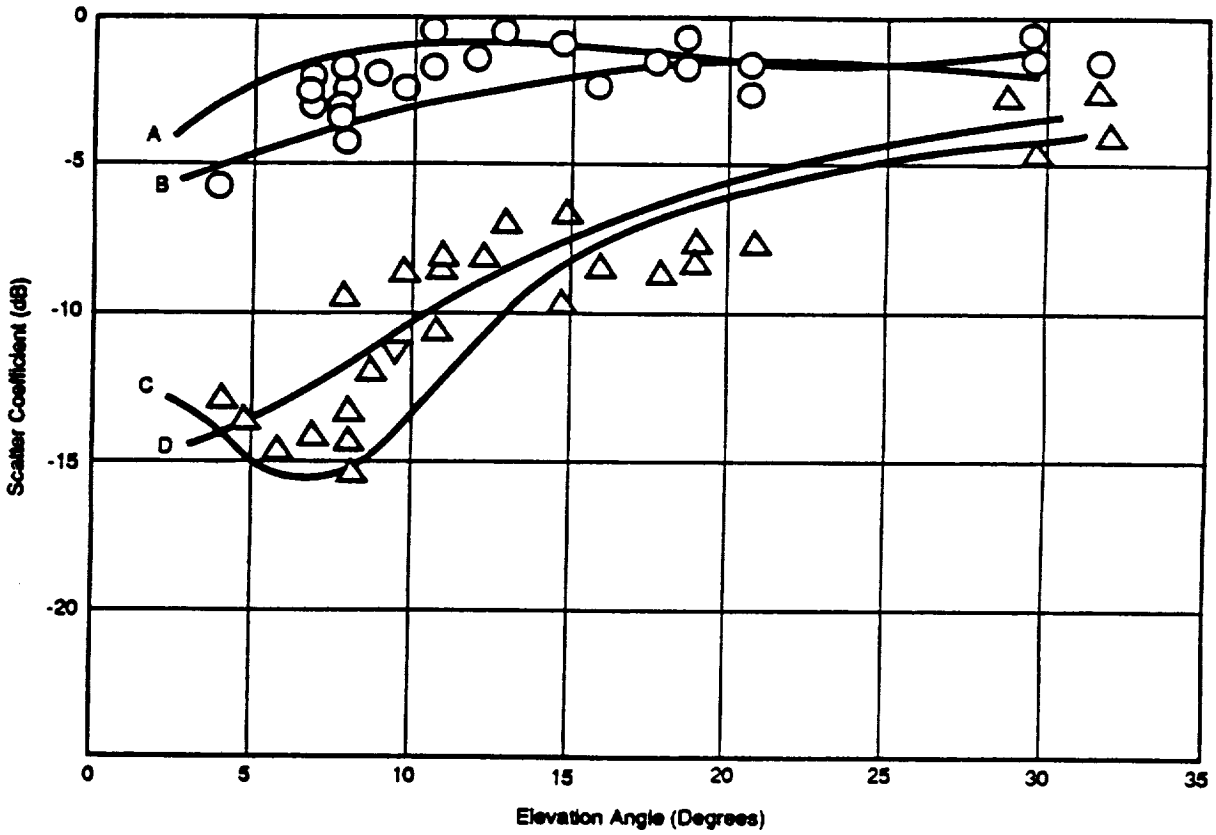

Figure 6 - Oceanic mean-square scatter coefficients vs elevation angle at 1.6 GHz

O - Horizontal polarization measurements
Δ - Vertical polarization measurements

A - Horizontal polarization prediction, 3° slope
B - Horizontal polarization prediction, 12° slope
C - Vertical polarization prediction, 3° slope
D - Vertical polarization prediction, 12° slope

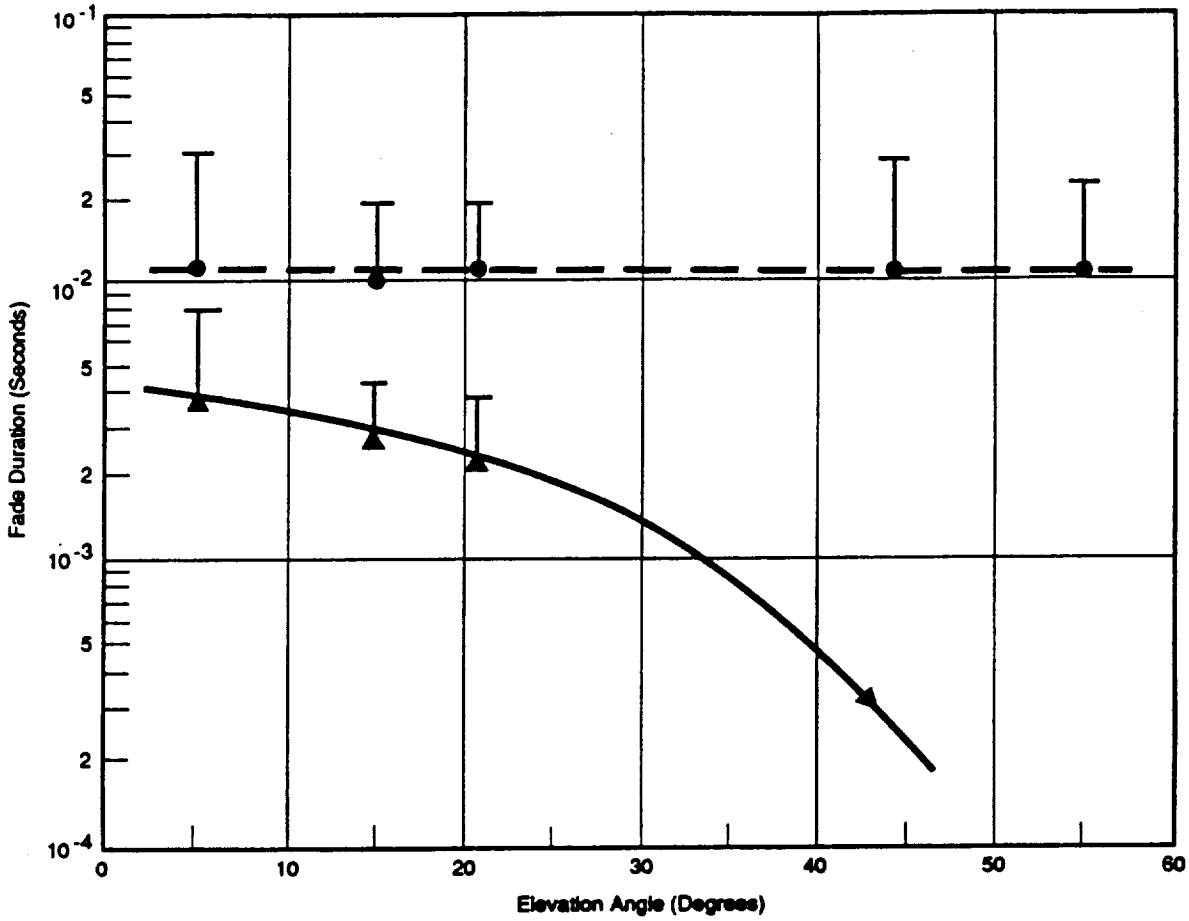

Figure 7 - Fade duration vs elevation angle for circular polarization at 1.6 GHz (antenna gain = 3.5 dBi); data collected over Atlantic Ocean and W. Europe

● Mean with 0 dB threshold
▲ Mean with -5 dB threshold
T Standard deviation added

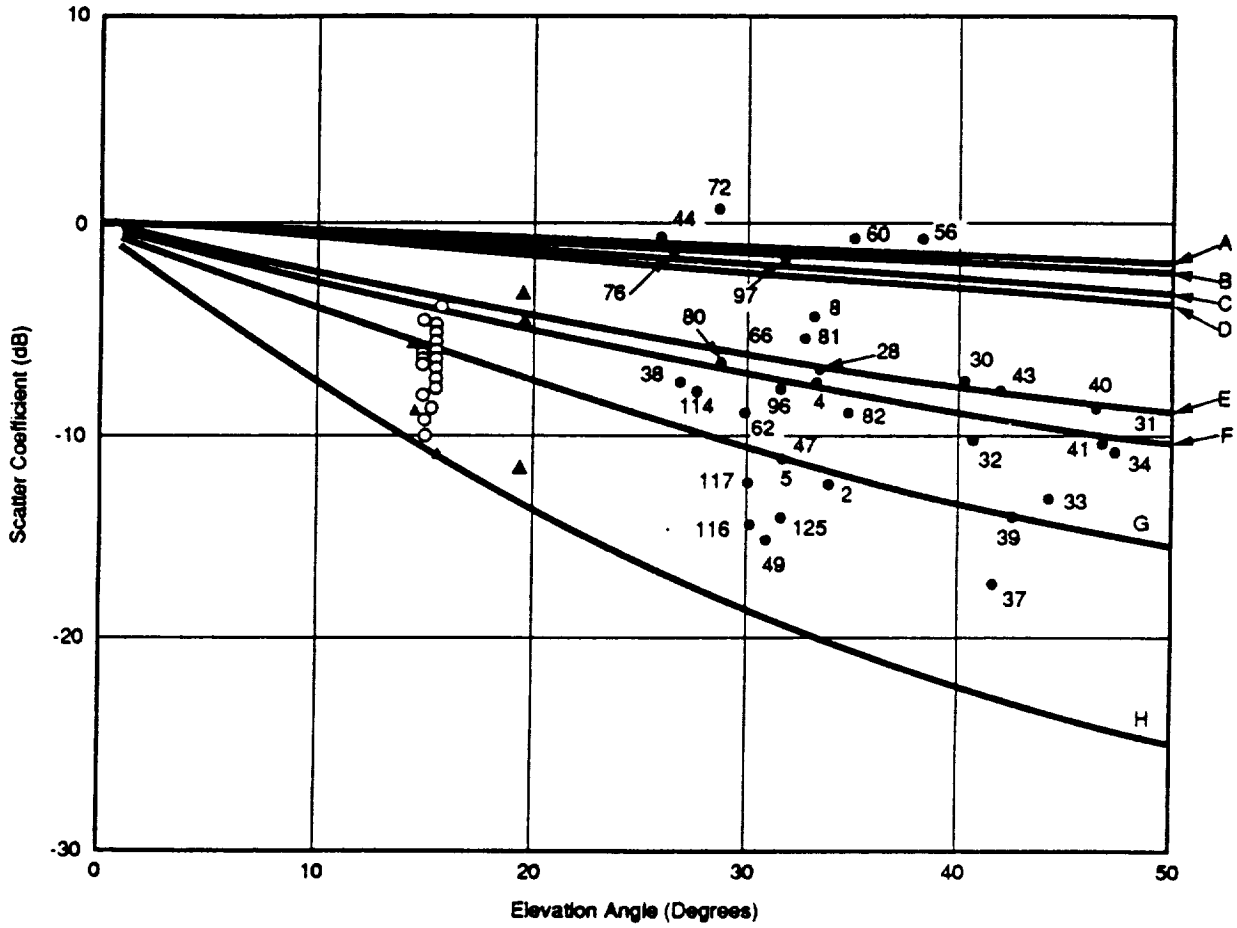

Figure 8a - Mean-square scatter coefficient for horizontal polarization vs elevation angle at 1.6-GHz; data collected over continental United States (numbers identify measurement runs)

Δ ATS-5 summertime data
O ATS-5 wintertime data

O ATS-6 data

A: Sea water
B: Fresh water
C: Marsh
D: Slightly wet soil

E: Ice
F: Moderately dry soil
G: Wet snow
H: Dry snow

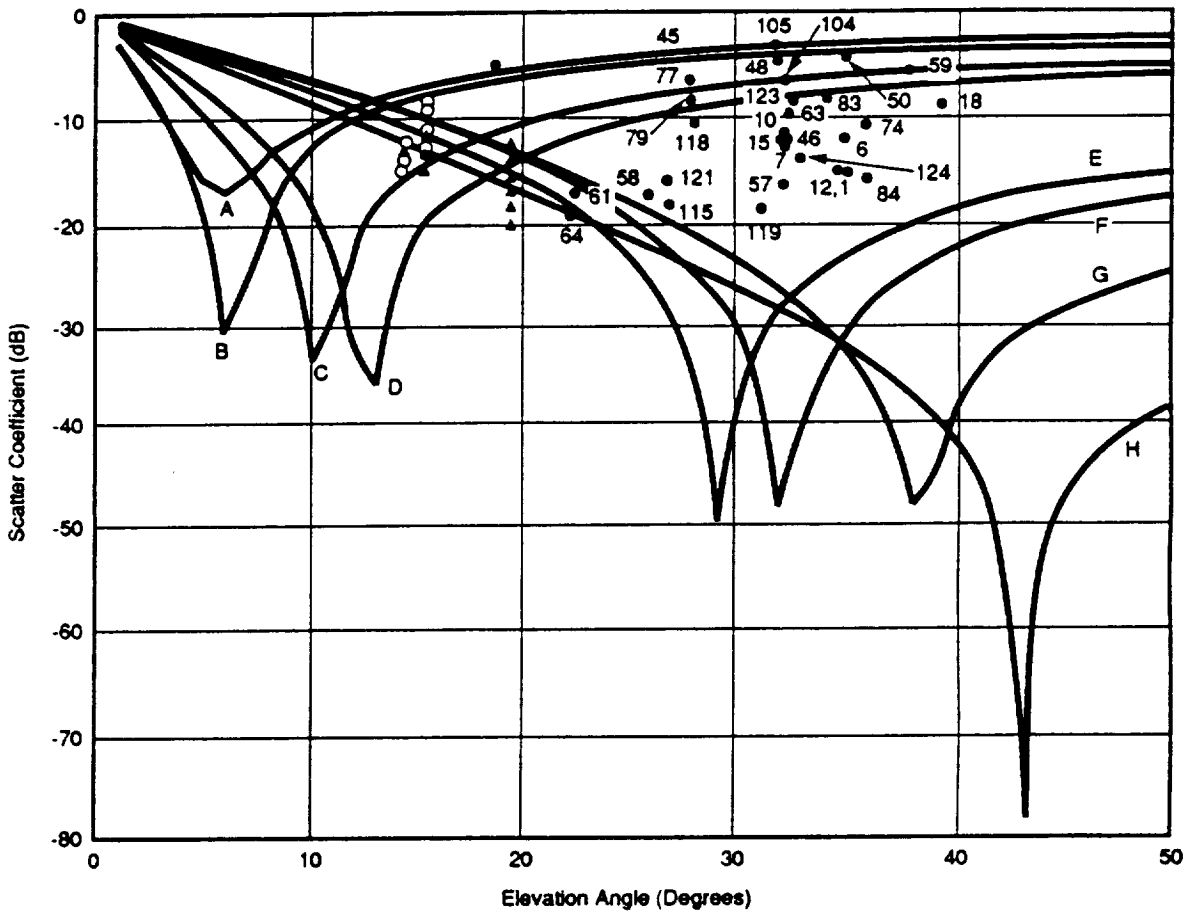

Figure 8b - Mean-square scatter coefficient for vertical polarization vs elevation angle at 1.6-GHz; data collected over continental United States (numbers identify measurement runs)

Δ ATS-5 summertime data
O ATS-5 wintertime data
O ATS-6 data

A: Sea water
B: Fresh water
C: Marsh
D: Slightly wet soil
E: Ice
F: Moderately dry soil
G: Wet snow
H: Dry snow

REFERENCES

DAVARIAN, F. [1988] Irreducible error rate in aeronautical satellite channels. *Electron. Lett.*, Vol. 24, 21, 1332-1333.

HAGENAUER, J., NEUL, A., PAPKE, W., DOLAINSKY, F. and EDBAUER, F. [1987 The aeronautical satellite channel, DFVLR, May.

KARASAWA, Y. and SHIOKAWA, T. [1984] Characteristics of L-band multipat fading due to sea surface reflection. *IEEE Trans. Ant. Prop.*, Vol. AP-32, 6, 618-623.

KORN, I. [1989] Coherent detection of M-ary phase-shift keying in the satellite mobile channel. To be published in *IEEE Trans. Comm.*

SCHROEDER, E.H., THOMPSON, A.D., SUTTON R.W., WILSON, S.G. and KUO, C.J [1976] Air traffic control experimentation and evaluation with the NASA ATS-6 satellite. The Boeing Company, Report No. FAA-RD-75-173, prepared for U.S. Dept. of Transportation. Vol. III, NTIS Accession No. D6-44048; Vol. V, NTIS Accession No. D6-44050, National Technical Information Service, Springfield, VA 22161, USA.

SLOBIN, S.D. [1982] Microwave noise temperature and attenuation of clouds: Statistics of these effects at various sites in the United States, Alaska, and Hawaii. *Radio Sci.*, Vol. 17, 6, 1443-1454.

STARAS, H. [1968] Rough surface scattering on a communication link. *Radio Sci.*, Vol. 3, 6, 623-631.

SUTTON, R.W., SCHROEDER, E.H., THOMPSON, A.D., and WILSON, S.G. [1973a] ATS-5 multipath/ranging/digital data L-band experimental program: Program summary. The Boeing Company, Report No. FAA-RD-73-57, prepared for U.S. Dept. of Transportation. NTIS Accession No. D6-60176, National Technical Information Service, Springfield, VA 22161, USA.

SUTTON, R.W., SCHROEDER, E.H., THOMPSON, A.D. and WILSON, S.G. [1973b] Satellite-aircraft multipath and ranging experiment results at L band. *IEEE Trans. Comm.*, Vol. COM-21, 5, 639-647.

YASUNAGA, M., KARASAWA, Y., SHIOKAWA, T. and YAMADA, M. [1986] Characteristics of L-band multipath fading due to sea surface reflection in aeronautical satellite communications. *Trans. IECE* (Japan), Vol. E69, 10, 1060-1063.

ZAKS, C. and ANDERSON, S. [1986] Aeronautical satellite data link measurement over the North Atlantic: Test results. *Proceedings*, Seventh Intl. Conf. on Digital Satellite Communications, Munich, FRG, May, 557-563.

Session 2

PROPAGATION EXPERIMENTS ABOVE 10 GHz

Chairman:

Dr. David V. Rogers
COMSAT Laboratories

RAIN ATTENUATION MEASUREMENTS: VARIABILITY AND DATA QUALITY ASSESSMENT*

Robert K. Crane

Thayer School of Engineering, Dartmouth College
Hanover, New Hampshire, 03755, USA

Year-to-year variations in the cumulative distributions of rain rate or rain attenuation are evident in any of the published measurements for a single propagation path that span a period of several years of observation. These variations must be described by models for the prediction of rain attenuation statistics. Now that a large measurement data base has been assembled by the International Radio Consultative Committee (CCIR), the information needed to assess variability is available. On the basis of 252 sample cumulative distribution functions for the occurrence of attenuation by rain (ACDFs), the expected year-to-year variation in attenuation at a fixed probability level in the 0.1 to 0.001 percent of a year range is estimated to be 27%. The expected deviation from an attenuation model prediction for a single year of observations is estimated to exceed 33% when any of the available global rain climate models are employed to estimate the rain rate statistics. The probability distribution for the variation in attenuation or rain rate at a fixed fraction of a year is lognormal. The lognormal behavior of the variate was used to compile the statistics for variability and to establish hypothesis tests for identifying outliers - the observed sample cumulative distribution function (CDF) that deviates significantly from the expected (modeled) ACDF.

1. INTRODUCTION

A number of the published or proposed models for the prediction of the statistical distributions of attenuation by rain depend upon parameters which must be set from the measured cumulative distributions of attenuation (ACDFs). The accuracy of such a model is then dependent on the quality of the data employed for parameter estimation. In recent years, it has been fashionable to test old and new attenuation prediction procedures against measured distributions stored in one or more data banks. The question arises as to how the data entered into a data bank may be examined or tested to detect bad data, data that could cause errors in the parameters needed for the models and data that could invalidate the use of a data bank for model evaluation. In this paper, a statistical test is presented for assessing the quality of rain attenuation distribution data. It was applied to the 1988 edition of the International Radio Consultative Committee (CCIR) data banks for slant path and terrestrial path propagation [CCIR, 1988]. The results show that 47 of the 252 ACDFs in the data banks are of questionable quality.

Any statistical hypothesis test for data quality assessment requires the use of a known probability distribution for the property to be tested and a standard or expected value for the property against which the observations may be compared. The reference standard must be a

*Submitted to Radio Science.

model which provides a prediction of the ACDF for the location and propagation path of interest. In the absence of long term temporal variations in rain statistics, the best model would be the average of a set of observations spanning many years for the same location and path (i.e. frequency, path length, elevation angle, polarization). The average annual distribution would then provide the reference for comparison for each of the observed annual distributions. The model ACDF is then the long term sample mean at each probability of occurrence. Unfortunately, no long term measurements are available.

A number of attenuation prediction models have been published recently that depend only on the location of a path (the rain climate) and the specific parameters for the path [COST 205, 1985a; CCIR, 1986a; Crane and Shieh 1989; Crane, 1985a]. When the predictions of these models are compared with observations, the models all perform equally. No statistically significant differences were evident in the root mean square deviations (RMSD) between measurement and prediction when the attenuation prediction procedures were used with the same rain climate model. Therefore, any of the models could be combined with a rain climate model to provide a reference for the estimation of variability. For this paper, two different attenuation prediction models and rain climate models were utilized to provide the reference ACDFs, the improved Two-Component rain attenuation model together with the Global rain climate model (T-C & Global) [Crane and Shieh, 1989] and the current version of the CCIR rain attenuation model together with the current CCIR rain climate model (CCIR & CCIR) [CCIR, 1986b; c; d].

Prior analyses of rain rate and attenuation prediction model behavior have shown that the deviations between measurements and model predictions at fixed probability levels are lognormally distributed. Sample deviation distributions were tested against the lognormal distribution, the percent normal distribution with the measurements used as reference (the distribution recommended by the CCIR [1986a] and employed for the analysis of some of the attenuation data in the COST 205 Project [1985a]) and the percent normal distribution with the model used as reference (a distribution also employed for the analysis of COST 205 data [COST 205, 1985b]). On the basis of Chi Square tests of goodness-of-fit, the use of either percent normal distribution could be rejected at the 20 percent significance level (and at the 0.5 % significance level) and, at the 20% level, the lognormal hypothesis could not be rejected [Crane and Shieh, 1989]. All statistics were therefore calculated using the natural logarithms of the measured or modeled attenuation values. The logarithmic transformation was necessary to generate a variate with a normal distribution. With this transformation, many of the standard tools for statistical inference become available for the assessment of data quality. For ease of interpretation, the results of some of the analyses were transformed back into the linear domain and expressed as a fraction in percent.

The year-to-year variations in the rain rate and attenuation sample cumulative distribution functions (CDFs) for sites with a sufficient run of data to estimate a geometric mean CDF is considered in section 2. In section 3, the variability relative to the T-C & Global and the CCIR & CCIR models is considered and a statistical model for the year-to-year variations is presented. The use of the variability estimates to identify outliers (questionable data) is discussed in section 4. Recommendations for data bank quality control are presented in section 5.

2. STATISTICAL VARIATIONS FROM THE SAMPLE GEOMETRIC MEAN DISTRIBUTION

Earlier evaluations of rain attenuation prediction procedures have shown that the observed cumulative distributions of rain attenuation display a natural variation from one year to the next, from one site to another and from path-to-path at the same site. The cumulative distribution of the fraction of a year the measured rain attenuation value exceeds specified thresholds (ACDF) is a random variable. The meteorological conditions along a propagation path change from year-to-year and, as a result, the attenuation statistics for a path also change from year-to-year. Data from eleven of the sites listed in the CCIR data bank for slant path rain attenuation measurements have between three and five single-year ACDFs; ten of the sites have simultaneous rain rate measurements (RCDFs) for each year of observations; seven of the sites with rain rate measurement data are from a single geographical region (Europe). Figure 1 displays the standard deviations of the annual deviations of the rain attenuation (DA) and rain rate (DR) values from the sample geometric means of the annual CDFs at 0.01% of a year for each of the sites. Figure 2 presents the simultaneous DA, DR deviation pairs for each year of observation for each site. The use of the geometric mean was necessary because of the logarithmic transformation employed in the calculation of the deviations. The data in Figure 2 are from 12 GHz satellite beacon observations made in Europe [COST 205, 1985a]. This subset of the data in the CCIR data bank was chosen because the COST 205 Project subjected their data to a strict regimen of data quality control.

The observations reveal the natural variability of the attenuation and rain rate deviations from the model (geometric mean) predictions. Table 1 lists the standard deviations for the attenuation and rain rate deviations from the geometric means of the ACDFs for each site at 0.01% of a year for the eleven sites with attenuation measurements, for all the sites with rain rate measurements and for the European composite (Figure 2). The table provides the expected 90% bounds for the variability model. The bounds are values from a Chi Square probability distribution with the

specified number of degrees of freedom (DoF) exceeded with probability 0.05 (lower Bound) and 0.95 (upper bound). The standard deviations for the model distributions, 0.29 (33%) for attenuation and 0.22 (24%) for rain rate, were selected to minimize the number of sites having standard deviation estimates lying outside the 90% bounds for each model. Only one site produced observed standard deviation estimates outside the model bounds (D3, Europe: an outlier). No convincing trend is evident in the observed standard deviations vs the climate model rain rates at 0.01% of a year (Figure 1). For the D2 climate region, the observed standard deviation values span all but the D3 value identified as an outlier. The simplest model, therefore, is to assume a constant variability over all climate regions. For rain attenuation, the modeled variability is the largest value that keeps all the observations above the 5% bound. Taking the one site as an outlier for both attenuation and rain rate, the rain rate variability value is the smallest that keeps the remainder of the observations within the 90% bounds (5% to 95%). The resulting model variabilities for a year of observation are plotted on Figure 1.

For attenuation by rain, the composite standard deviation for Europe was 0.31 for DA (0.25, 0.43: 10% confidence limits based on the observed composite standard deviation given in Table 2 as opposed to the 90% bounds on the variability model given in Table 1). To assist in interpreting the data, the standard deviation values were transformed to percentage by:

$$DA_{\%} = 100\,(\exp(DA_{LN}) - 1). \qquad (1)$$

The observed composite variability in rain attenuation is 37% at 0.01% of a year. For the simultaneous rain rate observations, the standard deviation of DR was 0.24 (27%). The DA and DR variations were partially correlated (Figure 2 and Table 2). The estimated correlation coefficient is 0.8. If a linear model is used to relate the deviation in the natural logarithm of attenuation from the model prediction to the deviation in the natural logarithm of rain rate from the model prediction (DA vs DR), the slope of the least-square-fit line is in close agreement with the exponent in the power law relationship between specific attenuation and rain rate when calculated for a large number of rain drop size distribution observations (slope = 1.1 and residual error = 0.23; least-square fit weighted by the relative frequency of occurrence of observations at different rain rates [Crane, 1971]) but deviates significantly from the exponent when calculated using a standard rain drop size distribution model [CCIR, 1986a]. The standard deviation of the residual error for the linear model is 0.18 (20%). The residual error represents the natural variations associated with fluctuations in the spatial extent of the region along a propagation path with rain in an equal probability model for attenuation by rain, and in measurement errors for either attenuation or rain rate.

The sample cumulative distribution functions (CDFs) for the deviations pooled from the 27 path-years of observations at the 7 European sites are presented in Figure 3. The distributions are plotted vs the expected distributions for zero mean normal processes with modeled standard deviations of 0.29 (33%) for attenuation by rain and 0.22 (24%) for rain rate. If the curve for the observed distribution lies along the 1:1 line, the observed distribution matches the assumed model distribution (lognormal distribution because the natural logarithms of the measured values are plotted). The expected 90% bounds for the ordered distributions (95% and 5%), calculated on the basis of the assumed model distributions and the number of CDFs in the data set, are also displayed in the figure. For a large number of ordered distributions (CDFs) of observed deviations, DA or DR, 90 percent of the CDFs should lie within the bounds at each probability value (variate) if the deviation processes are consistent with the assumed variability processes. Except for the single extreme negative value in either distribution (the D3 region outlier in Table 1, marked by ♦ in this figure), both CDFs lie within the 90% bounds. Therefore, the DA and DR distributions are consistent with the variability hypotheses at the 10% significance level. Different variability values could have been assumed to model both processes that would have kept all the observations within the 90% bounds but the resulting models would then have larger differences from the observations in the central region of the distributions where the observations should be better behaved statistically.

The CDFs displayed in Figure 3 are for 0.01 percent of a year. The data in the CCIR data banks have attenuation levels listed for other percentages of a year. Older versions of the data bank had entries at only a few probability levels (fractions of a year). The current edition of the data banks includes observations at more probability levels but, in some cases, the entries were obtained by interpolation from the values in the earlier editions (using straight line segments on a plot of the logarithm of the value vs the logarithm of the percentage of the year). To avoid any errors from interpolation over large differences in probability level or from the generation of correlations between values of the sampled ACDF at different probability levels, the CDFs for the reported attenuation deviations were calculated for the probability levels common to all versions of the data bank: 0.1%, 0.01% and 0.001% of a year. The resulting CDFs are displayed in Figure 4. Again, the measured deviations from the geometric mean are plotted vs the expected deviations for a lognormal process with a variability equivalent to 33%. The 90% bounds were plotted for the number of observations in the 0.01% data set (the same as for Figure 3). The deviation distribution values for the 0.1% and 0.001% probability levels all fall within the 90% bounds (see also Table 2). Because fewer path-years of data are present in the 0.1% and 0.001% CDFs, their 90% bounding curves should be spaced further apart than the bounds displayed in the figure.

Agreement between the CDFs for 0.1% and 0.001% and the 33% variability model is significant at better than the 10% level. Therefore, the observed variability is not a function of the the fraction of a year for probability levels in the 0.1% to 0.001% range. It is noted that this conclusion is contrary to the results reported by COST 205 [1985b] for the same data.

The 33% variability model for the deviations of attenuation (DA) and the 24% variability model for the deviations of rain rate (DR) observations from their sample geometric means at fixed probability levels from 0.1% to 0.001% of a year explain the data obtained in Europe and in the USA. The attenuation deviations are consistent with the 33% variability hypothesis as indicated in Table 1. For the rain rate measurements, the observed variability is significantly smaller for the sites in the USA than for the sites in Europe (16% vs 27%). To be consistent with the observations from both geographic regions, the year-to-year variation in rain rate must be close to the 24% value assumed for the variability model. The variability models for rain rate and rain attenuation therefore obtain for mid-latitude observations from 11 sites spanning latitudes from 30° to 67° encompassing 7 rain climates (Global model) and, for attenuation, elevation angles from 11° to 50° for frequencies near 12 GHz.

3. A REFERENCE FOR VARIABILITY ESTIMATION

The selection of standard deviation estimates for the characterization of variability is predicated on an assumed probability distribution for the deviations of the cumulative distributions of the measurements from their expected CDFs. The existence of a model for estimating the expected ACDF for a single year of data is necessary to calculate the observed deviations. The model used in section 2 was the geometric average ACDF. That model also assumed that the statistics of the deviations about the geometric average were stationary (ie. drawn from the same process which did vary in space or time).

Most of the measurements in the data banks are limited data sets of only one or two years duration. These observations were not used in the analysis of section 2 because insufficient data were available for a path to provide a reference distribution (sample geometric mean) for the estimate of the standard deviation. To extend the analyses to all the data in the data banks, an alternative to the geometric mean model is needed. One possibility is to employ an attenuation prediction procedure reported in the literature. Crane and Shieh [1989] found that the four best of the attenuation prediction procedures they tested provided estimates of measured ACDFs with prediction errors that did not differ significantly from each other when coupled with the same rain

climate model. The prediction errors should be larger than the intrinsic year-to-year variability because the climate modeling process is relatively coarse and the point-to-path transformation procedures only approximate the complex processes that occur in nature. The estimates made by Crane and Shieh on the basis of a lognormal distribution for prediction error suggest that the model prediction errors are of the order of 0.4 (50%).

Accepting an increase in apparent variability as the penalty for using an attenuation prediction model to make the entire data base available for the estimation of variability, any one of the attenuation prediction procedures could be selected to provide the reference. The only statistically valid procedure for model selection is to pick one that does not depend on parameters set by reference to the data in the data bank. If the data were used for parameter estimation, correlations would occur between the parameters and the data in the data bank that would reduce the apparent variability. The new Two-Component model (T-C) [Crane and Shieh, 1989] was selected to provide the reference for estimating variability. The selection was based on convenience; the model was resident on the computer system used in this analysis. None of the parameters of the T-C model were set using data in the data base. The empirical parameters in the model were obtained from analyses of weather radar and rain gauge data from Massachusetts, Tennessee, West Germany and Malaysia.

The CCIR model was also selected to provide a second variability estimate for comparison. Although the model employed by the CCIR [1986b; c; d] was fit to observations in the data banks, it has been used as a comparison standard in studies by the CCIR. The parameters in the current CCIR model were obtained in three steps. The horizontal, point-to-path variations were modeled at the 0.01% probability level using a procedure recommended by Lin [1975]. The parameters for this part of the model were least-square-fit to the attenuation and rain rate observations in the CCIR terrestrial path data bank. The extension of the model to include the effects of vertical variations along a slant path was accomplished by selecting a latitude dependent rain height (parameter) for use at 0.01% of a year that best fit the attenuation and rain rate observations in the slant path data bank (1985 edition). The prediction of attenuation at probability levels different from 0.01% of a year was made using a modification to the procedure developed by Fedi [1980]. The parameters for this procedure were obtained by a least-square fit to the attenuation observations from Europe in the data bank.

Single-year data from satellite beacon observations in Europe

Deviations in attenuation and rain rate at 0.01% of a year from the Two-Component rain attenuation and Global climate model (T-C & Global) predictions were estimated for the multiple-

year data employed for the analyses presented in Section 2. The results for the 27 path-years of simultaneous, single-year ACDFs and RCDFs from Europe are presented in Table 2. The standard deviations were 0.35 (42%) for DA and 0.35 (42%) for DR. The 10% confidence limits for DA enclose the 33% variability model. The DR value confidence limits do not enclose the 24% variability model estimate but do overlap the confidence limits for the DR estimate based on the sample geometric mean model. If the site identified as an outlier is not used in the analysis, the DA estimate is identical to the model prediction but the DR estimate still significantly overestimates the model prediction. For the 27 path-years of data, the results based on the use of the T-C & Global model are not significantly different from the results based on the geometric mean model (at the 10% significance level).

The CCIR slant path data bank contains 53 path-years of simultaneous, single-year ACDFs and RCDFs. The simultaneous DA and DR values for 0.01% of a year are presented in Figure 5. The observations were for frequencies in the 11.6 to 17.8 GHz range. The standard deviations were 0.31 (36%) for DA and 0.29 (34%) for DR. The DA value lies within the 10% confidence limits for the 27 path-years of data used to generate Figure 2 and the 9 path-years of data from the USA (Table 2). The 10% confidence limits on the DA estimate enclose the 33% variability model. The DR estimate also lies within the 10% limits for the American and European data but the 10% confidence limits on the DR estimate do not enclose the 24% variability model.

The DA and DR deviations plotted in Figure 5 include modeling errors, measurement errors and the expected increase in variance caused by the use of a limited number of rain climate regions. If a site is located at random within a rain climate region, a climate modeling error is generated because the RCDF is predicted to have the same distribution throughout the region but the actual CDF must vary from one region to the next. The component of the rain rate deviations at 0.01% caused by the use of a climate region model is given as a function of climate in Table 3. To estimate the RCDF deviations for the table, it was assumed that the deviations were uniformly distributed for locations selected at random within a climate zone. The limits for the uniform deviation process were taken to be the model RCDFs for the adjacent climate regions. The Global climate regions were originally defined to have the RCDFs for a region confined between the climate model RCDFs for adjacent regions (see Crane [1980] Figures 6 and 7). Climate regions B and D were subsequently subdivided because the span of the possible RCDFs was too large. If the standard deviation for the year-to-year variation process for rain rate, 0.21 (24%), is combined with the root mean square (rms) deviation for the climate estimate (0.17, Table 3), the result is a standard deviation estimate of 0.27 (31%) which lies within the 10% confidence limits for the DR estimates listed in Table 2. For the estimation of the attenuation deviations, the linear model

presented in Figure 2 generates a standard deviation estimate of 0.29 (33%) which also lies within the 10% confidence limits for the DA estimates.

For the prediction of attenuation, the expected standard deviation for DA is increased relative to the standard deviation for DR. Working back through the variance estimates, only 32 percent of the observed variance in DA corresponds to the use of the Global climate region model. The remainder is due to year-to-year variations caused in part by a lack of correlation between rain rate and attenuation deviations from the model predictions (see Figure 5). Therefore, the variability model has a component that changes only with location within a climate region but not with the length of an observation period and a component with a variance inversely proportional to the length of the observing period (the year-to-year variations). The variability in DA due to the use of the Global rain climate model is 18%; the variability due to year-to-year changes on a path is 27%: for a single year of observations the two combine to produce a variability of 33%. The use of a different climate model would produce a change in the climate model component of variability. For DR, the components of the model are 17% and 24% for site-to-site and year to year respectively with the estimated variability for the combination equal to 31%.

The observed correlation between the attenuation and rain rate deviations is only 0.6 (Figure 5) yielding a significantly larger residual error for a least-square-fit linear model for the deviations from the T-C & Global predictions. The slope for the linear model is not close to the expected value for the relationship between specific attenuation and rain rate at frequencies in the 11 to 18 GHz band. The intercept value suggests a modeling error (bias) in either attenuation or rain rate (or both). When the CCIR rain attenuation model and CCIR rain climate model (CCIR & CCIR) are used, the standard deviations are even larger (Table 2), 50% for DA and 52% for DR, but the the correlation between DA and DR is also larger, 0.8, yielding a residual error of 30% which is not significantly different (at the 10% level) from the 27% residual error for the T-C and Global model. When the CCIR model is combined with the observed rain rate values at 0.01% of a year, the attenuation prediction error is 40%, a number significantly larger than the expected residual error (18%, the residual error from Figure 2) when the effects of the annual and rain climate variations are removed from the prediction process.

The cumulative distributions of deviations from rain rate model predictions at 0.01% of a year (DR) are presented in Figure 6 for both the Global and CCIR rain climate models for the 54 path-years of single-year rain rate observations from Europe in the CCIR data bank. Both models have the same average prediction error (bias). The 90% bounds for the 31% variability model were plotted after adjustment for the prediction (or measurement) bias. The Global model predictions are consistent with the variability model bounds inferred from the deviations between

observation and the sample geometric mean model. For the Global rain climate model, the standard deviation is 0.29 (34%). The CCIR model predictions deviate significantly from the observations for nearly half the path-years of observations. For the CCIR rain climate model, the standard deviation is 0.42 (52%). Two conclusions may be drawn from this figure, 1) the Global rain climate regions are consistent with the observations but the Global rain rate model overestimates the observed rain rate at 0.01 percent of a year and 2) the CCIR model climate regions are not consistent with the observations, the standard deviation for DR is significantly larger than for the Global model (at the 10% significance level) and, for more than half the observations, overestimate the rain rate.

The cumulative distributions of deviations from rain attenuation model predictions at 0.01% of a year for the 54 path-years of single-year satellite beacon attenuation observations from Europe in the CCIR data bank are presented in Figure 7. In this figure, the results from the use of 3 different models are presented: the T-C attenuation prediction model with the Global rain climate model, the CCIR attenuation prediction model with the CCIR rain climate model and the CCIR attenuation prediction model with the measured cumulative rain rate distribution at 0.01% of a year. The predictions based on the use of climate models are unbiased; the predictions based on the rain rate measurements are biased. When combined with the Global rain climate model, the deviations from both The T-C and CCIR attenuation model predictions all lie within the 90% bounds for the 33% single-year variability model. When the CCIR rain climate model is used with the CCIR rain attenuation prediction model, the combination is unbiased but the deviations are significantly larger than observed when the Global climate model is employed (50% vs 36%, see Table 2). For the CCIR model combined with rain rate observations the predictions are biased but the standard deviation is only slightly larger than for the T-C and Global model (39% vs 36%) but significantly larger than expected when measurements are used to reduce the effects of climate model and year-to-year variations.

The deviations from model predictions at 0.1% and 0.001% of a year are also unbiased and consistent with the 33% variability hypothesis when the T-C and Global model is used as illustrated in Figure 8 (and Table 2). At 0.001%, the standard deviation for all the single-year ACDFs was 36%. At 0.1%, the standard deviation is 46% which is significantly larger than 33% (at the 10% significance level). At this fraction of a year, 32% of the observed deviations lie outside the 90% bounds. Four of the twelve deviation estimates that lie outside the bounds are from a single site. If the data from that site are not used in the analysis (the thin dashed curve in Figure 8), all but three of the remaining deviations lie within the bounds and the results are consistent with the 33% variability hypothesis at the 4% significance level. Therefore,

observations in the 0.1% to 0.001% of a year span of probability levels may be modeled as samples from a zero mean process with a standard deviation of 0.29 (33%).

The mean square deviation (MSD) calculated for different probability levels (fractions of a year) from a single ACDF using the natural logarithms of the ratio of measured-to-modeled values of rain attenuation should have a Chi Square distribution with the number of degrees of freedom equal to the number of probability levels (if independent of each other). This result obtains because the T-C & Global prediction model is unbiased with a constant variability over the range of probability levels available for analysis. If the reported ACDF represents the observed distribution and was not constructed by interpolation from a limited number of probability levels, the observations at probability levels separated by a factor of 3 should be independent. The cumulative distributions of root mean square deviation (RMSD) values for the ACDFs in the beacon data set from Europe with three (6 path-years of data), four (23 path-years) and five (25 path-years) probability levels (DoF = degrees of freedom) are plotted in Figure 9. The probability level samples used in the computation of a RMSD value for a single ACDF was continuous over the set, 1%, 0.3%, 0.1%, 0.03%, 0.01%, 0.003%, 0.001% of a year values, used in the analysis. At 3 DoF, the RMSD value will contain between one and two of the 0.1%, 0.01% or 0.001% values assumed to be without interpolation error. At 5 DoF, the actual number of degrees of freedom may be as small as 3 due to correlations caused by interpolation if used in the preparation of the ACDF for the data bank.

The plotting scales on Figure 9 are the observed RMSDs from the T-C & Global model vs the expected value of RMSD for a Chi Square process with the indicated number of degrees of freedom and variability. Agreement obtains if the plotted values lie within the 90% bounds for the ordered distributions. The bounds are plotted for all three distributions (thin lines with the same dash coding as the plotted CDFs). Markers are placed over the RMSD values (single path measurements) that exceed the 98% bound for agreement with the 33% variability hypothesis. For 4 and 5 probability levels, with the exception of the RMSD value for one ACDF, the ordered distributions lie within the 90% bounds. These RMSD values are therefore consistent with the unbiased variability model hypothesis at the 10% significance level. The one exception can be considered an outlier. At the 10% significance level, a hypothesis test for agreement with the variability model would decide that the exception has more variability than expected and may be considered suspect (it corresponds to the single outlier evident in Figures 3 and 4). For the RMSD values with three degrees of freedom, all but 1 lie outside the 90% bounds but only 2 are above the 98% bound for a single ACDF. RMSD values for 6 of 54 ACDFs lie outside the 90% bounds for

the model. All are well outside the bounds indicating that they are not consistent with the variability model or with the other observations presented in the figure and may be outliers.

Based on the beacon observations from Europe, the following conclusions may be drawn: 1) the T-C or CCIR rain attenuation models may be used as a reference for the estimation of variability if the Global rain climate model is employed as well, 2) the variability did not increase measurably with the use of an attenuation prediction model as a reference for estimating the expected long term geometric mean ACDF when compared with the predictions of the sample geometric mean calculated from a limited data set, 3) the CCIR rain attenuation model, when used with the CCIR rain climate model, is unbiased but the standard deviation of the deviations is larger than the natural variability of the rain attenuation process, 4) the increased standard deviation when using the CCIR rain climate model appears to be due to an incorrect identification of the climate regions, 5) the utilization of measured rain rate distributions produces both a bias and an increase in the standard deviation of the differences between model predictions and measurements and 6) the rain rate measurements, not the rain climate models, produce the bias evident in Figure 5.

Single-year data from all locations and types of measurements

The 31% variability model holds for the single-year rain rate observations made simultaneously with the satellite beacon measurements in Europe. However, the European data revealed a significant bias between the climate model predictions and measurements. The next question to be addressed is the consistency of the climate models when all the single-year data sets with simultaneous rain rate observations in the entire data base are employed in the analysis. Figure 10 presents the deviations between measured and modeled rain rate at 0.01% of a year for 111 path-years of data. The variability model distribution bounds are displayed together with the cumulative distributions of the deviations of measurements from the Global and CCIR rain climate model predictions. Both climate models are unbiased when compared to the larger set of data. The deviations from the Global model predictions lie within the variability model bounds for all path-years; the standard deviation of the DR values is 0.30 (35%) with confidence limits that enclose the variability model at the 10% level (Table 2). The deviations from the CCIR model predictions agree with the variability model only within the central region of the distribution ($\pm$ 0.5 standard deviations). The deviations from the CCIR model display a steeper slope (larger variability) than the model predictions and are not entirely consistent with a lognormal model because, with the steeper slope, a large number of outliers would occur for a variate greater than 0.27 (one standard deviation).

The 33% attenuation variability model holds for the single-year satellite beacon observations from Europe. Figure 12 presents the deviations between measured and modeled attenuation at 0.01% of a year for 106 path-years of data from terrestrial, satellite beacon and slant path radiometer measurements at frequencies ranging from 11 to 82 GHz, latitudes from -38° to 67° north, elevation angles from 7° to 53° for slant paths, horizontal distances from 1.3 to 25 km for terrestrial paths, and vertical, horizontal and circular polarizations. The variability model distribution bounds are displayed together with the cumulative distributions of the deviations of measurements from the T-C & Global model and the CCIR & CCIR model predictions. The deviations from the T-C & Global model predictions lie within the variability model bounds for all but 6 path-years; if the 6 path-years of data are excluded, the resulting DA is 0.31 (36%) with confidence limits that enclose the variability model (Table 2). The deviations from the CCIR & CCIR model predictions agree with the variability model only within the central region of the distribution (± 0.5 standard deviations). The deviations from the CCIR & CCIR model are consistent with a lognormal model with zero bias but with a significantly higher variance. The performance of the CCIR model is better when combined with the measured rain rate values at 0.01% of a year (CCIR & meas).

The deviations of the observations from the T-C & Global model predictions were investigated at 0.1% and 0.001% of a year. At 0.1%, the deviations have zero mean and are consistent with a 33% variability model as indicated in Figure 12. At this probability level, the standard deviation of all the ACDFs is 0.39 (47%) with confidence interval bounds that do not enclose the 33% model variability. If the 5 outliers evident in the figure are not used in the analysis, the resulting standard deviation is 0.33 (39%). This standard deviation is still larger than the model estimate at the 10% significance level but is consistent with the model at the 4% level. At 0.001% of a year, the T-C & Global model is biased and the variability is significantly larger than the model estimate. For all 58 ACDFs at 0.001%, the standard deviation in DA is 0.47 (63%). If five ACDFs from a single site in the USA are removed from the data set, the resulting CDF for the attenuation deviations has a small bias (the thin dashed 0.001% curve in Figure 12) and the resulting variability is 0.43 (54%). If the 3 additional outliers that deviate markedly from the model distribution are also removed, the resulting standard deviation is 0.29 (34%). For all but 8 of the observations (outliers from 4 sites), the data are consistent with the 33% variability model.

The RMSD values have Chi Square distributions as indicated in Figure 13. Seventeen out of 93 path-years of data with four or more degrees of freedom are outside the 90% bounds for the variability model. All but 8 of the 26 RMSD values with 3 degrees of freedom lie outside the variability model bounds. The remaining 71% of the observations are consistent with the

variability model at the 10% level. For 4 or more degrees of freedom, 82% of the RMSD values are consistent with the variability model and with each other (a best fit line passing through the origin would closely approximate the 1:1 line). For 3 degrees of freedom, the RMSD values are consistent with each other (lie along a straight line that passes through the origin) but with a variability model having roughly a 25 percent greater variability. Some of the observations could correspond to observations with fewer than 3 degrees of freedom. More than 40 percent of the observations are for data with probability levels greater than or equal to 0.03% of a year and none of the observations are for 0.001% of the year. For 4 degrees of freedom almost half the observations include 0.001% of a year and, for more degrees of freedom, the fraction of the observations including 0.001% of a year is even higher. The observations tend to show an increase in apparent variability with an increasing fraction of the measurements with probability levels greater than 0.1% of a year.

The single threshold for acceptance represents an approximate single ACDF hypothesis test for 4 or more probability levels (a single sample from a Chi Square distribution with 5 degrees of freedom) at a 2% significance level and may be applied without reference to any of the other RMSD values from the data bank. If the RMSD for a single-year ACDF lies above this threshold, it is considered an outlier and is suspect.

Multiple-year data sets from all locations

The single-year observations constitute only 132 of the 252 ACDFs in the combined CCIR data banks. The variability model must be extended to multiple-year ACDFs for comparison with the remainder of the observations in the data banks. The 33% variability model has two components, 0.17 (18%) due to the use of the Global climate regions and 0.27 (31%) due to the year-to-year variations at the same site. The former is fixed for a site for any length of data sequence but the latter may be reduced by combining observations from several years. The variance for the latter component is reduced by the number of years in the data sequence. To provide a composite variability model estimate, the square root of the sum of the variances for each component must be calculated. The thresholds for acceptance at the 2% significance level hypothesis test are listed as a function of the number of degrees of freedom and the number of years of observations in Table 4. For 5 DoF, the threshold for acceptance is plotted as a function of the length of the observation set in Figure 14. Nineteen of the 95 RMSD values with 5 degrees of freedom are above the 98% bound and are not consistent with the variability model.

The variability model estimate holds for integral years of observations. The rain attenuation process is assumed to be stationary over periods spanning an integral number of years but is not

stationary for arbitrary duration intervals due to the seasonal nature of the rain process. Experience suggests that seasonal variations are important. Results for 18 months of observation should be different if the measurement interval spans two normally rainy seasons or two dry seasons. The 98% threshold values (the modeled RMSD value that is expected to exceed 98 percent of the observations as a result of the natural year-to-year and within climate region variations) are calculated only for integral numbers of years. In Figure 14 the calculated threshold values are connected by straight lines. RMSD estimates are plotted for all the ACDFs with 5 DoF whether for an integral number of years or not.

The RMSD observation may be scaled to the expected value for a single year of observations by adjusting the RMSD value by the variability model estimate. For two years of observations, the apparent variability must be increased by the ratio of the variability estimate for a single year to the estimate for two years. With this adjustment, the threshold for acceptance (98% threshold) value does not depend on the duration of the measurements. The scaled RMSD values for all the paths in the data bank are presented in Figure 15. The threshold for acceptance is plotted as a function of the number of degrees of freedom (DoF) associated with each RMSD value. The 2% threshold (lower bound) is also displayed on the figure. If the observations are consistent with the variability model when adjusted to an equivalent single year of observations, 2 percent of the RMSD values should lie below the 2% threshold and 2% should lie above the 98% threshold. Four of 252 values lie below the 2% threshold in agreement with the model estimates but 47 lie above the 98% threshold in clear violation of the model estimate. The large number of values above the threshold for acceptance is an indication of contributions to the observed deviations from more than just the natural site-to-site and path-to-path variability of the rain attenuation process relative to the prediction model.

4. DATA QUALITY ASSESSMENT

The model for the site-to-site and year-to-year variability for a path is based on the lognormal distribution for the deviations of measurements from the reference ACDF for a path. The deviation model is assumed to hold for all climate regions, path geometries and probability levels within the 1.0% to 0.001% of a year range. The data presented in Section 3 represent all the ACDFs in the CCIR data banks (terrestrial plus slant path). The 90% bounds on the CDFs and 98% threshold for the RMSD estimates for single ACDFs represent the expected extremes due to chance variations in climate and rain conditions on the path. Errors in assigning the climate region, measurement errors due to the operation of the equipment and errors in the statistical adjustment for missing data

will create larger RMSD values. In using the observations to fix the level of variability, it is not possible to separate deviations due to natural causes or experimental error. The latter includes the effects of rain or snow on antenna components and radomes, the problems associated with receiver baseline variations due to either the receiver system or the satellite or the terrestrial transmitter system, insufficient dynamic range for the attempted measurements and delays in receiver recovery (lock) after completely losing the signal during a deep fade. Modeling errors could also contribute to significant deviations between model predictions and measurements. Considering that the geophysical effects are assumed to dominate the modeled deviation process, deviations that are significantly larger (outside the modeled bounds which explain a significant fraction of the observed deviations for a large number of propagation paths) must be due to experimental error and the ACDF producing the large deviation must be an outlier and identified as suspect.

The estimated bounds on the CDFs for deviations at fixed probability levels or for the RMSD values calculated from independent samples from each ACDF at fixed probability levels then can be used to assess data quality. Observed ACDFs yielding samples in the CDFs that lie outside the bounds should be flagged as questionable and requiring further scrutiny. Comparisons with the bounds on the sample cumulative distributions of the deviations or the RMSD values are useful only when comparing a group of observations to a model. Such comparisons are necessary to build and verify the model. After the model has been established, hypothesis tests should be conducted on each ACDF separately. Using the Global rain climate and a convenient path attenuation model to provide the reference, the observed RMSD of the ACDF from the reference ACDF should be tested using a Chi Square hypothesis test for the number of probability levels employed for the calculation of the RMSD value and the expected standard deviation of the natural variations about the model predictions (0.29 corresponding to a 33% variability when scaled to an equivalent single year of observations). Table 4 lists the threshold levels for questioning the quality of the ACDF to be tested. If the RMSD value lies below the level in Table 4, the observed RMSD is within the range expected for chance variations in the rain process and the data set should be accepted. Higher values are suspect and should be investigated further.

This data quality assessment procedure was developed for use with the T-C & Global model for generating the reference ACDF. Deviations may be generated relative to any convenient combination of rain attenuation and rain climate models. The expected variability values will change with the number of climate regions employed in the rain rate estimation model and the sophistication of the rain attenuation prediction procedure. With a large number of observed ACDFs, deviation CDFs may be constructed that display a degree of consistency between the individual deviation estimates when plotted against the predictions of standard probability models

(such as normal, Figure 7, or Chi Square, Figure 9). Consistency is indicated by approximate straight line segments such as would better fit the CCIR & CCIR model displayed in Figures 7 and 11 or the approximate straight line segment through the origin that would better fit the 3 DoF curve in Figure 13. These self consistent deviation models can then be used to establish the variability value needed for the hypothesis tests.

The quality assessment procedure based on the T-C & Global model was applied to the satellite beacon observations from the USA in the CCIR data banks. Fifteen of 58 ACDFs were judged to be questionable (Table 5). One of these was identified as being caused by a transcription error when assembling the data bank [Crane, 1989]. Ten of the 15 were from observations at a single site. A closer examination of the data showed good agreement with the variability model predictions at 0.01% of the year but poor agreement when the estimated attenuation values were either relatively large (greater than 16 dB) or small (less than 4 dB). The data can be considered suspect except within the central region of the ACDFs due to a limited dynamic range for measurements. After pruning the ACDFs to correct for the dynamic range limitations, all but three of the observations from the site are consistent with the variability hypothesis. None of the three remaining outliers are for an integral number of years of observations and agreement with the model should not be expected. The net result for the USA entries in the CCIR data bank, after correction and pruning, 7 ACDFs are still outliers. Three of the outliers should not be used in model development and testing because they do not correspond to integral numbers of years of observations. The remaining 4 are also suspect and should not be used for model development or testing.

The CCIR & CCIR model was also used to produce a list of outliers for the USA. Eleven of the ACDFs were identified as outliers. The transcription error was detected. The 4 outliers that remained after the analysis reported above using the T-C & Global model were from 3 different sites. Four of the outliers from relative to the CCIR & CCIR model were from the same three sites. The details differed in that different paths were identified as outliers. Not one of the ten paths from the single site were identified as outliers. The data from that site were in the data bank when the model parameters were set. As a result, complete sets of observations from other sites within the USA were identified as outliers even though agreement was obtained relative to the geometric mean model. In this case, the data can not be considered suspect but the rain attenuation prediction procedure should be questioned.

5. RECOMMENDATIONS

A model has been developed to estimate the expected year-to-year variations in rain rate or rain attenuation at fixed probability levels. A rain attenuation prediction model is expected to predict the long term geometric mean of the cumulative distribution function for rain attenuation. The variability model describes the expected variation of observed (or predicted) cumulative distribution functions about the long term geometric mean CDF. It should be used with the rain attenuation prediction procedure to provide a more complete statistical description of the rain attenuation process.

The model predictions provide a basis for assessing data quality. Reported CDFs of rain attenuation measurements should be tested by comparison with a model prediction. The prediction should be based on the use of a rain climate model together with the rain attenuation prediction procedure. The ACDF should not be a member of the data set used to generate the parameters for the model. The RMSD value for the natural logarithms of the ratios of measured to modeled attenuation at probability levels spaced by at least a factor of three should be calculated as a test statistic. The test value should be compared with the threshold values in Table 4 to decide on the quality of the data. If the test value is less than the threshold, the data should be added to the data bank. If not, the data should be considered suspect and subjected to further scrutiny.

REFERENCES

COST 205 [1985a]: Project Cost 205: Prediction of rain attenuation statistics *Alta Frequenza*, **LIV(3)**, 140-156.

COST 205 [1985b]: Project Cost 205: Statistical properties of attenuation due to rain, *Alta Frequenza*, **LIV(3)**, 133-139.

CCIR [1988]: Data Banks Used for Testing Prediction Methods in Sections E, F and G of Volume V, Doc 5/378(Rev.1) as updated through 26 Jan 1988, International Radio Consultative Committee, Int. Telecommun. Union, Geneva.

CCIR [1986a]: Attenuation by Hydrometeors, in Particular Precipitation, and other Atmospheric Particles, Rept 721-2, *Recommendations and Reports of the CCIR, 1986*, Volume V, Propagation in Non-Ionized Media , International Radio Consultative Committee, Int. Telecommun. Union, Geneva.

CCIR [1986b]: Propagation Data and Prediction Methods Required for Earth-Space Telecommunication Systems, Rept 564-3, *Recommendations and Reports of the CCIR, 1986*, Volume V, Propagation in Non-Ionized Media , International Radio Consultative Committee, Int. Telecommun. Union, Geneva.

CCIR [1986c]: Propagation Data and Prediction Methods Required for Line-of-Sight Radio-Relay Systems, Rept 338-5, *Recommendations and Reports of the CCIR, 1986*, Volume V, Propagation in Non-Ionized Media , International Radio Consultative Committee, Int. Telecommun. Union, Geneva.

CCIR [1986d]: Radiometeorological Data, Rept 563-3, *Recommendations and Reports of the CCIR, 1986*, Volume V, Propagation in Non-Ionized Media , International Radio Consultative Committee, Int. Telecommun. Union, Geneva.

Crane, R. K. [1971]: Propagation phenomena affecting satellite communication systems operating in the centimeter and millimeter wavelength bands, *Proc IEEE*, **59(2)**, 173-188.

Crane, R. K. [1980]: Prediction of attenuation by rain, *IEEE Trans Commun*, **COM-28(9)**, 1717-1733.

Crane, R. K. [1982]: A two-component rain model for the prediction of attenuation statistics, *Radio Sci*, **17(6)**, 1371-1387.

Crane, R. K. [1985a]: Comparative evaluation of several rain attenuation prediction models, *Radio Sci*, **20(4)**, 843-863.

Crane, R. K. [1985b]: Evaluation of global and CCIR models for estimation od rain rate statistics, *Radio Sci*, **20(4)**, 865-879.

Crane, R. K. [1989]: Propagation Modeling - Past, Present and Future, Sixth Int. Conf. Antennas and Propagation (ICAP 89), IEE Conf Publ 301, Part 2: Propagation, pp 263-267, London, UK.

Crane, R. K. and H-C. Shieh [1989]: A two-component rain model for the prediction of site diversity performance, *Radio Sci*, accepted for publication.

Fedi, F [1980]: Rain attenuation on Earth-satellite links: a prediction method based on joint rainfall intensity, Proc URSI Commission F Int. Symposium Effects of the lower atmosphere on radio propagation at frequencies above 1 GHz, Lenoxville, Que., Canada.

Lin, S. H. [1975]: A method for calculating rain attenuation distributions on microwave paths, *BSTJ*, **54**, 1051-1086.

Table 1 Estimated Deviations (in LN units) Relative to the Geometric Mean Model

			Rain Attenuation				Rain Rate	
	Global		DA		33% Model	DR	24% Model	
Location	Rzone	DoF	St.Dev		5%† 95%	St.Dev	5%	95%
Europe	B	2	0.18		0.07 0.50	0.18	0.05	0.37
	B1		0.33			0.37		
	D3		0.68	•		0.45	•	
	D2	3	0.13		0.10 0.47	0.14	0.07	0.35
	C		0.17			0.15		
	D1	4	0.12		0.12 0.45	0.11	0.09	0.33
	D3		0.35			0.20		
Composite (Figure 2)		20	0.31		0.21 0.36	0.24	0.16	0.27
USA	D2	2	0.08		0.08 0.50	0.23	0.05	0.37
	D2		0.19			0.12		
	D2		0.36			0.18		
	D2					0.10		
	D2*		0.59*	•				
	D2		0.18					

DA = LN(Ratio of Measured to Modeled Attenuation)
DR = LN(Ratio of Measured to Modeled Rain Rate)

• Indicates the standard deviation estimate is not within the 90% bounds for the variability model.
† Chi Square bounds on the variability model for the indicated number of degrees of freedom (DoF).
* Includes a known transcription error [Crane, 1989], the following line is for the same site and path but with the error corrected.

Table 2 Residual Errors for Single-Year Data Sets

Model Data Set	# ACDFs	DA:	UC	LC	DR:	UC	LC	corr coef	RE:	UC	LC
Geometric Mean											
Europe											
0.1%	17	0.20	0.30	0.15							
		23%	35%	17%							
0.01%	27	0.31	0.43	0.25	0.24	0.33	0.19	0.82	0.18	0.25	0.14
		37%	53%	29%	27%	38%	21%		20%	29%	15%
0.001%	14	0.22	0.35	0.16							
		24%	42%	18%							
USA											
0.01%	9	0.24	0.46	0.16	0.15	0.28	0.10	0.46	0.21	0.50	0.14
		27%	58%	18%	16%	33%	11%		24%	65%	15%
T-C & Global											
Europe											
0.01%	27	0.35	0.45	0.29	0.35	0.45	0.29	0.62	0.28	0.36	0.23
(same as above)		42%	57%	33%	42%	57%	33%		32%	44%	26%
0.01%	24	0.29	0.38	0.24	0.33	0.43	0.27	0.62	0.24	0.32	0.20
(same no outlier site)		33%	47%	27%	39%	54%	31%		27%	37%	22%
0.1%	38	0.38	0.47	0.32							
(full beacon)		46%	60%	38%							
0.1%	34	0.36	0.45	0.30							
minus 1 site		44%	57%	35%							
0.01%	53	0.31	0.37	0.27	0.29	0.35	0.25	0.61	0.24	0.29	0.21
(full beacon)		36%	44%	30%	34%	42%	29%		28%	34%	23%
0.001%	39	0.31	0.38	0.26							
(full beacon)		36%	46%	30%							
All											
0.1%	113	0.39	0.44	0.35							
		47%	55%	42%							
0.1%	108	0.33	0.38	0.30							
(no outliers)		39%	47%	35%							
0.01%	106	0.39	0.44	0.35	0.30	0.34	0.27				
		47%	55%	42%	35%	41%	31%				
0.01%	100	0.31	0.35	0.28							
(no outliers)		36%	42%	32%							
0.001%	58	0.47	0.56	0.41							
		60%	74%	51%							

DA = LN(Ratio of Measured to Modeled Attenuation)
DR = LN(Ratio of Measured to Modeled Rain Rate)
corr coef = Correlation coefficient
RE = Residual error
UC, LC = 10% significance level confidence interval bounds estimated using a Chi Square distribution with the observed standard deviation estimate and the number of degrees of freedom for the set of observations.

Table 2 Residual Errors (Continued)

Model Data Set	# ACDFs	DA:	UC	LC	DR:	UC	LC	corr coef	RE:	UC	LC
CCIR & CCIR											
Europe											
0.1%	45	0.33	0.40	0.28							
(full beacon)		39%	49%	33%							
0.01%	53	0.41	0.48	0.35	0.42	0.50	0.36	0.76	0.26	0.31	0.23
(full beacon)		50%	62%	42%	52%	65%	44%		30%	37%	25%
0.001%	39	0.41	0.51	0.35							
(full beacon)		50%	66%	41%							
All											
0.1%	121	0.40	0.45	0.36							
		50%	57%	44%							
0.01%	106	0.47	0.53	0.42	0.38	0.43	0.34				
		59%	69%	52%	46%	54%	41%				
0.001%	58	0.52	0.61	0.45							
		68%	84%	57%							

DA = LN(Ratio of Measured to Modeled Attenuation)
DR = LN(Ratio of Measured to Modeled Rain Rate)
corr coef = Correlation coefficient
RE = Residual error
UC, LC = 10% significance level confidence interval bounds estimated using a Chi Square distribution with the observed standard deviation estimate and the number of degrees of freedom for the set of observations.

Table 3 Estimated Variation Due to the Use of Climate Zones

Global E[RMSD] Climate Zone	RR 0.01% (mm/h)	LNRR	Uniform Adjacent Zones		Res. Error = 0.24	
A	10	2.30	0.25	29%	0.35	42%
B1	15.5	2.74	0.25	28%	0.34	41%
B2	23.5	3.16	0.17	19%	0.29	34%
C	28	3.33	0.12	13%	0.27	31%
D1	35.5	3.57	0.16	18%	0.29	34%
D2	49	3.89	0.17	18%	0.29	34%
D3	63	4.14	0.19	21%	0.30	36%
G	94	4.54	0.13	14%	0.27	31%
E	98	4.58	0.13	14%	0.27	31%
H	147	4.99	0.23	26%	0.34	40%
B	19.5	2.97	0.46	58%	0.52	68%
D = D2	49	3.89	0.45	57%	0.51	67%
F	23	3.14	0.53	70%	0.58	79%
Rms B1->E			0.17	18%	0.29	34%

Table 4 Thresholds for Acceptance (98% Bound)

DoF	Number of Years: 1	2	3	4	5	6	7	8	
1	0.676	0.549	0.500	0.474	0.457	0.446	0.438	0.431	Standard Deviation
2	0.574	0.467	0.425	0.403	0.389	0.379	0.372	0.367	LN(Measured to
3	0.526	0.428	0.389	0.369	0.356	0.347	0.341	0.336	Modeled Attenuation)
4	0.496	0.403	0.367	0.348	0.336	0.327	0.321	0.317	
5	0.475	0.386	0.352	0.333	0.322	0.314	0.308	0.303	
6	0.460	0.374	0.340	0.322	0.311	0.303	0.298	0.293	
7	0.448	0.364	0.331	0.314	0.303	0.295	0.290	0.286	
8	0.438	0.356	0.324	0.307	0.296	0.289	0.283	0.279	
1	97%	73%	65%	61%	58%	56%	55%	54%	Standard Deviation
2	78%	60%	53%	50%	48%	46%	45%	44%	Percent Equivalent
3	69%	53%	48%	45%	43%	41%	41%	40%	
4	64%	50%	44%	42%	40%	39%	38%	37%	
5	61%	47%	42%	40%	38%	37%	36%	35%	
6	58%	45%	41%	38%	37%	35%	35%	34%	
7	56%	44%	39%	37%	35%	34%	34%	33%	
8	55%	43%	38%	36%	34%	33%	33%	32%	

Table 5 Relative Performance of the Models Employed to Study Variability

Region	Data Bank	Data Type	Atten Model	Rain Model	Avg	RMSD	# >98%	# Paths
USA	CCIR	Satellite Beacon	T-C	Global	3.4%	49.4%	15	58
			CCIR	Global	-16.2%	49.9%	14	58
			T-C	CCIR	18.0%	62.1%	25	58
			CCIR	CCIR	-5.7%	44.1%	11	58
			CCIR	Measured	-22.7%	64.7%	17	43
	Thayer School	Satellite Beacon (same as above)	T-C	Global	5.4%	40.1%	5	55
			CCIR	Global	-17.5%	48.6%	8	55
			T-C	CCIR	26.6%	58.3%	15	55
			CCIR	CCIR	-5.7%	41.7%	8	55
	Thayer School	(full set)	T-C	Global	6.6%	37.0%	7	98
			CCIR	Global	-15.6%	52.4%	18	98
			T-C	CCIR	25.6%	53.6%	23	98
			CCIR	CCIR	4.6%	48.8%	23	98
EUROPE	CCIR	Satellite Beacon	T-C	Global	4.2%	40.5%	11	85
			CCIR	Global	0.1%	49.3%	16	85
			T-C	CCIR	2.6%	50.8%	23	85
			CCIR	CCIR	-0.7%	42.4%	15	85
			CCIR	Measured	18.2%	55.2%	20	76
ASIA	CCIR	Satellite Beacon	T-C	Global	-8.3%	70.3%	4	25
			CCIR	Global	-13.6%	58.7%	3	25
			T-C	CCIR	-12.6%	110.9%	12	25
			CCIR	CCIR	-17.9%	88.9%	7	25
			CCIR	Measured	-21.0%	70.7%	5	22
global	CCIR	Radiometer	T-C	Global	-5.4%	54.0%	12	44
			CCIR	Global	-17.6%	55.2%	13	44
			T-C	CCIR	-11.0%	65.3%	19	44
			CCIR	CCIR	-23.3%	51.6%	15	44
			CCIR	Measured	-49.9%	128.7%	14	20
global	CCIR	Terrestrial	T-C	Global	-15.1%	31.5%	5	40
			CCIR	Global	-2.6%	26.3%	2	40
			T-C	CCIR	-31.1%	66.6%	21	40
			CCIR	CCIR	-6.5%	31.5%	4	40
			CCIR	Measured	6.3%	20.9%	2	39
global	CCIR	Entire	T-C	Global			47	252
			CCIR	Global			48	252
			T-C	CCIR			100	252
			CCIR	CCIR			52	252
			CCIR	Measured			58	200

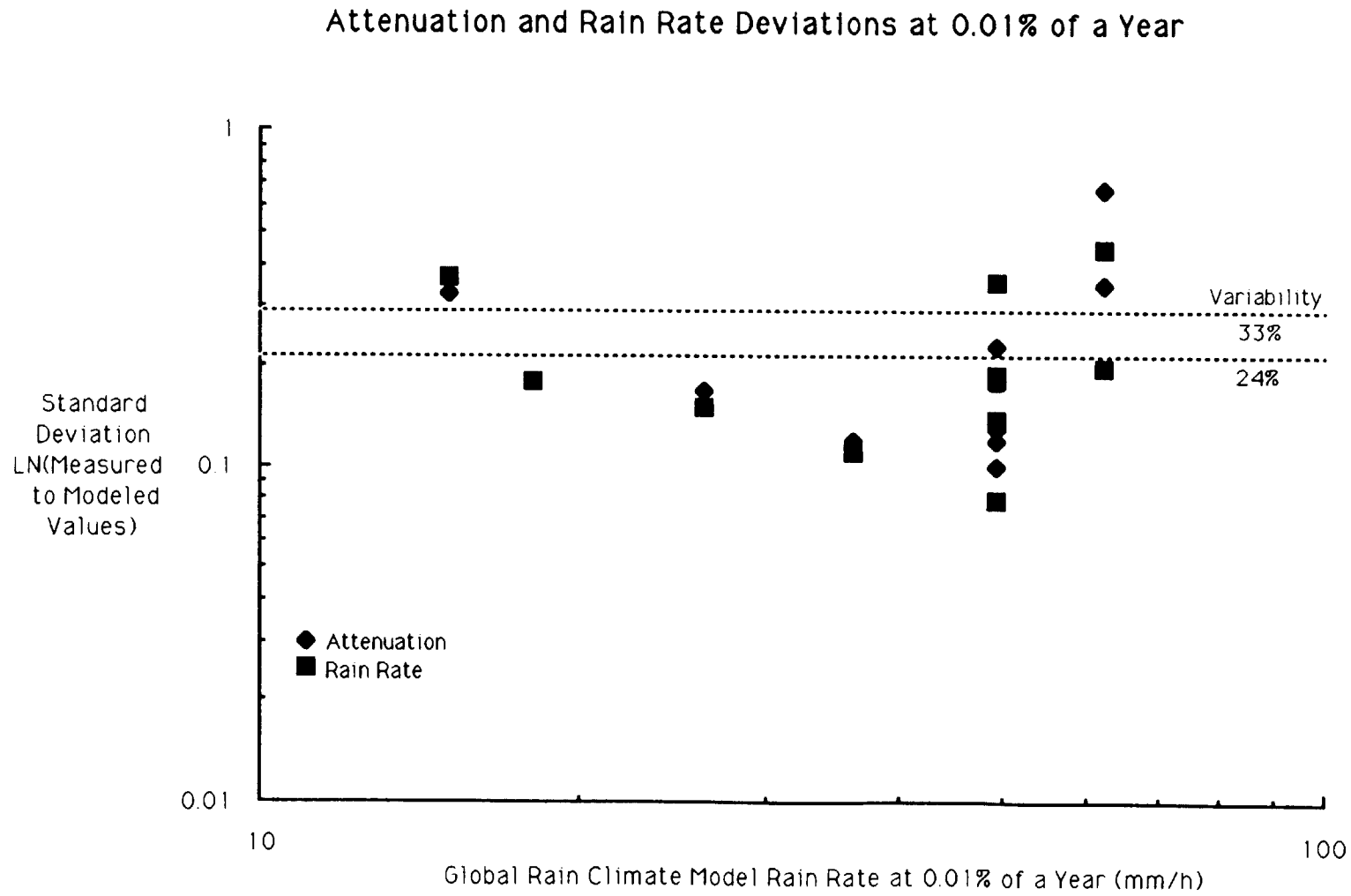

Figure 1 Standard deviation of the deviations of measured from modeled values for sites with three or more single-year sample cumulative distribution functions.

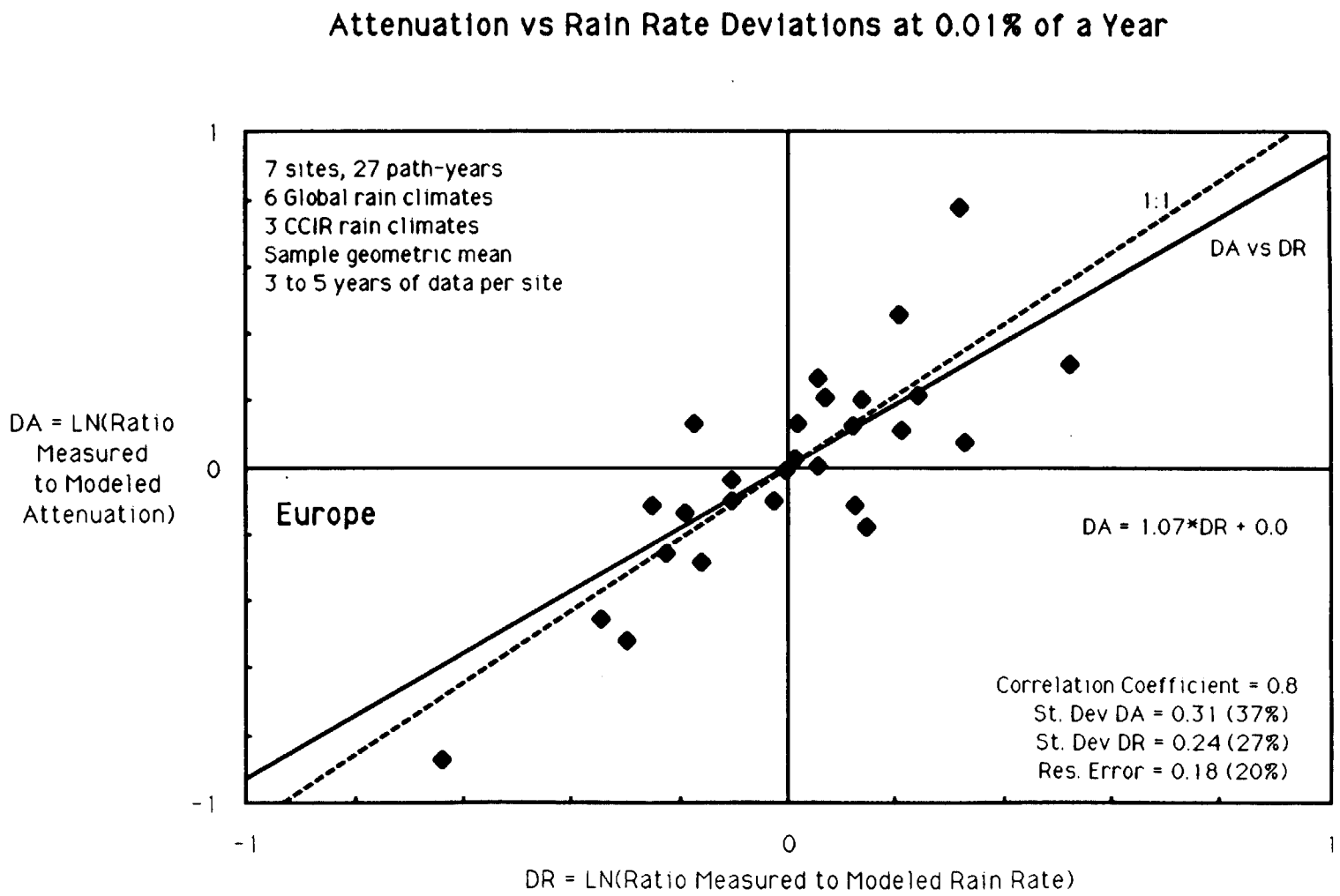

Figure 2 Rain rate and attenuation deviation pairs for sites with three or more single-year sample cumulative distribution functions.

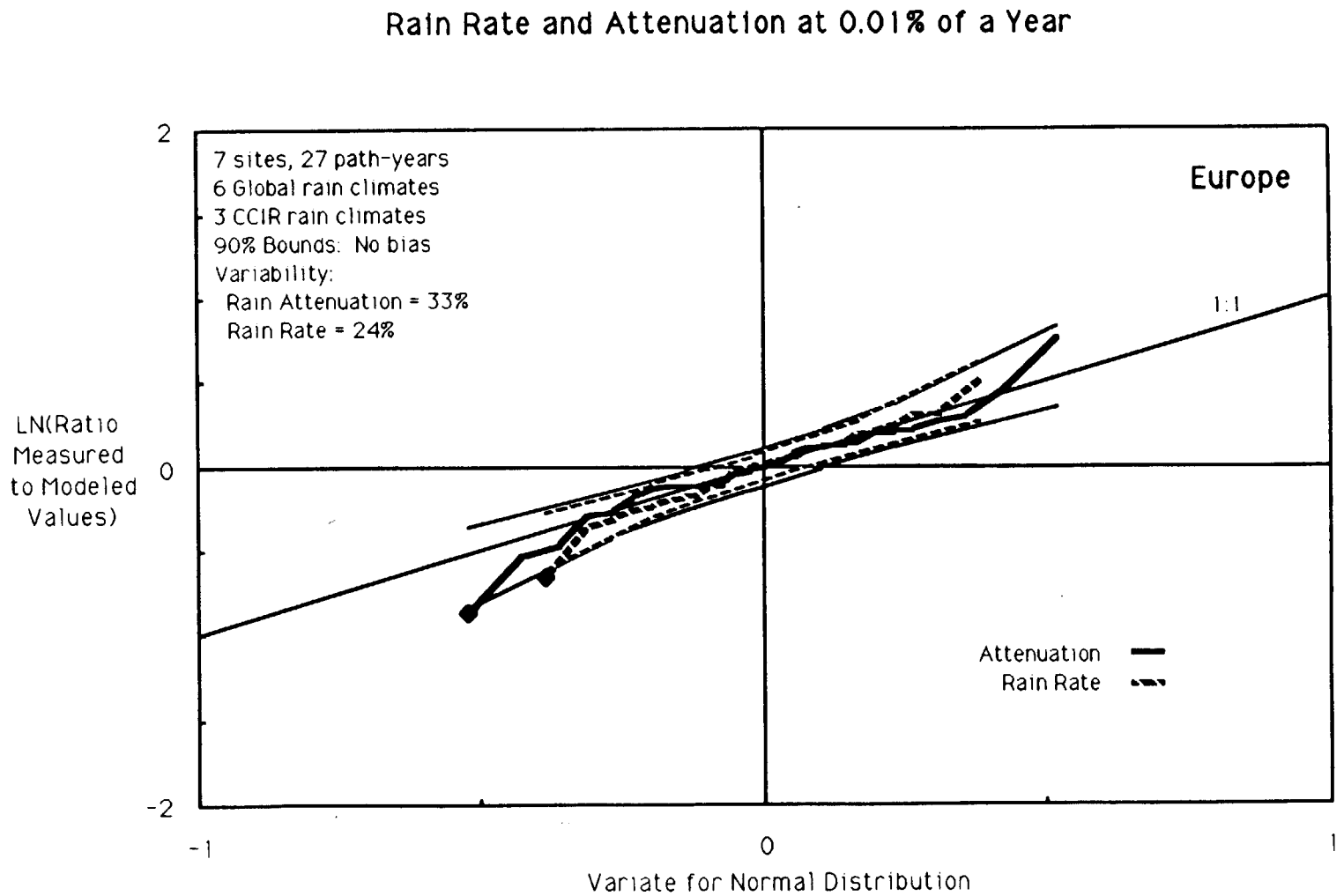

Figure 3 Cumulative distributions of deviations of measured from modeled values at 0.01% of a year for sites with three or more single-year sample cumulative distribution functions.

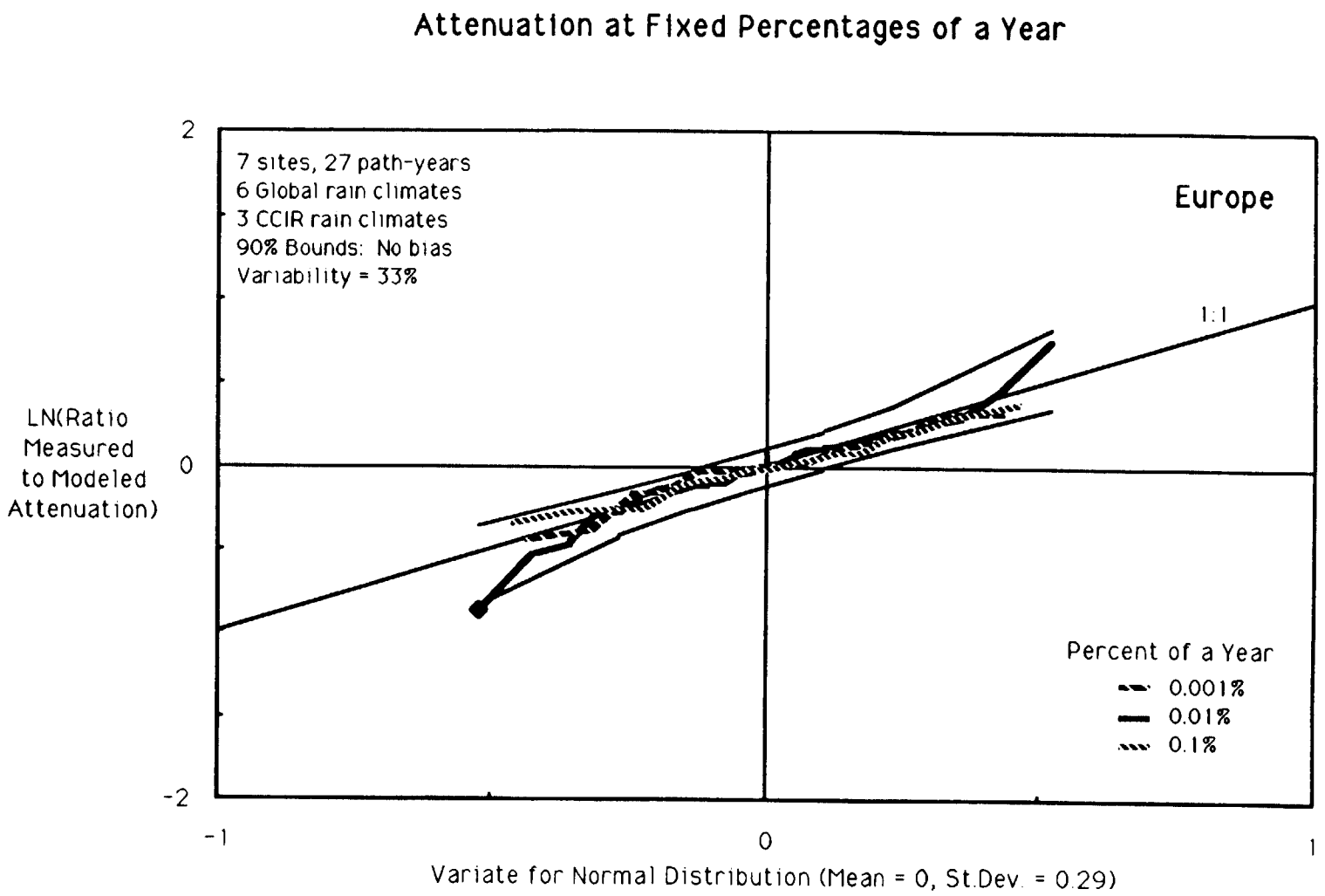

Figure 4 Cumulative distributions of deviations of measured from modeled attenuations for sites with three or more single-year sample cumulative distribution functions.

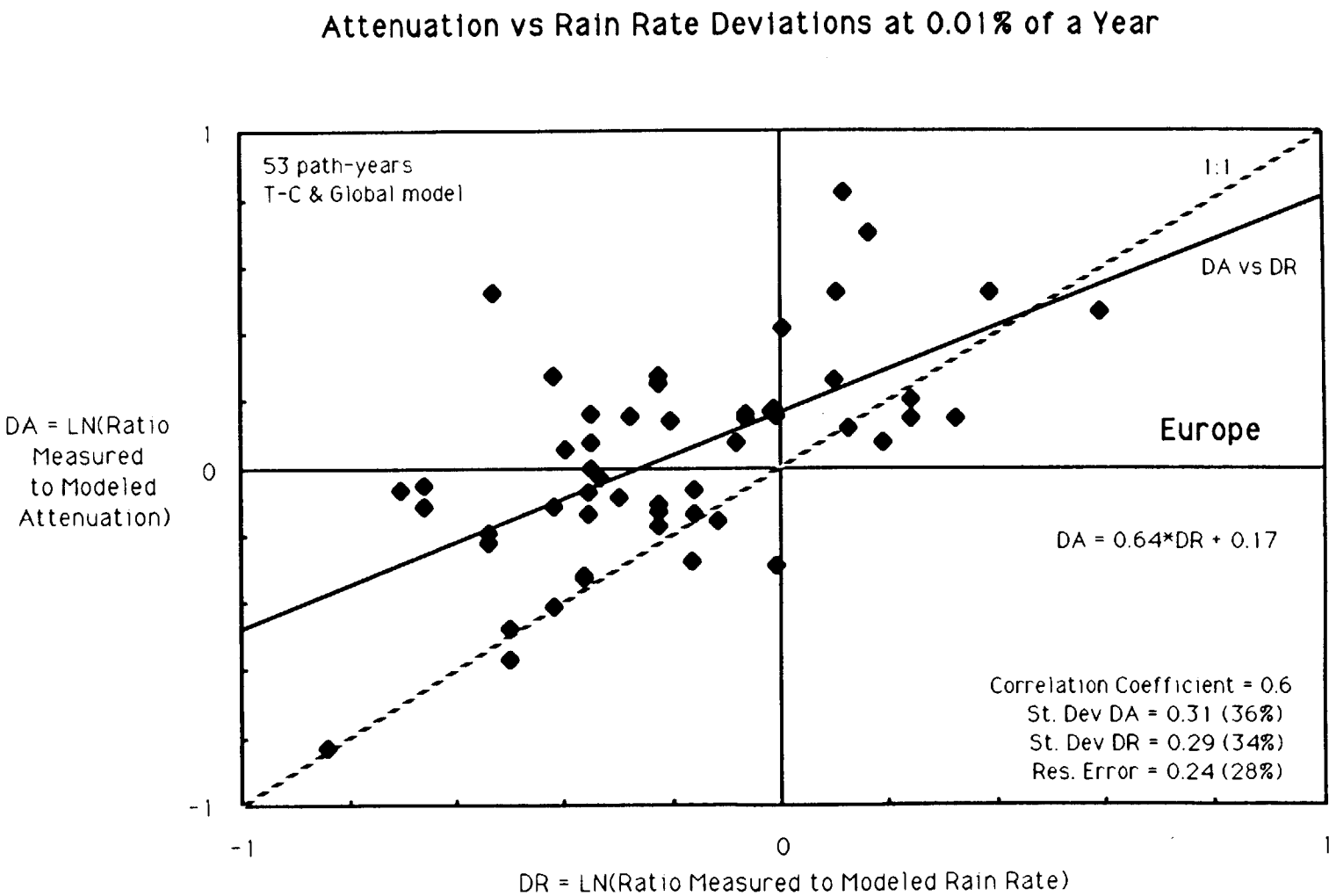

Figure 5 Rain rate and attenuation deviation pairs for single-year sample cumulative distribution functions for European satellite beacon data.

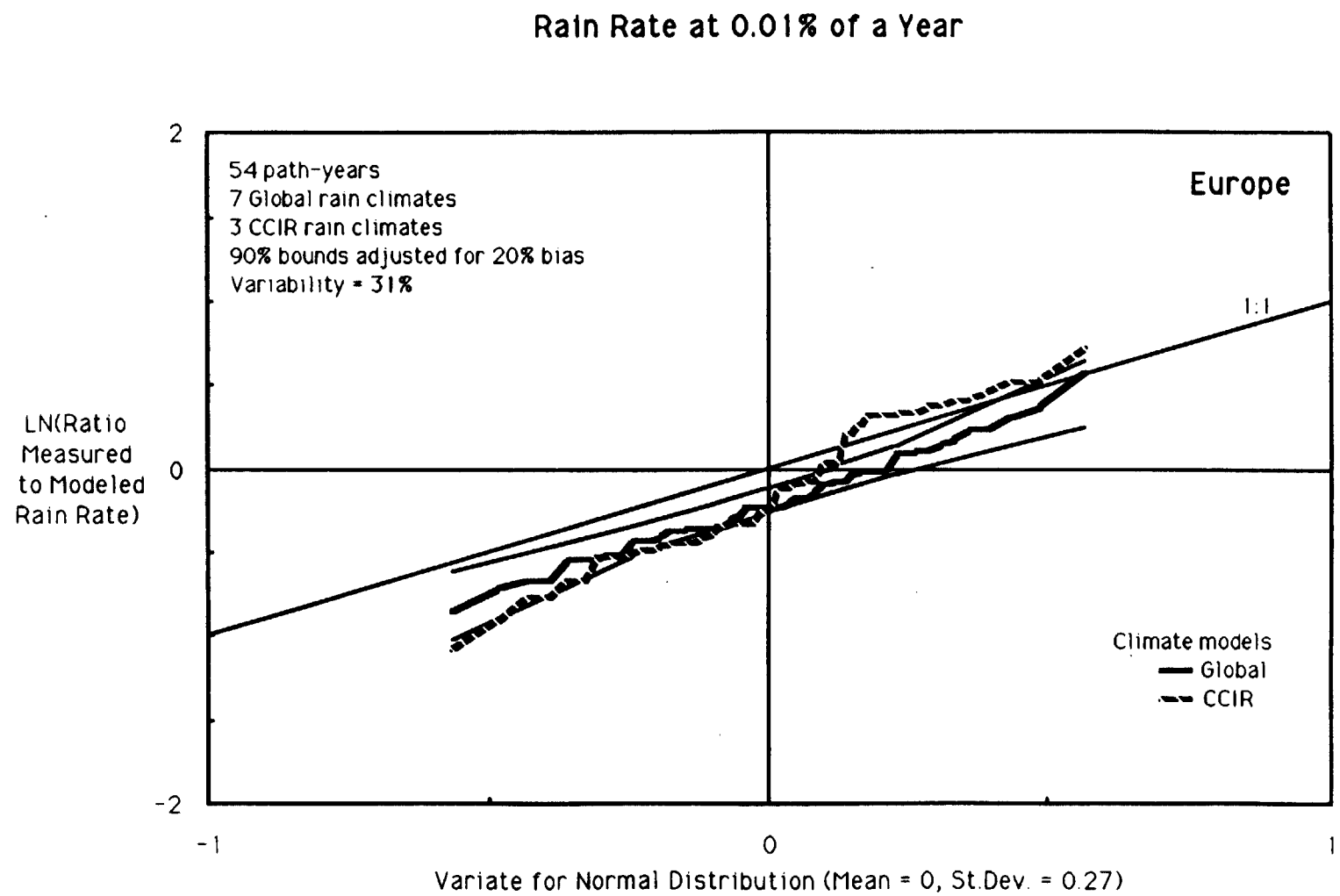

Figure 6 Cumulative distributions of deviations of measured from modeled rain rates at 0.01% of a year for single-year sample cumulative distribution functions for European satellite beacon data.

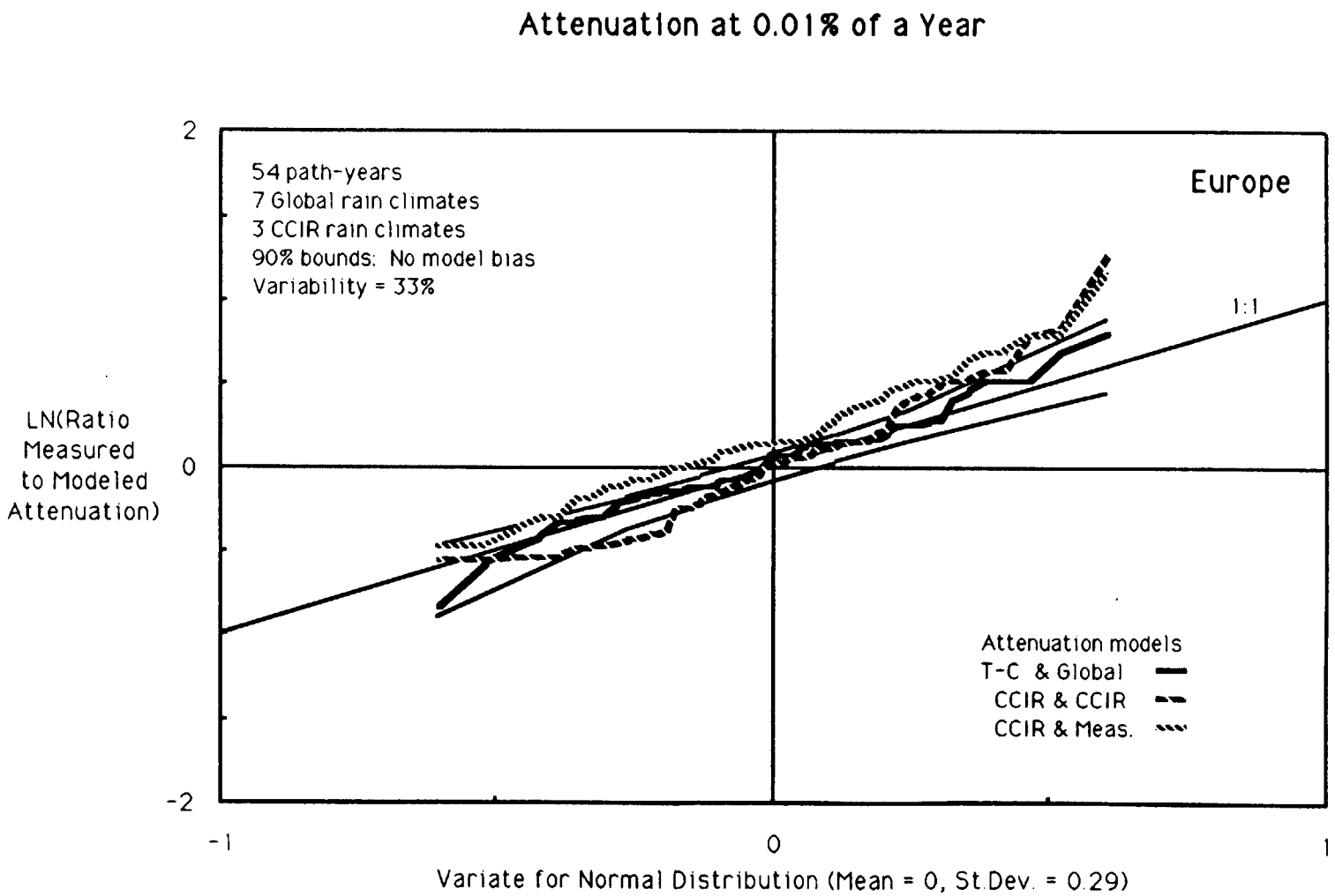

Figure 7 **Cumulative distributions of deviations of measured from modeled attenuation at 0.01% of a year for single-year sample cumulative distribution functions for European satellite beacon data.**

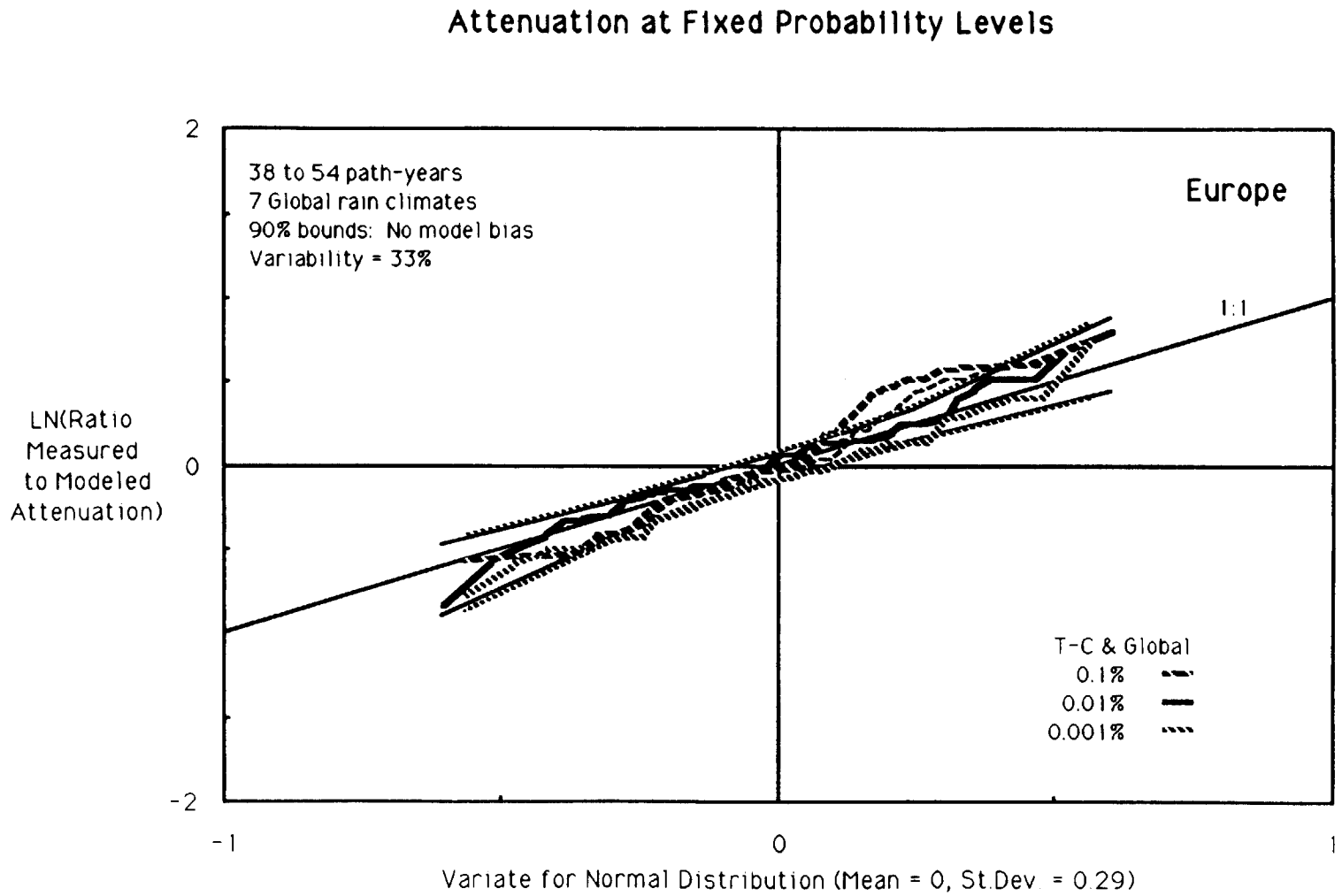

Figure 8 Cumulative distributions of deviations of measured from modeled attenuations at several probability levels for single-year sample cumulative distribution functions for European satellite beacon data.

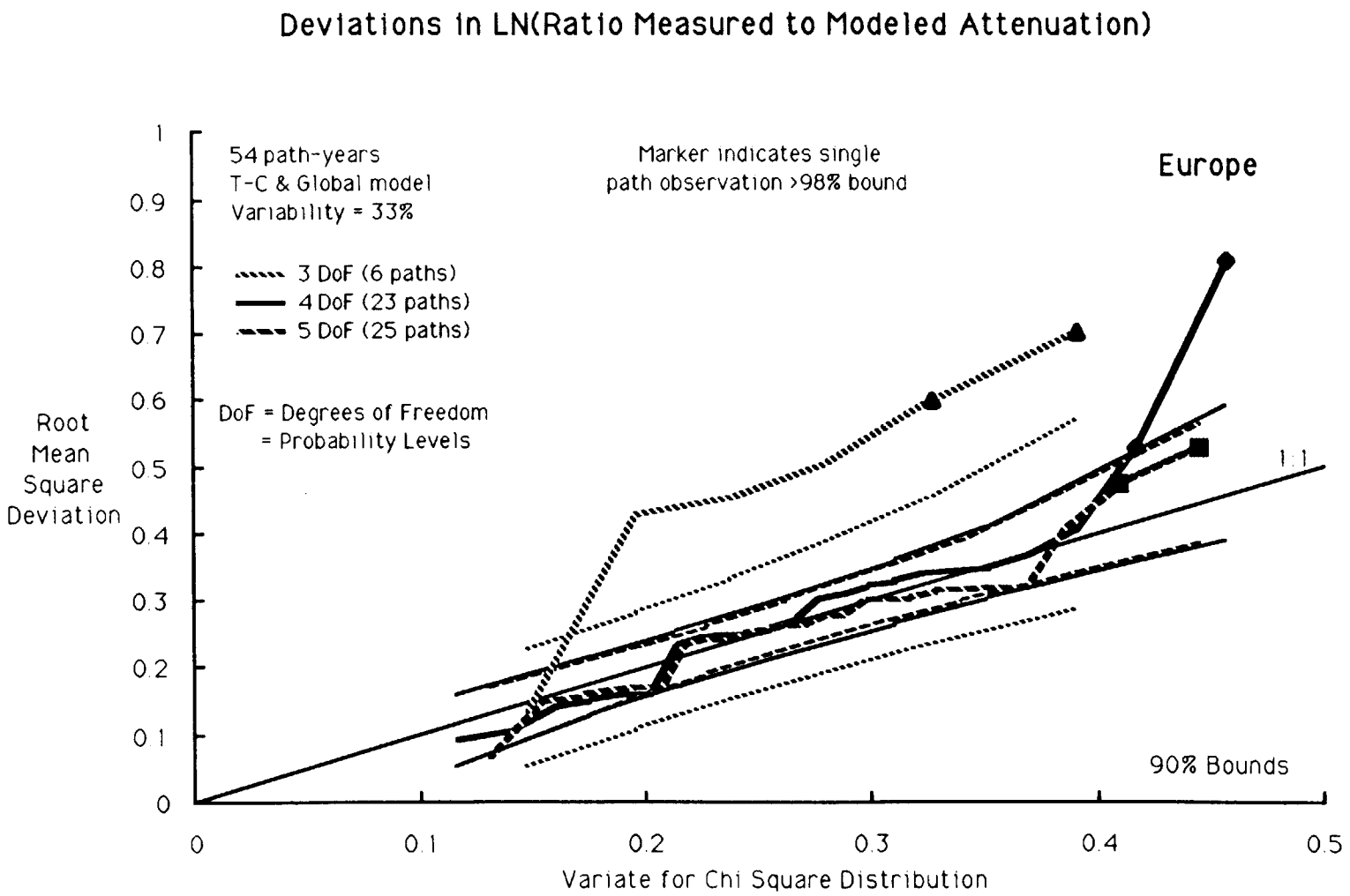

Figure 9 Cumulative distributions of the root mean square deviations of measured from modeled attenuations at several probability levels for single-year sample cumulative distribution functions for European satellite beacon data.

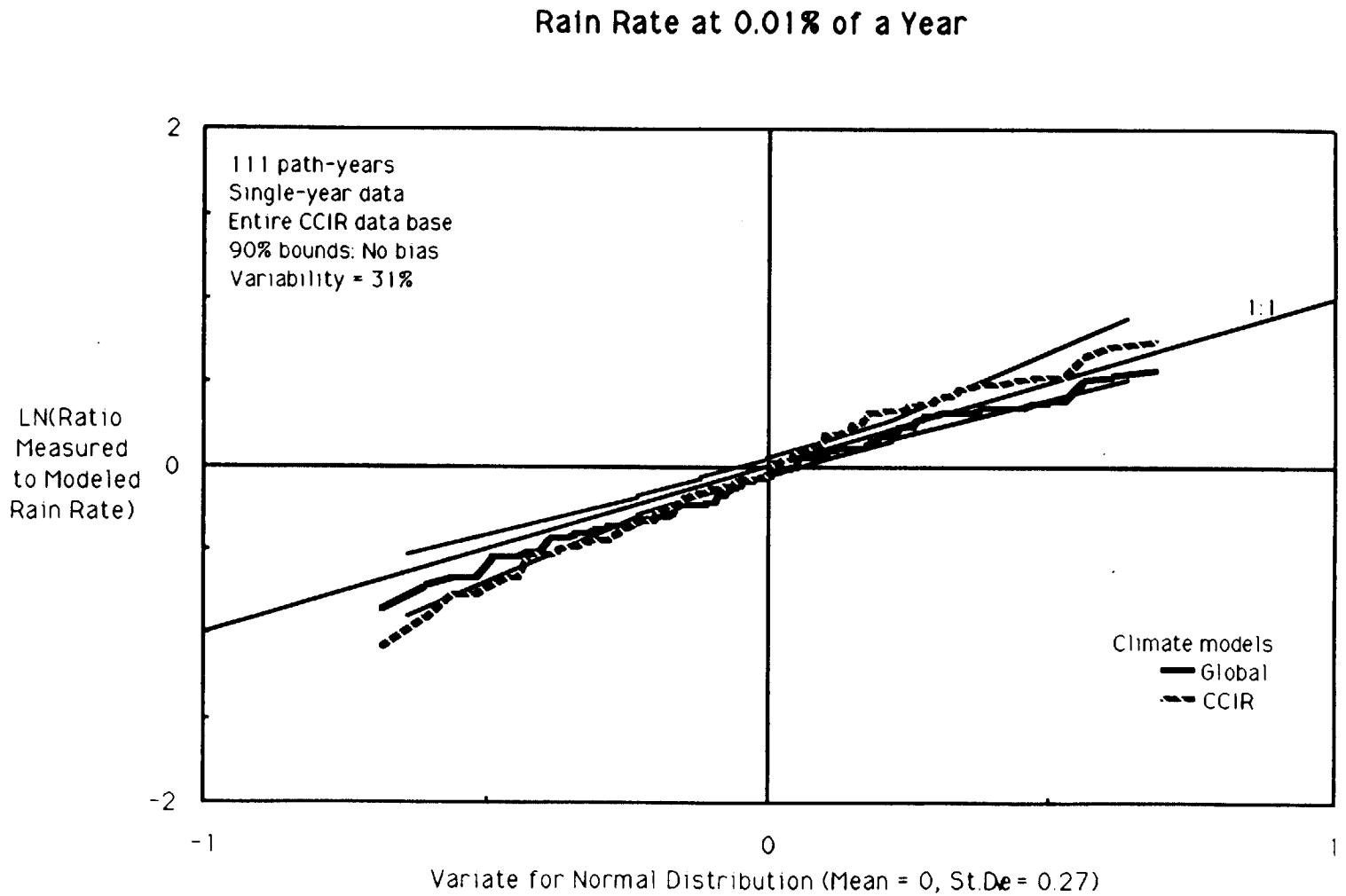

Figure 10 Cumulative distributions of deviations of measured from modeled rain rates at 0.01% of a year for single-year sample cumulative distribution functions for the CCIR data banks.

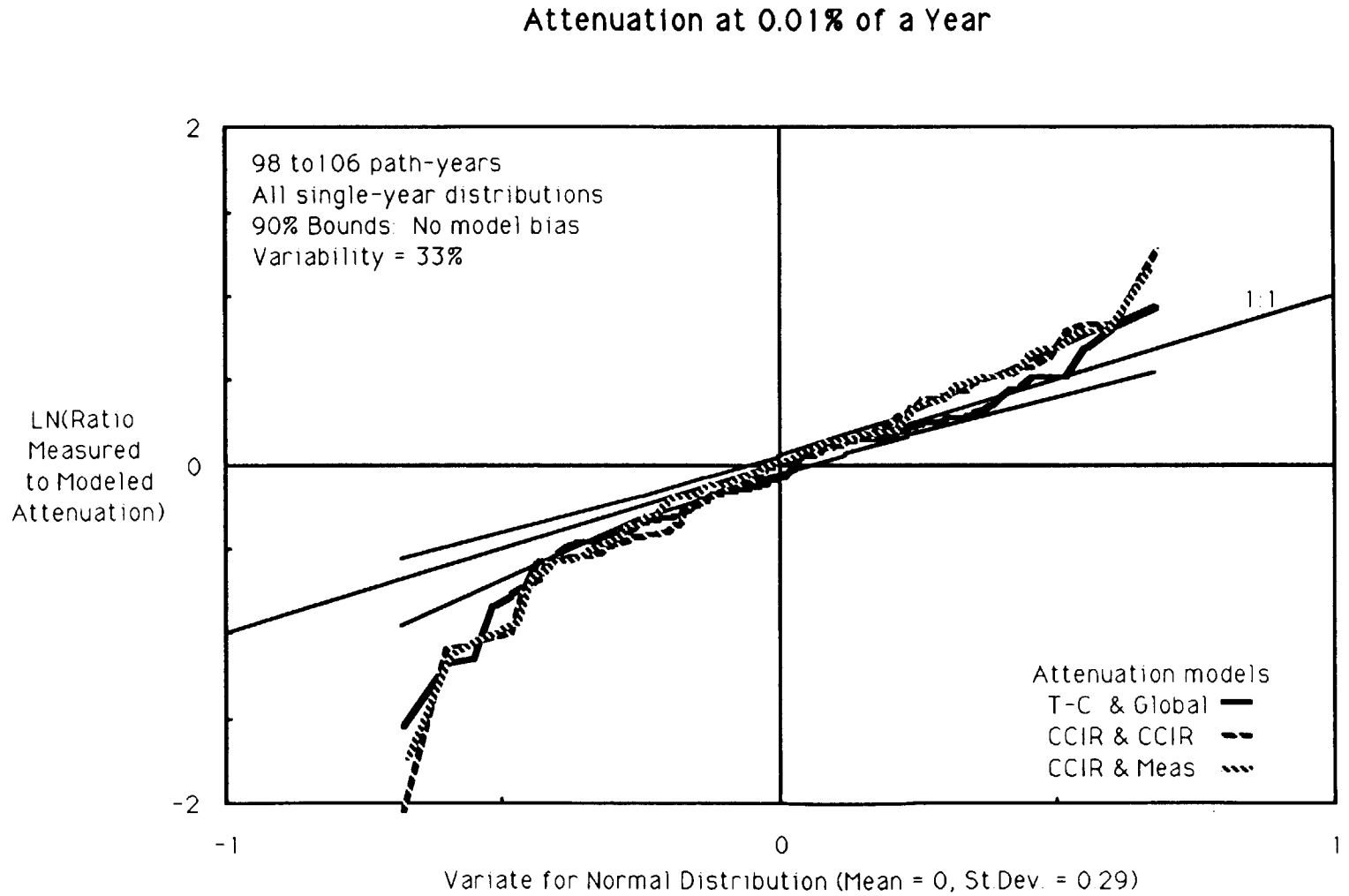

Figure 11 Cumulative distributions of deviations of measured from modeled attenuation at 0.01% of a year for single-year sample cumulative distribution functions for the CCIR data banks.

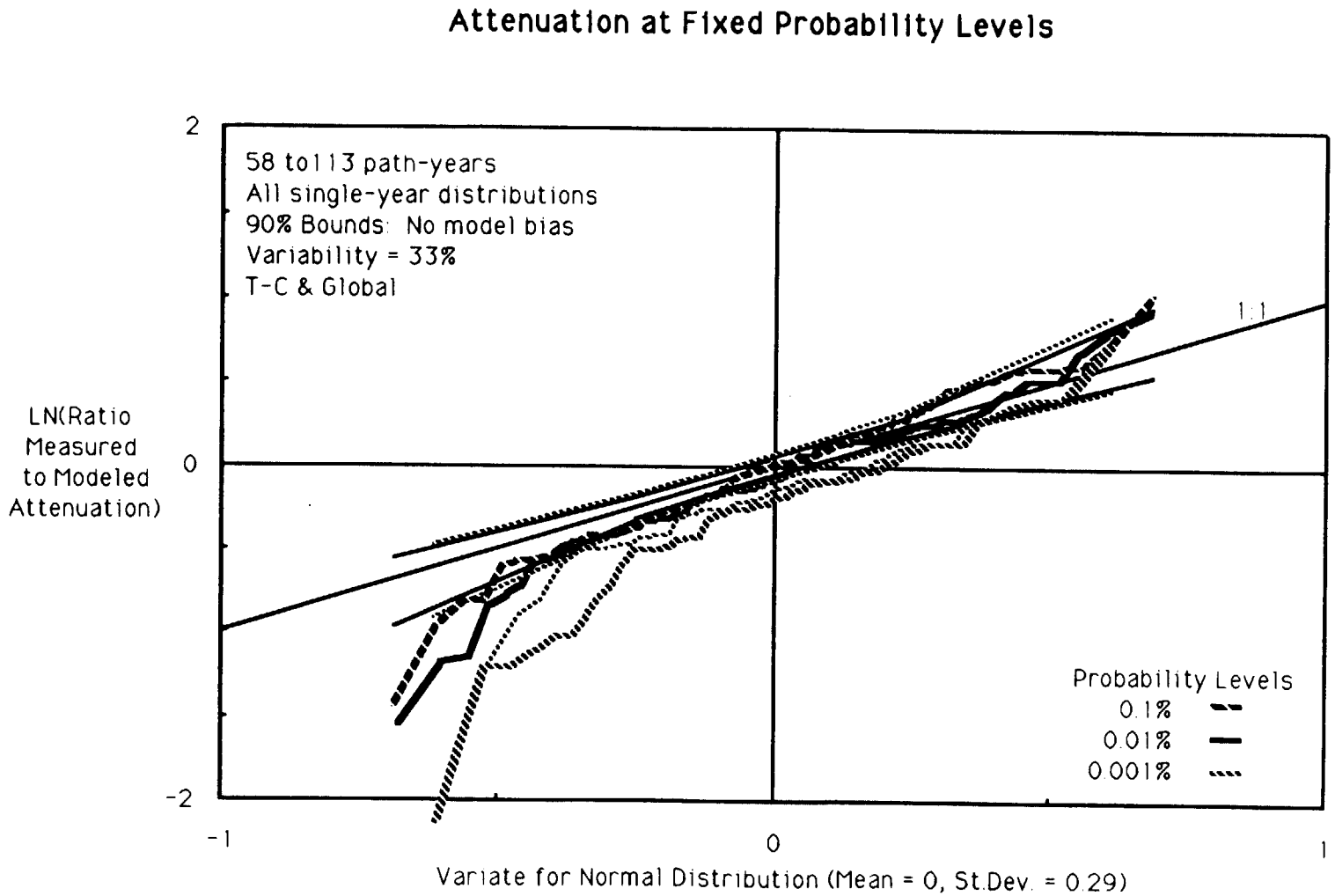

Figure 12 Cumulative distributions of deviations of measured from modeled attenuations at several probability levels for single-year sample cumulative distribution functions for the CCIR data banks.

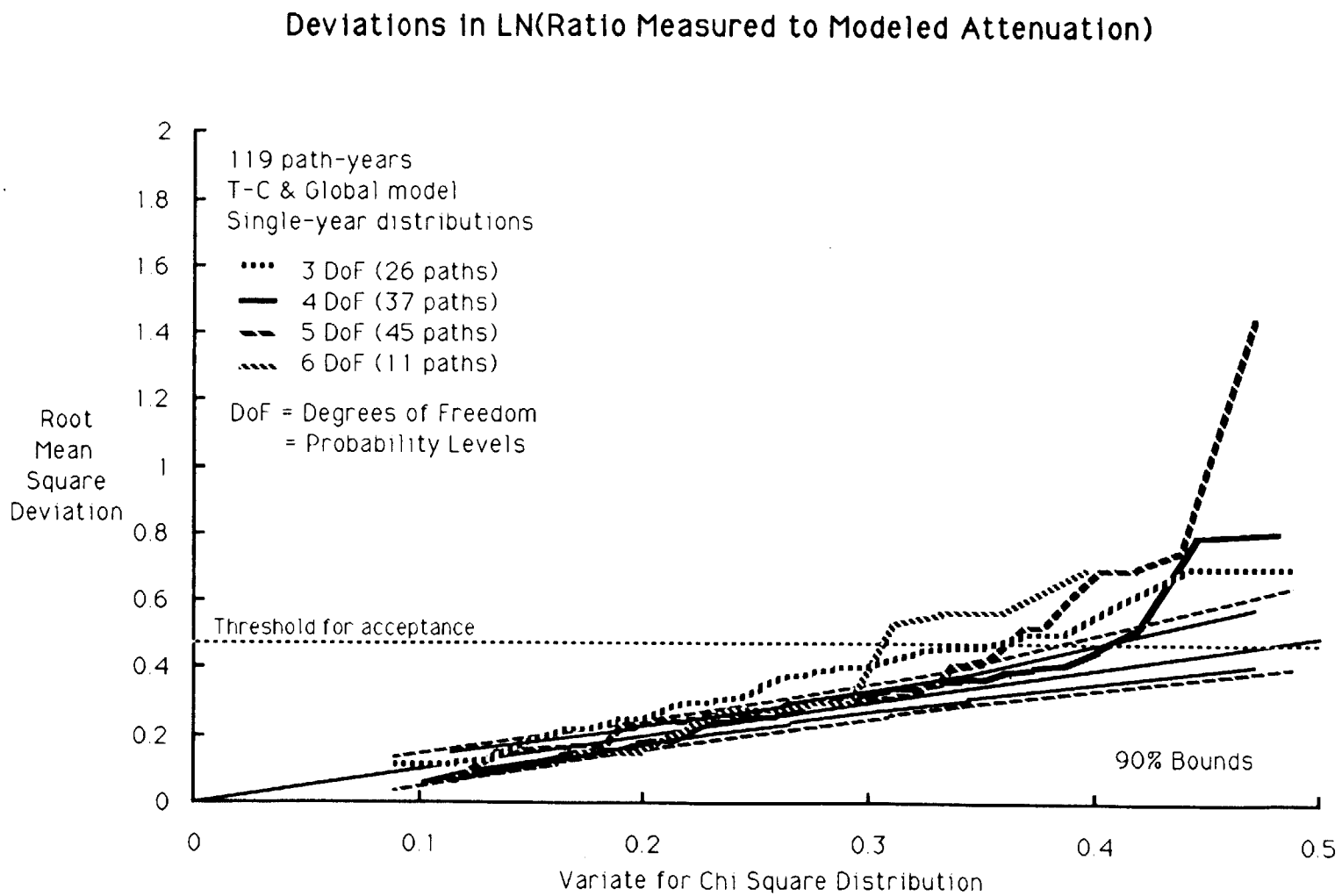

Figure 13 Cumulative distributions of the root mean square deviations of measured from modeled attenuations at several probability levels for single-year sample cumulative distribution functions for the CCIR data banks.

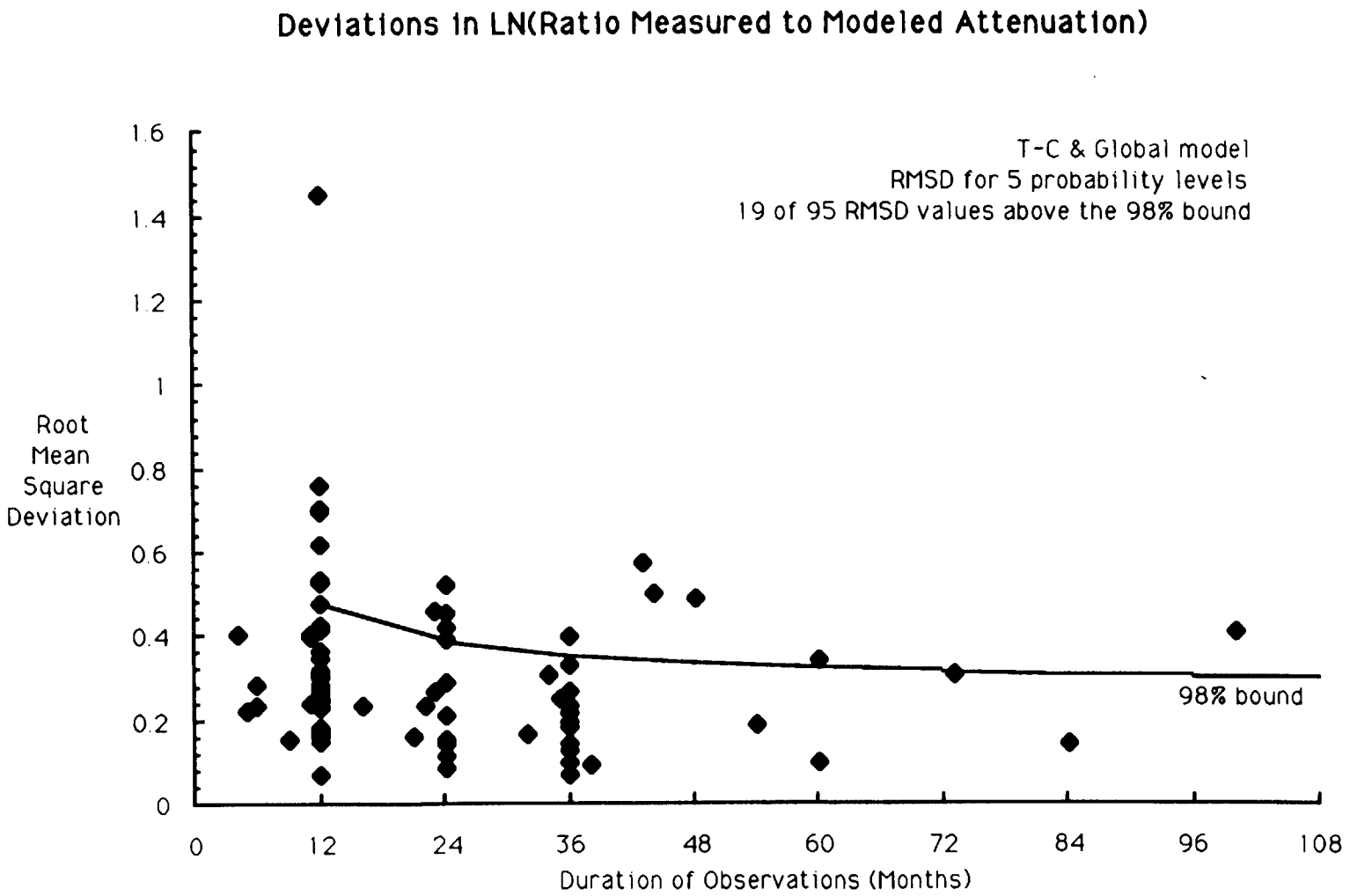

Figure 14 Root mean square attenuation deviations as a function of observation interval.

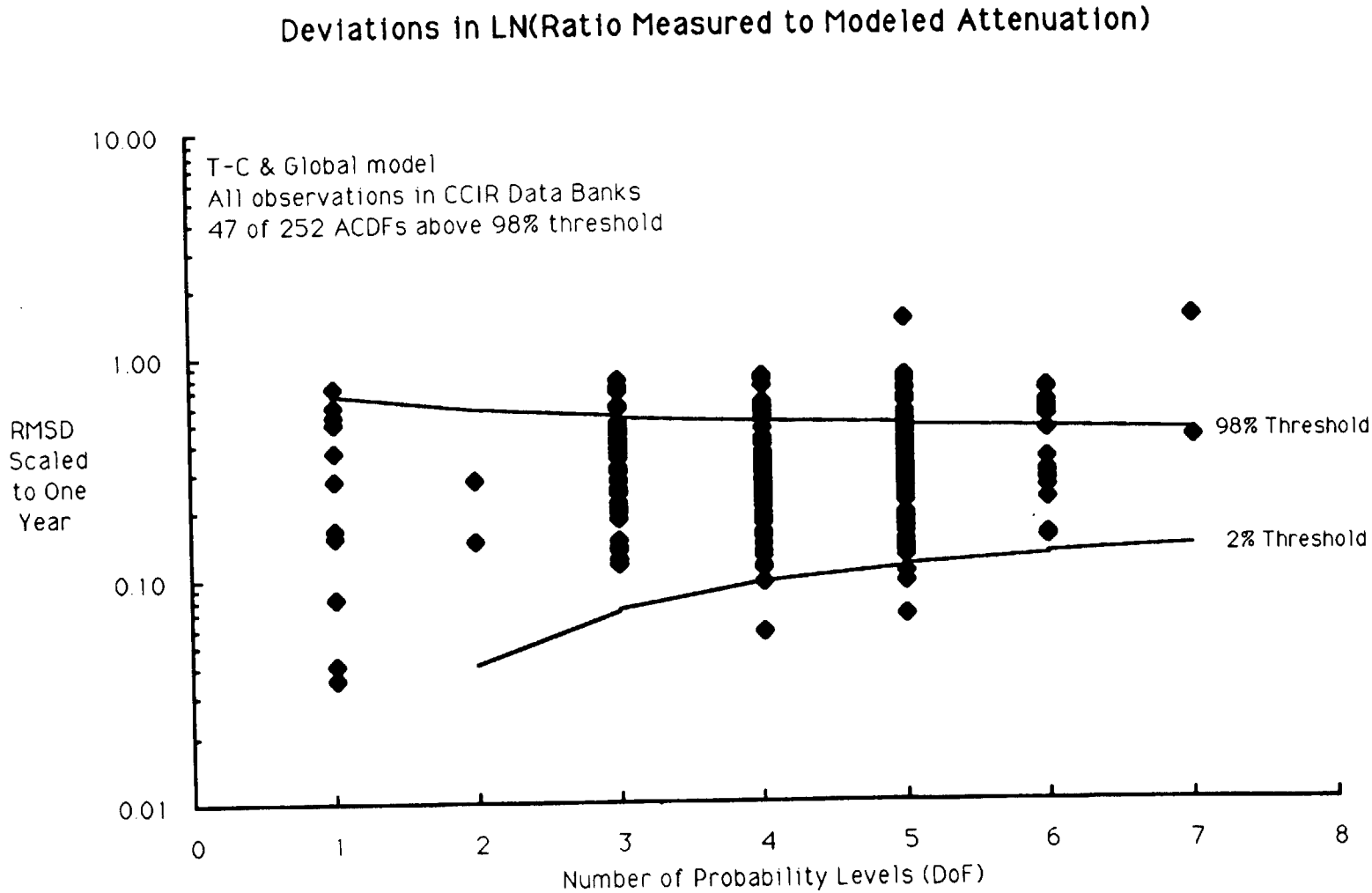

Figure 15 Root mean square attenuation deviations for the entire CCIR data base.

RAIN CORE STRUCTURE STATISTICS DERIVED FROM RADAR AND DISDROMETER MEASUREMENTS IN THE MID-ATLANTIC COAST OF THE U.S.

Julius Goldhirsh, Bert H. Musiani

The Johns Hopkins University, Applied Physics Laboratory, Johns Hopkins Road, Laurel, MD 20707

Abstract

During a period spanning more than 5 years, low elevation radar measurements (PPIs) of rain were systematically obtained in the mid-Atlantic coast of the United States. Drop size distribution measurements with a nearby disdrometer were also acquired during the same rain days. The drop size data were utilized to convert the radar reflectivity factors to estimated rain rates for the respective rain days of operation. Employing high level algorithms to the radar data, core values of rain intensities were identified (peak rainrates), and families of rainrate isopleths were analyzed. In particular, equi-circle diameters of the family of isopleths enveloping peak rain intensities were statistically characterized. The results presented herein represents the analysis (ongoing) of two rain days, 12 radar scans, corresponding to 430 culled rain rate isopleths from an available data base of 22000 contours, approximately 100 scans encompassing 17 rain days. The results presented show trends of the average rain rate versus contour scale dimensions, and cumulative distributions of rain cell dimensions which belong to core families of precipitation.

1. Introduction

The statistics associated with the structure and spacing of rain cells are important to communicators interested in modeling rain attenuation for earth-satellite and terrestrial communications [CCIR, 1986]. Such statistics enable the evaluation of fade margin requirements for both single site and space diversity configurations [Goldhirsh, 1982]. A number of investigators have previously defined rain cell structures in different ways. For example, Crane [1983] characterized a cell as the 3 dB down isopleth of a core value of reflectivity factor. He subsequently related the corresponding area to the area averaged rain rate. Lopez et. al [1984] defined rain cell area by the minimum rain rate contour separating two cores. For the isolated cell case, only the minimum detectable contour values were considered. Konrad [1978] characterized cell areas by the 10 dB down contours from the peak value where the area statistics were equally weighted independent of core values. In addition to the above, this effort differs from previous ones in the following ways: (1) The radar employed has a resolution significantly larger than those used by the other investigators (with the exception of Konrad [1978]), and (2) the previous results were generally expressed in terms of radar reflectivity factors or in terms of rainrates employing fixed empirical relations. This effort incorporated the results of drop size distribution measurements used to convert reflectivity factors to rainrates.

We extend a previous work by Goldhirsh and Musiani [1986] in which 22000 rate isopleths were generated from 100 low elevation azimuthal radar scans and disdrometer measurements encompassing 17 rain days. The radar measurements were made with the high power, high resolution SPANDAR radar at the NASA Wallops Flight Facility, Wallops Island, Virginia. In the previous analysis, the areas of the rainrate isopleths were calculated, and the probability densities and cumulative distributions associated with the equi-circle diameters of the rain rate isopleths were determined; an equi-circle diameter being defined as the diameter of a circle whose area equals the contour area. The previous analysis by the authors did not relate the cell dimensions to "core" rain or "peak" rain intensity levels of rain cells as we do here, but categorized the isopleths according to rainrate levels independently of whether it belonged to high or low core values.

2. Experimental Aspects

2.1 Radar Measurements

The nominal operating parametersof the SPANDAR radar are given in Table 1. Radar measurements of the rain structure were made over contiguous gates of 150 m in range within an annular region from 10 to 100 km from the radar. At a fixed elevation of 0.4^{o}, the azimuthal scan rate was $3^{o}/s$, and a set of radar measurements in range was obtained for approximately each 1^{o} azimuthal interval. The absolute calibration uncertainty of the radar was approximately 1 dB. The power measurements were integrated in real time via an interfacing processor and stored on a 9 track tape recorder for off-line reduction and analysis.

2.2 Disdrometer Measurements

A Rowland disdrometer [1979] was employed to measure the family of drop size distributions during each rain day in which radar data were accumulated. The disdrometer system is an electromechanical sensor comprised of a piezoelectric crystal imbedded in a plexiglass block. The sensor was calibrated such that raindrops of known diameters falling at terminal velocity on the sensor head generated unique voltages at the output of the crystal. These voltages were fed through an analog to digital converter, stored on magnetic tape, and analysed. Scatter plots of rain rate R (mm/h) versus radar reflectivity factor Z (mm^6/m^3) were generated for each rain day where each point on the scatter plot represented the acquisition of 1000 rain drops from which a single calculation was made of R and Z. Typically, scatter plots consisted of more than 100 distributions and sampling periods ranged from one to two hours. Least square R - Z regression relations were calculated having the form $R = a Z^b$ from which values of a and b were generated for each rain day.

In Table 2 is a listing of these disdrometer least square fit power relations for each of the 17 rain days in which disdrometer data were acquired. The rainrate standard errors were found to range between 14% and 40% with an overall average of 24%. The radar measured reflectivities for each of the rain days were converted to rainrates employing the best fit values a and b in Table 2. These relationships are plotted in Figure 1 as a demonstration of the variability of the R-Z relations in the mid-Atlantic

coast geographic region over which the measurements were made. We note that at $Z = 10^5$ mm^6/m^3, the span of rain rates range from $R \approx 1.5$ to 4 mm/h. At $Z = 10^5$ mm^6/m^3, R ranges from 40 to 100 m/h. It is interesting to note that the R-Z relation of Marshall-Palmer [1949] given by $R \approx .0365\ Z^{0.625}$ is bounded by the family of distributions in Figure 1 and results in R = 2.7 and 48.7 mm/h at $Z = 10^3$ and 10^5 mm^6/m^3, respectively.

3. Contour Levels

3.1 Method of Construction

As mentioned, a set of reflectivity levels were originally determined for approximately every 1^o in azimuth and 150 m in range. To mitigate the effects of noisy data, the reflectivity factors over three range bins were averaged. As mentioned, they were converted to rain rates using the measured relationships given in Table 2. The corresponding rain rates were subsequently mapped onto an X-Y grid indicating the east-west and north-south distance locations relative to the SPANDAR radar. They were then binned over rainrate intervals defined by the "Level Numbers (LN)" in Table 3. An algorithm was implemented which did the following: (a) identified contiguous values of LN, (b) connected a line between the contiguous values of LN, and (c) recognized when the line closed upon itself to establish a closed contour.

A second algorithm was developed which identified clusters of rain rate isopleths which enveloped "core" rainrates. Those isopleths which identified the same core value were grouped into a family of contours and are referred to as a "core family". For each isopleth belonging to a core family, the area, centroid location, maximum and minimum lengths from the centroid to each respective contour, and core orientation (angles relative to north in which the maximum and minimum lengths are directed) were determined. The core family characteristics were then grouped in terms of their core levels (peak rainrates) for statistical analysis. As an example, we show in Figure 2 a complex set contours in the south-west quadrant belonging to core families whose exterior are at levels 5 and greater. These contours were derived from radar measurements made on February 17, 1983. In Figure 3, we have zoomed in on a family of contours associated with the core level LN = 9 (32 - 43 mm/h) whose core centroid is located at approximately X = - 43.5 km, Y = - 28.5 km relative to the radar (see arrow in Figure 2).

3.2 Data Base

In Table 4 are summarized the data bases available for analysis. The data covers an approximate five and one half year period encompassing 17 rain days and all seasons. Approximately 100 scans (PPIs) are available for analysis over which more than 22000 closed contours require culling. As of this writing, the statistics associated with 430 culled contours have been reduced and analyzed. These data encompass the rain days January 2, 1979 and February 17, 1983 and correspond to 12 radar scans. The effort is continuing with the goal to analyze the full data base.

4. Results

In Figure 4 are shown conditional cumulative distributions for a family of contours corresponding to the peak rain rate for LN = 7. These statistics address the question, "Given rain rate isopleths belonging to a core value of LN = 7 (18 - 24 mm/h), what is the probability that the isopleths have equi-circle diameters which exceed given values?" Only contours of level 5 and greater are considered in this analysis due to excessive computer times at the smaller levels. Furthermore, only contours with rainrates which monotonically increase (or are constant) within each contour were considered in the determination of the statistics. We note (Figure 4) that the distributions have approximate exponential shapes for diameters greater than 1 km. Families of distributions have also been determined for core levels 8 and 9 (not shown) showing similar exponential decrease in probability with increasing diameter. In Figure 5 is shown a family of curves depicting the average equi-circle diameters (ordinates) for core level numbers ranging from 7 to 11. The abscissa represents the center rainrates in the intervals defined in Table 3.

5. Summary and Conclusions

The results presented herein provide rain cell structure information for modelers of slant path attenuation interested in the attenuation effects of precipitation for earth-satellite or terrestrial communication configurations operating at frequencies above 10 GHz. The developed algorithms enable the grouping of families of rainrate isopleths belonging to core values of rain intensities. Preliminary analyses for two rain days show well defined trends in the contour diameter cumulative distributions and average equi-cell diameter variations with rainrate. It is observed in Figure 5 that core rainrates with greater intensities contain significantly more structure and larger cell diameters than cells having lower core rainrates. The overall average equi-circle diameter for each core family with good approximation linearly decreases with increasing rainrate over the indicated range of values. For diameters greater than 1 km, the cumulative probability distributions of contour diameters exponentially reduce with increasing diameter (Figure 4). The exponential decay in the cumulative distributions is consistent with the cell results of Goldhirsh and Musiani [1979] for the combined cell diameter case.

6. Acknowledgements

The authors are grateful Norman Gebo, Norris Beasley and George Bishop for assisting in acquiring the radar and disdrometer data base at the NASA Wallops Flight Facility at Wallops Island, VA. This work was supported by the Communications Division of NASA Headquarters under contract to APL # N00039-89-C-5301.

References

CCIR (International Radio Consultative Committee), "Recommendations and Reports of the CCIR, 1986", Propagation in Non-Ionized Media, Vol V, XVIth Plenary Assembly, Dubrovnk, 1986.

Crane, R. K, "An Analysis of Radar Data to Obtain Storm Cell Sizes, Shapes and Spacings, "Thayer School of Engineering, Dartmourth College, Hanover, NH, Tech Rep, Apr, 1983.

Goldhirsh, J., "Space Diversity Performance Prediction for Earth-Satellite Paths Using Radar Modeling Techniques", Radio Science, Vol 17, No. 6, pp 1400-1410, Nov- Dec, 1982.

Goldhirsh, J., and B. Musiani, "Rain Cell Size Statistics Derived from Radar Observations at Wallops Island, Virginia", IEEE Transactions on Geoscience and Remote Sensing, Vol GE-24, No. 6, November, pp 947 - 954, 1986.

Konrad, T. G., "Statistical Models of Summer Rainshowers Derived from Fine Scale Radar Observations", J. Applied Meteorology, Vol 17, No 2, pp 171 - 188, Feb., 1978

Lopez, R. E., D. O. Blanchard, D. Rosenfield, W. L. Hiscox and M. J. Casey, "Population Characteristics, Development Processes and Structure of Radar Echoes in South Florida", Monthly Weather Rev., Vol 112, pp 56 - 75, Jan., 1984.

Marshall, J. S. and W. McK. Palmer, "The Distribution of Raindrops with Size", J. Meteorology, Vol 6, pp 243-248, 1949.

Rowland, J. R., "Comparison of Two Different Raindrop Disdrometers", Proc. 17th Radar Meteor. Conf, Seattle, WA, Oct. 26-29, pp398-405, 1979.

Table 1
Nominal Radar Parameters for SPANDAR

Radar Location	Lat = 37^{o}_{o} 51' 16.8" N
	Long = 75 30' 48.4" W
Radar Name	SPANDAR (FPS 18)
Peak Power	1 megawatt
Center Frequency	2.84 GHz
Diameter of Dish	18.3 m
Gain	50.6 dB
Beamwidth	0.4^{o}
Pulse Width	1 μsec
Range Resolution	150 m
Prf	320 Hz
Freq Diversity:	
# of Steps	24
Step Size	> 11 MHz
Polarization	Vertical
# of Samples	128
Sampling Time	0.4 sec
# of Gates	871
Calib Error	+/- 1 dB

Table 2

Listing of Disdrometer Derived Best Fit $R = aZ^b$ Parameters where [R] = mm/h and [Z] = mm^6/m^3 (Julian days indicated in parentheses)

Day	a	b	% SE
6/6/77 (157)	7.03×10^{-3}	0.812	24.6
6/9/77 (160)	6.20×10^{-2}	0.566	24.8
8/24-25/77 (236)	9.73×10^{-3}	0.780	29.0
9/14/77 (257)	3.68×10^{-2}	0.655	17.8
11/27/78 (331)	5.71×10^{-2}	0.572	29.8
1/2/79 (002)	4.0×10^{-3}	0.86	30.0
1/24/79 (024)	4.52×10^{-2}	0.644	26.1
3/6/79 (065)	1.90×10^{-2}	0.751	39.7
4/4/79 (094)	3.15×10^{-2}	0.676	18.9
5/31/79 (151)	7.86×10^{-3}	0.767	19.8
6/11/79 (162)	3.26×10^{-2}	0.615	22.9
9/5/79 (248)	7.235×10^{-3}	0.796	--
3/14/80 (073)	7.41×10^{-2}	0.566	24.1
4/10/80 (100)	1.79×10^{-2}	0.674	28.5
4/15/80 (105)	3.85×10^{-2}	0.604	14.2
11/15/83 (319)	1.65×10^{-2}	0.739	17.4
2/17/83 (048)	3.6×10^{-2}	0.625	19.4

Table 3

Contour Level Numbers (LN), Corresponding Rainrate and Nominal (MP) dBZ Intervals

Contour Level # LN	Rain Rate Interval (mm/hr)	Nominal dBZ Interval
0	>.5	>18
1	0.5-1	18-23
2	1-2	23-28
3	2-4	28-33
4	4-8	33-37
5	8-12	37-40
6	12-18	40-43
7	18-24	43-45
8	24-32	45-47
9	32-42	47-49
10	42-56	49-51
11	56-75	51-53
12	75-100	53-55
13	100-133	55-57
14	133-205	57-60
15	>205	>60

Table 4

Data Base Available for Analysis

Number of Rain Days	17
Winter	6
Spring	6
Summer	3
Fall	2
Number of Scans (PPIs)	96
Number of Total Contour	22,308

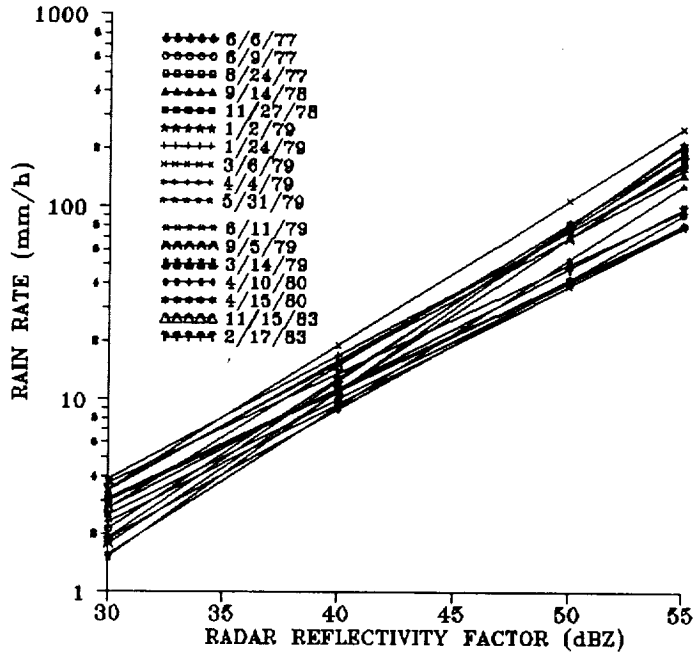

Figure 1 Family of disdrometer derived R-Z relations where each curve represents a different rain day (Table 2).

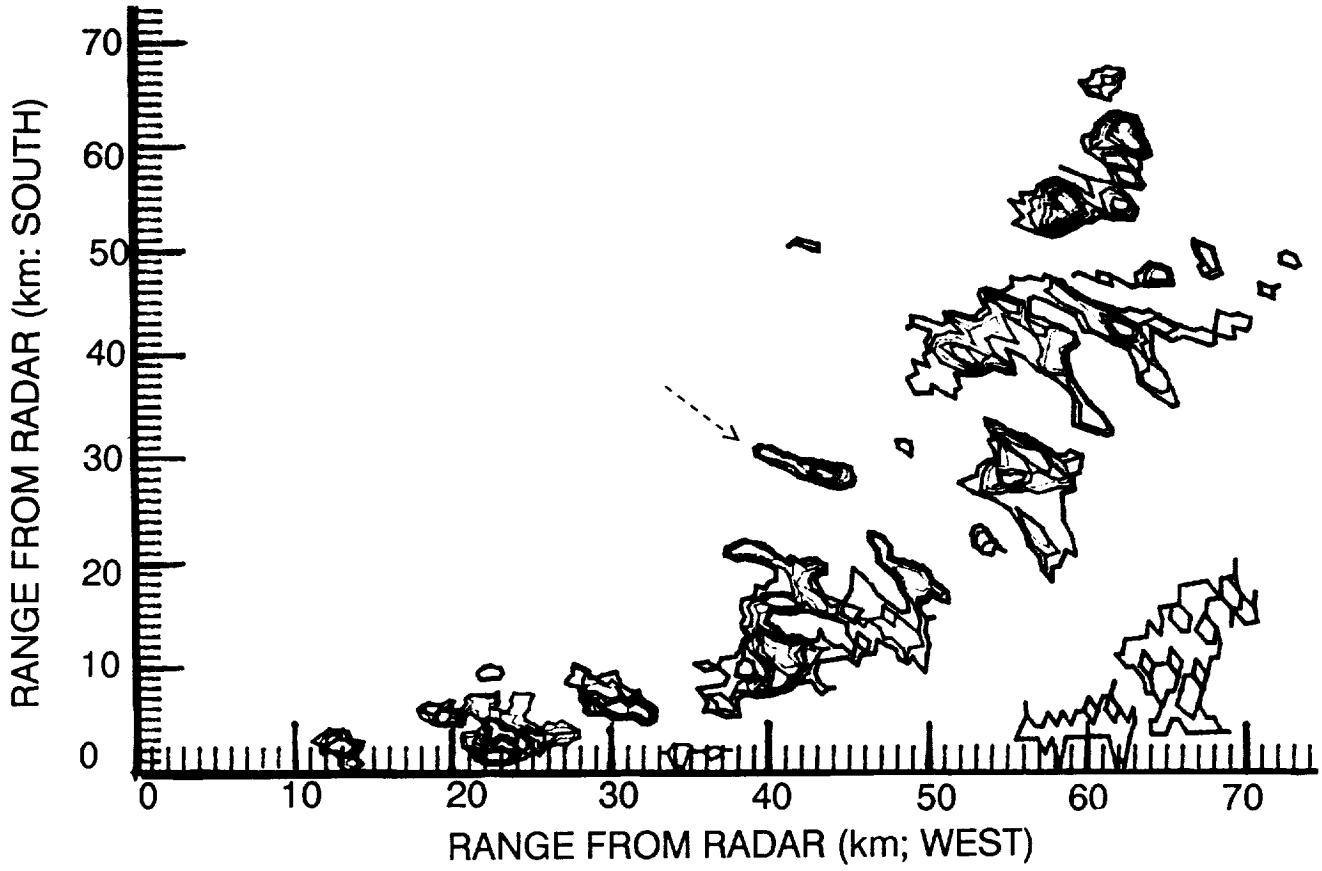

Figure 2 Rainrate isopleths belonging to core cells in the southwest quadrant of a radar scan on February 17, 1983. Exterior isopleths are level 5 or greater.

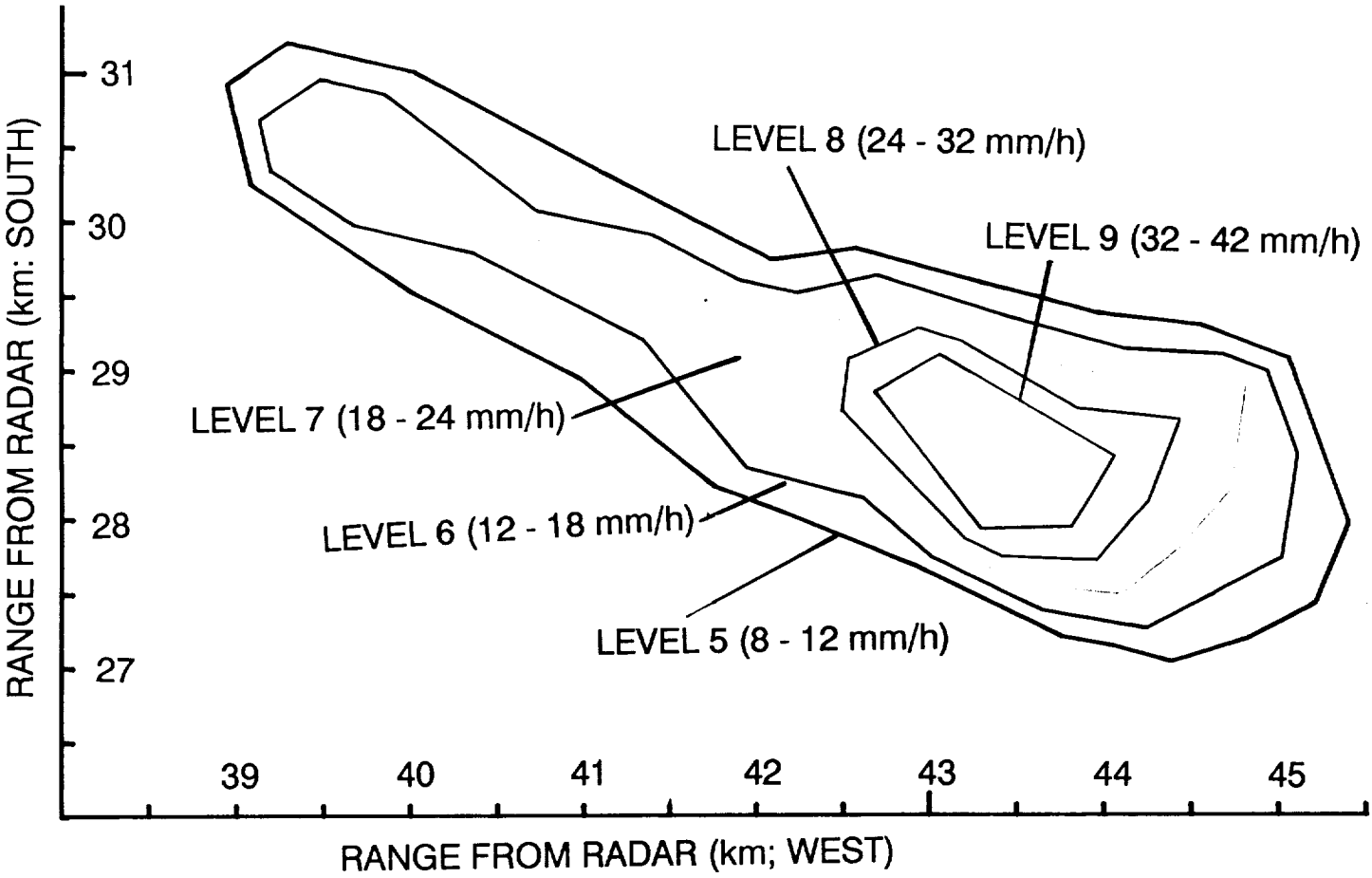

Figure 3 Zoomed in contour family of isopleths belonging to the core cell LN = 9 at X = -43.5 km, Y = -28.5 km (Figure 2).

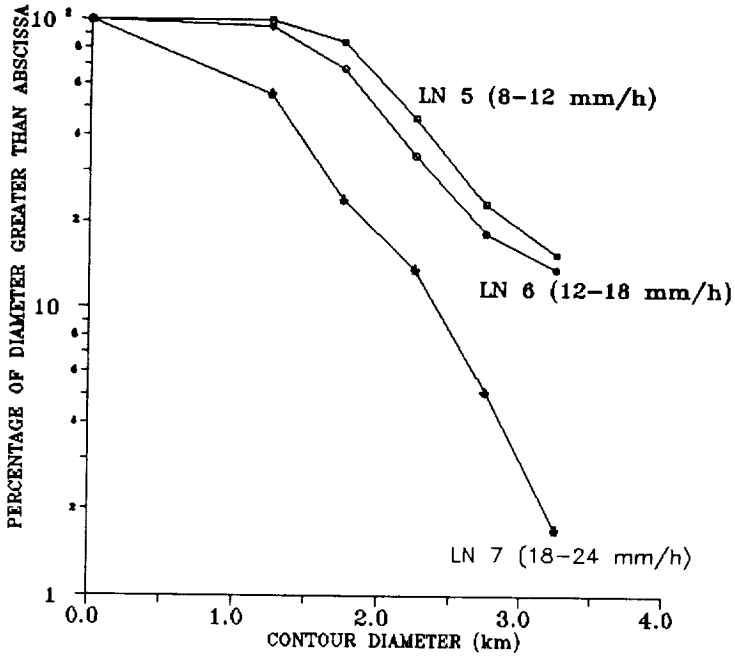

Figure 4

Cumulative distributions for the isopleths belonging to the core family LN = 7.

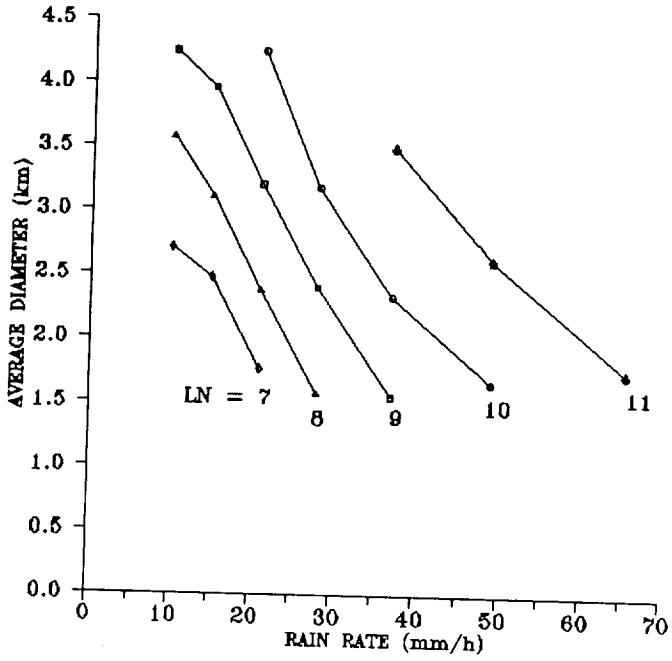

Figure 5

Average diameter versus center rainrates for core families in the level range LN = 7 to 11 (Table 3).

OBSERVATIONS OF ATTENUATION AT 20.6, 31.65 AND 90.0 GHz - PRELIMINARY RESULTS FROM WALLOPS ISLAND, VA

J. B. Snider, M. D. Jacobson, and R. H. Beeler
NOAA/ERL/Wave Propagation Laboratory

Abstract - Ground-based radiometric observations of atmospheric attenuation at 20.6, 31.65 and 90.0 GHz were made at Wallops Island, VA during April and May 1989. Early results from the analysis of the data set are compared with previous observations from California and Colorado. The relative attenuation ratios observed at each frequency during clear, cloudy, and rainy conditions are shown. Plans for complete analysis of the data are described.

1. Introduction

During 1987 and 1988 the NOAA/ERL/Wave Propagation Laboratory (WPL) transportable three-channel ground-based radiometer measured atmospheric attenuation at 20.6, 31.65, and 90.0 GHz at San Nicolas Island, CA (July 1987) and Denver, CO (December 1987 and August 1988). From April 11 to May 8, 1989, additional measurements were made at Wallops Island, VA (hereafter referred to as Wallops for brevity). Because of the relatively short time between observations and the June 1989 NASA Propagation Experimenters (NAPEX) meeting, and because all supporting data have not yet been made available, the material presented in this paper is preliminary and incomplete. However, since both the quality and the variety of the data collected at Wallops were exceptional, it is desirable to present some early results.

2. Description of Experiment

The observations at Wallops were made in conjunction with an experiment designed to investigate the measurement of atmospheric moisture by an array of ground-based remote sensors and in situ balloon-borne humidity sensors. The experiment, ATmospheric Moisture Intercomparison Study (ATMIS), was conducted primarily during the nighttime hours from April 11 to April 18. The organizing agency for ATMIS was NASA/Goddard.

During ATMIS, joint observations of water vapor were made simultaneously by radiometers operated by Jet Propulsion Laboratory (JPL), NASA/Goddard, Pennsylvania State University (Penn State), and WPL, and by an ultraviolet lidar operated by NASA/Goddard. In addition, when clouds were present, simultaneous observations were made by the SPANDAR radar operated by the Applied Physics Laboratory of Johns Hopkins University. Supporting data consisted of several radiosondes daily, each equipped with three different types of humidity sensor, and a lidar ceilometer and multi-beam

Doppler acoustic sounder, both owned and operated by Penn State. During the week of the ATMIS, and for the following three weeks, the WPL radiometer operated mostly in the zenith direction providing both water vapor data and atmospheric attenuation data. However, on a few occasions the system was employed in an azimuthal scan mode to make joint observations with other radiometers having scan capability to determine the homogeneity of the water vapor field. Other brief interruptions of the attenuation measurements were necessary for instrument calibration. Approximately 570 hours of attenuation data were collected by the WPL system.

Procedures employed by the WPL microwave radiometer in the measurement of atmospheric attenuation have been described at previous NAPEX meetings and in the literature (Westwater et al., 1988; Westwater and Snider, 1989) and will not be presented here. However, whereas previous observations have employed either 60- or 120-sec averaging times, we used a 30-sec interval at Wallops in order to extend subsequent spectral analysis to higher temporal frequencies.

3. Preliminary Results

Weather at Wallops varied from clear and dry to four events in which the precipitation rate was perhaps the highest observed to date (inferred from the attenuation values as quantitative precipitation rates were not measured). Because of the high rainfall rates, radiometer saturation at all frequencies occurred on a few occasions. More typically, however, saturation was found to occur at 90 GHz but not at the two lower frequencies. Saturation events have been removed from the data set by limiting attenuation values derived from the radiometer data to less than 12 dB. A case where saturation occurs is indicated in the time series of Fig. 1.

Cumulative distributions of zenith attenuation are presented in Fig. 2, along with means and standard deviations. Note that at a relatively wet location such as Wallops, the atmospheric attenuation at 20.6 GHz generally exceeds that at 31.65 GHz. This is in contrast to the situation at Denver in December where attenuation at 31.65 GHz exceeds that at 20.6 GHz for about 65 percent of the time. The general shape of the distribution is similar for Denver and Wallops since some precipitation occurred. However, for SNI where no precipitation fell, the distributions are dissimilar. Table I contains a statistical comparison of our radiometrically-derived atmospheric attenuation at various locations.

In another useful type of comparison that deserves increasing attention, we examined the ratios of attenuation observed at the three frequencies for both combined clear-cloudy conditions and for

clear conditions at Wallops. Results for the former are in Fig. 3a, which shows how the ratios vary as conditions change from clear to cloudy to precipitating. In general, the attenuation ratios remain relatively constant on the right side of the distributions. This portion of the distribution is associated with clear weather and non-precipitating clouds. However, on the left side of the distribution, where precipitation and high liquid water contents are present, the ratios change rather dramatically, approaching a factor of 9 for the 90/20 GHz attenuation ratio.

Similar data for the clear weather case (Fig. 3b) show a much smaller variation, in general, although some non-linear effects occur during conditions of higher atmospheric moisture. Understanding these effects, of course, is critically important to the eventual extension of the satellite communication bands to 90 GHz and higher. During the next year, we plan to investigate attenuation ratios in greater detail and include the data sets collected earlier in the NAPEX program. Fig. 4 contains attenuation ratio data observed in Denver during August 1988 for clear, cloudy, and rainy conditions.

4. Future Plans

Plans for future analysis of the Wallops data set include studies similar to those previously reported as well as new investigations:

- Comparisons of measured and calculated values of atmospheric absorption and attempts to improve present absorption models. The simultaneous observations of atmospheric humidity by three different types of sensor may help shed new light upon the modelling problem.

- Further study of regression relationships for prediction of attenuation between various frequencies.

- Refinement of liquid absorption models.

- Further studies of the attenuation ratios observed during the Wallops observations and extension of the study to the entire data set.

Table I - Comparison of 20.6/31.65/90.0 GHz Attenuation Statistics For Three Locations at Various Times of the Year. Clear and Cloudy Data Combined.

Location	20.6 GHz Mean	20.6 GHz Std. Dev.	31.65 GHz Mean	31.65 GHz Std. Dev.	90.0 GHz Mean	90.0 GHz Std. Dev.
			(All values are in dB)			
San Nicolas (el 13 m) July 1987	0.398	0.113	0.321	0.096	1.128	0.498
Denver (el 1611 m) Dec. 1987	0.159	0.068	0.158	0.081	0.411	0.323
Denver (el 1611 m) August 1988	0.497	0.195	0.278	0.259	1.190	1.850
Wallops Is. (el 2 m) April/May 1989	0.428	0.291	0.398	0.407	1.239	1.323

References

Westwater, E. R., J. B. Snider, and M. J. Falls, 1988: Observations of Atmospheric Emission and Attenuation at 20.6, 31.65, and 90.0 GHz by a Ground-based Radiometer, NOAA Technical Memorandum ERL WPL-156, November 1988, pp16.

Westwater, E. R., and J. B. Snider, 1989: Ground-based Radiometric Observations of Atmospheric Emission at 20.6, 31.65, and 90.0 GHz, Proc. Sixth International Conference on Antennas and Propagation ICAP 89, Part 1: Antennas April 1989, pp 229-233.

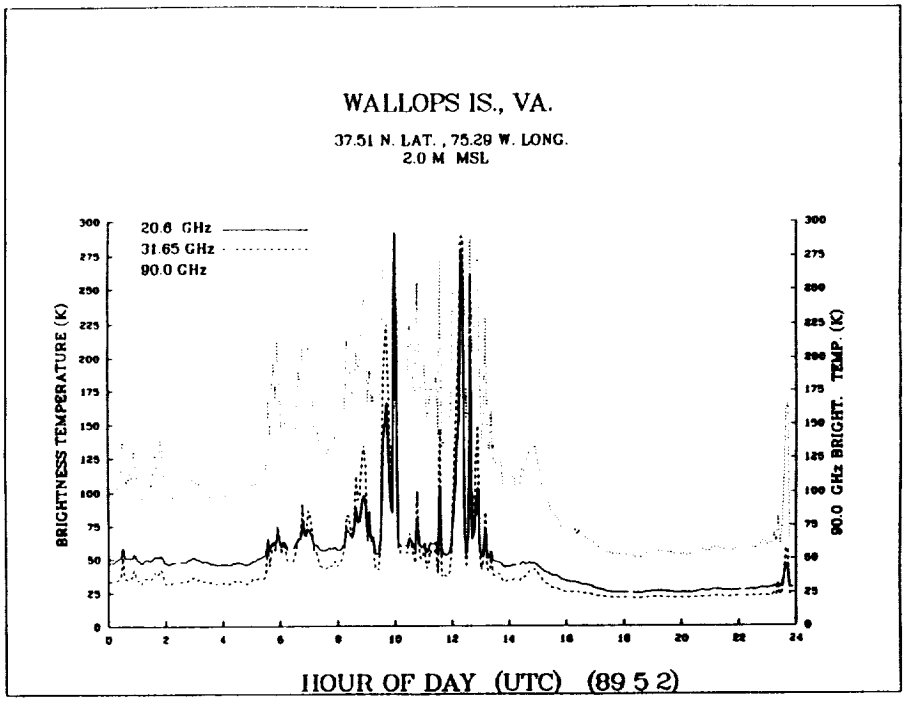

Figure 1. Time series of brightness temperatures at 20.6, 31.65, and 90.0 GHz during clouds and precipitation. Radiometer saturation at all frequencies occurs near 1000 and 1210 UTC.

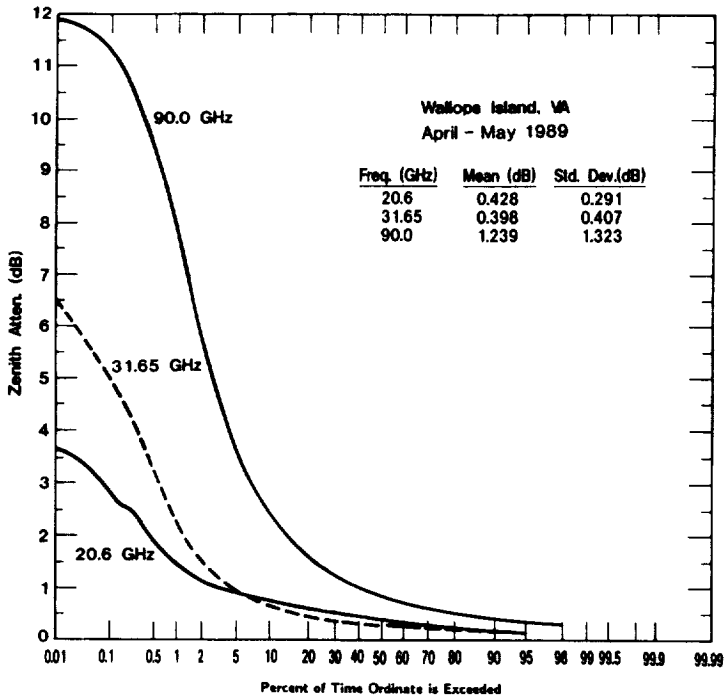

Figure 2. Cumulative distributions of zenith attenuation at Wallops Island, VA, for clear and cloudy conditions.

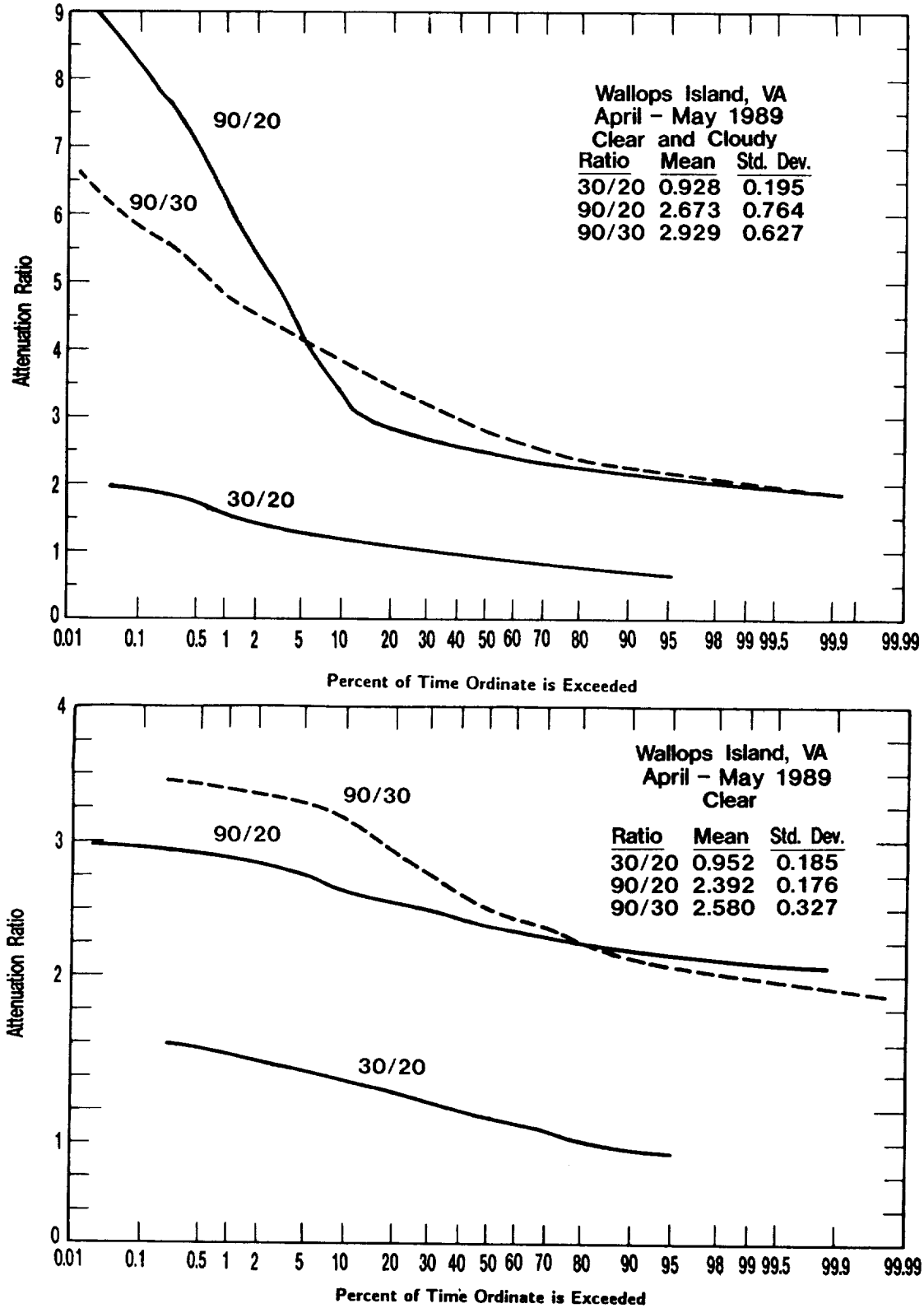

Figure 3. Cumulative distributions of attenuation ratios for (a) clear and cloudy conditions, and (b) clear conditions. Wallops Island, VA, April-May 1989.

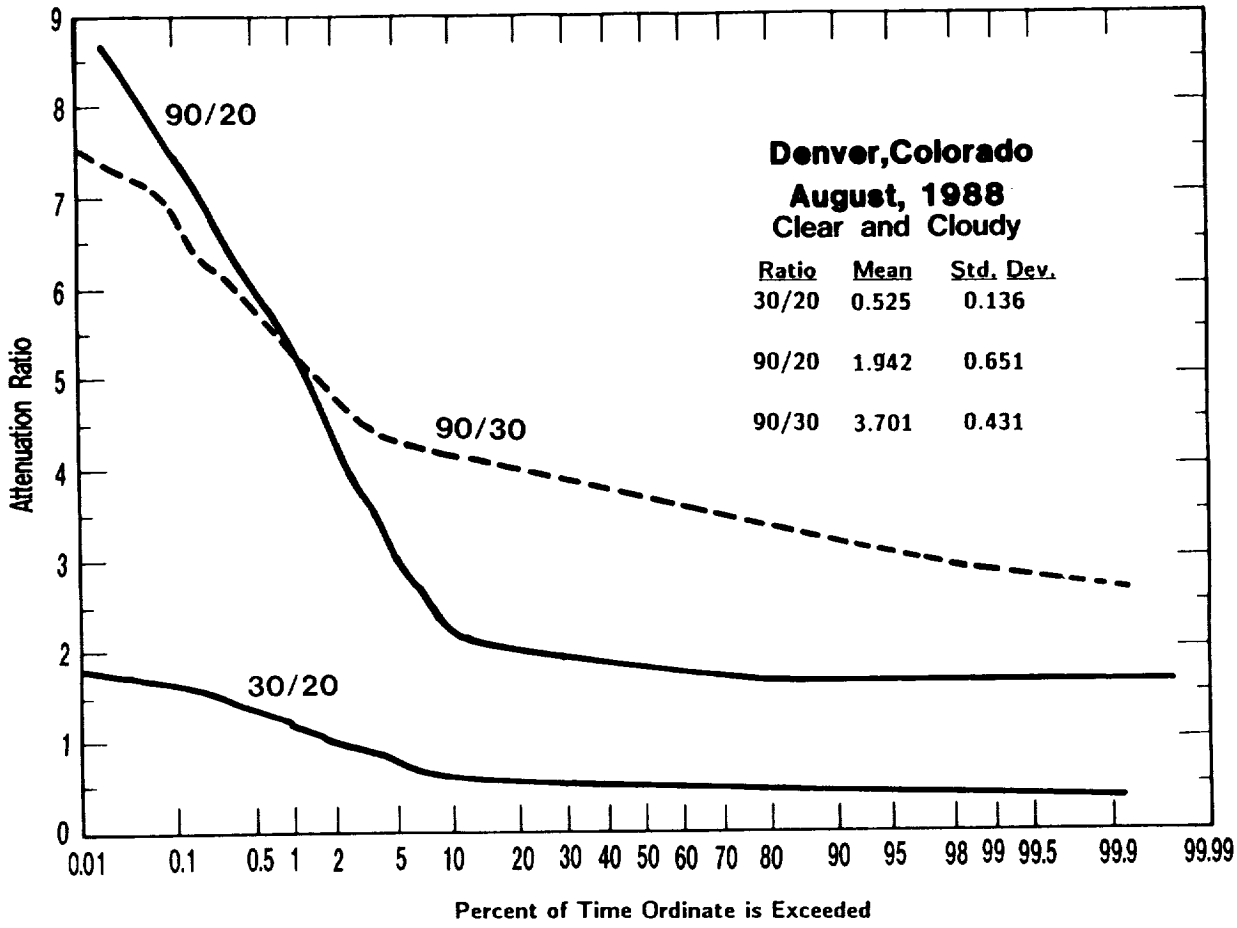

Figure 4. Cumulative distributions of attenuation ratios for clear, cloudy, and rainy conditions at Denver, CO, August 1988.

RADIOMETRIC OBSERVATIONS AT 20.6, 31.65, AND 90.0 GHZ: CONTINUING STUDIES

Ed R. Westwater, Michael J. Falls, Ermanno Fionda*,
and
Jack B. Snider

NOAA/ERL/Wave Propagation Laboratory
Boulder, Colorado 80303

* Fondazione Ugo Bordoni
Rome, Italy

Abstract -- Ground-based radiometer measurements at 20.6, 31.65, and 90.0 GHz have been analyzed to provide attenuation statistics, thus extending the data base of previous NAPEX studies. Using data from colocated radiosondes, comparisons of measurements and calculations of brightness temperatures are presented. The oxygen absorption model of Rosenkranz (1988) and the water vapor absorption models of Liebe (1989) and of Waters (1976) are used in the study. Data from July 1987 at San Nicolas Island, California, and from December 1987, August 1988, and November 1988 at Denver, Colorado, are included in the study. Joint-attenuation statistics at 20.6 and 31.65 GHz are presented for two locations of the Colorado Research Network (Denver and Platteville) for December 1987 and August 1988.

1. Introduction

In the work reported in the Proceedings of NAPEX XII (Davarian, 1988), Westwater et al. (1988) presented attenuation statistics derived from radiometric data taken at 20.6, 31.65, and 90.0 GHz. These data were taken with the NOAA steerable-beam three-channel radiometer. Statistics were presented for San Nicolas Island, California, July 1987, and for Denver, Colorado, December 1987. In this paper we present single-station attenuation statistics for the same three frequencies at Denver, August 1988; in the companion paper by Snider et al.(1989), an extended set of statistics is presented for Wallops Island, Virginia, April 1989. We also present a summary of our results in modeling clear air absorption. Finally, we use data from the Colorado Research Network of dual-channel radiometers to derive joint-station attenuation statistics for Denver and Platteville.

2. Clear Air Thermal Emission: A Comparison of Theory and Experiments

As discussed by Westwater et al. (1988), the NOAA steerable-beam radiometer is calibrated by the "tipping curve" method. If independent measurements are available of the atmospheric variables describing the thermal emission, i.e., the vertical distributions of temperature, pressure, water vapor, and cloud liquid, then measurements and calculations can be compared to study absorption models. In particular, various absorption models for oxygen and for water vapor can be compared in this way. Our procedure (Westwater et al., 1989) is to calculate, for each height level at which meteorological data are available, the absorption coefficient. Brightness temperatures are then calculated by numerically integrating the radiative transfer equation. Since the rawinsonde data that we

used to provide meteorological data do not measure cloud liquid, we restricted our comparison set for this section to clear sky conditions.

During 1987 and 1988, ground-based zenith-viewing observations of atmospheric thermal emission were made at the frequencies of 20.6, 31.65, and 90.0 GHz. At the locations of the experiments, San Nicolas Island, California, and Denver, Colorado, rawinsonde observations of temperature and humidity were also available. Two types of rawinsonde observations were available: standard soundings taken by the National Weather Service and those from a relatively new rawinsonde package, the Cross-chain Loran-C Atmospheric Sounding System (CLASS). The meteorological data were then used with radiative transfer computer programs that calculated brightness temperature and total attenuation. The resulting brightness temperatures could then be directly compared with measurements. Absorption algorithms of Liebe (1989), Waters (1976), and Rosenkranz (1988) were used in the comparison study. Composite results comparing theory and measurements are shown in Figs. 1-3. Somewhat surprisingly, at 20.6 and 31.65 GHz, the relatively old model of Waters is in better agreement with the measurements than that of Liebe; however, at 90.0 GHz, the model of Liebe is clearly superior. We intend to continue this analysis as more data become available.

3. Single-station Attenuation Statistics

The methods used in deriving attenuation from emission, as well as our procedures for editing of data, were described by Westwater et al. (1988). We continued the Denver, Colorado, analysis by deriving statistics at 20.6, 31.65, and 90.0 GHz for the month of August 1988; these results are shown in Fig. 4. Primarily because of the influence of liquid-bearing cumulus clouds, much higher attenuations were encountered than during December in Denver, or July in San Nicolas Island. The analysis of the new Wallops Island data is given by Snider et al. (1989).

4. Joint-station Attenuation Statistics

As described by Westwater and Snider (1987), the Wave Propagation Laboratory operated a research network of dual-frequency radiometers in the front range of eastern Colorado. We chose to analyze joint-station attenuation statistics (at 20.6 and 31.65 GHz) for Denver and Platteville, located about 40 km apart. Two months were chosen: 1987 December and 1988 August.

As was discussed previously, all data represent 2-min averages. Since the clocks at the two sites were not synchronized, we first ran the time series through a time matching algorithm: data were paired such that the maximum time difference associated with a pair was 1 min. Then, statistics were derived for each station, both individually and jointly, for the paired data. Thus, data for which there were gaps at at least one station, were not included in the statistics. Plots of the individual attenuation statistics are in Figs. 5 and 6. Although the cumulative distributions are somewhat different, both the means and the standard deviations are statistically indistinguishable.

We also developed joint statistics in the following manner: let $(\tau_D)_i$ and $(\tau_P)_i$ be the ith data pair for Denver and Platteville. For the ith pair, we calculated the corresponding quantities - maximum (τ_{Di}, τ_{Pi}) and minimum (τ_{Di}, τ_{Pi}). Then we computed the cumulative distribution from the time series of both the minimum and maximum of the two-station distributions. These joint statistics, for 20.6 and 31.65 GHz, are shown in Figs. 7 and 8. Note that for the August statistics, a difference in maximum to minimum of about 6 dB is achieved at 31.65 GHz.

5. Plans

We will continue the analysis of the Wallops Island data to compare clear air calculations of brightness temperature with measurements. This comparison will be broadened to include all of our existing data including data with clouds. We will also examine the newest cloud models. Some of our existing 6-channel data at Stapleton Airport will support this effort. In addition, at least one 3-day period of rain will be analyzed.

In the near future, WPL will have at least four dual-channel radiometers available. We propose to deploy these radiometers at various spacings in the Denver area to develop a reasonable set of space and time diversity statistics.

We plan to extend the diversity analysis of existing dual-channel radiometer data of Denver and Platteville to cover a time period of at least 2 years.

We propose to make joint observations of slant-path attenuation in conjunction with the microwave radiometers and receivers being built by Virginia Tech in support of the OLYMPUS project. For this collaboration, we would operate the three- channel steerable radiometer at the Blacksburg, Virginia, receiver site. A tentative time for the joint experiments would be summer 1990.

References

Davarian, F., ed, "Proceedings of the Twelth NASA Propagation Experimenters Meeting (NAPEX XII)," held at Syracuse University, Syracuse, New York, June 9-10, 1988. JPL Publication 88-22.

Liebe, H. J., "MPM - An atmospheric millimeter-wave propagation model," International J. Infrared Millimeter Waves, Vol. 10, No. 6, pp. 631-650, 1989.

Rosenkranz, P. W., "Interference coefficients for overlapping oxygen lines in air," J. Quant. Spectrocs. Radiat. Transfer, Vol. 39, pp. 287-297, 1988.

Snider, J. B., M. D. Jacobson, and R. H. Beeler, "Observations of attenuation at 20.6, 31.65, and 90.0 GHz--preliminary results from Wallops Island, VA," Proc. NAPEX XIII, 1989.

Waters, J. W., "Absorption and emission of microwave radiation by atmospheric gases." In Methods of Experimental Physics. M. L. Meeks, ed., Vol. 12, Part B. Radio Astronomy, Academic Press, New York, Section 2.3, 1976.

Westwater, E. R. and J. B. Snider, "Microwave radiometer facilities at the Wave Propagation Laboratory," Proc. NAPEX XI, JPL D-4647, pp. 24-27, Aug. 1987.

Westwater, E. R., J. B. Snider, and M. J. Falls, "Ground-based radiometric observations of emission and attenuation at 20.6, 31.65, and 90.0 GHz," Proc. NAPEX XII, JPL Publication 88-22, pp. 114-125, Aug. 1988.

Westwater, E. R., J. B. Snider, and M. J. Falls, "Ground-based radiometric observations of atmospheric emission and attenuation at 20.6, 31.65, and 90.0 GHz: A comparison of measurements and theory," submitted to IEEE Trans. Antennas Propag. 1989.

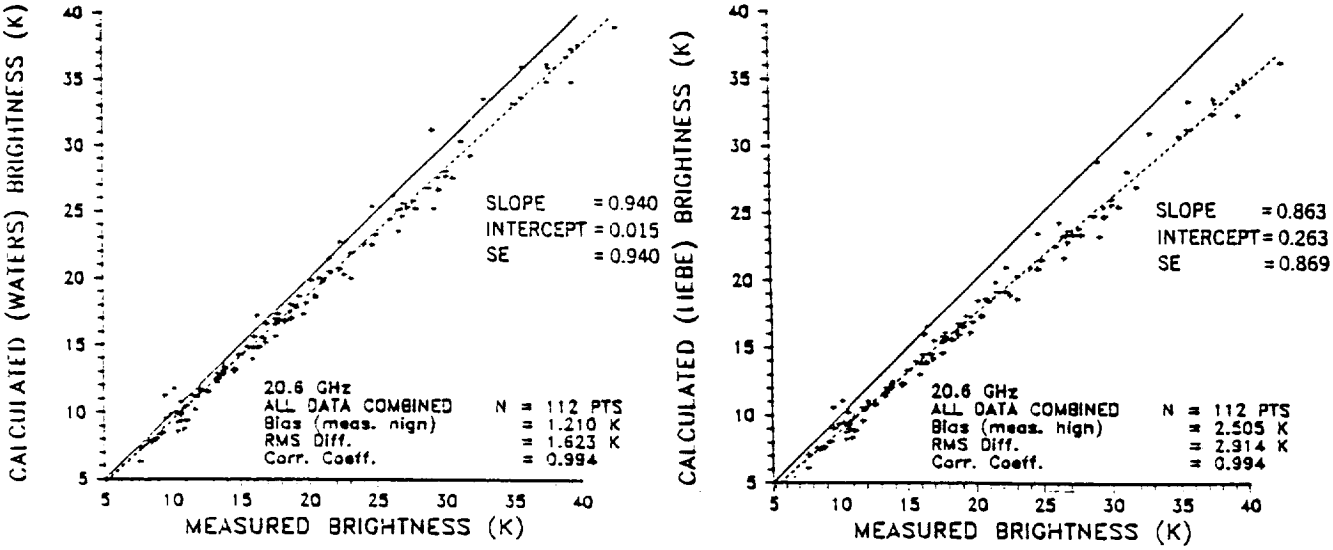

Figure 1. Comparison of measured and calculated brightness temperatures at 20.6 GHz. Data included in the comparison are from San Nicolas Island, California, July 1987, and from Denver, Colorado, December 1987, August 1988, and November, 1988. Oxygen attenuation calculated from the model of Rosenkranz (1988).

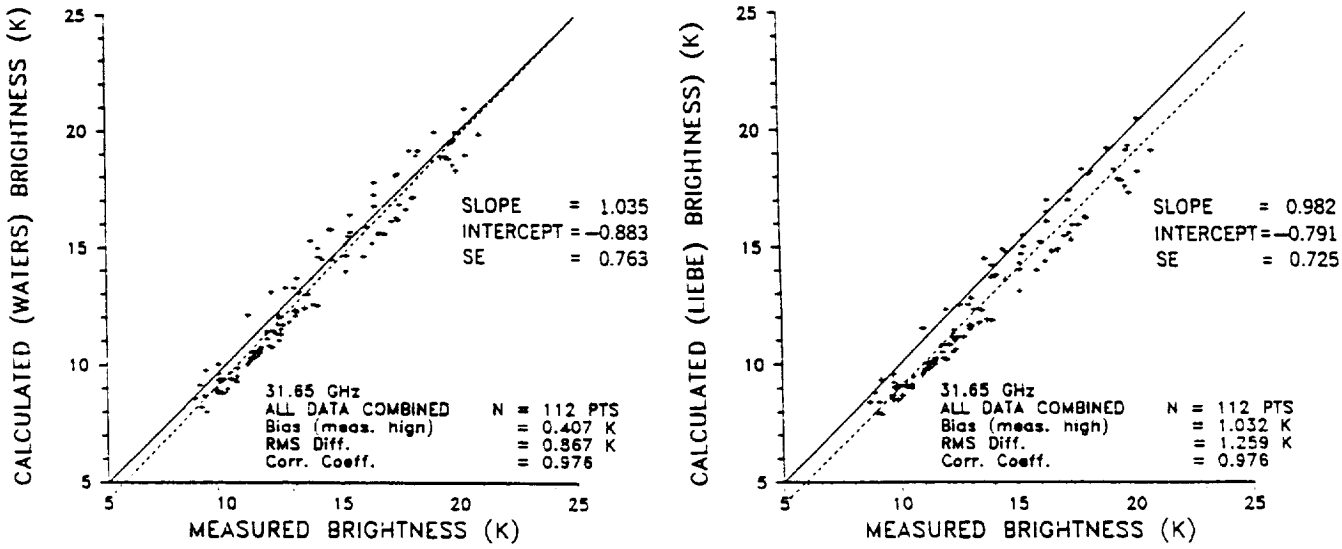

Figure 2. Comparison of measured and calculated brightness temperatures at 31.65 GHz. See Figure 1 caption for details.

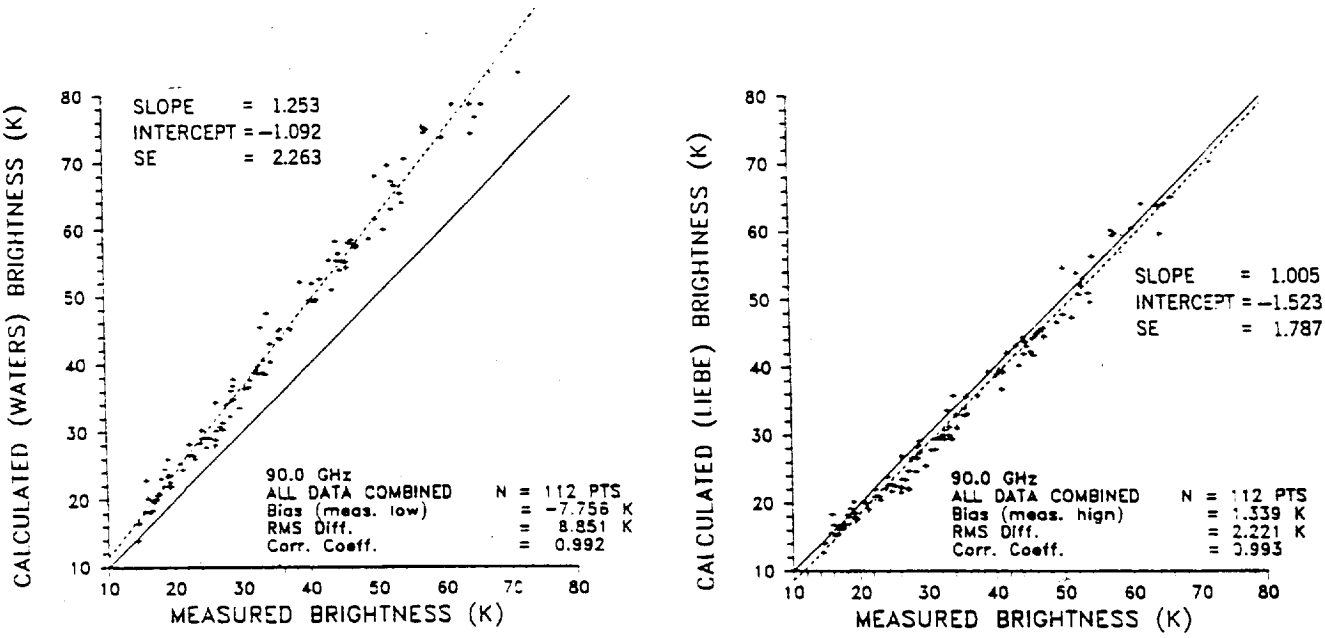

Figure 3. Comparison of measured and calculated brightness temperatures at 90.0 GHz. See Figure 1 caption for details.

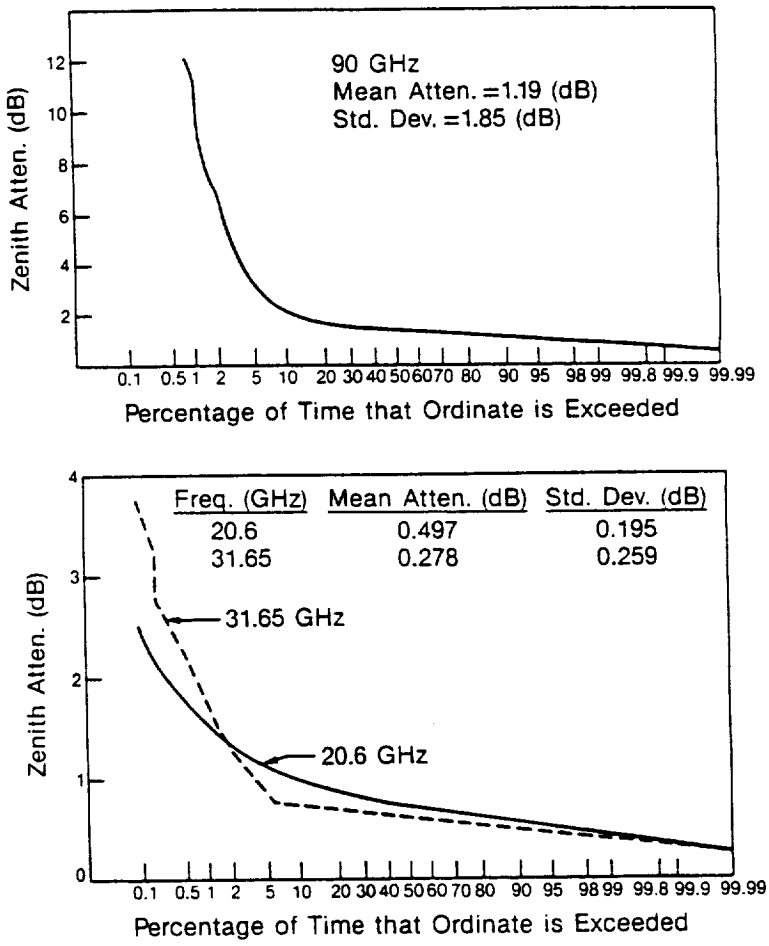

Figure 4. Cumulative distribution of zenith attenuation measured by a 3-channel radiometer at Denver, Colorado, August 1988. Data consisted of 17,792 2-min averages.

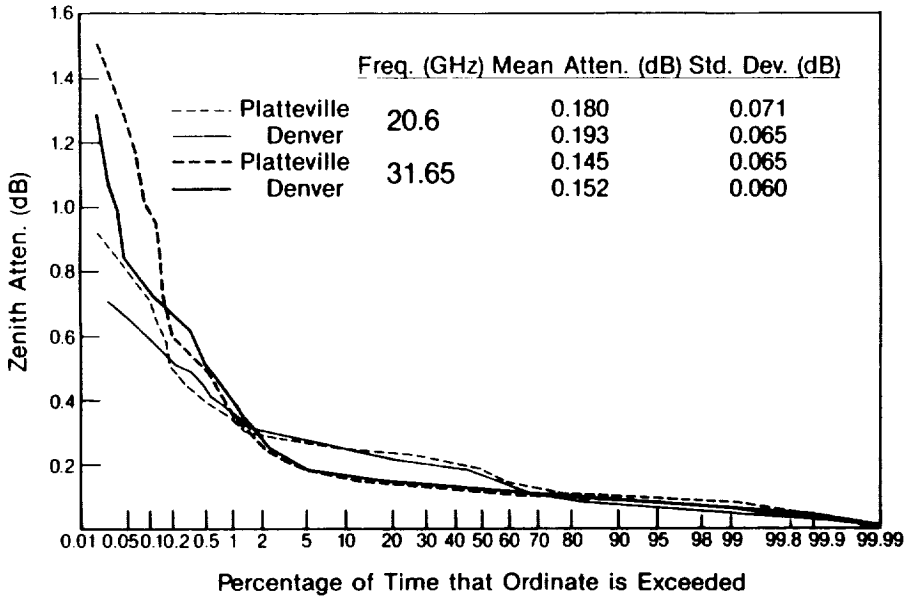

Figure 5. Cumulative distribution of zenith attenuation measured at 20.6 and 31.65 GHz at Denver and Platteville, Colorado, December 1987. Data consisted of matched pairs of 10780 2-min averages.

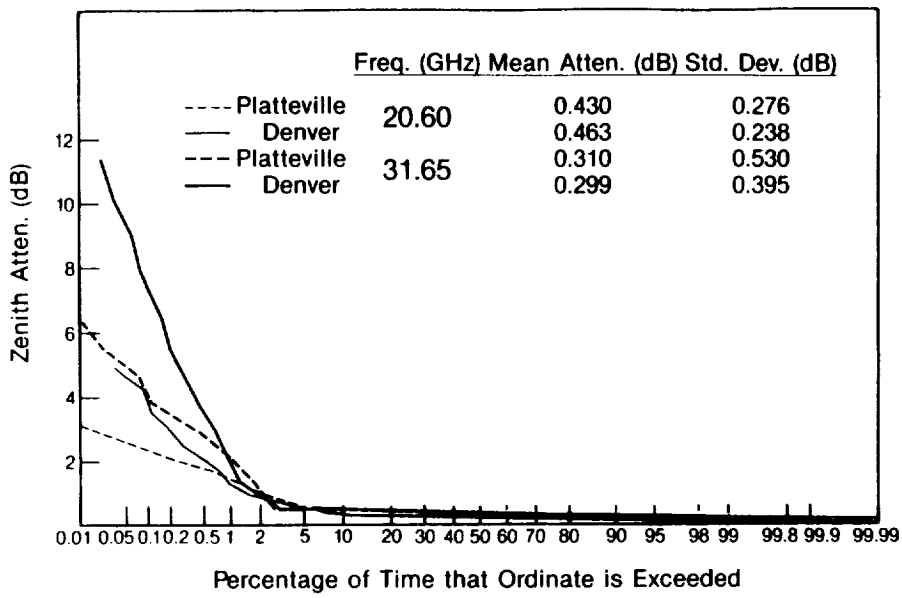

Figure 6. Cumulative distribution of zenith attenuation measured at 20.6 and 31.65 GHz at Denver and Platteville, Colorado, August 1988. Data consisted of matched pairs of 9175 2-min averages.

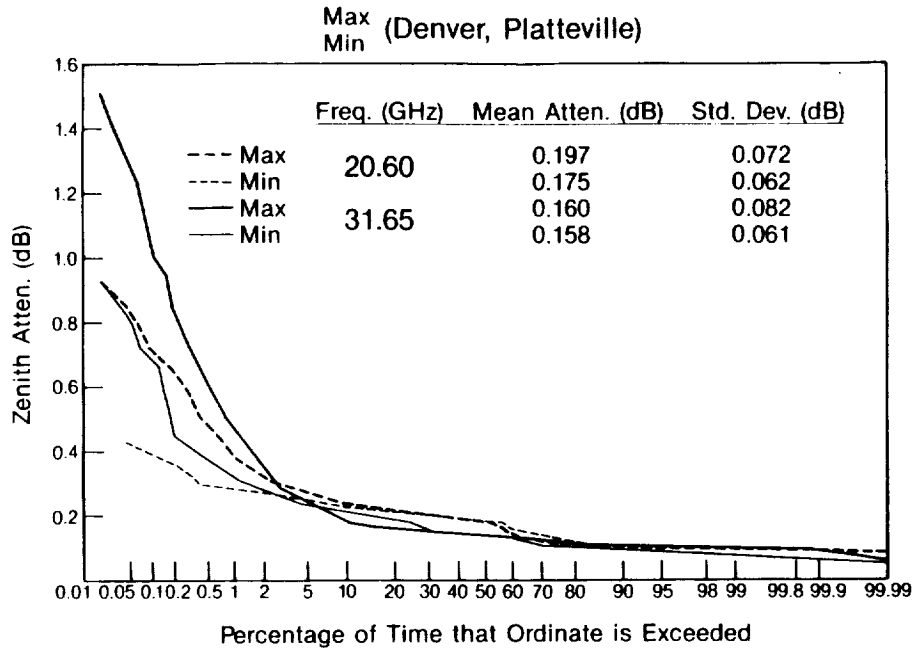

Figure 7. Joint cumulative distribution of minimum and maximum zenith attenuation at 20.6 and 31.65 GHz for Denver and Platteville, Colorado, December 1987. Distributions were derived from 10780 matched pairs of 2-min averages.

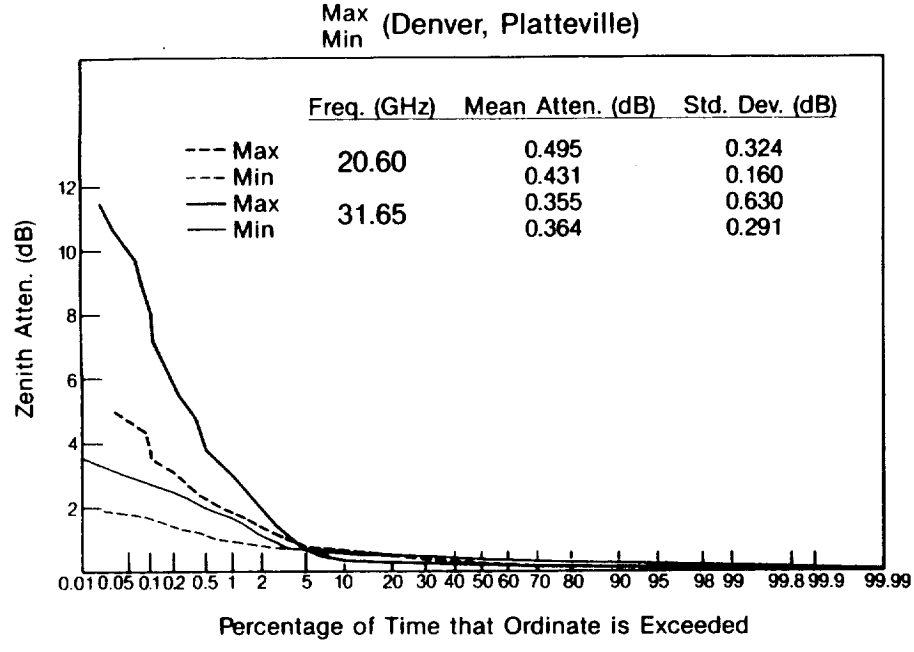

Figure 8. Joint cumulative distribution of minimum and maximum zenith attenuation at 20.6 and 31.65 GHz for Denver and Platteville, Colorado, August 1988. Distributions were derived from 9175 matched pairs of 2-min averages.

LOW ELEVATION ANGLE KU-BAND SATELLITE MEASUREMENTS AT AUSTIN, TEXAS

Wolfhard J. Vogel, Geoffrey W. Torrence, Murali Ranganathan*

Electrical Engineering Research Laboratory
The University of Texas at Austin
10100 Burnet Rd., Austin, TX, 78758

Abstract--At low elevation angles, the propagation of satellite signals is affected by precipitation as well as by inhomogeneities of the refractive index. Whereas precipitation causes fades for relatively small percentages of time, the refractive index variability causes scintillations which can be observed for most of the time. An experiment is now under way in Austin, Texas, in which the right-hand circularly polarized 12 GHz beacon of INTELSAT-V/F10 is observed at a 5.8 degree elevation angle, along with the radiometric sky temperature, the rainfall rate, humidity, pressure, temperature, and wind speed and direction. The objective of these measurements is to accumulate a database over a period of 2 years and to analyze the probabilities and dynamical behavior of the signal variations in relation to the meteorological parameters. This paper describes the hardware and software used for the data acquisition and analysis and presents results from the first year of measurements.

1. Introduction

Line of sight satellite communications links to earth operating at wavelengths shorter than 3 cm are subject to degradation brought about by the interaction of electromagnetic waves with some of the constituents of the troposphere. The most basic effect is the attenuation of the signal. Energy is removed from the wave either by absorption or redirection. At the frequency of interest here, 12 GHz, absorption is caused all of the time and at a relatively constant small rate by oxygen and water vapor and for a small fraction of the time and at large rates by rain or other hydrometeors. The second loss mechanism, redirection, is mainly associated with the time-varying inhomogeneities of the refractive index. The received power undergoes variations, because the phase front of the wave has been distorted or redirected. This effect is enhanced on paths with elevation angles below about 10 deg, where it occurs most of the time.

The objective of this research project is to make continuous measurements of the signal amplitude received from a

This research was supported by INTELSAT under Contract INTEL-540B. The opinions expressed are not necessarily those of INTELSAT.

*Now with Electro-Mechanics Co., Austin, Texas

satellite at 5.8 deg elevation and to correlate these data with simultaneously collected radiometric sky temperatures as well as local meteorological quantities. The motivation for the effort arises from the desire to utilize existing or new satellites to provide service to locations with elevation angles below current standards. In order to do this, however, the performance statistics underlying the service have to first be known or made predictable.

Many measurements have been performed on paths with elevation angles greater than 15 deg and prediction models developed for rain attenuation [CCIR, Rep. 721-2] and clear-air scintillations [CCIR, Rep. 718-2] are available. More recent measurements on low elevation angle paths have been summarized by Karasawa, Yamada, and Allnutt [1988], who proposed a new scintillation prediction technique incorporating meteorological parameters. The data obtained in this experiment will be used to further refine low elevation angle rain attenuation and scintillation models.

2. Experiment Description

Both the 11.198 GHz beacon receiver as well as the radiometer make use of the same 2.4 m conical horn-reflector antenna, employing opposite sense circular polarizations. The antenna's apex protrudes into a temperature controlled building, where it feeds the front-end electronics. Following down-conversion, intermediate frequency signals are sent to the back-end of the receivers and the data acquisition system, located directly below the antenna.

The beacon receiver is not of phase-locked loop design, but utilizes a 32 channel filterbank. The filters have a bandwidth of 100 Hz and are spaced at 50 Hz intervals.[Dinn and Zimmerman, 1978] The data acquisition program adjusts a synthesizer to track the satellite beacon within a particular filter. This design assures that the receiver measures fades to the noise threshold without data loss due to loss of lock conditions or lock acquisition delays. Samples of beacon data with low and normal scintillations and from a rain event are given in Figure 1.

The radiometer is of continuously calibrating, gain controlled, Dicke-switched design, implemented in a desk-top computer. It has three states, switching between (1) the antenna, (2) a computer controlled comparison load, and (3) the comparison load plus a noise source. The gain of the radiometer is adjusted to keep the output voltage during the third phase at a constant level. The radiometer's temperature to voltage conversion gain and noise temperature are monitored and used to calculate the measured sky temperature. The coupling of the antenna to the ground has been estimated to be 4 K. This estimate is based on comparing sky temperatures measured in clear air with calculations using the CCIR [Rep. 718-2] procedure.

Meteorological parameters measured at the site are the ambient temperature, pressure, relative humidity, wind speed, and wind direction. A tipping bucket rain gauge is used to measure rainfall rates.

All data are recorded by a desk-top computer based data acquisition system. The beacon level is recorded twice a second or every 10 seconds, depending on its variability and level; the sky temperature and meteorological quantities are recorded every 10 seconds.

3 Data Analysis Procedures

3.1 Quality Control

The raw data of each month go through a quality control inspection procedure. This consists of an interactive but highly automated program, displaying each hour's data graphically and allowing the operator to make appropriate editing decisions for abnormal conditions. The decisions are recorded in an ASCII file as a macro command, to be executed again by the data analysis program, when it expands the unedited raw data into calibrated and corrected time series of .5 second beacon samples and 10 second samples of all other quantities. Most of the exceptions are handled automatically by the quality control program, but full operator control is always available. The program also calculates 6 minute averages of the fade level and sky temperature, values used for the determination of the free-space and clear-air levels, as explained below. At each stage of these procedures, ASCII data files can be produced for plotting of any of the intermediate results.

The abnormal or exceptional conditions for which a macro entry is produced include any condition which is not the fast recording mode with all systems fully operational. Some of these conditions are the calibration periods, solar transit, and receiver malfunctions.

3.2 Clear-Air Level Estimation

The 6 minute averages for the beacon fade and the sky temperature calculated during the quality control pass of the data are recorded and used for the estimation of the free-space and the clear-air fade levels. The free-space fade level is the average signal fade relative to a level without any gaseous absorption and without antenna misalignment or receiver offset drift. As the gaseous absorption is about 1 dB at Ku band at 5.8 deg elevation, the normal free-space fade level is about 1 dB. The clear-air level is taken relative to this prevailing gaseous attenuation, i.e. the normal clear-air fade level is 0 dB.

The free space fade level for each 6 minute interval of a particular day is estimated using data including the three days

immediately before and after the day in question. Only data for which the sky temperature is less than 90 K are considered in the procedure. This avoids including rain fade events into the estimation. After subtracting from the beacon level the gaseous attenuation calculated from the measured sky temperature, only effects due to antenna misalignment and gain offsets remain. The 7 days of data are then subjected to a diurnal decomposition, which reveals both the moving average and the seasonal component.

Shown in Figure 2 for 25 days, the seasonal component has a 24 hour period and typically about 1 dB peak-to-peak deviation, because the receiving antenna is fixed but the satellite apparent azimuth and elevation are changing due to the motion of the spacecraft (.25 deg). A sidereal shift is noticeable.

The beacon fade levels are corrected with the smoothed diurnal variation estimates and the moving averages. The clear-air gaseous absorption estimate for each day is based on the lower quartile of the sky temperature derived attenuation, excluding fade events. The error of this estimate is probably of the order of .1 dB.

4. Results

The cumulative distribution of the beacon signal has been plotted (Fig. 3) on a logarithmic percentage scale. The solid curve represents the attenuation. The dashed curve, the enhancements, is derived from 100% minus the percentage the attenuation exceeded the ordinate. In April 1989 fades exceeded 16.7 dB and enhancements 2.5 dB for 0.1% of the time. The asymmetry of the plot is due to rain fades.

Slant path-length for typical water vapor content of 10 to 20 g/m^3 in Austin is about 10 airmasses or 25 km [Altshuler, 1986] at 5.8 deg elevation. Considerable signal level variations result in clear and cloudy turbulent air. As shown in Fig. 4, at a 0.1% probability level, the rms scintillations exceeded 4.7 dB in April 1989. This compares to below 2.0 dB for Dec. 1988, the most quiet month of the year.

Estimating the physical temperature from a regression analysis of the path transmission, defined by $10^{(-F/10)}$ with F the fade in dB, and the radiometric sky temperature resulted in 271.3 K for June 1988, based on equal probability values. Even though a single aperture is used for the two measurements, beam-filling effects, scintillations, as well as vertical temperature gradients can cause wide variations of the instantaneous value. This is demonstrated in Fig. 5, which shows an event which started with a temperature of 284 K. When the storm receded, the measured medium temperature dropped to only 239 K. Nevertheless, Fig. 6 shows that a median linear relationship between sky temperature and beacon transmission can be established. For April 1989, the dashed lines give event count contours (10 sec

samples) and the dotted curves are the 10th, 50th and 90th cumulative percentiles of the events.

5. Summary

A long term low elevation angle beacon experiment is now under way in Austin, Texas at Ku band. The effects of turbulence and rain will be measured and used to predict the performance of such links at other locations. While radiometers are invaluable to establish the clear air signal level, results point out the difficulty of estimating slant path fades other than averages from radiometric measurements, especially at low elevation angles, where the dynamic behavior of the channel is important.

6. Acknowledgements

The authors appreciate the superb construction of the filterbank by G. A. Zimmerman and H. J. Bergmann at BTL in the days of COMSTAR.

References

Altshuler, E. E., "Slant Path Absorption Correction for Low Elevation Angles",IEEE Trans. Antennas Propagat., Vol. AP-34, No. 5, pp. 717-718, 1986

CCIR, Report 721-2: Attenuation by hydrometeors, in particular precipitation, and other atmospheric particles, Study Group V, ITU, Geneva, 1986

CCIR, Report 718-2: Effects of tropospheric refraction on radiowave propagation, Study Group V, ITU, Geneva, 1986

Dinn, N. F., and G. A. Zimmerman, "COMSTAR Beacon Receiver Diversity Experiment", BSTJ, Vol 57, No. 5, pp 1341-1367, 1978

Karasawa, Y., M. Yamada, and J. E. Allnutt, "A New Prediction Method for Tropospheric Scintillation on Earth-Space Paths", IEEE Trans. Antennas Propagat., Vol. AP-36, No. 11, pp. 1608-1614, 1988

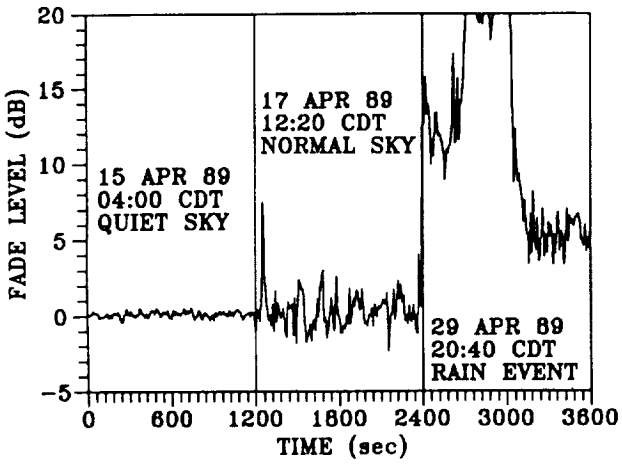

Fig. 1. Examples of beacon data with varying conditions

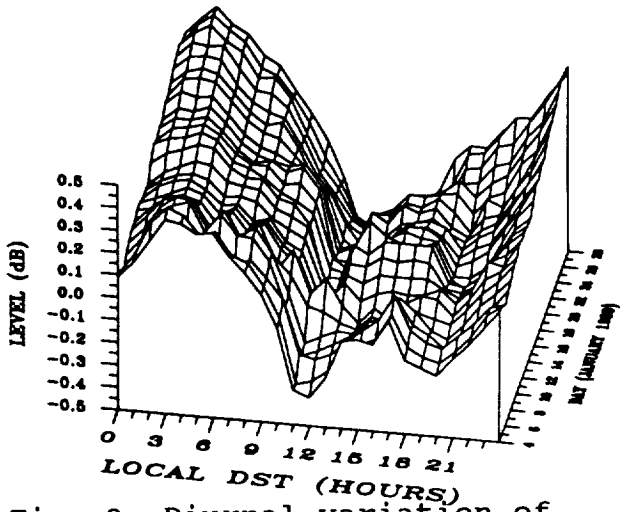

Fig. 2. Diurnal variation of the beacon level

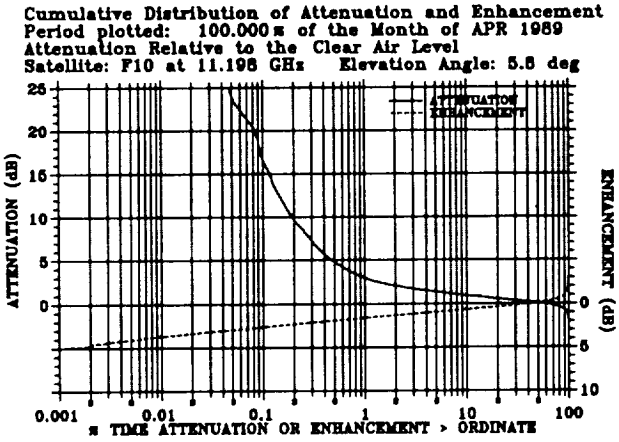

Fig. 3. Fade and enhancement distribution, Apr. 1989

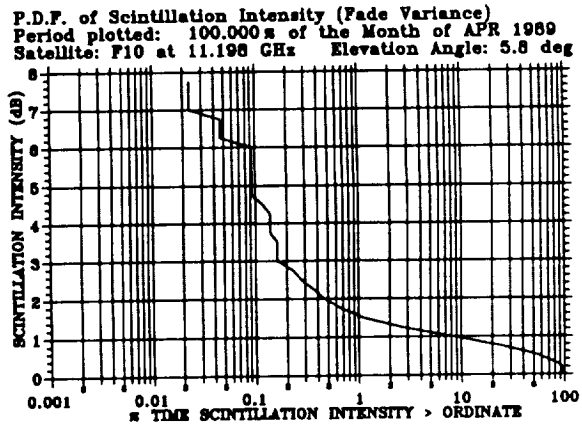

Fig. 4. Fade variance for Apr. 1989

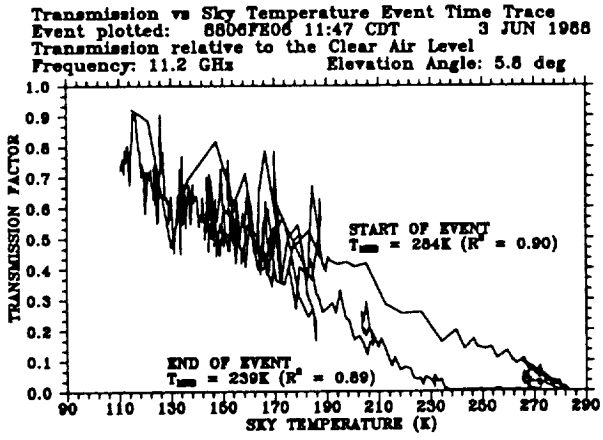

Fig. 5. An event trace for beacon transmission and the sky temperature

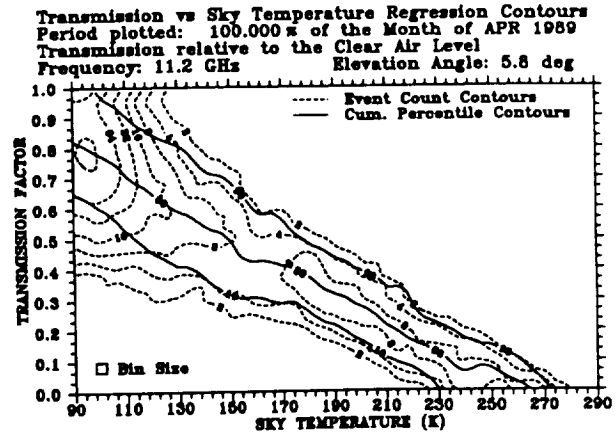

Fig. 6. Transmission factor vs. sky temperature regression contours

Atmospheric Transmission Calculations for Optical Frequencies

Kamran Shaik

Jet Propulsion Laboratory
California Institute of Technology
Pasadena, California 91109

Abstract

A quantitative study of the transmission loss through the entire atmosphere for optical frequencies likely to be used for an earth-space communication link using existing databases on scattering and absorption characteristics of the atmospheric constituents is presented.

1.0 Introduction

Laser communication technology can potentially provide (i) an enormous data bandwidth for significantly improved channel performance, (ii) an advantage in weight, size, and power consumption over conventional systems in use today, and (iii) non-interacting multiple access link geometries that are amenable to extensive frequency reuse, and secure systems with low probability of interception and jamming. For these reasons, the development of an optical communication systems for deployment in space is being actively pursued at the Jet Propulsion Laboratory (JPL).

Development of robust line-of-sight earth-space optical communication depends on an accurate description of the expected propagation loss through the atmosphere. In the absence of thick clouds, which can completely close down a communication link, the transmission loss is primarily due to absorption and scattering by molecules, aerosols, fog, haze, and other particulate matter in the atmosphere. The present work attempts to quantify these adverse atmospheric effects on light propagation to provide reasonable estimates of link budgets for optical communications.

2.0 Transmission Calculations

2.1 Transmission Codes

The High Resolution Transmittance (HITRAN) computer code, developed at the Air Force Geophysics Laboratory (AFGL), is one of the most complete compilations of molecular absorption data [1]. The compilation gives various line parameters for almost 350,000 lines over a spectral region from ultra-violet to millimeter waves with a resolution of 10^{-5} nm^{-1}. This code can be used to make a detailed study of laser frequencies which are likely to be used for communication purposes and ensure that the carrier frequency does not fall on a strong absorption line. However, the computer codes LOWTRAN (Low Resolution Trans-

mission) and FASCOD (Fast Atmospheric Signature Code), also developed by AFGL, are better suited for the analysis at hand [2-3]. Both LOWTRAN and FASCOD include the ability to compute transmission loss due to thin cirrus clouds, aerosols, and haze. Also, these computer codes can account for changes in transmission loss due to station altitude and the zenith angle of the signal beam. The resolution of these codes (20 cm^{-1}) is lower than the HITRAN database, but it does not represent a problem as it compares well with the obtainable laser line widths.

2.2 Results

The data and the results of the investigation are shown in a compact graphic form in figs.1-5. The parameters relevant to the calculation are labeled on the graph. Fig.1 shows a plot of transmission values over a large range of optical frequencies at sea level for clear skies.

Fig.2 shows a transmission vs. altitude plot for Nd:YAG and doubled Nd:YAG wavelengths (1.064 μm and 0.532 μm respectively), which are likely to be used for an earth-space optical communication link. For example, it is seen that the transmittance improves by about 10% as the ground station altitude is changed from 1 Km to 4 Km. Fig.3 shows the effect of altitude over a range of optical frequencies.

Fig.4 depicts the effect of meteorological visibility on transmittance for 0.532 and 1.064 μm wavelength. For reference, a visibility of 17.0 Km represents clear weather and a visibility of 23.5 Km is defined to be standard clear.

With increasing zenith angle the signal beam has to travel a longer distance in the atmosphere. This results in a decreasing transmittance with the zenith angle, as shown in Fig.5.

3.0 Conclusion

A preliminary site-independent study using generalized atmospheric models to quantify transmittance at optical frequencies for an earth-space path have been completed. The work also quantifies the effect of altitude, which will be helpful in the process of site selection for a ground station. Once a site for the ground station has been selected, a more accurate atmospheric profile for the chosen area can be developed and used to obtain still better estimates of the link loss due to the atmosphere.

4.0 Acknowledgement

The author wishes to thank Kelly Cowles and Garret Okamoto for their help, especially in the acquisition and installation of the necessary computer codes.

5.0 References

1. L.S. Rothman *et al.*, 'AFGL Atmospheric Absorption Line Parameters Calculation: 1982 Edition,' Appl. Opt., vol.22, pp.2247-2256, 1983.

2. F.X. Kneizys *et al.*, 'Users Guide to LOWTRAN7,' Report no. AFGL-TR-88-0177, AFGL, 1988.

3. S.A. Clough *et al.*, 'Atmospheric Radiance and Transmittance: FASCOD2,' Sixth conf. on Atmospheric Radiation, Williamsburg, Va., pp.141-144, 13-16 May, 1986.

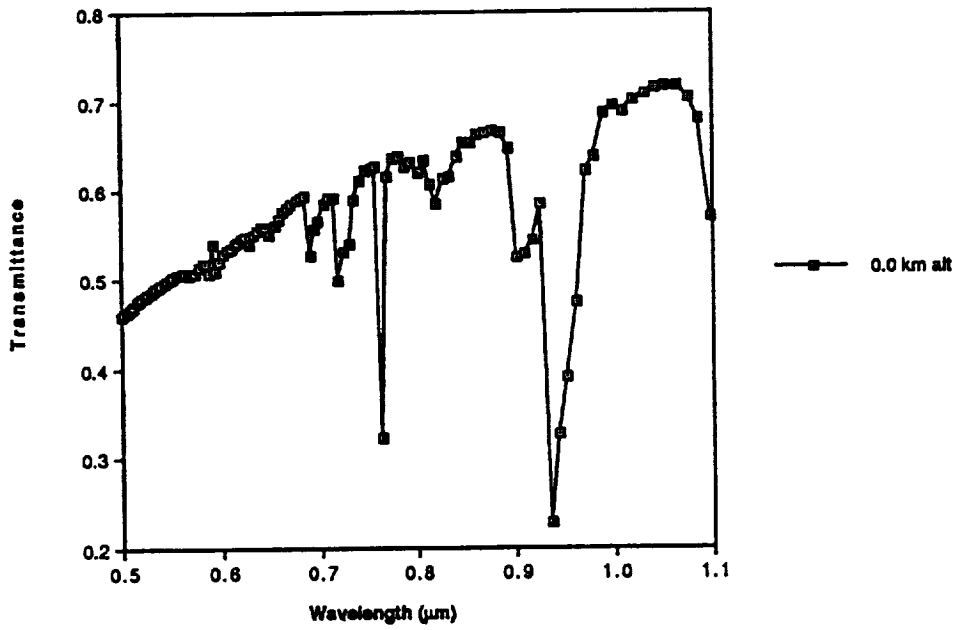

Fig. 1. Transmittance vs. Wavelength with
(i) 1976 U. S. Standard Atmosphere
(ii) Cirrus Attenuation, NOAA Model
(iii) Zenith Angle = 0 degrees
(iv) Visibility = 17.0km

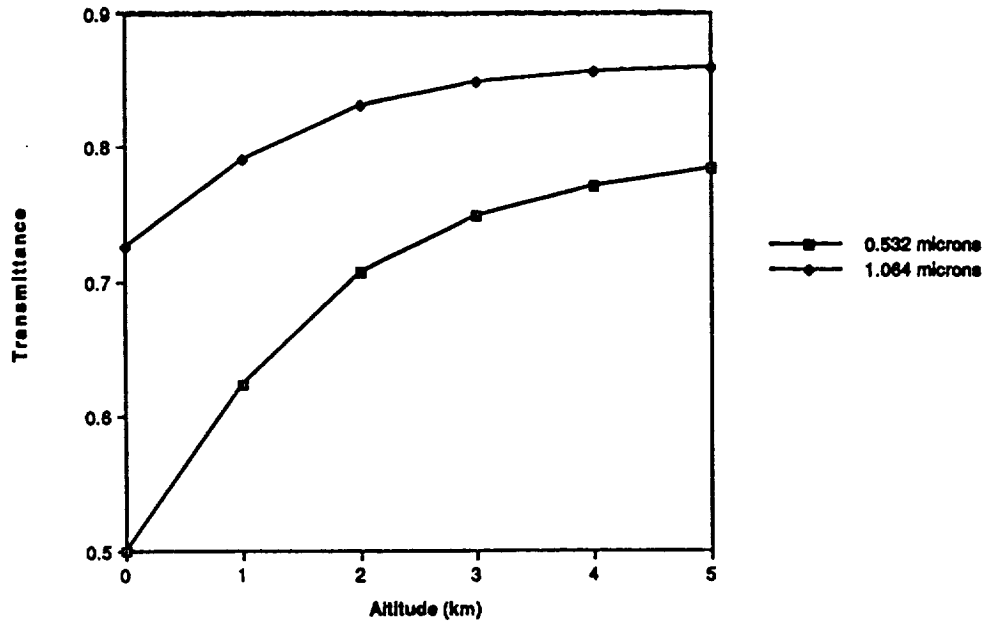

Fig. 2. Transmittance vs. Altitude with
(i) Midlattitude Winter Atmosphere
(ii) Cirrus Attenuation, NOAA Model
(iii) Zenith Angle = 0 degrees
(iv) Visibility = 17.0km

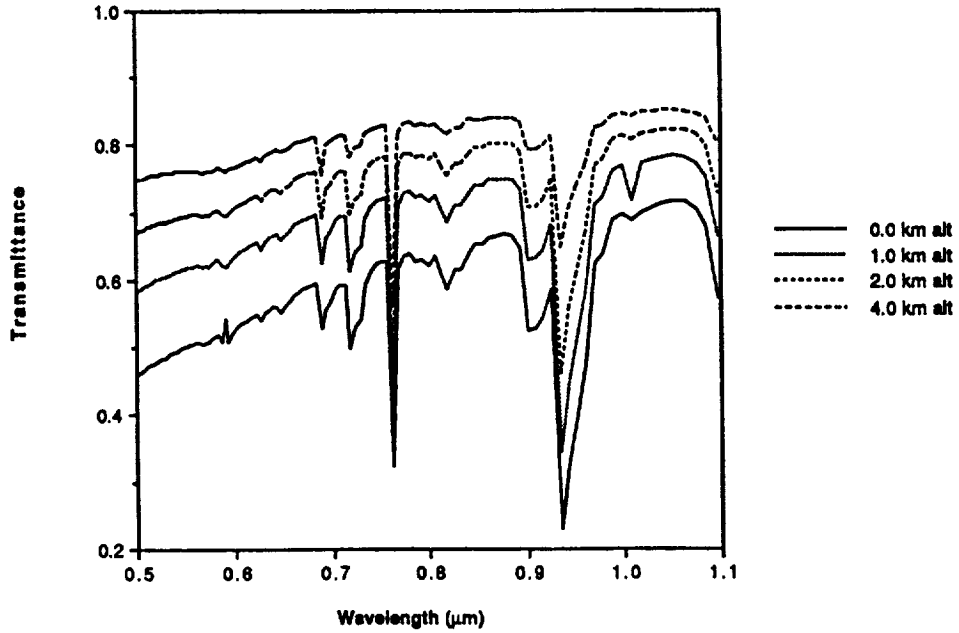

Fig. 3. Transmittance vs. Wavelength with
(i) 1976 U. S. Standard Atmosphere
(ii) Cirrus Attenuation, NOAA Model
(iii) Zenith Angle = 0 degrees
(iv) Visibility = 17.0km

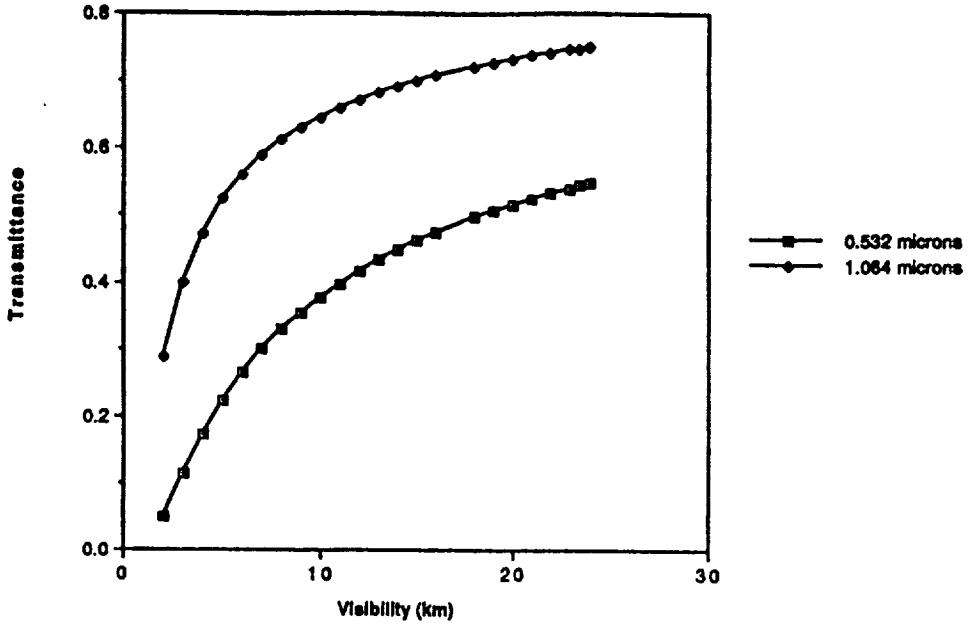

Fig. 4. Transmittance vs. Visibility with
(I) 1976 U. S. Standard Atmosphere
(II) Cirrus Attenuation, NOAA Model
(III) Zenith Angle = 0 degrees
(iv) Altitude = 0.0km

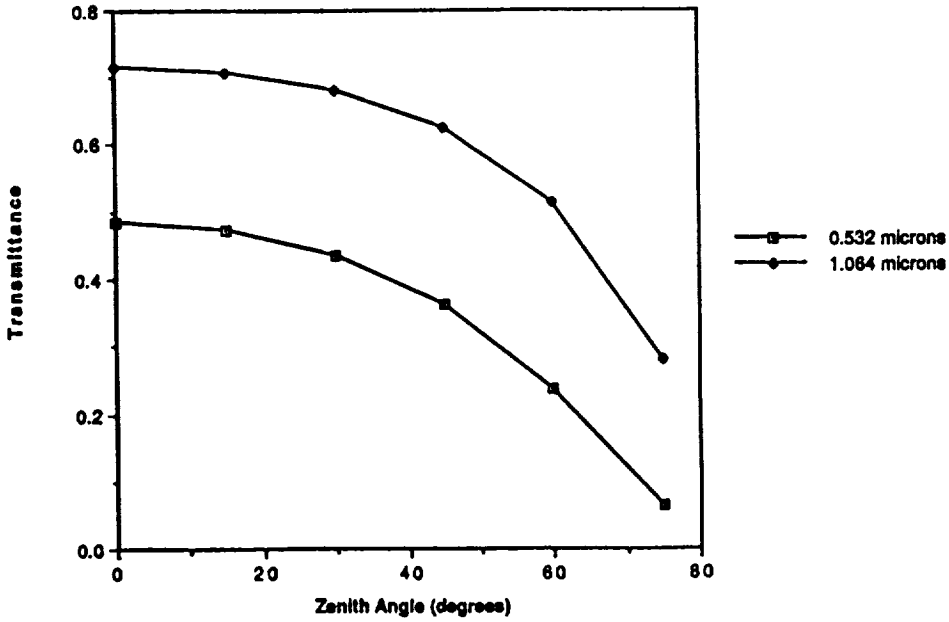

Fig. 5. Transmittance vs. Zenith Angle with
(I) 1976 U. S. Standard Atmosphere
(II) Cirrus Attenuation, NOAA Model
(III) Visibility = 17.0km
(iv) Altitude = 0.0km

RECENT ACHIEVEMENTS OF OPEX

Bertram Arbesser-Rastburg and Owen Turney

European Space Research and Technology Centre
Noordwijk, The Netherlands

Abstract: A group of propagation researchers have joined to prepare for a major campaign of propagation experiments for fixed satellite services using the Olympus satellite. For several years the receiving hardware and data processing procedures have been planned, now, with the launch of the Olympus satellite imminent, experimenters are eager to start the "real work". The aim of this paper is to give a short review of the accomplishments made since the last NAPEX meeting.

1. Introduction

The launch of the European Space Agency's (ESA) OLYMPUS experimental satellite is scheduled for mid 1989. This marks the entry into a new phase for the OLYMPUS Propagation EXperiment (OPEX) group. Some of the experimenters are already fully prepared to start the measurements; the coding of the data processing software is underway and the communication links for distributing vital information are being set up.

2. The OPEX Group

OPEX was set up under ESA auspices in 1980 with the objective of standardizing the essential procedures in equipment calibration and data handling necessary to achieve results that are directly comparable. Much experience was drawn from the COST (CoOperation Scientifique et Technique) activities (actions 25 and 205) that had led to the first Europe-wide collection of Ku-band satellite propagation statistics (Fedi, 1985). Further details on the development of OPEX can be found in the referenced literature (Brussaard, 1988).

Today the OPEX community includes approximately 70 organisations. Of these, about 30 are preparing to make measurements. They are equally divided amongst:

- Universities
- PTTs or Telecommunication entities
- Private or governmental research institutions

Three of the participants are from outside Europe, namely:

- CRC in Ottawa, Canada
- Virginia Tech in Blacksburg, VA

- North Carolina State University in Rayleigh, NC.

The chairman of the OPEX group is Professor Gert Brussaard from the Technical University of Eindhoven in the Netherlands.

3. ESA's role in OPEX

ESA has the overall responsibility of the satellite mission and also has taken on responsibility for three principal aspects of the OPEX collaboration:

- to act as a focal point
- to study new hardware designs for receivers and radiometers
- to have the common data processing software developed

The Propagation Section at ESTEC is in charge of these activities and some more details with particular respect to recent achievements are given below.

3.1 Coordination

ESA is providing an administrative and organisational infrastructure which gives the OPEX group a focal point for information and coordination. Up to now this function mainly concentrated on keeping an electronic mailing list, organizing the OPEX meetings and producing proceedings of the meetings.

More recently a database with information on the different propagation experiments has been established which allows the scope for co-operation between experimenters to be quickly assessed, either in getting their hardware operational or in exchanging data. In the future (once the satellite is in orbit) also the regular dissemination of orbital element data and manoeuvre information will be provided. Communication will be via telex, e-mail and fax.

One of the difficult points in coordinating this collaborative activity is the fact that there is some diversity in the size and scope of individual experiments and in the finances available. This also means that not all the groups arrive at the same level of readiness simultaneously. However, the general enthusiasm of the experimenters and the openness of the discussions make it easy to deal with these discrepancies.

With the number of active experimenters close to 30 it was also found useful to set up smaller working groups of specialists to examine in detail particular questions and to apply their expertise to important decisions. Such a "small user group" was established to monitor the development of software.

3.2 Hardware studies

The Agency has contracted out theoretical and development studies relating to experimental hardware. Specifically the areas of Beacon Receivers and Radiometers were investigated. To this end two studies were completed recently:

- The digital beacon receiver which had been developed by Signal Processors Ltd (Cambridge, U.K.) was delivered to ESTEC as a functional prototype for one receive channel. Instead of a PLL a digital Fourier transform processor is used for carrier frequency tracking. This allows tracking of the signal down to a C/No level of about 15 dB below the point where a PLL receiver (50 Hz loop-BW) "drops out".

- The study of a 20/30 GHz radiometer to measure the liquid water and the water vapor content of the atmosphere has resulted in a design recommendation that combines high accuracy, simple maintenance and low price. The study was carried out by FARRAN Technology (Ballincollig, Ireland)

Apart from these studies directly relevant to OPEX, ESA is also planning for future propagation experiments.
The 44.6/89.2/133.7 GHz beacon payload for the next generation ESA communication satellite (SAT-2) has been studied by Contraves Italiana (Rome, Italy). The study showed that such a payload can be realized with a total weight of less than 15 kg (with redundancy on all active components) and a power consumption of less than 50 Watts.

3.3 Data Processing Software Development

The OPEX group considered in detail standard procedures for both earth station dependent data processing and station independent data analysis. The aim being to ensure that the formation of event data and its subsequent comparison and exchange could be carried out without worries regarding varying data treatment procedures.

ESA placed a contract with Siemens Austria and CSR Ltd (U.K.) for the study of standardized procedures and software for the processing of propagation data. This study resulted in a clear definition of the software requirements and the architectural design and was completed in January 1989.

Now the contract for the development of the software is underway and will be completed by May 1990. The work is being carried out by Siemens Austria (Vienna) with support from IAS (Graz, Austria). The software design and development must take into account the different computer systems used by the experimenters. To ensure portability UNIX and VMS have been chosen as operating systems and a limited number of computer systems are going to be supported. The chosen targets are 80386 based PCs with

AT bus, VaxStations and HP9000 workstations. The adoption of "standard" software tools and packages was also found to be a necessity. The WIMP (Windows, Icons, Mouse, Pointing) based interface "X-Windows" and the graphics package "GKS" (Graphical Kernel System) were selected for the human-computer-interface and for graphics respectively. The programming language chosen is "C" and the C-ISAM library is used for data and file handling tasks.

The design was user driven at all stages. This involved frequent liaison and demonstrations with the so called Small User Group, representing the wider body of OPEX. On completion of the software development full documentation including a Software User Manual will be issued to users.

4. OPEX Meetings

Two OPEX meetings have been held since last summer. The first one, OPEX 11 was held in June 1988 in Copenhagen, being hosted by the Danish PTT. There were more than 50 participants representing nearly all experimenters and some of the companies involved in the design of experimental hardware and software.

OPEX 12 took place in Vienna in April 1989 with the support of Siemens Austria and T.U. Graz. Again, close to 60 people turned up. The status of the satellite and payload as well as the ground segment and standardized software were discussed in detail. Numerous presentations were also given on both, status of preparations as well as useful observations relevant to making propagation measurements. All papers and reports were jointly published in conference proceedings. For the OPEX group the OLYMPUS Utilisation Conference which also took place in Vienna immediately after the OPEX meeting provided an ideal opportunity to find out about the four other OLYMPUS payloads and their uses.

A redraft of the OLYMPUS Propagation Package User Guide was also issued, containing important results of tests on the payload transmit system.

5. Plans

After the Olympus satellite has reached its final orbital position at 19 deg West (approximately 22 days after launch), a phase of careful in-orbit testing will commence. This will take over two months. The beacon payload will be tested for e.i.r.p. (co- and cross-polar), polarisation orientation, power- and frequency stability and phase noise. The tests will be carried out in Redu (Belgium) using specially built measurement stations. After completion of the IOT the propagation measurements can start.

The software development will arrive at a down-scaled prototype of the pre-processing package in November of this year and the final acceptance test (for the 80386-software) is scheduled

for April 1990. It is planned to have a small training workshop for the users at this time.

6. Conclusion

It has been a busy and productive year for OPEX. The preparation of facilities to receive the OLYMPUS propagation beacons made a big step forward in most places. Some old ground stations have been refurbished, many have been constructed "from scratch" and are ready to start measurements as soon as they can pick up a signal from 19 degrees West. We are all confident that the careful planning, attention to detail and co-operation on a wide scale will ensure the success of this campaign.

References

Brussaard, G. "The Olympus Propagation Experiment OPEX: A Unique Example of European Cooperation", ESA Bulletin, No 54, pp. 34-38, May 1988

Brussaard, G. "OPEX- Olympus Propagation Experiment", Proceedings NAPEX XII, Syracuse, N89-11090, pp. 140-145, Aug 1988

TIME CHART OLYMPUS DATA PROCESSING

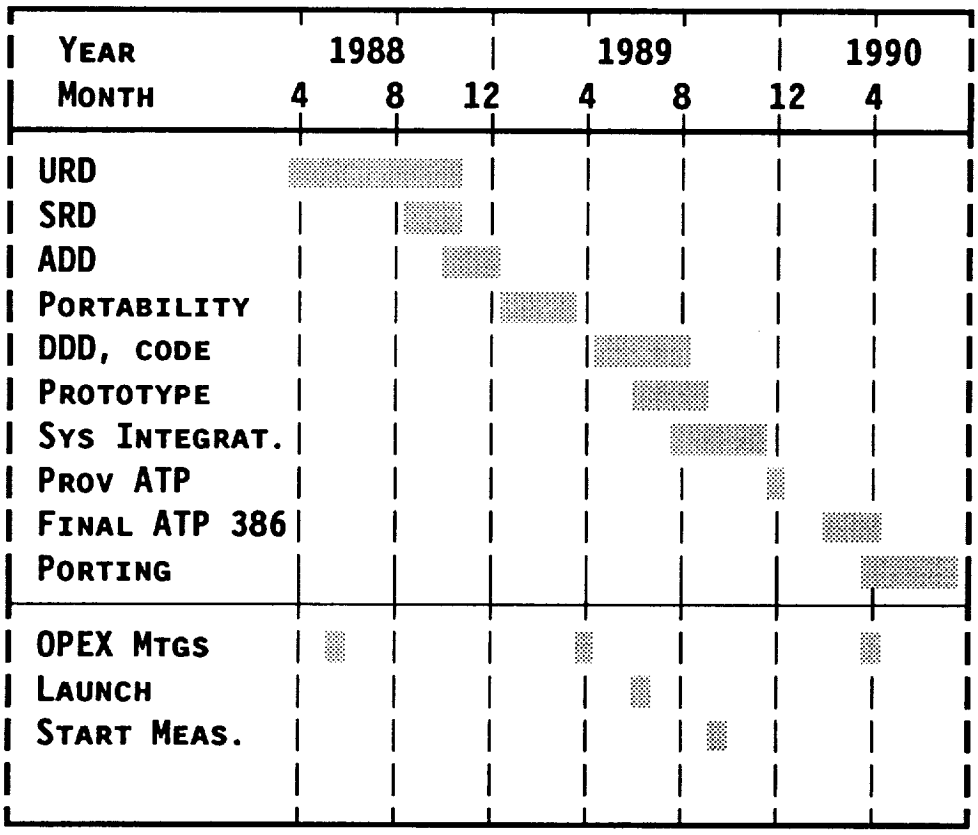

URD...USER REQUIREMENT DOCUMENT
SRD...SOFTWARE REQUIREMENT DOCUMENT
ADD...ARCHITECTURAL DESIGN DOCUMENT
DDD...DETAILED DESIGN DOCUMENT

THE ITALSAT EXPERIMENT

by A. Paraboni,

Dipartimento di Elettronica del Politecnico di Milano, Piazza L. da Vinci 32, 20133 Milano, Italy

FOREWORD

This note gives some succint information on the ITALSAT millimetric waves propagation experiment, to be conducted with the ITALSAT satellite, whose launch is foreseen in the middle of 1990.

The main purpose of the ITALSAT project is the one of experimenting advanced technologies and techniques employing the 20/30 GHz bands in wideband telecommunications.

Among the most qualified features of this system there certainly are the multispot antenna (covering the Italian territory by six beams with full connectivity among them in the preoperational version) and the exchange function performed directly on board.

The preoperational version will also carry an advanced propagation payload allowing measurement in the 40 and 50 GHz bands. These beacons, in addition to the telemetry one at 20 GHz, are the ones which constitute the subject of the present note.

The satellite is owned by the Italian Research Council (CNR) and the management, originally committed to the Piano Spaziale Nazionale, has been passed today to a new body recently created, the Italian Space Agency (ASI), to which requests for further information can be addressed.

ITALSAT is being entirely developed and realized by SELENIA SPAZIO.

The scientific responsibility of the propagation experiment, lays, on behalf of ASI, under the author of the present note, who is also member of the Centro di Studio per le Telecomunicazioni Spaziali (a body of the CNR situated by the Politecnico di Milano), in which operates as a researcher.

THE PROPAGATION EXPERIMENT

ITALSAT will allow propagation experiments in the 20-40 and 50 GHz frequency bands.

Remarkable characteristics of the satellite transmitter are the following:

-European antenna coverage

-long duration (5 years)

-high EIRP

-coherence among all the transmitted signals

-dual polarisation transmission at 50 GHz (commutation at 1KHz)

-angular modulation of the 40 GHz beacon (sidelines at +500Mhz from the central line)

Exploiting all the possibilities offered by the satellite it will be possible to achieve a very accurate and complete characterization of the radio channel practically up to the higher limit of the present frequency allocation recently established by the WARC.

Indeed, in addition to attenuation and depolarisation, measurable at all frequencies (only in North Europe the 20 GHz beacon is not available), the following activities will be possible:

-complete identification of the depolarising channel at 50 GHz (similarly to OLYMPUS at 20 GHz), which allows characterization in any polarisation;

-identification of the frequency response (amplitude and phase distortion) around 40 GHz by comparing the amplitude and phase of the sidelines;

-identification of the phase characteristic of the transfer channel across the entire band, by comparing the phase shifts of all the received signals (20,40 and 50 GHz);
-assessment of the dynamic characteristics of the received signal, including rapid variations (scintillations), owing to the high EIRP and phase stability of the on board source;
-assessment of the frequency scaling techniques, both long and short term, up to high attenuation levels;
-assessment of the incoherent scattering by water particles, even if only in particular meteorological conditions.

Naturally the value of the direct measurements can be strongly enhanced by associating to the beacon receivers some ancillary instruments such as one or more radiometers, rain-gauges, meteorological radars and other meteorological instruments. As well known, this allows determining the relation existing between directly measured and estimated attenuation and calibrating these "indirect" estimators for extensive measurements taken elsewhere. In addition the radiometer can "calibrate" the beacon itself by providing the correct zero reference.

By coordinating the measurements taken by various experimenters through Europe other fundamental achievments can be pursued. Among them it is worth reminding the climatological characterization of the European area and the large scale correlation of fading, recently recognized as a necessary input for the design of advanced satellite systems based on the "on-board resource sharing" philosophy.

As the past experience with SIRIO, OTS and COST 205 has

shown, the significance of propagation experiments is dramatically increased if a good coordination level among the participants can be reached.

Moreover it is now evident that the coordination problems are enormously reduced if things are prepared well in advance.

Bringing ahead these previous experiences the OPEX (Olympus Propagation Experiment) group has been set up some years ago and has now reached an excellent level of coordination: procedures are being agreed and written within a common frame aiming at arriving to the complete interchangeability of all the data among experimenters and, more importantly, to the habit of putting and facing problems in a collective manner.

Of course we hope that this experience will be continued with ITALSAT, where, due to the new and perhaps more critical aspects being investigated, the coordination becomes a still more necessary prerequisite.

The long term scientific objectives that can be pursued with ITALSAT are very stimulating and perhaps hard foreseeing in their globality.

In the past, when the bands to be investigated were below 20 GHz, it was clear that attenuation by rain, specially convective rain, was the major problem to be tackled. The scientific comunity went far beyond this subject however! In fact the extraordinary collective effort of investigation throughout the world lead to significant achievments also in neighboring fields as meteorology, remote sensing and basic EM theory.

The attenuation measurements in itself were taken in a different way, enlarged and additioned with other measurements just as the requirements of the telecommunication engineering were pointed out. Along this line we have arrived to the threshold of the millimetric waves (30 GHz) which are going to be investigated with the forthcoming satellite OLYMPUS. At millimetric waves the new scenario for the propagation activity, to be performed with ITALSAT, will surely lead us to tackle different problems, most of them hard to be foreseen from the present standpoint.

The well established availability and quality objectives in the probability range 0.01-0.1 percent of time will probably lead to absolutely unfeasible system margins so that scaling rain attenuation up to the corresponding levels will probably constitute little more than a theoretical exercise.

On the other hand increasing the probability other phenomena become important, if not dominant in some cases (stratified rain, brightband, scintillation by irregularities of the refractive index, absorption by water vapour in gaseous or saturated form, depolarisation by ice needles, etc.).

For instance attenuation by clouds at 50 GHz is expected to be of the order of 1.5 dB in average, possibly much higher in extreme cases. Similarly scintillations of a 2-3 dB peak to peak should not be uncommon even for high elevation links.

From what precedes it seems that predictions will no more entirely based on rain gauge data but possibly on different meteorological data according to prediction rules still to be devised and tested.

In addition to these activities, somehow 'traditional' with respect to the technical objectives, one can consider the possibility of investigating on different and non-traditional areas (but perhaps important for the future systems as well) pertaining to the electromagnetic propagation basics: incoherent radiation, ray bending and multipath, which are probably of greater importance at 40/50 GHz and surely better observable with antenna systems of limited size.

EXPERIMENT DEFINITION

The ITALSAT propagation meaurements are performed on down links at the three frequencies 20,40 and 50 GHz.

The payload characteristics are given in the additional material annexed, which gives the footprint of the onboard antennas, the EIRP values (with the associated fluctuations) and other various figures pertaining to the transmitter. It is important to remind that the three beacons are coherent to each other so that the receiver locking can be virtually based on the signal arriving at earth with greater strength at a particular instant.

The following paramaters can be directly measured:

1) CPA level at 20 GHz in vertical polarisation
2) CPA level at 40 GHz in circular polarisation
3) CPA level at 50 GHz in vertical and horizontal polarisations
4) XPD level and phase at 20 GHz
5) XPD level and phase at 40 GHz
5) XPD level and phase at 50 GHz
6) differential level and phase between the two polarisations at 50 GHz (fast commutated at 1 Khz rate)
7) differential phase shift between the sidelines and the carrier at 40 GHz (phase distortion)
8) differential amplitude between the sidelines at 40 GHz
9) differential phase between any pair of lines at 20,40 and 50 GHz
10) cross polar levels and phases of the sidelines at 40 GHz

Unfortunately the 20 GHz beacon is not visible from all sites in Europe as power budget constraints, due to the use as

telemetry beacon, put an inferior limit to the antenna gain.

Reception of this frequency concurrently with the others is however extremely important both for the assessment of the frequency scaling technique down to the previously explored frequencies and for the possibility of simultaneous measurements with OLYMPUS (orbital diversity assessment).

In any case the coordination of the ITALSAT measurements with the OLYMPUS ones will offer the unique possibility of testing the effectiveness of the large scale diversity techniques at different frequencies, in addition to the more obvious, but all the same important, possibility of extending the number of points where measurements are taken, with benefit for climatology and modelling purposes.

In Italy three large stations are foreseen; one in Spino d'Adda, near Milan, menaged by the Centro di Studio per le Telecomunicazioni Spaziali of the Consiglio Nazionale delle Ricerche (CSTS/CNR), a second in the Rome managed by the Istituto Superiore delle Poste e Telecomunicazioni and Fondazione Ugo Bordoni (ISPT/FUB) and a third one in Turin, managed by the Centro Studi e Laboratori Telecomunicazioni (CSELT).

The link budget of the receiving stations, which will receive the three signals using a common phase locked source, is shown table 1.

With the margins reported, a worst case operativity of some 0.05% (in Italy) is foreseen (locking at 50 GHz); obviously this is expected to increase noticeably by exploiting the possibility to lock the lower frequency beacons. The table is all the same useful as reference for stand alone receivers.

TABLE 1

ITALSAT PROPAGATION EXPERIMENT LINK BUDGET

Frequencies(GHz)	20	40	50
EIRP(dBW-mod. carriers)	23.7	24.8	26.8
Free space attn. (dB)	209.6	215.6	217 5
Antenna diameter(m)	3.5	3.5	3.5
Antenna gain (DB)	55.1	60.6	62.3
Receiver noise factor(dB)	4	5	6
Overall noise temp.(°K)	728	917	1154
G/T (dB)	26.5	30.9	31.6
C/N per Hertz (DB)	69.3	68.7	69.5
PLL bandwidth (dBHz)	20	20	20
C/N in 100 Hz (DB)	49.3	48.7	49.5
C/N limit (DB)	7	7	7
Dynamic range(dB)	42.3	41.7	42.5

Additional information concerning the

ITALSAT PROPAGATION EXPERIMENT

MAIN SATELLITE CHARACTERISTICS (prop. exp.)

EUROPEAN ANTENNA COVERAGE

LONG DURATION

HIGH EIRP

COHERENCE AMONG ALL THE TRANSMITTED SIGNALS

DUAL POLARISATION TRANSMISSION AT 50 GHz

ANGLE MODULATION OF THE 40 GHz BEACON

ITALIAN STATIONS FOR THE ITALSAT PROPAGATION EXPERIMENT:

SPINO D'ADDA	by	CNR/CSTS
ROMA	by	ISPT/FUB
TORINO	by	CSELT

EXPERIMENTAL ACTIVITIES ALLOWED BY ITALSAT

PREDICTION OF PROPAGATION PARAMETERS FOR FUTURE SYSTEMS DESIGN (CPA, XPD, PHASE SHIFTS ETC.)

IDENTIFICATION OF THE EM CHANNEL PROPERTIES

ASSESSMENT OF METHODOLOGIES FOR INDIRECTLY ASSESSING PROPAGATION PARAMETERS (RADIOMETERS, RADARS)

CHARACTERIZATION OF WIDE AREAS WITH RESPECT TO THE STATISTICS OF VARIOUS PARAMETERS

DEVISING/ASSESSING OF PREDICTION METHODS FOR SINGLE AND MULTIPLE STATISTICS IN LITTLE KNOWN PROBABILITY RANGES

IDENTIFICATION OF THE DOMINATING MECHANISMS AFFECTING PROPAGATION AT MILLIMETER WAVES

ATMOSPHERE SOUNDING

SYSTEM-ORIENTED INVESTIGATIONS (small/large scale diversity, common on board resource systems up-path power control systems

PHYSICAL AND STATISTICAL MODELS

RADIO MEASUREMENTS ALLOWED BY ITALSAT

ATTENUATION AT 20, 40 AND 50 GHZ

DEPOLARISATION AT 20, 40 AND 50 GHz

COMPLETE IDENTIFICATION OF THE DEPOLARIZING CHANNEL AT 50 GHz

IDENTIFICATION OF THE FREQUENCY RESPONSE (channel amplitude and phase distortion) AT 40 GHz

IDENTIFICATION OF THE PHASE CHARACTERISTIC OF THE TRANSFER CHANNEL ACROSS THE ENTIRE BAND

ASSESSMENT OF THE DYNAMIC CHARACTERISTICS OF THE RECEIVED SIGNALS (scintillations, fade duration and slopes etc.)

ASSESSMENT OF THE FREQUENCY SCALING TECHNIQUE

ASSESSMENT OF THE INCOHERENT SCATTERING BY WATER PARTICLES (even only in particular meteo. conditions)

ELECTRICAL PARAMETERS MEASURABLE AT THE ITALSAT RECEIVER

CPA LEVEL AT 20 GHz IN VERTICAL POLARISATION

CPA LEVEL AT 40 GHz IN CIRCULAR POLARISATION

CPA LEVEL AT 50 GHz IN VERTICAL AND HORIZONTAL POL.

XPD LEVEL AND PHASE AT 20 GHz

XPD LEVEL AND PHASE AT 40 GHz

XPD LEVEL AND PHASE AT 50 GHz (both hor. and vert, pol)

DIFFERENTIAL LEVEL AND PHASE BETWEEN THE TWO POLARISATIONS AT 50 GHz (fast commutated at 1KHz)

DIFFERENTIAL PHASE SHIFT BETWEEN THE SIDELINES AND THE CARRIER AT 40 GHz (phase distortion)

DIFFERENTIAL AMPLITUDE BETWEEN THE SIDELINES AT 40 GHz)

DIFFERENTIAL PHASE BETWEEN ANY PAIR OF LINES AT 20,40 AND 50GHz

CROSS POLAR LEVELS AND PHASES OF THE SIDELINES AT 40 GHz

UNUSUAL MEASUREMENT OF PROBABLE INTEREST AT MILLIMETRIC WAVES

INCOHERENT RADIATION

RAY BENDING

MULTIPATH (?)

ITALSAT PROPAGATION EXPERIMENT
LINK BUDGET (italian stations)

frequencies	20	40	50
EIRP	23.7	24.8	26.8
fr.sp. attn.	209.6	215.6	217.5
antenna diam.	3.5	3.5	3.5
antenna gain	55.1	60.6	62.3
noise fact.	4	5	6
temperature	728	917	1154
G/T	26.5	30.9	31.6
C/N per Hz	69.3	68.7	69.5
PLL bandw.dB	20	20	20
C/N in 100 Hz	49.3	48.7	49.5
C/N limit	7	7	7
dynamic range	42.3	41.7	42.5

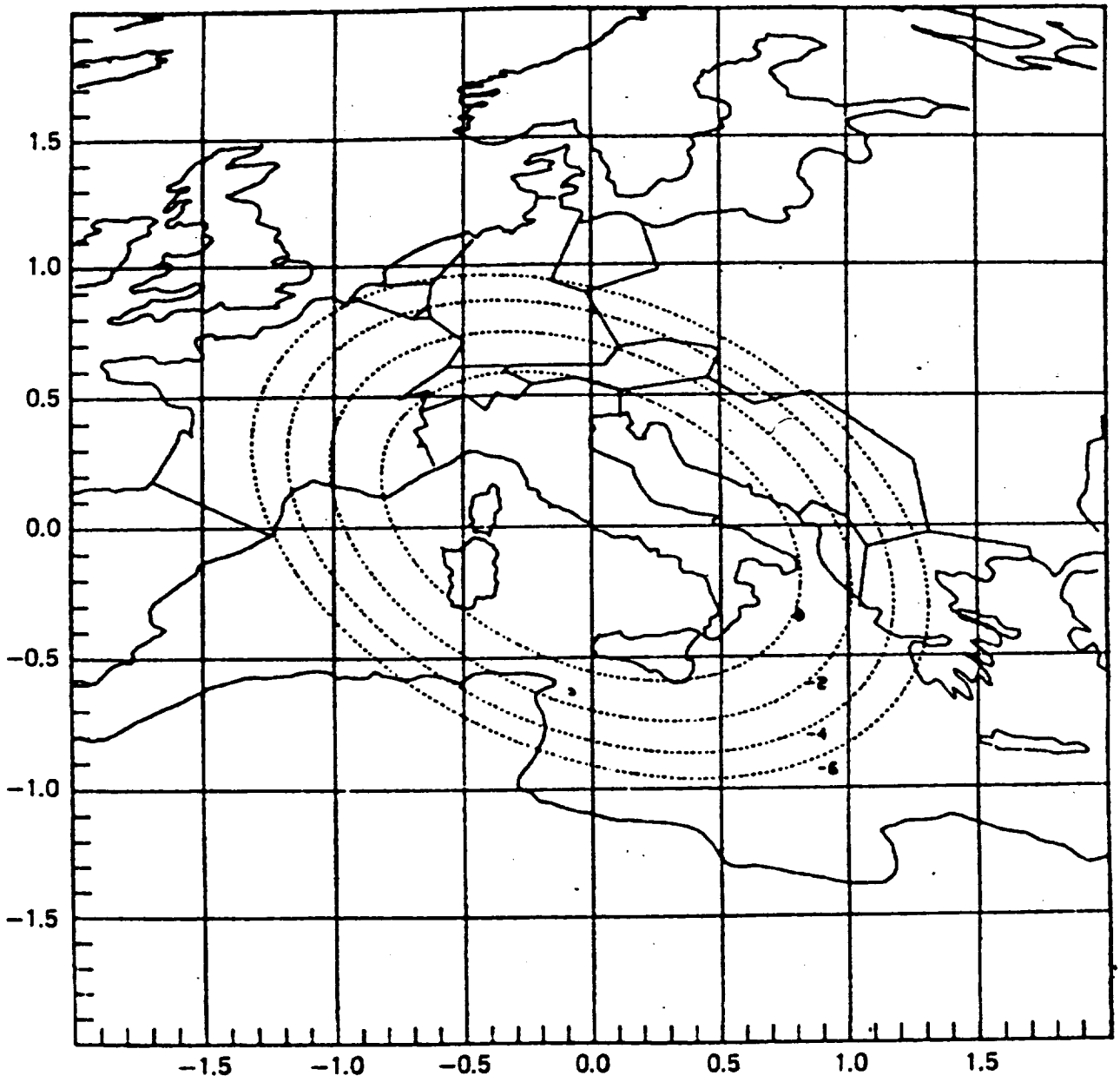

20 GHz beacon coverage

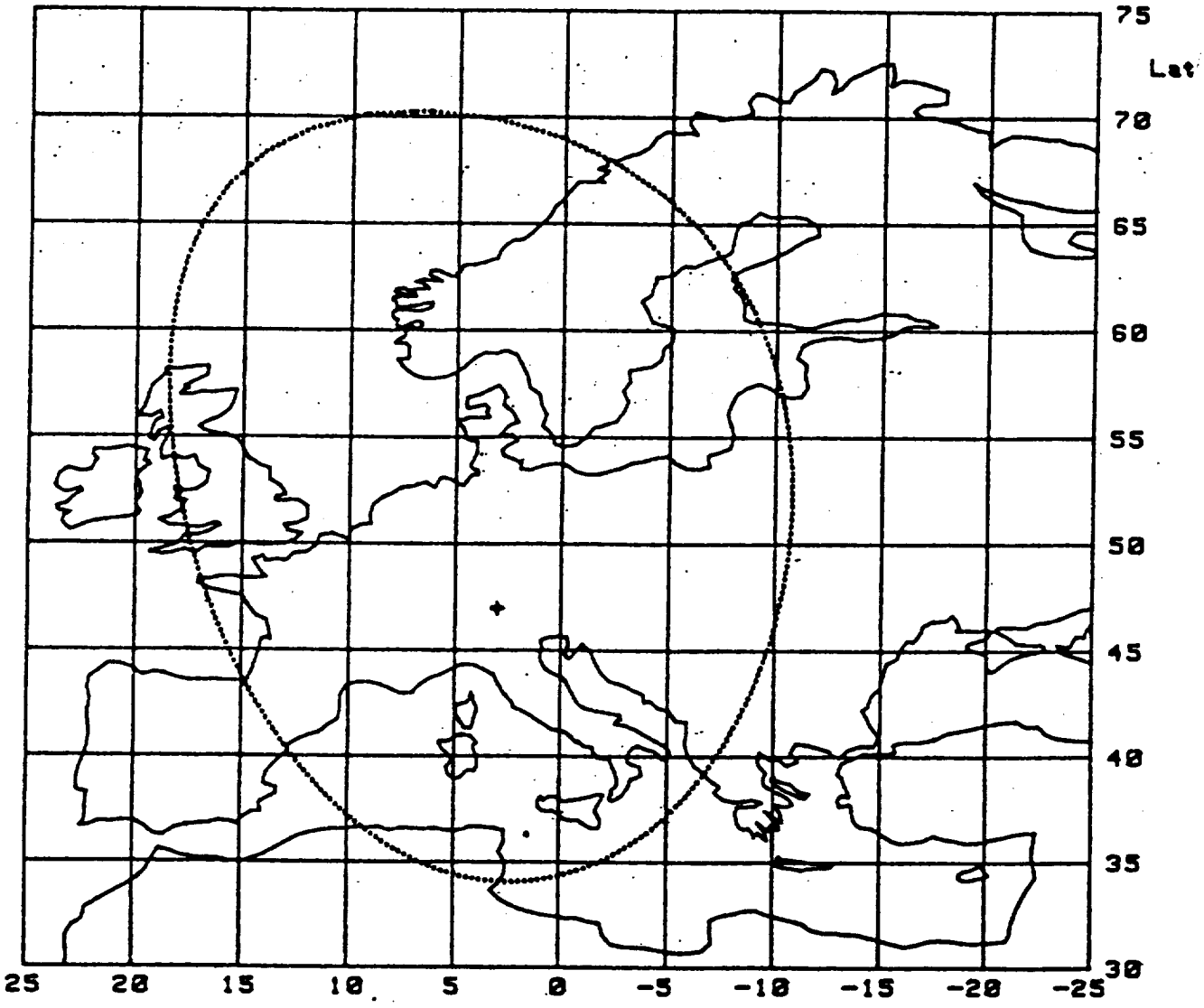

40/50 GHz beacon coverage

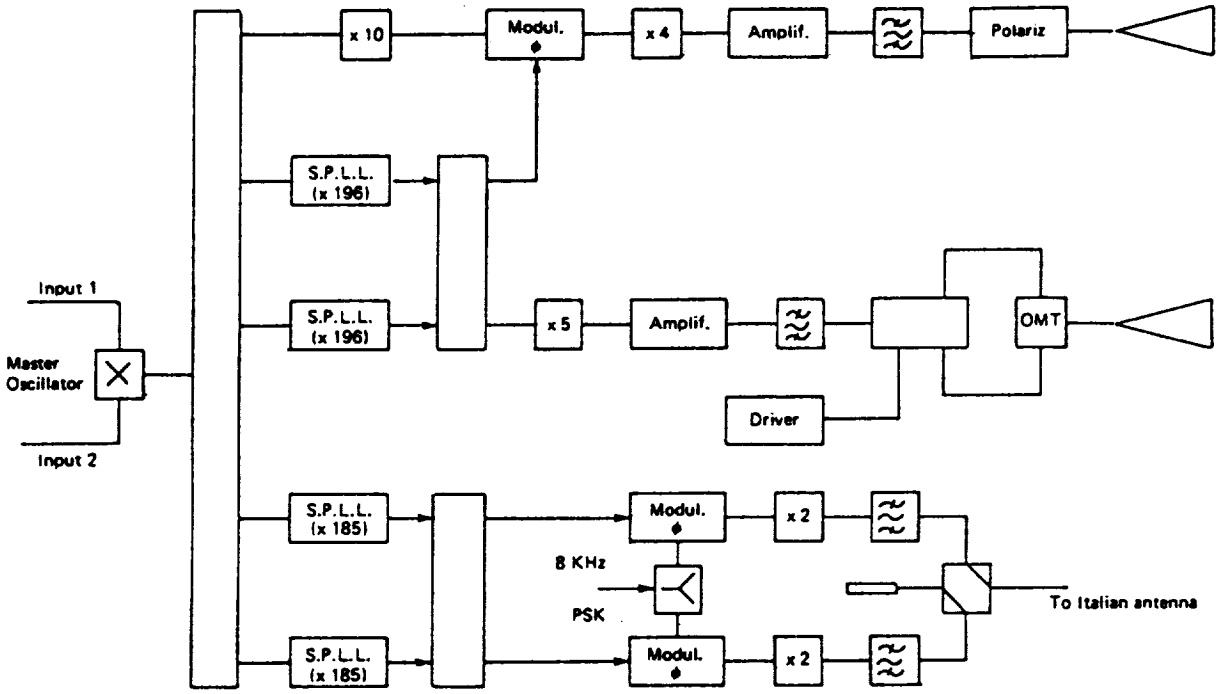

Synthesis of the ITALSAT beacon frequencies

Session 3

ADVANCED COMMUNICATIONS TECHNOLOGY SATELLITE

Chairman:

Dr. Faramaz Davarian
Jet Propulsion Laboratory

ADVANCED COMMUNICATIONS TECHNOLOGY SATELLITE (ACTS) PROGRAM

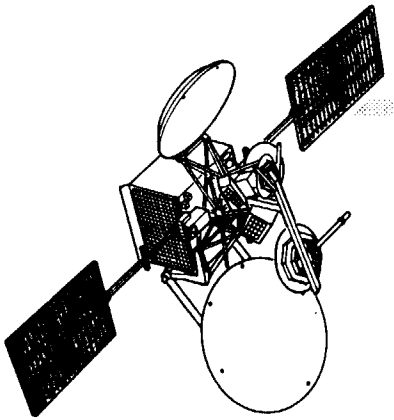

Presentation to:

NAPEX

Dean A. Olmstead

NASA Headquaters

June 30, 1989

ACTS

NASA

ACTS

PROGRAM OVERVIEW

WHAT IS ACTS?

- ADVANCED COMMUNICATIONS TECHNOLOGY SATELLITE (ACTS)
- AN EXPERIMENTAL SATELLITE SPONSORED BY NASA TO PAVE THE WAY FOR NEXT GENERATION COMMUNICATION SATELLITE
- INCORPORATE ADVANCED CONCEPTS
  - — ELECTRONICALLY HOPPING SPOT-BEAM ANTENNAS
  - — ONBOARD PROCESSING AND SWITCHING
  - — KA-BAND TRANSMISSION
- REDUCE RISK SUFFICIENTLY TO STIMULATE COMMERCIAL USE OF TECHNOLOGIES
- TARGET LAUNCH DATE: MAY. 1992
- MISSION LIFE: 2-4 YEARS

OBJECTIVES OF ACTS PROGRAM

- Maintain U.S. Position of Preeminence in the World's Communications Satellite Market in the Face of Strong Foreign Competition
  - — Balance of Trade
- Develop Advanced High Risk Technologies Which Fall Outside Sponsorship Capability of the Private Sector
- Encourage Widest Possible Participation by all U.S. Institutions in the Program (Private, Government, DOD, Academia)
- Improve Productivity of Future NASA Missions Through Technology Advances in Communications

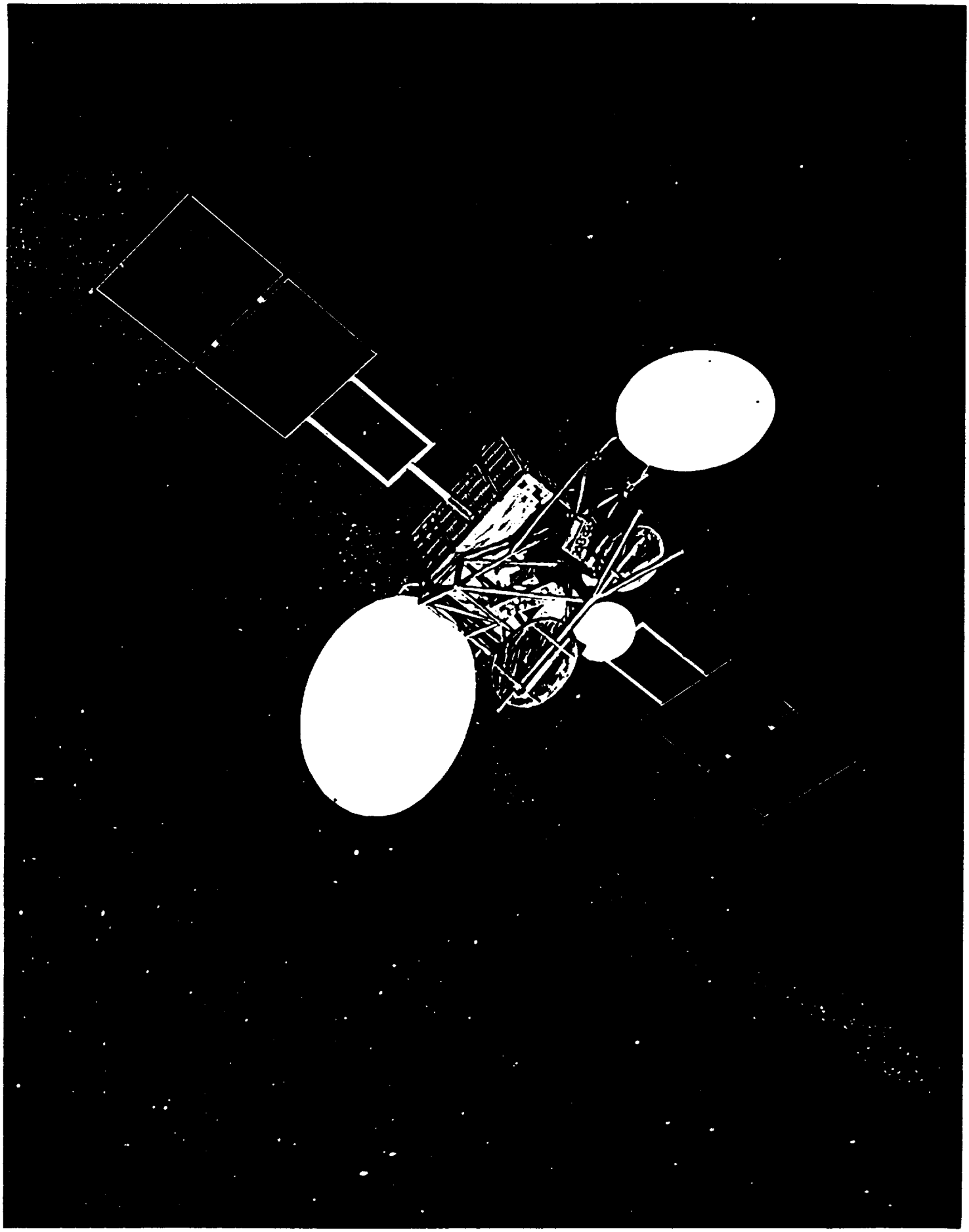

NASA

ACTS ADVANCED COMMUNICATIONS TECHNOLOGY SATELLITE

NASA HEADQUARTERS

- OFFICE OF SPACE SCIENCE AND APPLICATIONS
  Dr. L.A. Fisk
- DIRECTOR OF COMMUNICATIONS & INFORMATION SYSTEMS DIVISION
  Ray J. Arnold

ACTS PROGRAM MANAGER
Dean A. Olmstead
DEPUTY PROGRAM MANAGER
William T. Kondik
PROGRAM EXPERIMENTS MANAGER
William T. Kondik (Acting)

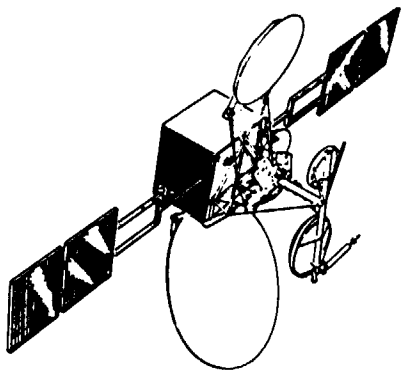

NASA LEWIS RESEARCH CENTER

- SPACE FLIGHT SYSTEMS DIRECTORATE
  Vernon J. Weyers

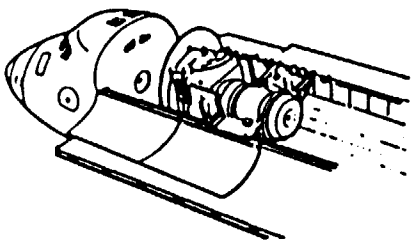

ACTS PROJECT OFFICE

PROJECT MANAGER
Dr. Richard T. Gedney
PROJECT EXPERIMENTS MANAGER
Ronald J. Schertler

EC89-305(1)
1-26-89

ACTS Team

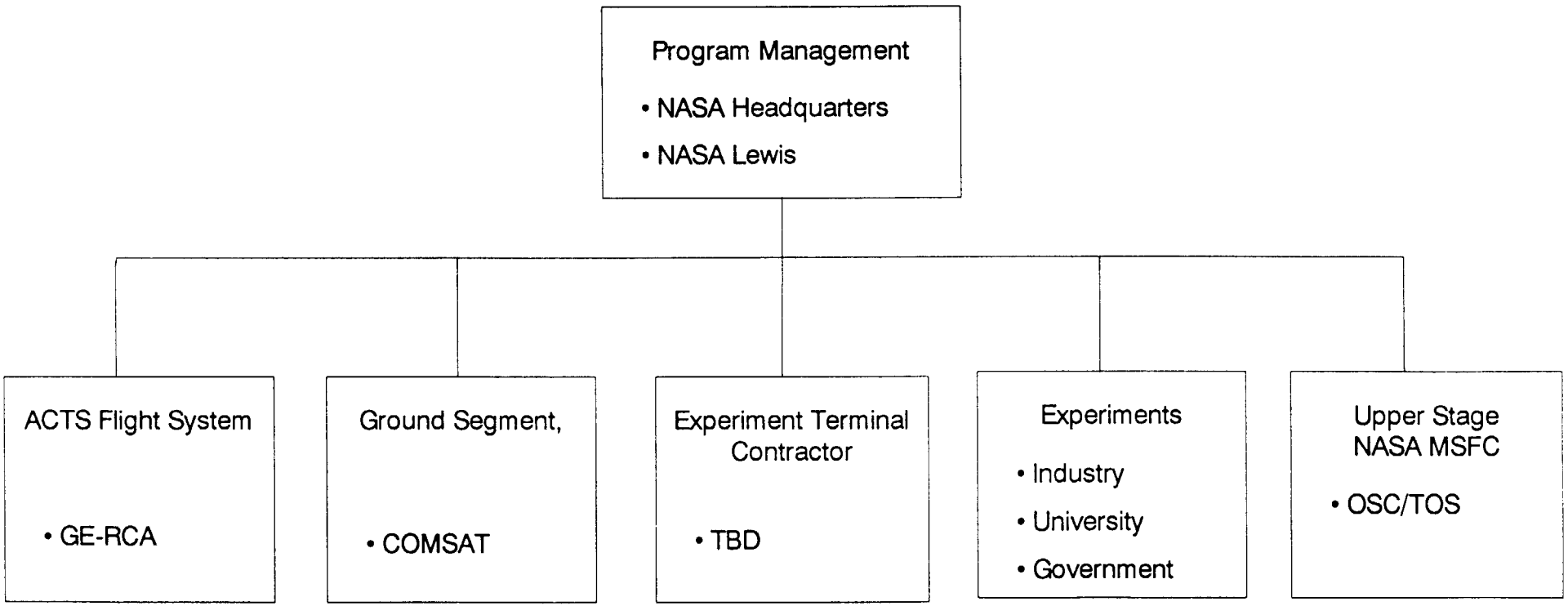
Program Management
• NASA Headquarters
• NASA Lewis
ACTS Flight System
• GE-RCA
Ground Segment,
• COMSAT
Experiment Terminal Contractor
• TBD
Experiments
• Industry
• University
• Government
Upper Stage NASA MSFC
• OSC/TOS

NASA ADVANCED COMMUNICATIONS TECHNOLOGY SATELLITE (ACTS)

MAJOR PROGRAM ELEMENTS

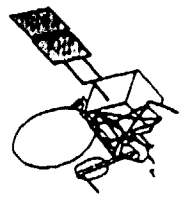

CY'S

79 80 81 82 83 84 85 86 87 88 89 90 91 92 93 94 95 96

OPERATIONAL MARKET AND SYSTEMS STUDIES

EXPERIMENTAL SYSTEM DEFINITION STUDIES

SPACECRAFT AND GROUND TERMINAL SYSTEMS TECHNOLOGY DEVELOPMENT

ACTS FLIGHT AND GROUND SYSTEMS DEVELOPMENT

NOTICE OF INTENT

NASA RESEARCH ANNOUNCEMENT

ACTS LAUNCH

EXPERIMENTS PLANNING EXPERIMENTER TERMINAL DEVELOPMENT

CONDUCT EXPERIMENTS

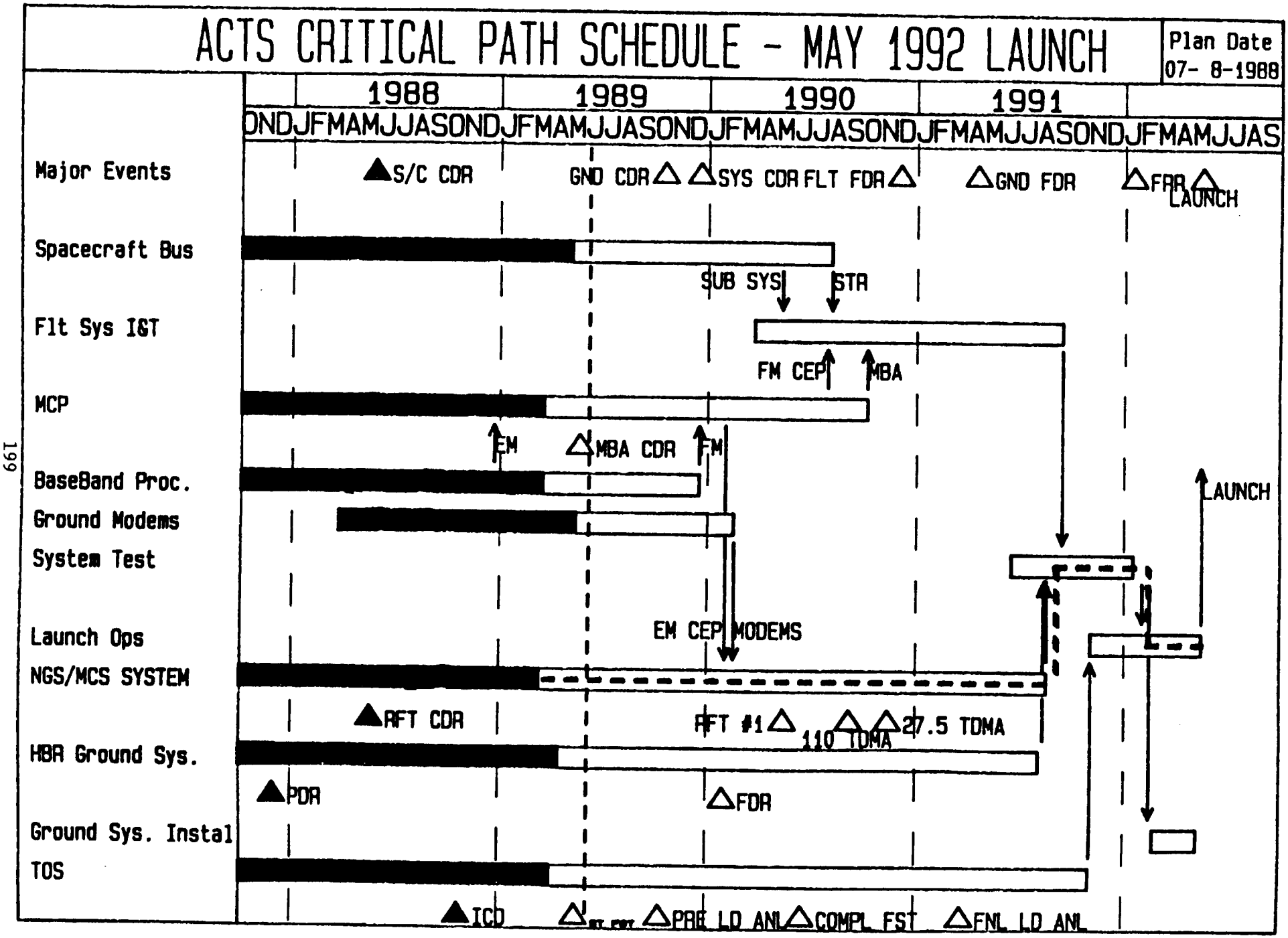
ACTS CRITICAL PATH SCHEDULE - MAY 1992 LAUNCH
Plan Date
07- 8-1988
1988
1989
1990
1991
ONDJFMAMJJASONDJFMAMJJASONDJFMAMJJASONDJFMAMJJAS
Major Events
S/C CDR
GND CDR
SYS CDR
FLT FDR
GND FDR
FRR
LAUNCH
Spacecraft Bus
SUB SYS
STR
Flt Sys I&T
FM CEP
MBA
MCP
EM
MBA CDR
FM
BaseBand Proc.
Ground Modems
System Test
LAUNCH
Launch Ops
EM CEP MODEMS
NGS/MCS SYSTEM
RFT CDR
RFT #1
110 TDMA
27.5 TDMA
HBR Ground Sys.
PDR
FDR
Ground Sys. Instal
TOS
ICD
PRR LD ANL
COMPL FST
FNL LD ANL

ACTS PROGRAM NEARLY 3/4 COMPLETED

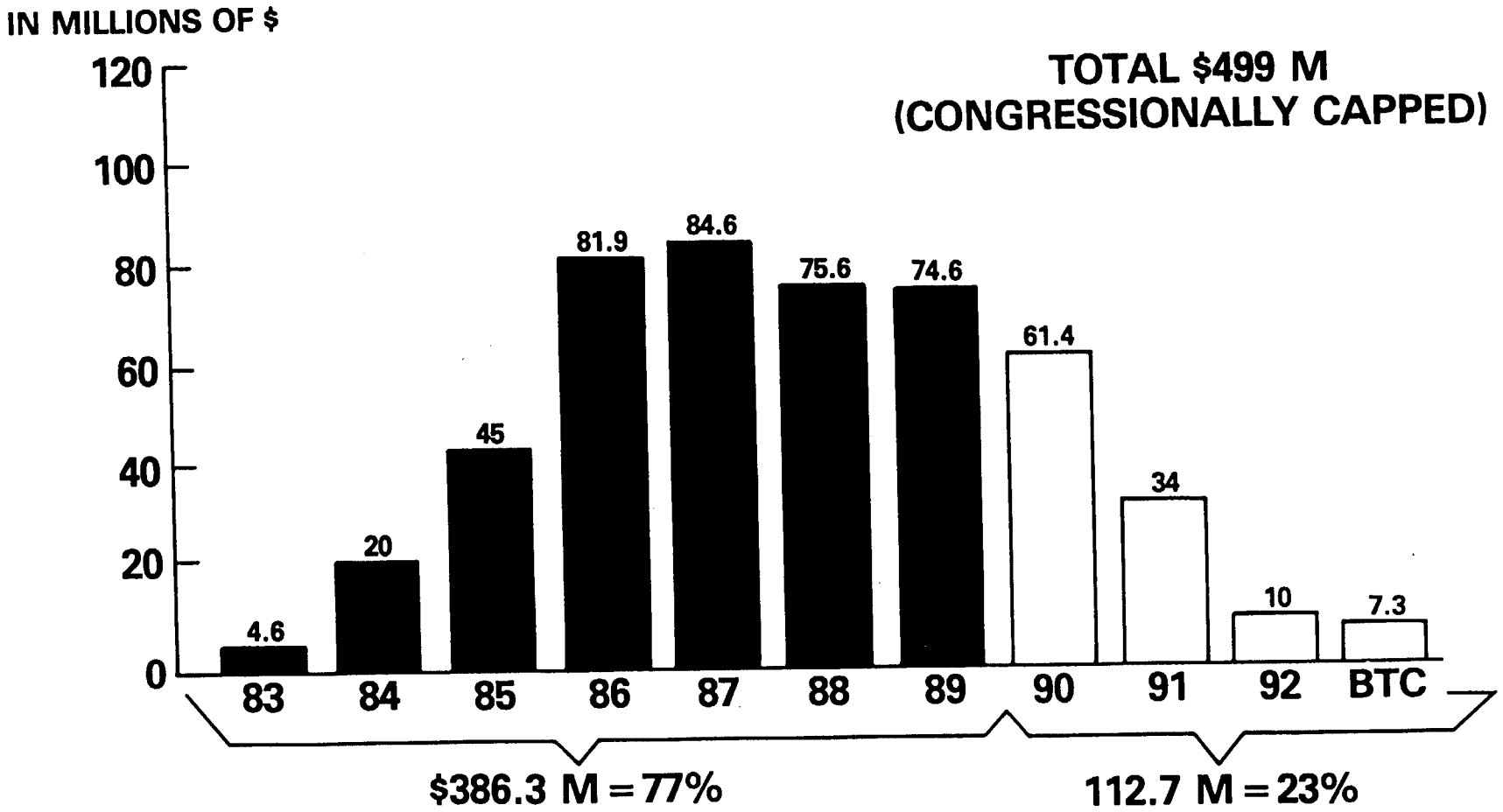

EC89-306(1)
1-26-89

ACTS

SYSTEM DESCRIPTION

Spacecraft Configuration

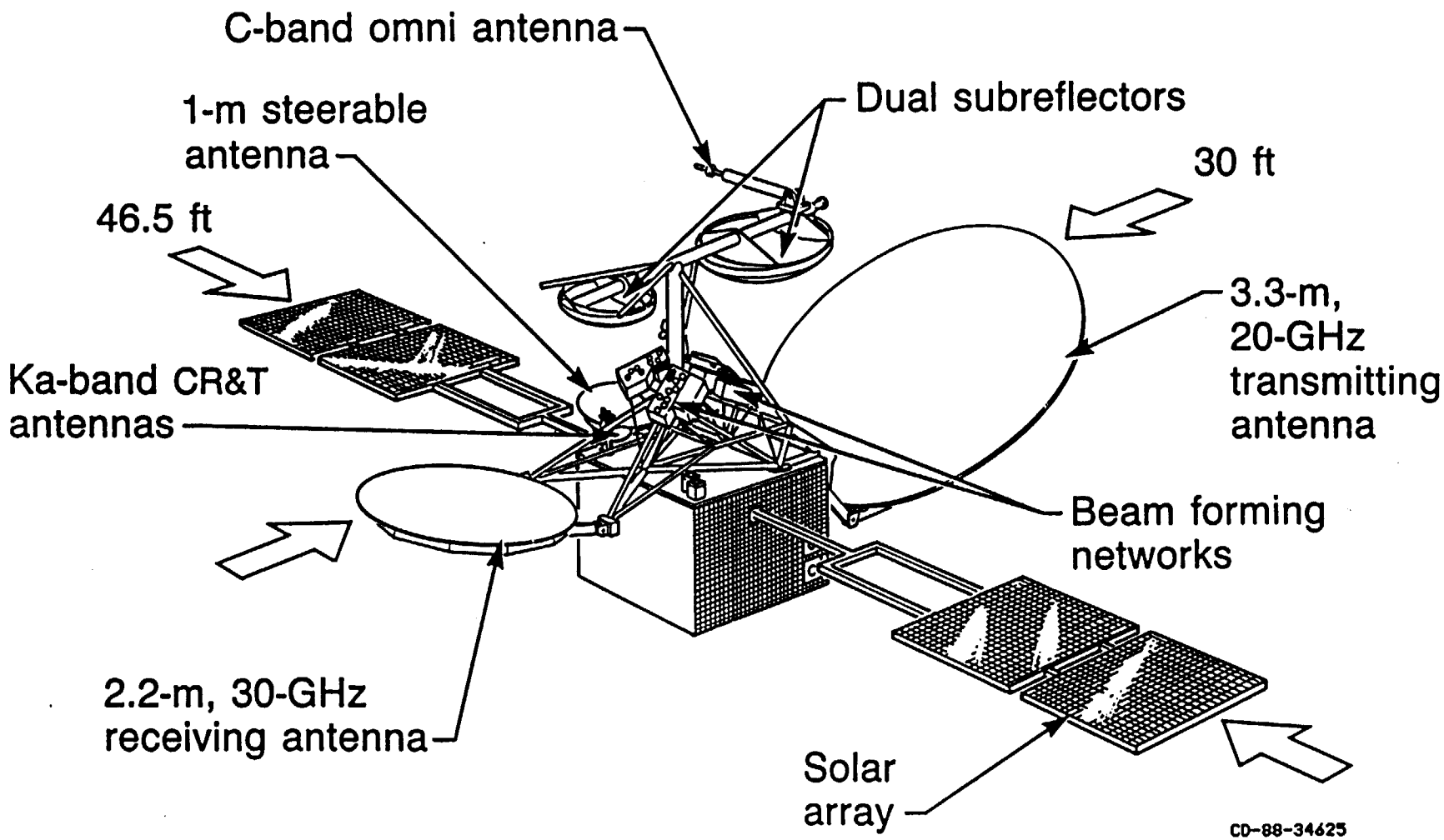

ACTS

NASA

FUNCTIONAL OVERVIEW OF ACTS FLIGHT SEGMENT

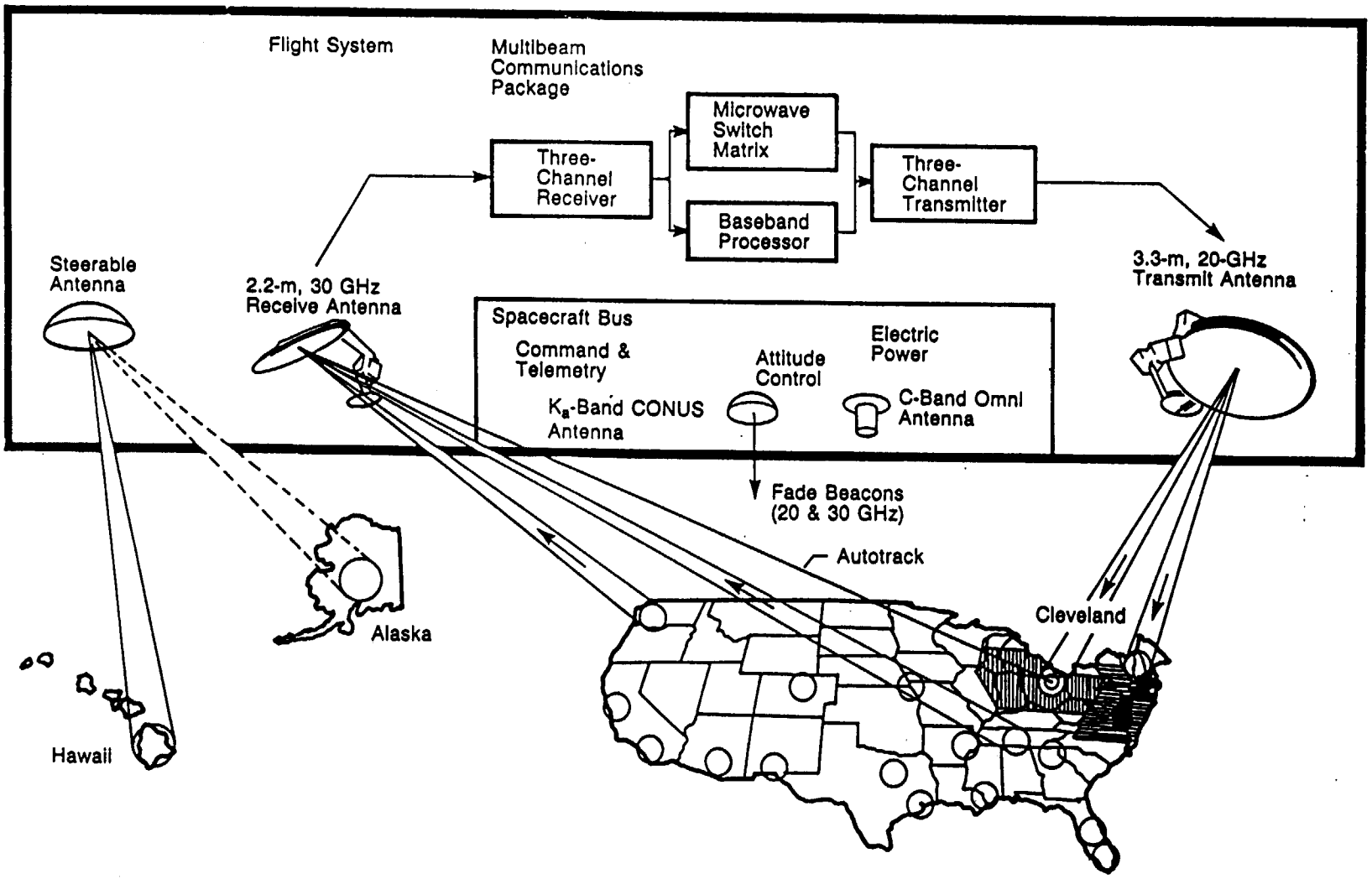

FUNCTIONAL OVERVIEW OF THE ACTS GROUND SYSTEM

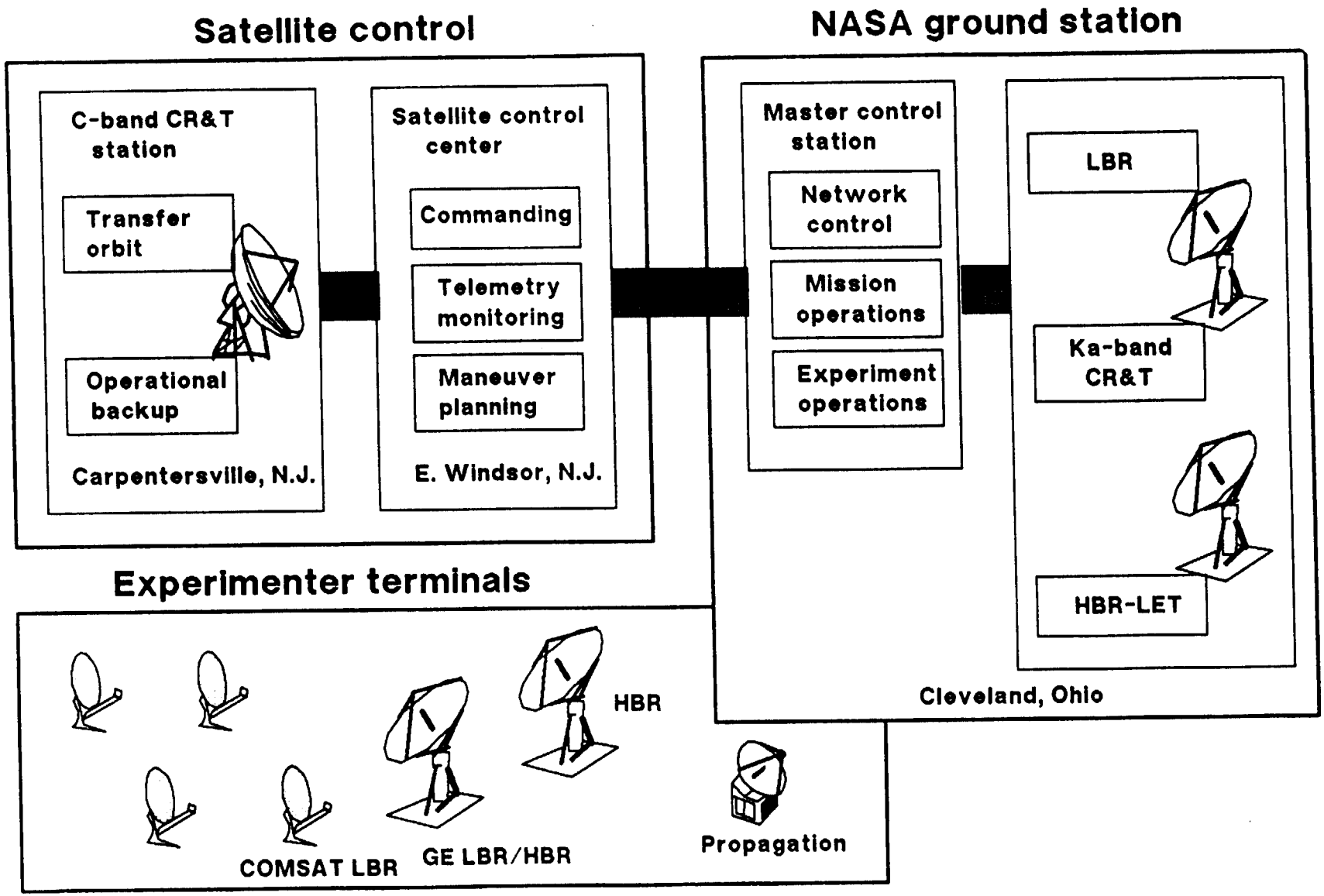

BENT PIPE vs SWITCHING SATELLITE

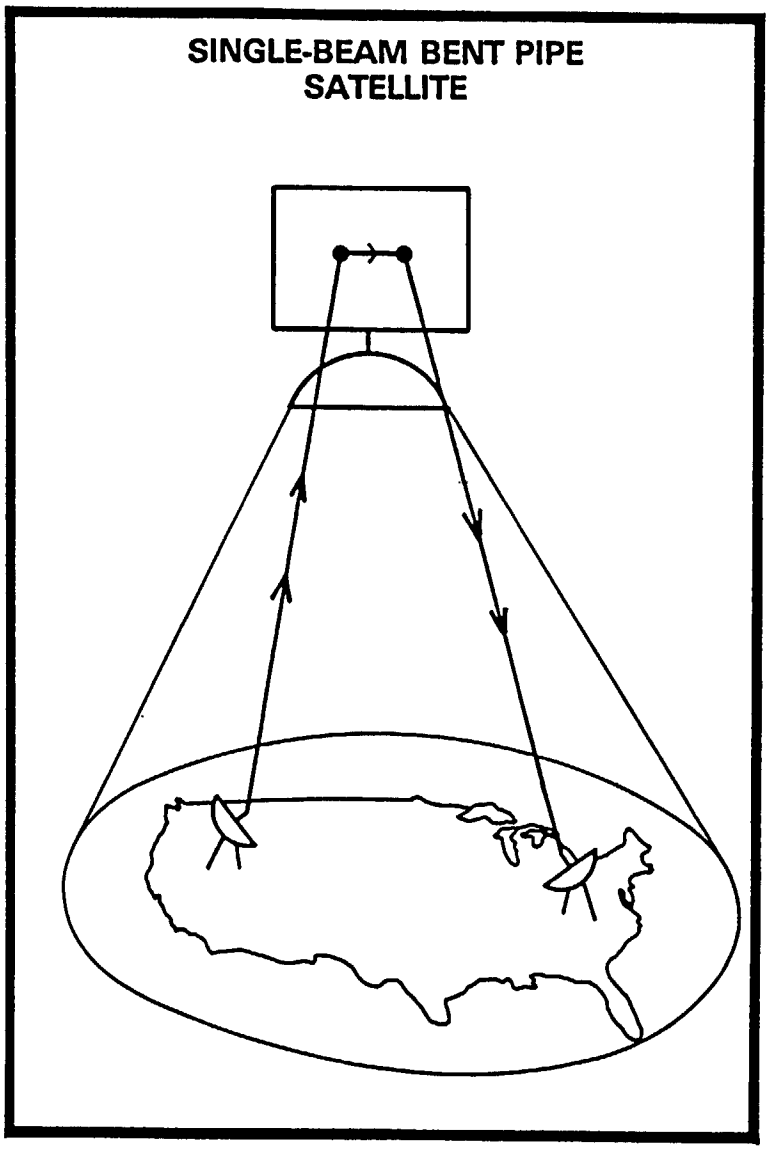

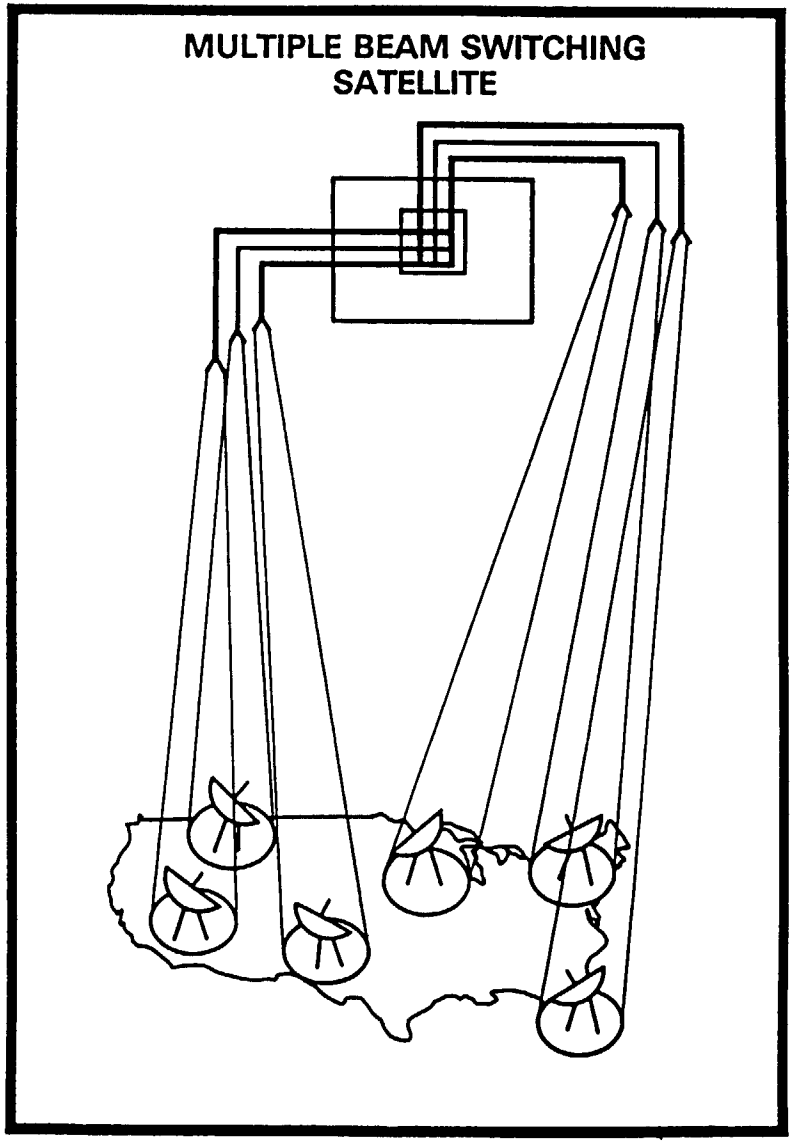

ACTS Multibeam Antenna Coverage

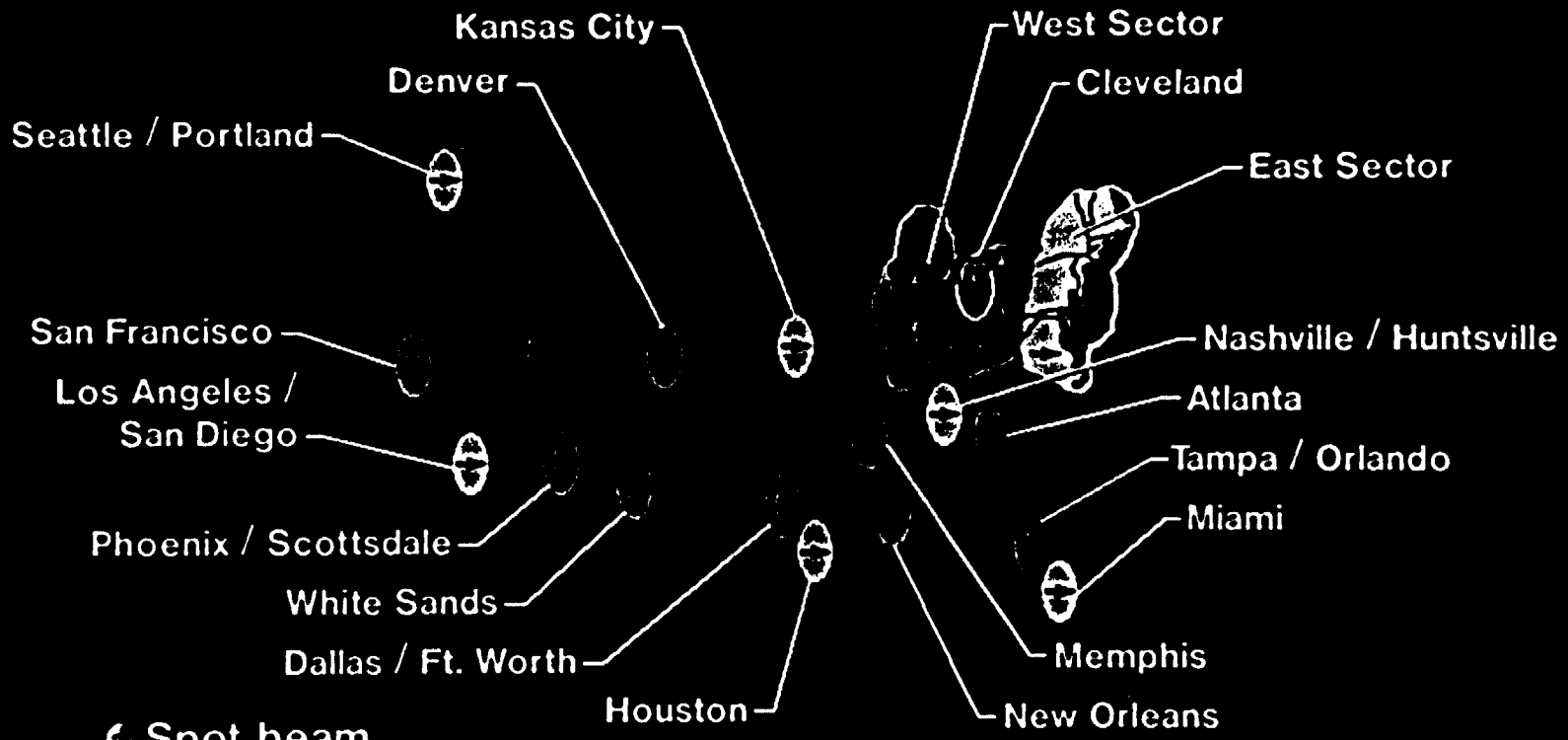

- Spot beam
- Fixed beam
- Polarization

ACTS at 100° west

- Steerable antenna will cover all of U.S. including Alaska and Hawaii

ACTS

NASA

ACTS Mechanically Steerable Beam Antenna Coverage

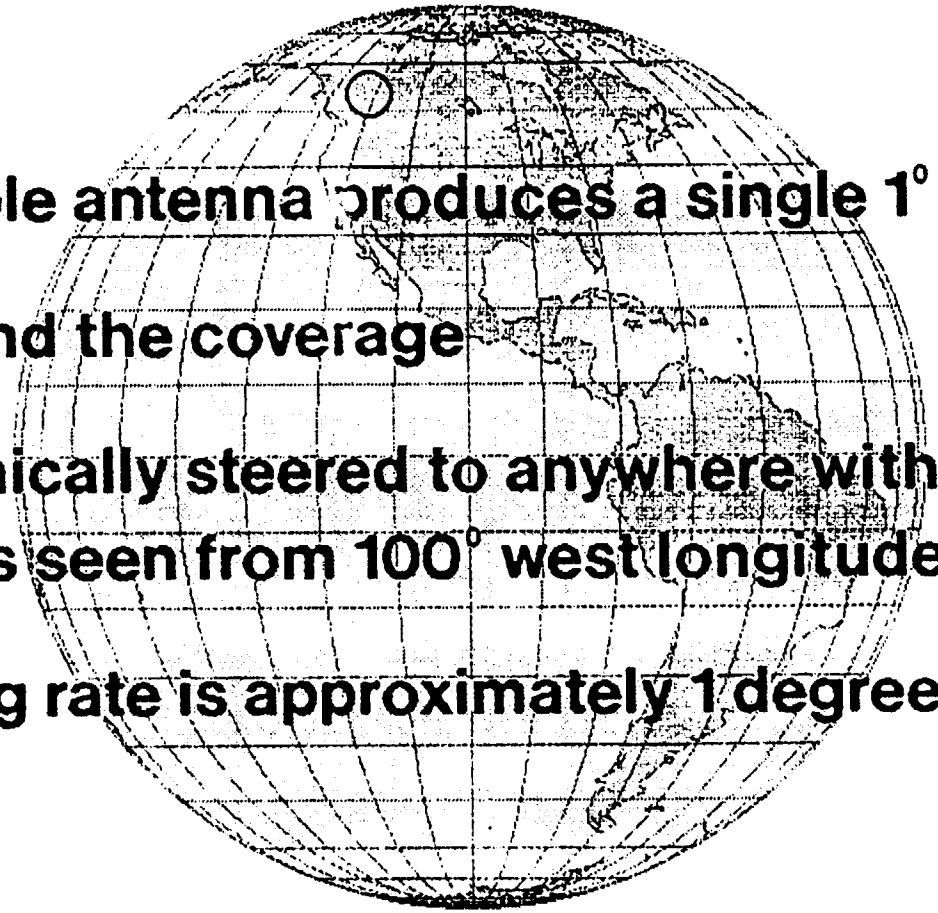

Steerable antenna produces a single 1° beam

To extend the coverage

Mechanically steered to anywhere within disk of earth as seen from 100° west longitude

Steering rate is approximately 1 degree / minute

CD-30157

ACTS Communications System

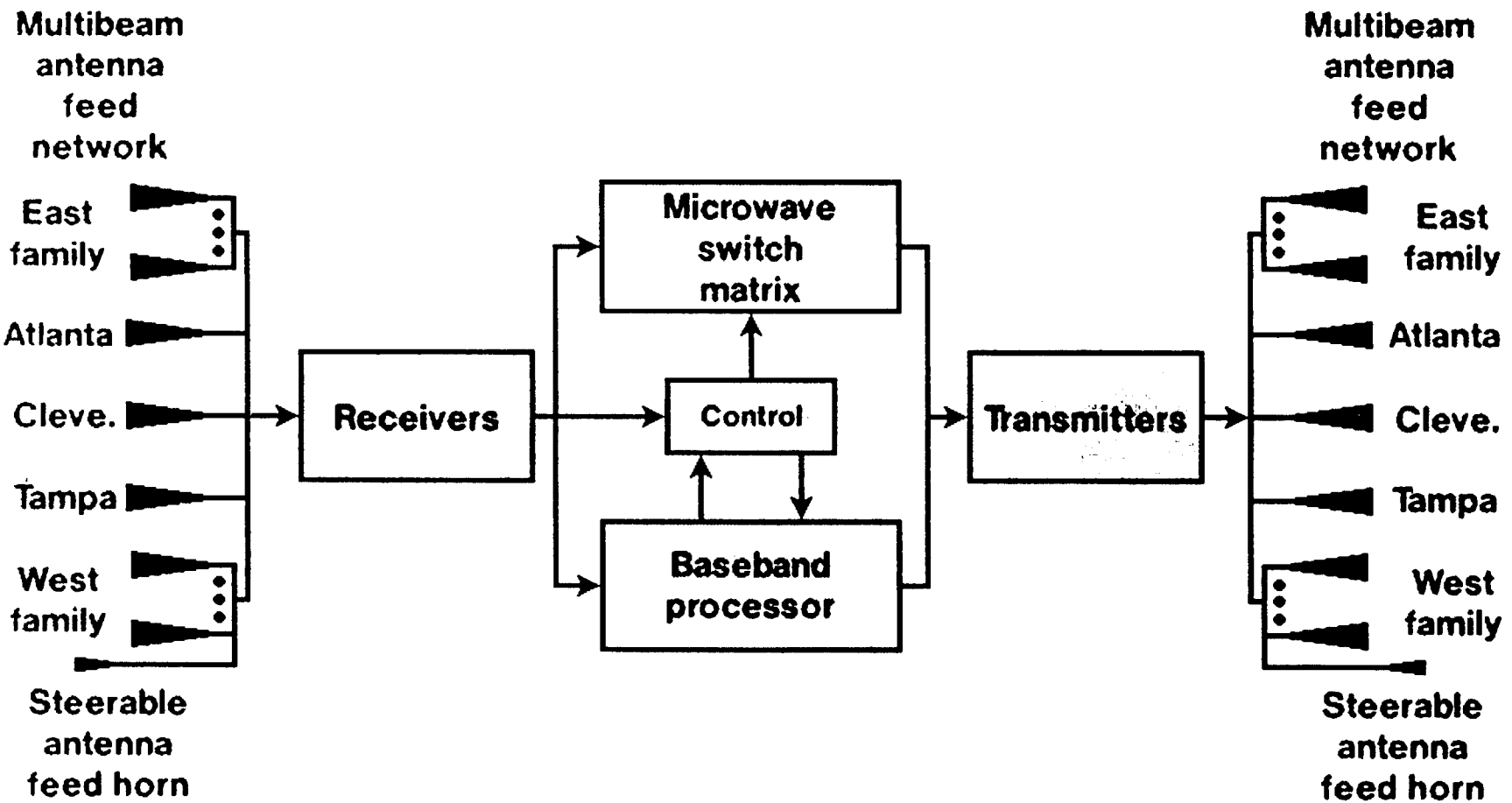

ACTS

NASA

Baseband Processor Mode
(OSBS-TDMA)

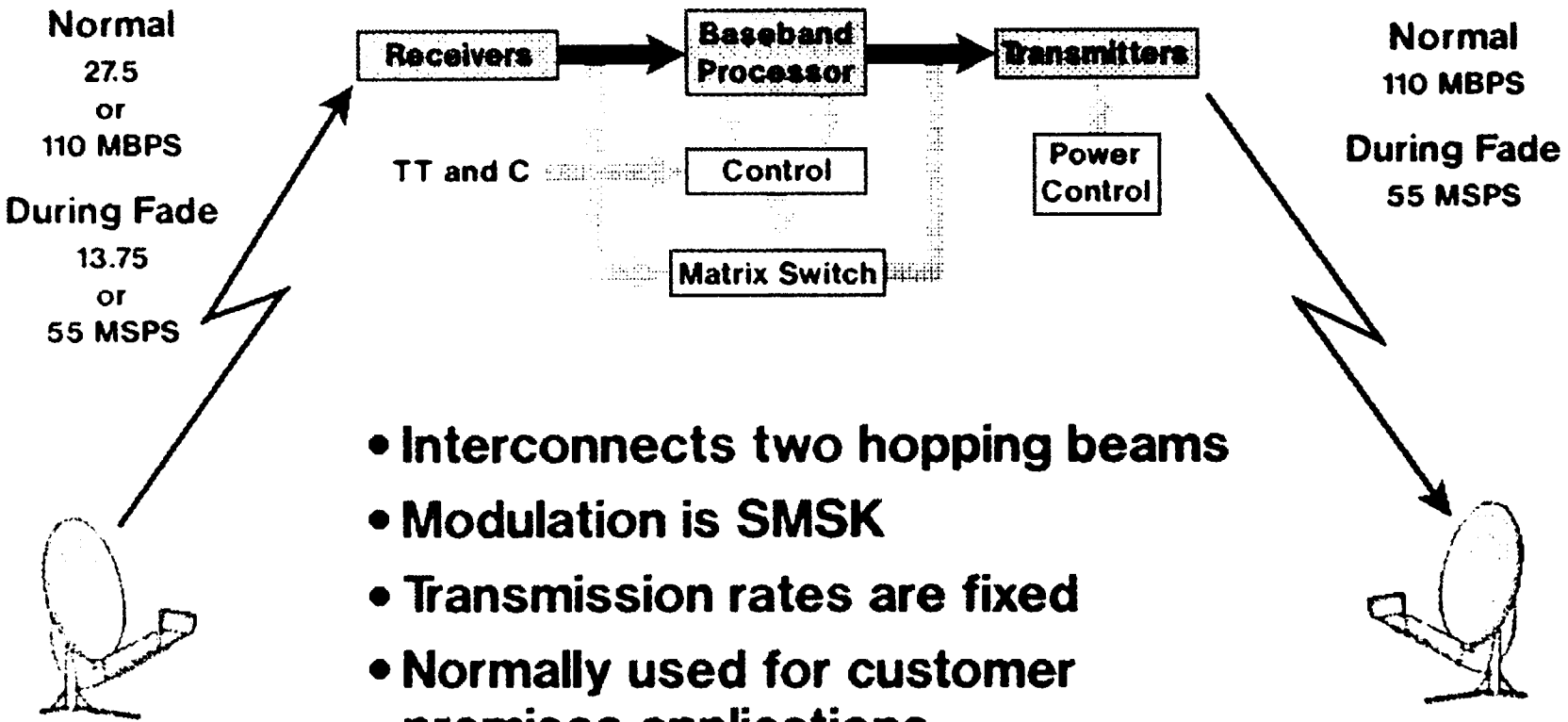

- Interconnects two hopping beams
- Modulation is SMSK
- Transmission rates are fixed
- Normally used for customer premises applications

Satellite Switching: What is on the Horizon?

- Bent pipe (no switching)
- All commercial satellites currently in orbit

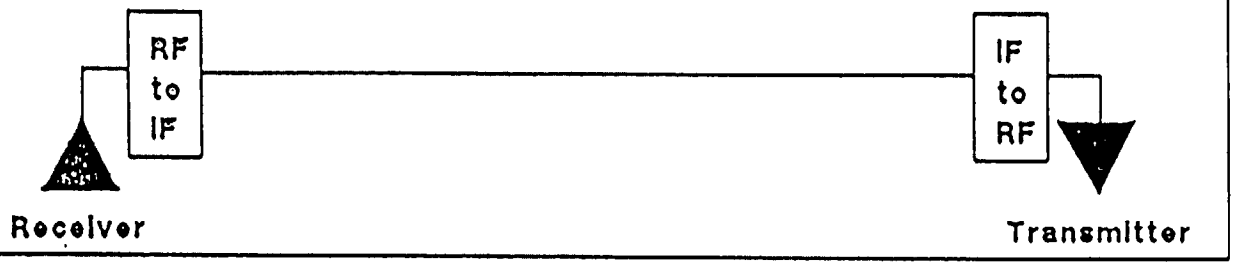

- Satellite switched TDMA (SS/TDMA)
- INTELSAT VI (1989)

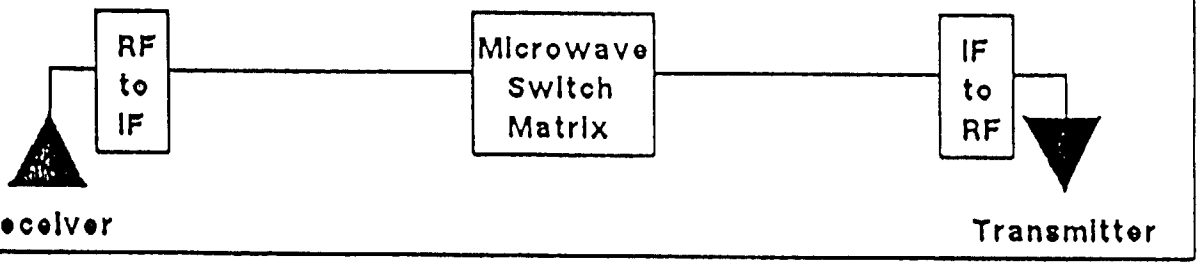

- Baseband switched TDMA (BBS/TDMA)
- ITALSAT (1991)

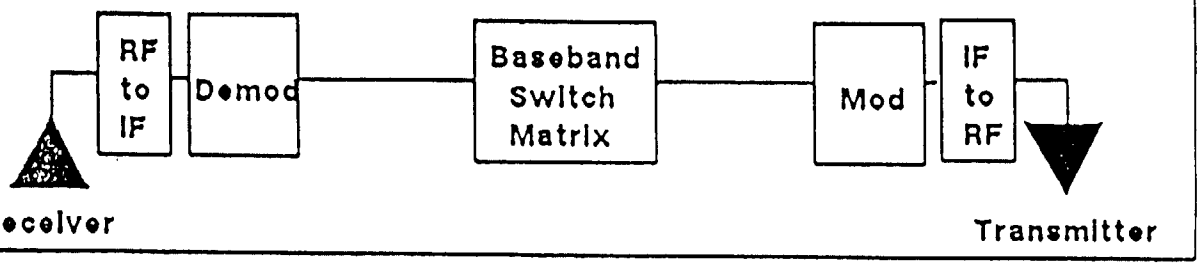

- Onboard stored baseband switched TDMA (OSBS/TDMA)
- ACTS (1992)

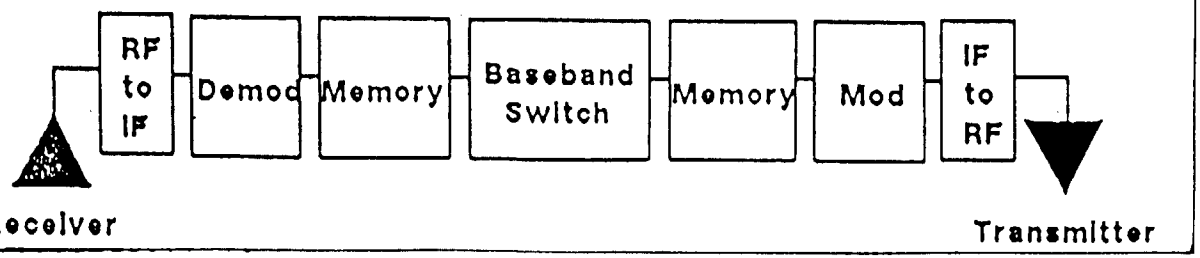

Microwave Switch Matrix Mode
(SS-TDMA)

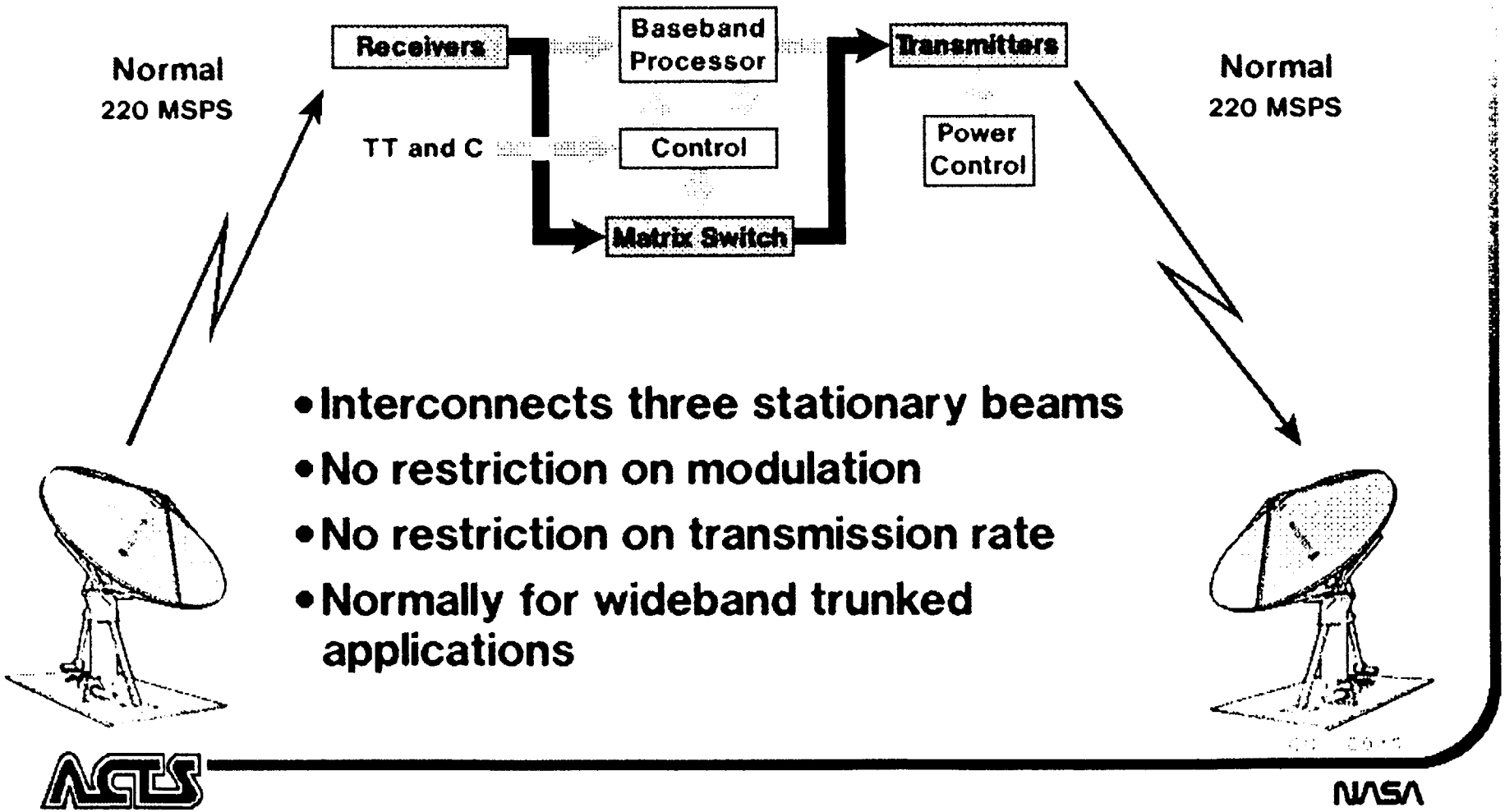

- Interconnects three stationary beams
- No restriction on modulation
- No restriction on transmission rate
- Normally for wideband trunked applications

ACTS

NASA

ACTS

EXPERIMENTS PROGRAM

PROGRAM GOALS

	GOAL	APPROACH
ACTS Overall Program	• Support Continued U.S. Industry Leadership In The World Communications Satellite Market	– Develop Advanced Technologies – Use Technologies In An Experiment Program
ACTS Experiments Program	• Stimulate Commercial Use of ACTS Technologies	– Demonstrate Technical Feasibility *Through Technical Performance Evaluation Experiments* – Demonstrate Applications *Through Applications Experiments* – Encourage Widest Possible Participation by All U.S. Institutions in the Program (Private, Government, DOD, Academia)

SUPPORT TO NON-NASA EXPERIMENTS

- NASA PROVIDES:
  - Spacecraft Time During Experiment Period
  - Master Control Station Operations
  - Experiment Planning and Technical Support as Requested
  - Access to NASA Facilities for Cooperative Experiments
  - Engineering Measurements Aboard Spacecraft and at Master Control Station (MCS)
  - Industry Source for Experimenter Ground Terminals
- EXPERIMENTERS PROVIDE:
  - Experiment Definition and Design
  - Experimenter Working Group Support
  - Special User Equipment
  - Experiment Operations
  - Analysis of Experiment Results
  - User Charges for Ground Terminals

ACTS PROPAGATION CONCERNS, ISSUES, AND PLANS

Faramaz Davarian
Jet Propulsion Laboratory
California Institute of Technology
Pasadena, California 91109

ACTS counters fading by resource sharing between the users. It provides a large margin only for those terminals which are at risk by unfavorable atmospheric conditions. A moderate power margin, known as the clear weather margin, is provided to all active users. Each user monitors one of the ACTS beacons continually to assess atmospheric conditions. If a severe reduction in the received beacon power is detected, the network master control station (MCS) is notified via orderwire channels. The MCS responds by instructing the terminal to reduce its bit rate and invoke coding. The MCS will also notify the terminal at the other end of the link as well as the satellite on-board processor. Both measures reduce the error rate in the data flow caused by atmospheric fading. ACTS, as an experimental satellite, provides a 5-dB clear weather margin and 10-dB additional margin via rate reduction and encoding. For the uplink, this margin may be increased by exercising uplink power control.

In achieving these goals, the radiowave propagation community faces a number of challenges. Among them are:

A) The 5-dB clear weather margin will be used for fade condition detection. Is this margin sufficient? Could we reduce this margin? For example, if our research shows that this margin can be reduced to 2 dB, a power saving of approximately 50% will result. This results in substantial reductions in cost for operational systems.

B) To invoke fade countermeasure, the system must determine that a fade is imminent. A conservative approach (delayed decision) will prove detrimental to the link experiencing a fade, whereas, overreaction can overburden an operational system. Hence, we need to develop techniques which can accurately predict fades in real time. Figure 1 depicts two fade scenarios that require two different responses. This figure shows the received signal power as a function of time (note that the time scale has been intentionally left out). The solid line shows a fade which requires a system response to counter the effect of fading, whereas, the dashed line shows a fade which does not require a system response. A 5-dB margin is also marked on Figure 1.

C) To facilitate the resource sharing feature of ACTS, nation-wide fade statistics are needed.

Our studies will focus on two issues: general needs and ACTS-specific needs. The general needs include:

A) Propagation data for VSAT with small power margin

B) Propagation data on short-term fades and fade slope

C) Fade countermeasure techniques

D) Nation-wide fade statistics

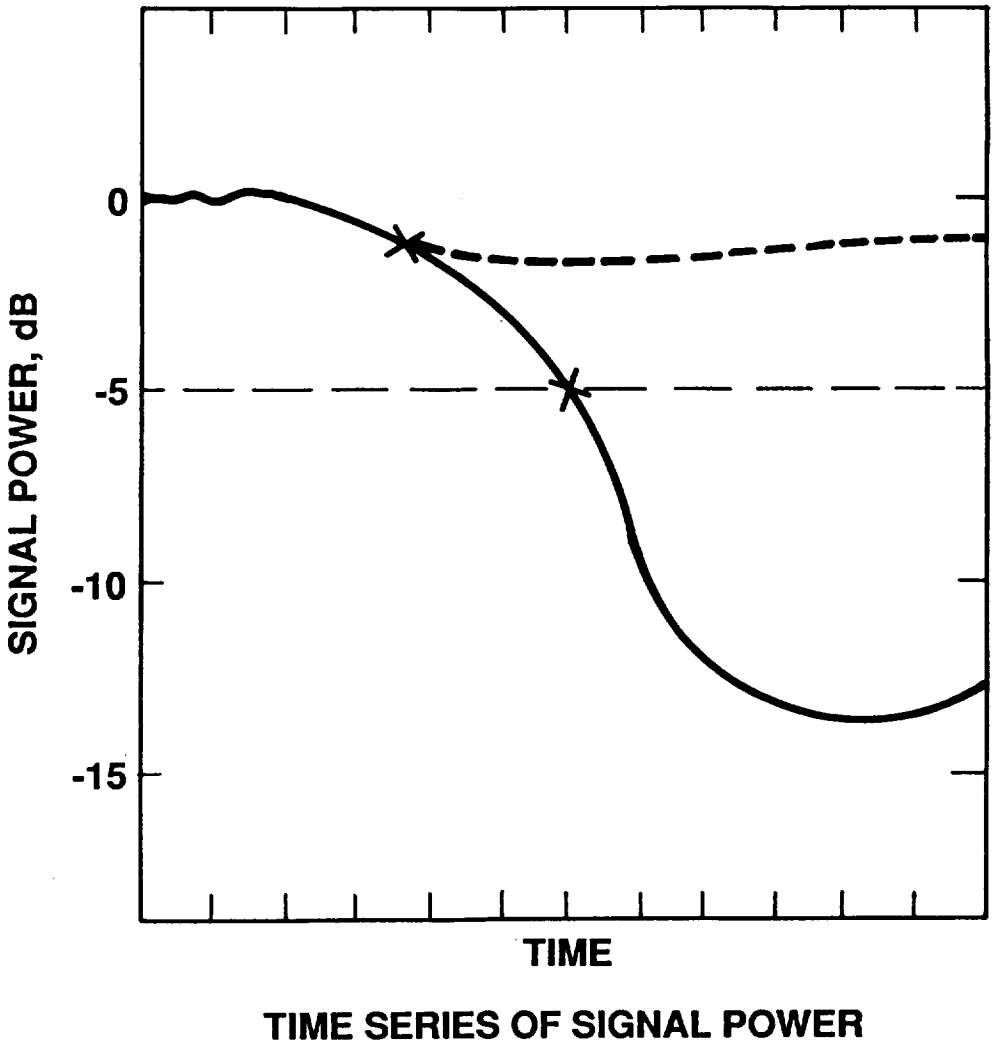

Figure 1. Fade Dynamics

To address ACTS-specific needs, an environment will be cultivated wherein propagation experts can develop, test and refine their models and schemes in a unified fashion. Furthermore, advice and assistance will be given to ACTS users.

What is required in the context of ACTS propagation needs is a convenient environment that propagation experts can conduct propagation studies. This environment should provide the experts with statistically significant observations. Data must be taken in climatologically diverse areas for long time durations. Fade countermeasure schemes must be tested thoroughly. Data collected and analyzed by different centers must be presented with a uniform and consistent format. ACTS experimenters in other areas, i.e., communications, data transmission, protocol, etc., should not be burdened with propagation issues. ACTS users should be able to receive advice and assistance from the ACTS propagation experimenters group. This must be performed in a manner convenient to ACTS users. Although many propagation research centers will participate in this task, a single organization must oversee the effort for cohesiveness of the endeavor.

NASA's Propagation Program is organizing a cohesive effort to respond to ACTS propagation needs. Our plans call for the development of low-cost propagation terminals consisting of beacon receivers, radiometers, and data acquisition systems, which will be loaned to different research centers and universities for data collection and analysis. The Propagation Program has already begun this effort by participating in the Olympus experiment, which is described in the article by Professor Stutzman of Virginia Tech. Table 1 shows the chronological order of events.

Table 1. Chronological Order of Events

Year	Activity
1989	Construct beacon receivers, radiometers, and a data acquisition system for the OLYMPUS experiment
1990	Perform OLYMPUS propagation experiments and collect data
	Design and build a prototype ACTS beacon receiver system
	Build a CODE* terminal
1991	Complete the OLYMPUS experiments
	Evaluate ACTS prototype propagation terminal using OLYMPUS
	Build 8 to 10 ACTS propagation terminals
1992	Start ACTS experiments

*CODE is an acronym for the cooperative OLYMPUS data exchange, a feature which allows an experimenter to exchange data with other OLYMPUS experimenters.

A reasonable question to ask is where should the ACTS propagation terminals be placed. In attempting to answer this question, we note that although ACTS beacons are received anywhere in the U.S. mainland, the spot beams are not available everywhere. To enjoy the potential benefits of proximity to a communications terminal, one may suggest to place the propagation terminals where communications coverage is also available. Of course, selecting a site based on spot beam availability alone is hardly a sufficient reason. Therefore, we note the Global Rain Climate map of the U.S., which includes an overlay of ACTS coverage areas as depicted in Figure 2. The map in Figure 2 is a clue for the answer to the above question.

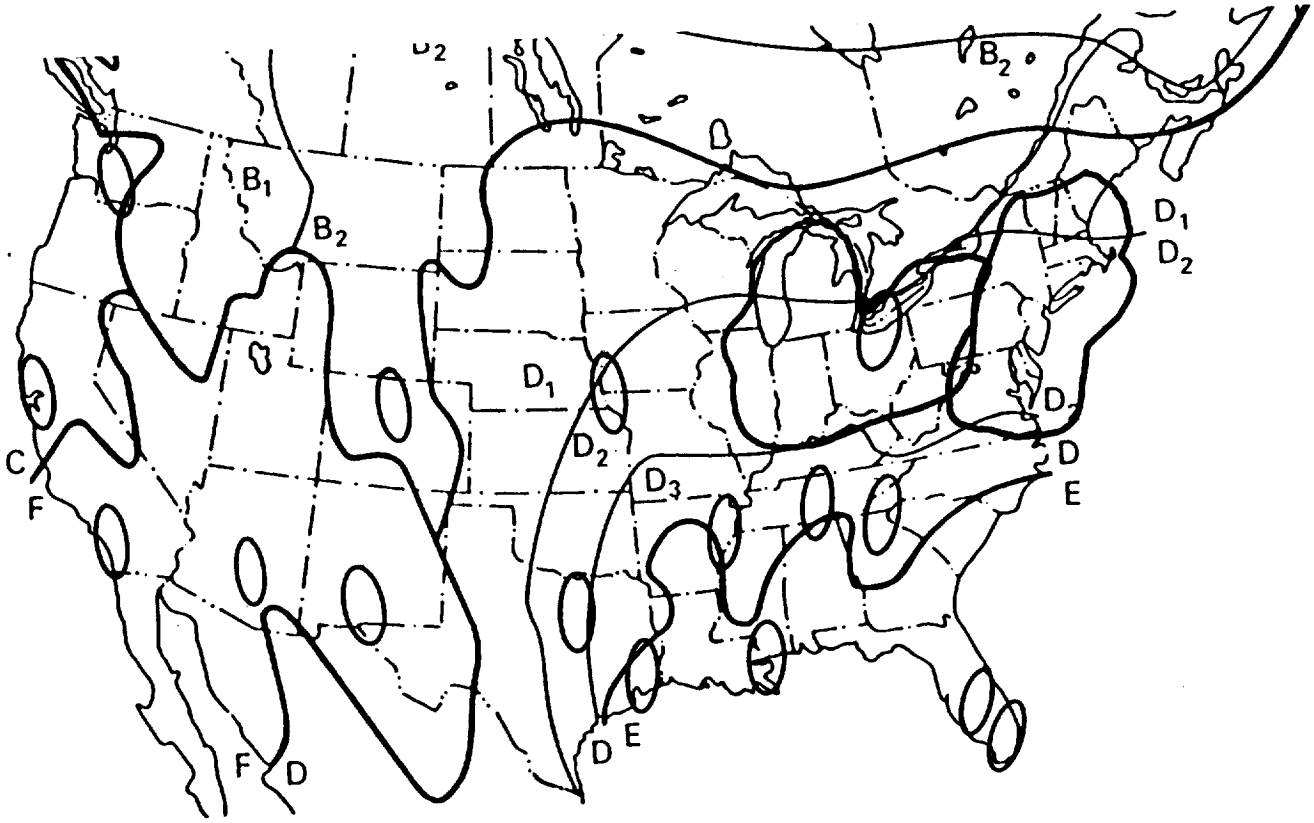

Figure 2. Rain Rate Regions for the Continental U.S.: Crane Global Model, 1980

However, before selecting the locations for ACTS propagation terminals we need to consider one more parameter, namely the existing propagation data. For this purpose, we may refer to Figure 3, where the 20/30-GHz data availability in the U.S. is shown. Figure 3 reveals that most of the past data were taken at the east coast and the south. There are no data available from the west, southwest, north, and the Rockies. Hence, we need to make sure that the areas that lack propagation data receive attention.

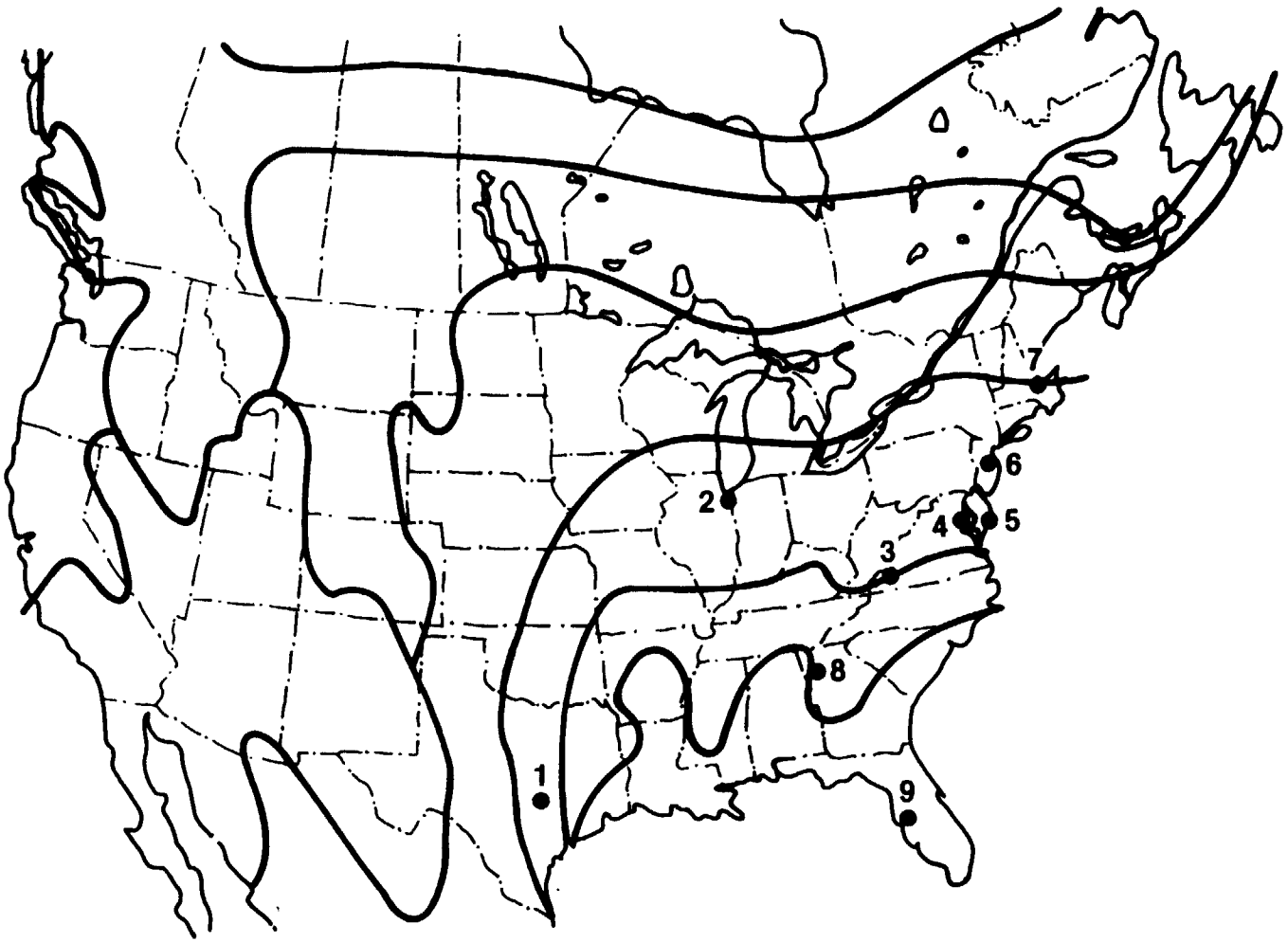

LEGEND:

1. **AUSTIN, TX**
2. **GRANT PARK, IL**
3. **BLACKSBURG, VA**
4. **CLARKSBURG, MD**
5. **WALLOPS ISLAND, VA**
6. **HOLMDEL, NJ**
7. **WALTHAM, MA**
8. **PALMETTO, GA**
9. **TAMPA, FL**

Figure 3. 20/30-GHz Data Availability

With considerations given to Figures 2 and 3, a suggested set of locations for placing ACTS propagation terminals emerges. Table 2 shows these locations. Note that according to the Global Rain-Zone Model there are 8 rain zones in the U.S. Table 2 suggests one terminal per rain zone with the exception of zone D1, which is allotted two terminals. Also note that with the exception of the terminal in zone B1, all the other terminals are in areas that receive ACTS communications coverage.

The Propagation Program will sponsor a two-day workshop on ACTS propagation in Fall 1989. It is hoped that most of the issues addressed in this article will be discussed thoroughly in the workshop. The theme of the workshop is "Planning ACTS Propagation Studies, and Standardization of Propagation Data Collection and Reduction."

Table 2. Suggested Set of Locations Using Crane's Zones

Zone	Location	Number of Stations
B1	Idaho	1
B2	Denver	1
F	Los Angeles/Phoenix/White Sands	1
C	San Francisco/Seattle	1
D1	New Hampshire/Michigan	2
D2	Blacksburg	1
D3	Atlanta	1
E	New Orleans/Tampa/Miami/Houston	1
	Total	9

U.S. ACTIVITY WITH THE OLYMPUS SATELLITE

Warren L. Stutzman

Satellite Communications Group
Bradley Department of Electrical Engineering
Virginia Tech
Blacksburg, VA 24061

Richard Campbell
Department of Electrical Engineering
Michigan Tech
Houghton, MI 49931

Future communication systems will move toward the 20/30 GHz frequency range for wider bandwidth and reduced interference, and will use small earth terminals (VSATs). Previously, communication systems used large earth terminals with wide fade margins to achieve high reliability. Modest reliability requirements coupled with fade compensation techniques (uplink power control, variable rate encoding, dynamic resource sharing, etc.) have made inexpensive, low margin VSAT terminals practical. Past propagation experiments accumulated data for the wide margin system configurations; however, emphasis must now shift to the measurement and modeling of low margin systems. This requires accurate measurement of fade statistics and fade dynamics for low/moderate fading. Fade dynamics now play an important role in the design of compensation schemes.

The European Space Agency satellite OLYMPUS is scheduled for launch this June and will be ready for use in October. OLYMPUS has 12, 20, and 30 GHz beacons (more accurately 12.5, 19.77, and 29.66 GHz). Virginia Tech and Michigan Tech are working with NASA/Jet Propulsion Laboratory on an OLYMPUS experiment and hardware development program. Receiving systems at 12, 20, and 30 GHz will be installed at Virginia Tech.

OLYMPUS beacons provide coverage of the east coast of the United States sufficient for attenuation measurements. The elevation angle to Blacksburg, Virginia, is 14 degrees. A unique feature of the OLYMPUS beacon package is that the three spacecraft beacons are derived from a common oscillator, yielding coherent beacons. The Virginia Tech OLYMPUS receivers are designed to take advantage of this coherence by deriving frequency locking information from the 12 GHz

receiver for all three frequency receivers. This widens the effective dynamic range of the 20 and 30 GHz receivers, which are more susceptible to fading during a rain event. A useful dynamic range of 34 dB is expected from both the 20 and 30 GHz receivers.

Clouds and scintillation can produce up to 3 dB attenuation at 30 GHz on a 14 degree elevation angle path and may be present for a high percentage of the time. It is important in a slant path propagation experiment to be able to set the "clear air reference" level accurately. We are incorporating radiometers at each beacon frequency into our receiving system to aid in setting this clear air reference level. The radiometers are of the total power design; the RF and IF sections are housed in temperature controlled environments to keep gain constant.

The east coast of the United States is far off boresight of the OLYMPUS 20 and 30 GHz antennas. As a result, there will be a loss of antenna gain from the satellite, not exceeding 8 dB at 30 GHz. There is sufficient EIRP from the beacons for good measurements to be made with moderate sized antennas. Cross-polarization measurements are not feasible, however, because the satellite antennas have low XPD well away from boresight.

Figure 1 illustrates the planned hardware for the OLYMPUS experiments. The objectives of the experiment are summarized in Table 1. The receiving antennas are 12, 5, and 4 feet in diameter at 12, 20, and 30 GHz, respectively. Thus, the 20/30 GHz portion of the experiment will employ VSAT class terminals. There is a second 20 GHz receiver identical to the first for the purpose of examining small scale diversity. Although widely spaced diversity terminals have been studied for deep fade cases, short baseline diversity for low/moderate fading has not.

Table 1 summarizes the components of the experiment. Fade measurements are directed toward producing data necessary to assemble information on the following: fade occurrence frequency, fade duration and fade interval statistics, frequency scaling of attenuation, and fade slope data. Small scale diversity will be examined as well.

Figure 2 gives a block diagram level overview of a typical channel and Figure 3 shows one of the four RF front ends. In all cases a common IF frequency of 1120 MHz is used. Receiver hardware and software have been designed to be used directly (or in some cases with modification) with ACTS. The analog receiver includes a digital detection scheme developed at Virginia Tech. It produces a 16-bit digital output directly from a 10 kHz signal for in-phase and quadrature-phase

components, allowing amplitude and phase extraction via software in the Data Acquisition System (DAS). The sample rate is variable between 10 and 100 Hz.

The total power radiometers at 12, 20 and 30 GHz use the same front ends as the main receivers. A 25 MHz band of noise is filtered at the 1120 MHz IF, and detected with a square-law diode. A noise calibrator is included which injects a known level of excess noise into the radiometer front end at regular time intervals. Two point calibration of the radiometers is accomplished using hot and cold loads. The total power radiometer is very sensitive to gain changes in the RF and IF amplifiers, which produce the same changes in the radiometer output as variations in antenna noise temperature. All components in the radiometers will be in temperature controlled environments with better than $1^{o}C$ temperature stability. MMIC amplifiers will be used in the 1 GHz IF stages. These amplifiers have heavy feedback and show very small gain drift with temperature.

The data acquisition system (DAS) software developed for this project is a menu driven package that permits data collection and preview/display. Propagation data from as many as eight channels will be collected, stored, and displayed in real time. Included in the data analysis system display are status information for system components as well as weather conditions.

Table 1
Components of the OLYMPUS Experiment at Virginia Tech

Attenuation Measurements

Attenuation data will be collected from the 12, 20, and 30 GHz OLYMPUS beacons during a one year period for the following uses:

- Fade statistics
- Fade duration
- Fade interval
- Frequency scaling of attenuation
- Support of studies mentioned below

Radiometric Measurements

Radiometric data will be collected to assist in setting reference levels to improve low level attenuation measurement accuracies. However, such data may be useful in its own right.

Fade Slope Measurements

Statistics on the rate at which individual fades begin and end (in dB per second) will be accumulated and correlated with the physics of propagation.

Small Scale Diversity

A moveable 20 GHz terminal will be stationed near the main 20 GHz terminal.

Attenuation data at the diversity station will be compared to that for the main terminal during the same sub-year time interval.

Diversity gain will be examined for each station as a function of baseline distance.

Uplink Power Control

Attenuation data on 20 GHz will be used to test various uplink power control algorithms to predict how fading could be relieved if uplink power control is used.

Meteorological Support

Tipping bucket rain gauges
X-band PPI radar

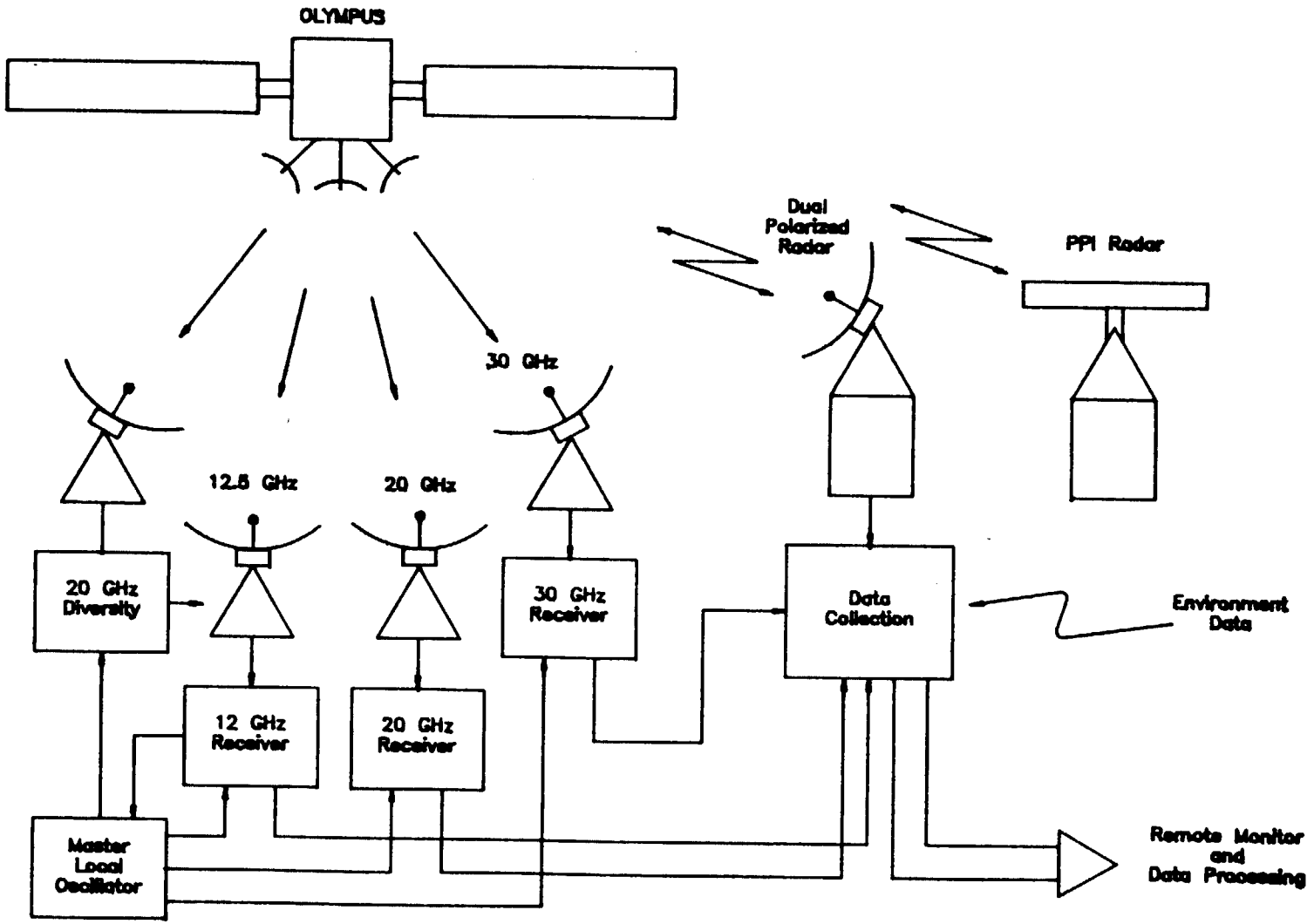

Figure 1. Overview of the proposed OLYMPUS experiment at Virginia Tech.

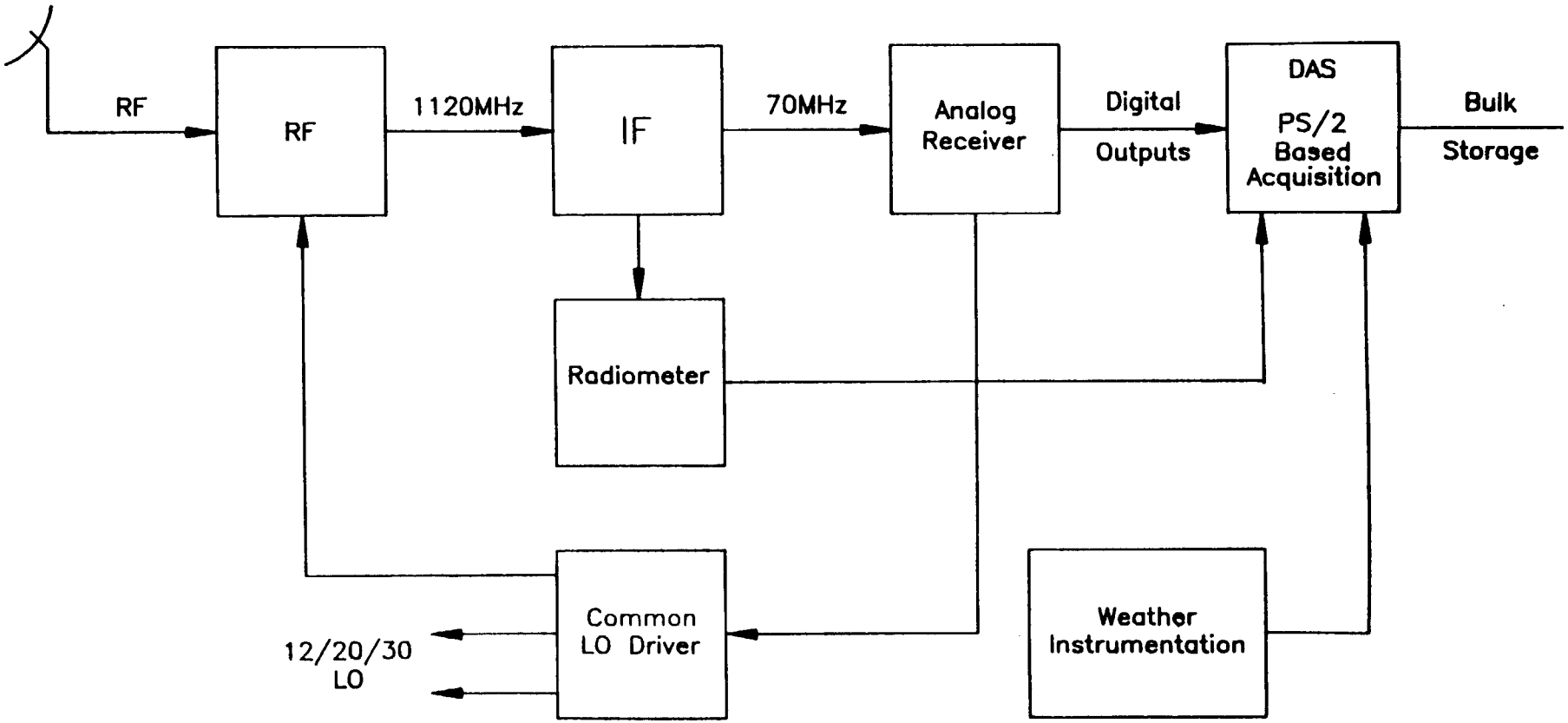

Figure 2. Block diagram of one OLYMPUS receiver.

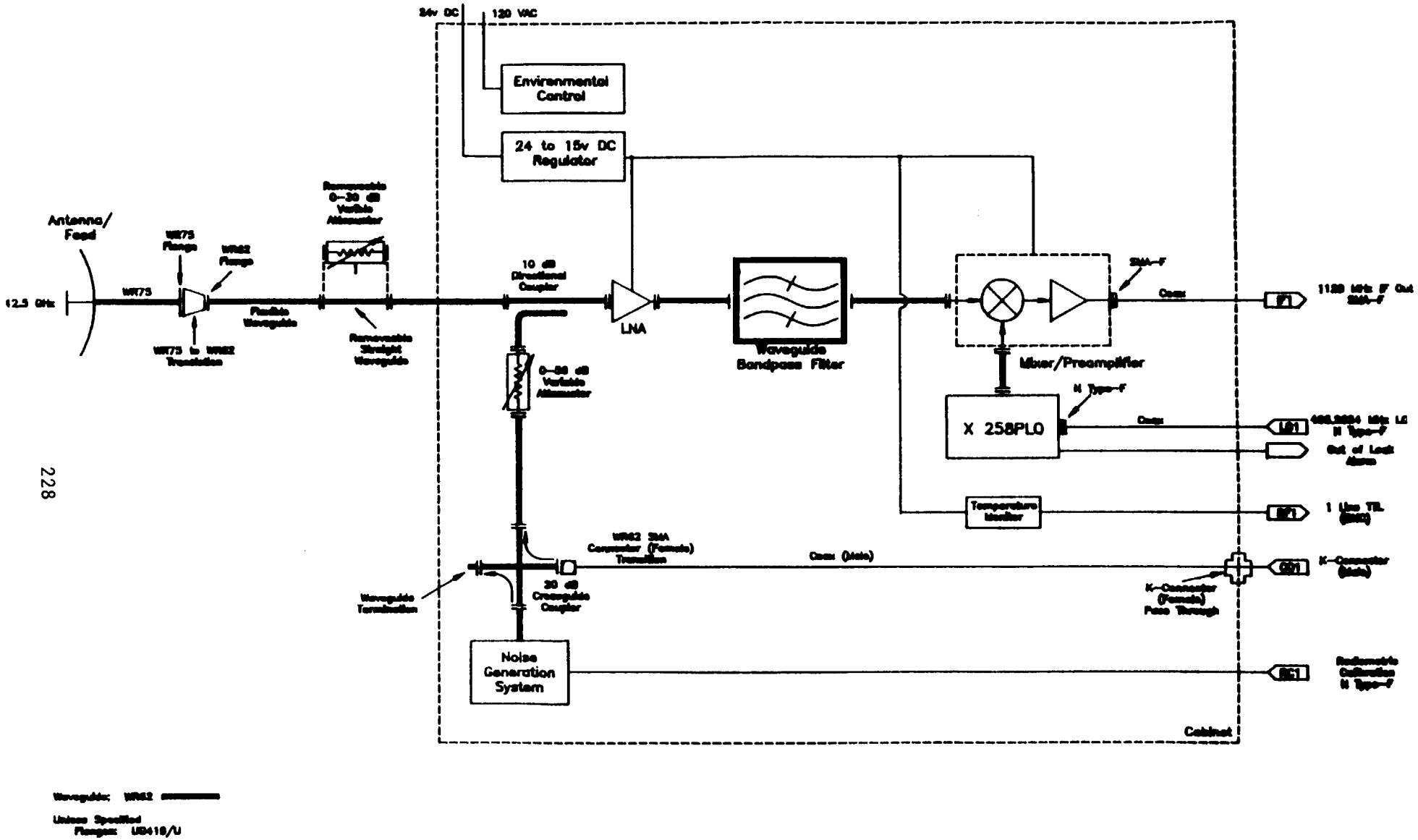

Figure 3. Block diagram of OLYMPUS the 12.5 GHz RF section.

PROPAGATION EXPERIMENTS MANAGEMENT PLAN

John Kiebler
NASA Headquarters
Washington, DC 20546

PROPAGATION EXPERIMENTS PROGRAM (PEP)

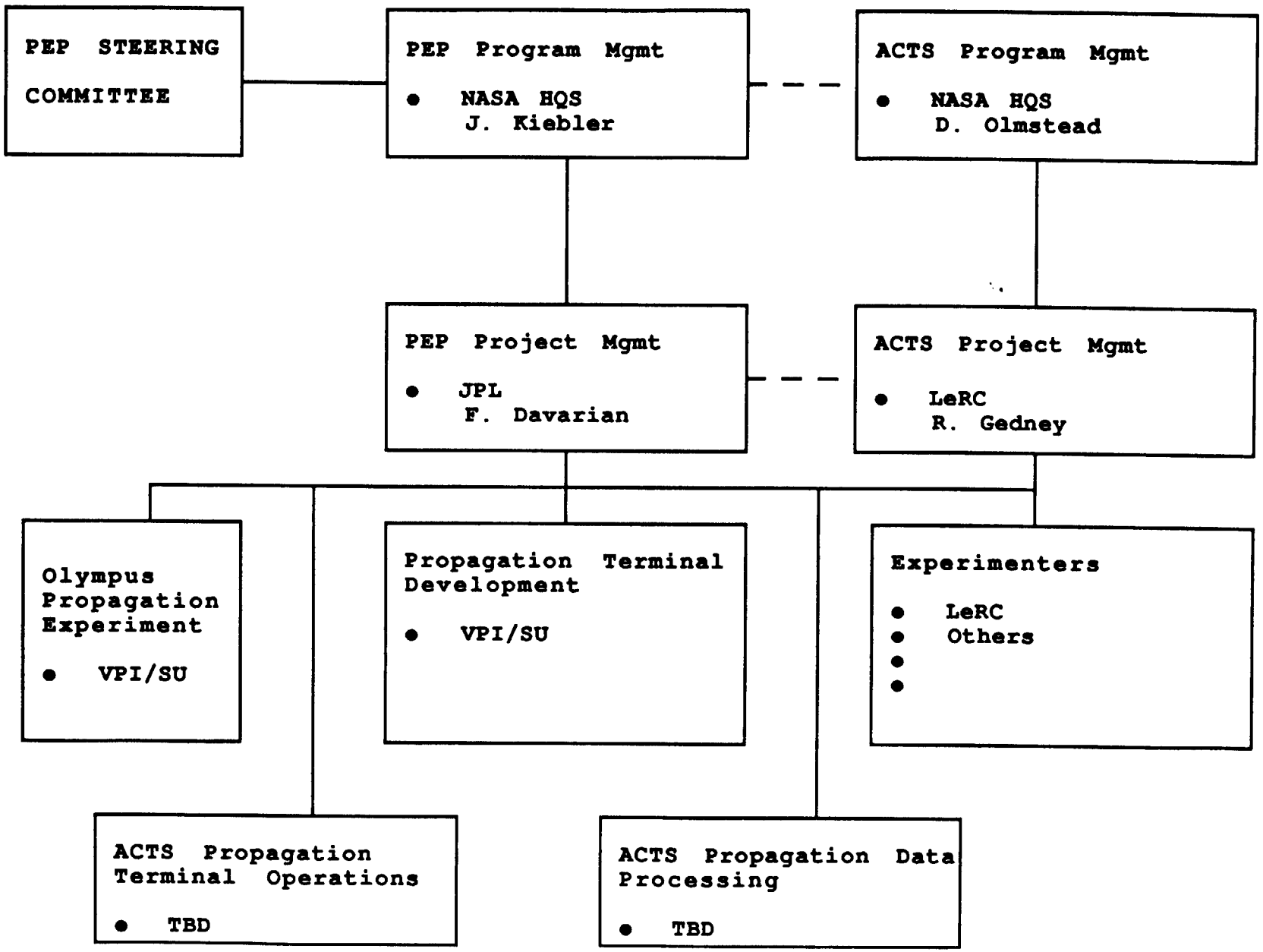

FUNCTIONS OF ACTS PROPAGATION EXPERIMENTS PROGRAM (PEP) COMMITTEE

- Foster awareness of the opportunity to conduct propagation measurements using ACTS within the government, industry and university communities.
- Critique PEP plans and recommend changes.
- Serve as a liaison between the ACTS Project Office and the propagation community in propagation related matters and issues.
- Advise NASA on propagation related experiments that should be conducted. Act as a catalyst to foster their development within the propagation community.
- Advise NASA on solicitation and selection criteria for propagation experiments.
- Review and coordinate all ACTS propagation experiment.
- Advise NASA on the types of technical information and documentation that is required for proposing, developing and conducting ACTS propagation experiments.
- Provide advocacy for the ACTS experiments program.
- Maintain cognizance of spacecraft development progress and advise on issues germane to propagation experiments program.

WORKSHOP ON ACTS EXPERIMENT PLANNING

AND

MEASUREMENT AND DATA REDUCTION STANDARDIZATION

- OBJECTIVE
  - PROVIDE A FORUM FOR DISCUSSIONS RELATED TO PROPAGATION
  - DISCUSS AND IDENTIFY ACTS PROPAGATION NEEDS WITH EMPHASIS GIVEN TO SYSTEM ASPECTS
  - DISSEMINATE UP-TO-DATE CHARACTERISTICS OF ACTS BEACONS AND SPACECRAFT
  - PLAN A COHESIVE SET OF EXPERIMENTS
  - INTRODUCE A UNIFORM APPROACH TO DATA COLLECTION AND REDUCTION

WORKSHOP FORMAT AND AGENDA

- PARTICIPANTS
  - INVESTIGATORS OF THE NASA PROPAGATION PROGRAM
  - REPRESENTATIVES OF THE ACTS PROGRAM OFFICE AND CONTRACTORS
  - EXPERIMENTERS WHO HAVE PREVIOUSLY INDICATED INTEREST IN CONDUCTING ACTS PROPAGATION EXPERIMENTS
  - OTHERS FROM THE PROPAGATION COMMUNITY
- DURATION
  - TWO DAYS
- AGENDA
  - DAY 1:
    - PRESENTATIONS ON ACTS BEACONS AND SPACECRAFT
    - DESCRIPTION OF OLYMPUS EXPERIMENT DESIGN AND STATUS
    - PRESENTATION OF STRAWMAN PLANS FOR ACTS PROPAGATION EXPERIMENTS
  - DAY 2:
    - DISCUSSIONS, CRITIQUE OF STRAWMAN PLANS
    - PREPARATION OF RECOMMENDED EXPERIMENT PROGRAM BY PARTICIPANTS
- PLACE AND TIME
  - JPL OR ENVIRONS
  - LATE 1989

TECHNICAL REPORT STANDARD TITLE PAGE

1. Report No. 89-26	2. Government Accession No.	3. Recipient's Catalog No.
4. Title and Subtitle Proceedings of the Thirteenth NASA Propagation Experimenters Meeting (NAPEX XIII)		5. Report Date August 15, 1989 6. Performing Organization Code
7. Author(s) Faramaz Davarian, Editor		8. Performing Organization Report No.
9. Performing Organization Name and Address JET PROPULSION LABORATORY California Institute of Technology 4800 Oak Grove Drive Pasadena, California 91109		10. Work Unit No. 11. Contract or Grant No. NAS7-918 13. Type of Report and Period Covered JPL External Publication
12. Sponsoring Agency Name and Address NATIONAL AERONAUTICS AND SPACE ADMINISTRATION Washington, D.C. 20546		14. Sponsoring Agency Code

15. Supplementary Notes

(Held at the Red Lion Inn, San Jose, California, June 29-30, 1989)

16. Abstract

The NASA Propagation Experimenters Meeting (NAPEX), supported by the NASA Propagation Program, is convened annually to discuss studies made on radio wave propagation by investigators from domestic and international organizations. NAPEX XIII was held on June 29 and 30, 1989, at the Red Lion Inn, San Jose, California, and consisted of representatives from England, Italy, Japan, the Netherlands, and the United States. The meeting was organized into three technical sessions: The first focused on mobile satellite propagation; the second examined the propagation effects for frequencies above 10 GHz; and the third addressed studies devoted exclusively to the Olympus/Advanced Communications Technology Satellite ACTS) Program.

17. Key Words (Selected by Author(s))	18. Distribution Statement
Communications Optics Wave Propagation	Unclassified--Unlimited

19. Security Classif. (of this report)	20. Security Classif. (of this page)	21. No. of Pages	22. Price
Unclassified	Unclassified	233	